SLAC–487
UC-414

LONGITUDINAL DYNAMICS AT THE STANFORD LINEAR COLLIDER*

R.L. Holtzapple

Stanford Linear Accelerator Center
Stanford University
Stanford CA 94309

SLAC–Report–487
June 1996

Prepared for the Department of Energy
under contract number DE–AC03–76SF00515

Printed in the United States of America. Available from the National Technical Information Service, U.S. Department of Commerce, 5285 Port Royal Road, Springfield VA 22161.

---

* Ph.D. thesis, Stanford University, Stanford CA.

Abstract

Experiments were performed on the Stanford Linear Collider to study the longitudinal properties of the electron and positron beams beginning in the damping ring to the end of the linac. The measurements were performed with a streak camera and wire scanners. In the damping ring, single particle as well as high current behavior was measured. The effects of shaping the bunch distribution in the bunch compressor and the longitudinal wakefield energy loss in the linac are presented. The longitudinal beam dynamics are also simulated and compared to the measurements.

Acknowledgments

Many people contributed to this work and I am grateful to all the help and support you all have provided.

I would first like to thank my thesis advisor, Bob Siemann, for the support and guidance during my graduate career. In theory a thesis advisor is someone who serves not only as a supervisor but also a mentor. I cannot imagine anyone being more supportive, helpful, and enthusiastic than Bob.

These experiments were made possible by the effort of many people from the SLC Accelerator Physics Group and the Accelerator Theory and Special Projects Group. They are: Karl Bane, Vern Brown, Franz-Josef Decker, Keith Jobe, Patrick Krejcik, Doug McCormick, Michiko Minty, Nan Phinney, Tor Raubenheimer, Marc Ross, Robert Siemann, Jim Spencer, David Whittum, and Mark Woodley.

I would like to thank the members that served on my reading and dissertation committee. They are Richard Bube, James 'Ewan' Paterson, John Seeman, Robert Siemann, and Todd Smith.

During my time at Stanford I made many friends and I would like to thank them all for all the help and support they gave me. They are: Helmut and Edith Marsiske, Garth Jensen, Sing-Foong Cheah, Suzanne Jones, Karl Ecklund, Nancy Mar, Angela Catera, and of course I cannot forget Dennis T. Palmer.

I am also grateful to Constantine Simopoulos for his advice and support and many enlightening discussions not only about physics but many other topics.

I would like to thank the United States government, which supported my work at SLAC though the Department of Energy, contract DE-AC03-76SF00515.

I would like to extend my gratitude to all my family members for all the support and encouragement. They are: Robert, Sara, Claire, Joy, William, Don, Merle, Paula, Lynda, Kyle, Josh, Ineko, Meghan, Jim, Olivia, Kip, Shannon, Gregg, Tim, Christine, Bobby, Matthew, Kevin, and Tyler. Having family that live near by makes graduate life much easier.

Finally and most importantly, I would like to thank Sarah and Emma Holtzapple for their patience and support through all the joys and frustrations during our stay at Stanford. I just hope that Emma has as much enjoyment with physics as her dad.

Table of Contents

Abstract ii

Acknowledgments iii

Table of Contents iv

List of Tables v

List of Figures vii

1 Introduction 1

2 Longitudinal Dynamics for Linear Colliders 13
2.1 Longitudinal Dynamics in Damping rings 13
2.2 Wakefields 24
2.3 Potential Well Distortion and Instabilities in the Damping Ring 29
2.4 Bunch Compression 37
2.5 Longitudinal Dynamics for the SLC Linac 45
2.6 Longitudinal Simulations 56

3 Apparatus for Measurements 65
3.1 Streak Camera 65
3.2 Synchrotron Light Optics in the Damping Ring and Linac 71
3.3 Experimental Technique for the Streak Camera 79
3.4 Bunch Length Cavity 93
3.5 Wire Scanner 100
3.6 Measurement of the Resistive Impedance and Synchronous Phase 104
3.7 Method of Data Analysis 107

4 Results 113
4.1 Damping Ring Results 113
4.2 Bunch Compressor and Linac Results 142
4.3 Simulation of Longitudinal Dynamics 157

5 Conclusions 171

References 174
Appendix Feedback Circuit for the Pulsed Laser and Streak Camera 174
Bibliography 177

List of Tables

Table 1.1.1. The present performance for the SLC [Emma, 1995] and LEP [Myers, 1995 and LEP Design Report, 1984]. 6

Table 3.3.1. The trigger delay time for the four speeds of the streak camera. The delay time is the change in time from the previous time setting. 85

Table 3.3.2. The streak camera resolution results. 92

Table 4.1.1. The damping ring and streak camera parameters for the injection measurements. 116

Table 4.1.2. The fitted parameters in equation 4.1.3. 118

Table 4.1.3. The damping ring and streak camera parameters for the synchrotron period measurement. 118

Table 4.1.4. The damping ring and streak camera parameters for the filamentation measurement. 120

Table 4.1.5. The fitted parameters from equation 4.1.4 fit to the data in figure 4.1.5. 121

Table 4.1.6. The initial conditions for the injection measurements. 122

Table 4.1.7. The results of the transverse and longitudinal damping time for the electron and positron damping rings. 122

Table 4.1.8. The conditions for the positron bunch length versus RF accelerating voltage at low current. 123

Table 4.1.9. The store time, bunch length, and asymmetry factor from the asymmetric Gaussian fit to the 25 streak camera profiles. 125

Table 4.1.10. The conditions for the equilibrium bunch length measurement. 125

Table 4.1.11. The results from measuring the electron bunch length as a function of current. 127-128

Table 4.1.12. The conditions for the electron bunch length versus current measurements. 128

Table 4.1.13. The results from measuring the positron bunch length as a function of current. 130

Table 4.1.14. The conditions for the positron bunch length versus current measurements. 130

Table 4.1.15. The conditions for the positron and electron bunch length versus RF accelerating voltage at high current. 131

Table 4.1.16. A table of the inductive impedance elements in the damping ring vacuum chamber [K. Bane et al, 1995]. 137

Table 4.2.1a. The electron compressor results. The errors quoted are the rms error except for the current measurement where the error listed is the standard deviation. 144-145

Table 4.2.1b. The positron compressor results. The errors quoted are the rms error except for the current measurement where the error listed is the standard deviation. 145

Table 4.2.2. The damping ring and streak camera parameters for the injection measurements. 147

Table 4.3.1a. The initial conditions of the electron bunch. 157

Table 4.3.1b. The positron bunch initial conditions. 158

List of Figures

Figure 1.1.1. The experimental ratio of the cross section of hadron production and muon pair production for electron colliders [Hollebeek, 1984]. 4

Figure 1.1.2. The cross section as a function of center of mass energy for electron colliders [Richter, 1987]. 5

Figure 1.2.1. The layout of the Stanford Linear Collider. 7

Figure 1.2.2. At time $t \approx 0\,\mu$sec, there are two electron bunches and two positron bunches in their respective damping rings. The electron bunches have been damping for approximately 8 msec and one positron bunch has been damping for approximately 16 msec, and the other for 8 msec. 8

Figure 1.2.3. At time $t \approx 3\,\mu$sec, both electron bunches and one positron bunch (the one that has damped for 16 msec) are extracted from the damping rings, are compressed, and injected into the linac. The spacing between each subsequent bunch is 60 nsec. The positron bunch and the first electron bunch, called the production bunch, will collide later in the cycle. The second electron bunch, called the scavenger bunch, is used to produce the positrons for a subsequent cycle. 8

Figure 1.2.4. At time $t \approx 7\,\mu$sec, the scavenger electron bunch is deflected to the positron target approximately two thirds of the way down the linac. The production and positron bunches continue traveling toward the end of the linac. 8-9

Figure 1.2.5. At time $t \approx 10\,\mu$sec, the production and positron bunches enter the arcs and the new positron bunch travels to the beginning of the pre-linac. 9

Figure 1.2.6. At time $t \approx 12\,\mu$sec, the production and positron bunches are traveling through the arcs. The electron gun produces two new electron bunches which are accelerated in the pre-linac and are injected into the electron damping ring. The new positron bunch is injected into the pre-linac, accelerated, and injected into the positron damping ring. 9

Figure 1.2.7. At time $t \approx 15\,\mu$sec, the production and positron bunches collide at the detector and the new positron and two electron bunches are at the beginning of the damping cycle in their respective rings. 9

Figure 1.2.8. At time $t \approx 8\,m$sec the three bunches are extracted again from the damping rings and the process repeats. 10

Figure 2.1.1. Layout of the positron (south) damping ring. 14

Figure 2.1.2. The electron longitudinal phase space with and without damping. 15

Figure 2.1.3. The potential energy term for the RF bucket. 19

Figure 2.1.4. A plot of the longitudinal phase space for the SLC damping ring RF bucket. 20

Figures 2.1.5. (a) The injected bunch and bunch after one-quarter of a synchrotron period later in the damping ring RF bucket. (b) The phase space after the bunch has been fully filamented. 21

Figures 2.1.6. (a) The bunch is injected into the RF bucket with its mean offset in energy. (b) The longitudinal phase space of the bunch after filamentation. 21

Figure 2.1.7. The bunch before and after filamentation. At $t \approx 4.5\,m$sec the longitudinal phase space for the bunch has fully damped. 22

Figure 2.2.1. Simulation of the wakefield lines from a Gaussian bunch traveling through a LEP RF cavity [T. Weiland, 1980]. 24

Figure 2.2.2. A source charge q_1 passes through a rotationally symmetric cavity followed by a test charge q_2. 25

Figure 2.3.3. The longitudinal wake potential as a function of time. 26

Figure 2.3.4. The transverse wake potential as a function of time. 28

Figure 2.3.1. The bunch distribution as a function of the current for a purely inductive impedance where the nominal bunch length is the same in all cases and B is proportional to current. 33

Figure 2.3.2. The bunch distribution as a function of the current for a purely resistive impedance. The factor D is proportional to the current. 34

Figure 2.4.1. The electron bunch compressor, the North Ring to Linac (NRTL) transport line. 37

Figure 2.4.2. The longitudinal phase space of the beam entering the RF accelerating section (a), after the RF accelerating section (b), entering the linac fully compressed (c), under compressed (d), and over compressed (e). 38

Figure 2.4.3. The bunch length versus RF voltage for various initial bunch lengths and energy spreads for the SLC bunch compressor. 40

Figure 2.4.4. The energy spread of the beam entering the linac as a function of the RF voltage. 41

Figure 2.5.1. A cross section view of the accelerating structure for the SLC linac. 45

Figure 2.5.2. The spacing of three particles in the bunch traveling on the RF accelerating wave. 46

Figure 2.5.3. The longitudinal wake voltage per accelerating cavity for the accelerating structure in the SLC linac. 47

Figure 2.5.4. One girder of the SLC linac accelerating structure at the beginning (sector 2) of the linac. There are four quadrupole magnets per girder in this region to tightly focus the beam at low energy. 48

Figure 2.5.5. The energy gain as a function of time for the SLED II klystron pulse [SLAC Report 229 June 1980]. 50

Figure 2.5.6. An illustration of beam blow up in the SLC due to transverse wakefields [J. Seeman, 1991]. 52

Figure 2.6.1. An illustration of the asymmetric Gaussian with $D = 5.00\ mm$ and three different asymmetry factors A. 57

Figure 2.6.2. (a) A histogram of the bunch distribution described by an asymmetric Gaussian with $\sigma = 6.60$ mm and A=0.41. (b) A histogram of the energy distribution with an initial mean energy of $\langle E \rangle = 1190$ MeV and energy spread of $\frac{\sigma_E}{\langle E \rangle} = 9.0\text{x}10^{-4}$. 57

Figures 2.6.3. The initial longitudinal phase space of the bunch in the damping ring. 58

Figure 2.6.4. The phase space of the bunch after the RF accelerating section for the compressor amplitudes of 30 and 40 MV. 59

Figure 2.6.5. (a) The longitudinal phase space after the bunch compressor. (b) Histograms of the bunch distributions after the compressor. 59

Figure 2.6.6. (a) Current transmission from simulation for various compressor voltages and initial bunch lengths. (b) The simulated transmission loss in the compressor transport region for two different energy apertures. 60

Figure 2.6.7. The longitudinal phase space at the end of the linac for two different compressor setting and linac phases without the longitudinal wakefield energy loss. 61

Figure 2.6.8. The wakefield energy loss as a function of current and bunch location in the SLC linac. 62

Figure 2.6.9. A simulation of the energy spread of the bunch plotted at each quadrupole in the linac. The initial energy spread of the bunch is 1.1% and at the end of the linac is 0.12%. 63

Figure 2.6.10. (a) The macro particle longitudinal phase space at the end of the linac for three different RF phases. (b) A histogram of the energy distribution at the end of the linac for three different RF phases. 63

Figure 3.1.1. The layout of the various components of the Hamamatsu streak camera. 65

Figure 3.1.2. (a) The four photons that make up the pulse of light that enter the streak camera are separated in time. (b) The four photons entering the streak camera. 66

Figure 3.1.3. The trigger signal is synchronized with the arrival of the photoelectrons at the deflecting plate. 67

Figure 3.1.4. The output of the streak camera. 67

Figure 3.2.1. The synchrotron radiation spectrum as a function of frequency. $S\left(\omega/\omega_c\right)$ is the normalized synchrotron radiation spectrum [H. Wiedemann, 1995]. 71

Figure 3.2.2. The general layout of the synchrotron light set up in the damping ring. 72

Figure 3.2.3. The damping ring optics set up used to transport the visible synchrotron radiation to the streak camera. 73

Figure 3.2.4. The location of the lenses in the damping ring optics line used to focus the synchrotron light onto the streak camera slit 74

Figure 3.2.5. The first mirror used to transport the synchrotron light out of the vault at the end of the linac. The bend magnet which deflects the electrons and positrons is located upstream of this mirror. The mirror is tilted to deflect the synchrotron light out of the plane of the beam and onto the second mirror. The beams are about 30 cm apart at the mirror. 74

Figure 3.2.6. The optics layout for the streak camera at the end of the linac. 75

Figure 3.2.7. The location of the lenses in the linac optics line used to focus the synchrotron light onto the streak camera slit. 76

Figure 3.2 8. The geometry of the optical path length for the bend magnet which produces the synchrotron light for bunch length measurements [Munro and Sabersky, 1980]. 76

Figure 3.3.1. The experimental set-up for taking data with the Hamamatsu Streak Camera. 79

Figure 3.3.2. (a) The linac trigger system for the streak camera. (b) The damping ring trigger system for the streak camera. 81

Figure 3.3.3. Two chopper wheels placed together allows the opening angle to be varied. The phase calibration was done with a photo detector mounted at three different angles. A positive angle for this orientation is below the horizontal axis. 82

Figure 3.3.4. A schematic of the calibration electronics for the light chopper. 83

Figure 3.3.5. The calibration of the phase of the chopper. Measuring the angle of the incident light from the horizontal axis gives the chopper phase needed for measurement. 83

Figure 3.3.6. A schematic of the experimental set-up for the beam finder. 86

Figure 3.3.7. Two bunch length profiles at the end of the linac taken by the streak camera. 86

Figures 3.3.8. The measured bunch length dependence on light intensity at the south damping ring (positron) with a current of $I=3.6x10^{10}$. The measurement consists of taking 5 streak camera profiles at each density filter setting. The figure is a plot of the mean and rms error of each density filter setting. 87

Figure 3.3.9. The calibration curve for the streak camera for the streak speeds of: (a) 60 psec/10 mm, (b) 200 psec/10 mm, (c) 500 psec/10 mm, and (d) 1200 psec/10 mm. 88

Figures 3.3.10. The dependence of the measured damping ring bunch length on the streak camera slit width. The measurement consists of taking 7 streak camera profiles at each slit width. The mean and rms error is plotted at each setting. The light intensity is adjusted at each slit width to avoid systematic errors. 89

Figures 3.3.11. The measured electron bunch length at the end of the linac as a function of interference filter acceptance. The measurement consists of taking 10 streak camera profiles and plotting the mean and rms error for each filter acceptance. The light intensity is adjusted at each setting to avoid systematic errors caused by light. 90

Figure 3.3.12. Streak camera images of the titanium sapphire laser pulse at the 60 ps/10mm setting for the slit width of: (a) 20 μm, (b) 50 μm, (c) 100 μm. 91

Figure 3.3.13. Streak camera images of the titanium sapphire laser pulse at the 200 ps/10mm setting for the slit width of: (a) 30 μm, (b) 100 μm, (c) 150 μm, (d) 200 μm. 91

Figure 3.3.14. The measured resolution corrected bunch length squared as a function of slit width squared for the streak speeds of (a) 60 ps/10mm, and (b) 200 ps/10mm. 92

Figure 3.4.1. The bunch length cavity set-up at sector 25 of the linac. 95

Figure 3.4.2. The bunch length cavity readout system for the bunch length cavity signal. 95

Figure 3.4.3. The laboratory set-up for calibrating the diode detector. 96

Figure 3.4.4. (a) The diode detector output voltage as a function of the input voltage. (b) The diode detector output voltage as a function of the input power. 96

Figures 3.4.5. (a) The detector signal as a function of the compressor voltage at a current of 3.5×10^{10} particles per bunch. (b) The detector signal as a function of current with the compressor set at 43.5 MV. 97

Figures 3.4.6. (a) The current signal at the detector as a function of compressor voltage. This indicates that the current was constant during calibration. (b) The GADC signal as a function of compressor voltage at a current of 3.4×10^{10}. A linear fit to the data is shown in the figure. 98

Figure 3.4.7. The electron bunch length as a function of the compressor voltage using the streak camera. The streak camera measurement is used to calibrate the RF cavity signal. 98

Figure 3.5.1. The SLC wire scanner support card. The fork is stepped across the beam and the wires measure the x, y, and u beam size [M.C. Ross, 1991]. 100

Figure 3.6.1. A schematic of the instrument used to measure the synchronous phase of the damping ring [M.A. Allen, 1975]. 105

Figure 3.6.2. A phasor diagram of the voltages in the damping ring cavities. The dashed line shows the direction of the actual beam voltage. The beam voltage is measured at the synchronous phase ϕ_s from the crest of the RF voltage. 106

Figure 3.7.1. (a) A streak camera image. The horizontal lines mark the location where the vertical columns are summed. (b) A profile of the summed vertical columns. 107-108

Figure 3.7.2. (a) A streak camera profile for a full compressed bunch (36MV) fit to a asymmetric Gaussian distribution with the background subtraction. (b) The normalized bin profile for the fully compressed distribution. 110

Figure 3.7.3. (a) Transverse measurement of the beam fit to a Gaussian distribution. The current of the beam is 3.5×10^{10} particles per bunch and $\sigma = 580\,\mu m$. (b) Transverse measurement of the beam fit to an asymmetric Gaussian distribution. The beam current for the figure is 3.8×10^{10} particles per bunch and the compressor voltage was 22 MV. 111

Figure 3.7.4. A measurement of the transverse size of the beam when the compressor is set to (a) 40 MV and (b) 42 MV. The distribution is fit to a Gaussian in the figure (b). 111

Figure 3.7.5. The normalized horizontal bunch width for the electron beam for a compressor setting of (a) 36MV (b) 42MV. 112

Figure 4.1.1. The (a) electron and (b)positron horizontal beam sizes measured with a wire scanner and fit to an asymmetric Gaussian distribution. 114

Figure 4.1.2. (a) A histogram of the 25 streak camera measurements of the bunch length of the beam injected in the south damping ring (positrons). (b) The bunch distribution of the injected positron bunch fit to an asymmetric Gaussian distribution. 115

Figure 4.1.3. A plot of the mean bunch length as a function of damping ring turn number in the south damping ring. The solid line is the fit to the data. The dot-dash line is a connection of all the data points. 117

Figure 4.1.4. The bunch length as a function of turn number in the positron damping ring starting at turn (a) 2101, (b) 3101, and (c) 4101. 119

Figure 4.1.5. The bunch length as a function of store time. The curve is the fit to the data. 121

Figure 4.1.6. The bunch length as a function of RF accelerating voltage measured in the positron damping ring. The dot dash line is the theoretical bunch length. 123

Figure 4.1.7. The sum of 25 streak camera profiles for turn: (a)38,001, (b)55,001, and (c)80,001 in the positron damping ring. 124

Figure 4.1.8. This plot is a sum of approximately 25 streak camera profiles of the electron bunch at three different currents of (a) $1.0x10^{10}$, (b) $2.73x10^{10}$, and (c) $3.83x10^{10}$ particles per bunch. The data are fit to an asymmetric Gaussian distribution. 126

Figure 4.1.9. (a) The bunch length as a function of current in the electron damping ring. The data points are the mean bunch length and the rms error fit to a quadratic function. (b) The asymmetry factor as a function of current in the electron damping ring. The data points are the mean asymmetry factor and the rms error fit to a quadratic function. 127

Figure 4.1.10. This plot is a sum of approximately 25 streak camera profiles of the positron bunch at three different currents of (a) $0.6x10^{10}$, (b) $2.3x10^{10}$, and (c) $3.3x10^{10}$ particles per bunch. The data is fit to an asymmetric Gaussian distribution. 128-129

Figure 4.1.11. (a) The bunch length as a function of current in the positron damping ring. The data points are the mean bunch length and the rms error fit to a quadratic function. (b) The asymmetry factor as a function of current in the positron damping ring. The data points are the mean asymmetry factor and the rms error fit to a quadratic function. 129-130

Figure 4.1.12. The bunch length as a function of RF accelerating voltage for the (a) positron and (b) electron damping rings. 131

Figure 4.1.13. The horizontal beam size measured with a wire scanner for the beam exiting the damping ring for a current of (a) $3.8x10^{10}$ and (b) $3.7x10^{10}$. 132

Figure 4.1.14. The energy spread of the electron damping ring as a function of current when the RF gap voltage was (a) 765 kV and (b) 940 kV. 133

Figure 4.1.15. The calibration of the wire scanner with the RF accelerating wave. The constant terms are shown in the figure. 134

Figure 4.1.16. The electron bunch distribution measured by the wire scanner for the current of (a) $0.6x10^{10}$, (b) $2.0x10^{10}$, and (c) $3.8x10^{10}$ particles per bunch. 134-135

Figure 4.1.17. A comparison of the bunch length measurements with the streak camera and wire scanner for the electron damping ring. The RF accelerating voltage in the electron damping ring is 785 kV during the wire measurements. 135

Figure 4.1.18. The bunch length versus accelerating voltage for electrons measured with the wire scanner. The current of the bunch is $3.8x10^{10}$ particles per bunch for this measurement. 136

Figure 4.1.19. The bunch length as a function of current for the old vacuum chamber, measured with a wire scanner, and the new vacuum chamber, measure with the streak camera. 137

Figure 4.1.20. The bunch distribution in the electron damping ring at a current of $4.5x10^{10}$ particles per bunch for the old and new vacuum chambers [K. Bane et al, 1995]. 138

Figure 4.1.21. The electron damping ring distribution for a current of (a) $0.65x10^{10}$ ppb and (b) $2.2x10^{10}$ ppb fit to function 4.1.5 to determine the resistive impedance of the damping ring. 139

Figure 4.1.22. The resistance as a function of current for the (a) electron damping ring and (b) positron damping ring. 140

Figure 4.1.23. The synchronous phase as a function of current for the (a) electron and (b) positron damping ring. 140

Figure 4.2.1. The particle transmission at high intensity through the (a) electron and (b) positron compressor transport lines as a function of compressor voltage. 142

Figure 4.2.2. The results of the energy aperture measurement in the electron transport line. The data are fit to straight lines for positive and negative compressor voltages to determine the half current energy aperture. The fit I_n and I_p refer to the negative and positive compressor voltages. The current of the bunch was I=4.0x10^{10} ppb during the measurement. 143

Figure 4.2.3. The (a) electron and (b) positron bunch length as a function of compressor voltage. 145

Figure 4.2.4. The electron distributions for the compressor settings of (a) 30 MV, (b) 36 MV, and (c) 42.5 MV. 146

Figure 4.2.5. The positron distributions for the compressor setting of (a) 30 MV, (b) 36 MV, and (c) 43 MV. 146-147

Fig 4.2.6. The energy spread at the end of the linac for (a) electrons and (b) positrons. Plotted is the mean energy spread, and the errors are the standard deviations of the measurements. 149

Figure 4.2.7. Typical horizontal beam size profiles for a compressor voltage of (a) 30 MV, (b) 36 MV, and (c) 42 MV. 149-150

Figure 4.2.8. The (a) electron and (b) positron energy width at the end of the linac as a function of compressor voltage. Plotted is the mean energy width and standard deviation is denoted as the error. 150

Figure 4.2.9. The normalized bunch length cavity signal is plotted on the left y axis and streak camera bunch length is plotted on the right y axis as a function of compressor voltage for the (a) electron, and (b) positron bunch. The units of the cavity signal is GADC counts per current counts. The current counts are proportional to the particles per bunch. These units will be denoted by GADC/Q. 151

Figure 4.2.10. The correlation of the positron current entering the linac as measured by a toriod and the current measured by the gap current monitor located at the bunch length cavity. The compressor setting for the positron beam is 30 MV during this measurement. The error was determined by the χ^2 fit to the data. 153

Figure 4.2.11. A correlation between the streak camera bunch width measurements and the positron damping ring RF accelerating voltage for the compressor voltage of (a) 30 MV, and (b) 32MV. 154

Figure 4.2.12. The correlation between the bunch width and current for the positron bunch when the compressor is set to (a) 40 MV and (b) 30MV. 155

Figure 4.2.13. The correlation between positron bunch width and compressor voltage for compressor setting of (a) 44MV, (b) 43MV. 156

Figure 4.3.1. A simulation of the longitudinal phase space of the beam when the mean of the beam is put on the valley of the RF wave with an amplitude of 27 MV. (a) The phase space after the compressor RF section and (b) after an energy aperture of -2.0%. 158

Figure 4.3.2. Simulation of the energy aperture at a current of 4.0×10^{10} ppb and an energy acceptance of 1.8 %. The current is fit to straight lines to determine the compressor voltages where half of the current is lost. 159

Figure 4.3.3. The half current RF amplitude at high current (I=4.0×10^{10} ppb) for the electron transport line when the bunch is put on the (a) valley and (b) crest of the RF wave. 159

Figure 4.3.4. The measurement and simulation of the current transmission through the compressor transport line for the (a) electron and (b) positron beams. 160

Figure 4.3.5. The measured and design dispersion for the electron transport line. 161

Figure 4.3.6. The χ^2 value as a function of T_{566} term with R_{56}=-582 mm/%. This simulation was done for the electron bunch with a compressor setting of 40 MV. For this particular simulation, χ^2 is at a minimum at -1450 mm/%^{2}. 162

Figure 4.3.7. A comparison of the measured and simulated RMS and bunch widths as a function of compressor voltage for the (a) electron and (b) positron bunches. 162-163

Figure 4.3.8. The simulated electron distributions for the compressor settings of (a) 30 MV, (b) 36 MV, and (c) 42.5MV. 163-164

Figure 4.3.9. The simulated positron distributions for the compressor settings of (a) 30 MV, (b) 36 MV, and (c) 43MV. 164

Figure 4.3.10. A (a) histogram of the energy distribution, (b) the longitudinal wakefield energy loss per cavity, and (c) the longitudinal phase space at the end of the linac for the electron bunch when the compressor voltage is 30 MV. 166

Figure 4.3.11. A (a) histogram of the energy distribution, (b) the longitudinal wakefield energy loss per cavity, and (c) the longitudinal phase space at the end of the linac for the electron bunch when the compressor voltage is 36 MV. 166-167

Figure 4.3.12. A (a) histogram of the energy distribution, (b) the longitudinal wakefield energy loss per cavity, and (c) the longitudinal phase space at the end of the linac for the electron bunch when the compressor voltage is 42 MV. 167-168

Figure 4.3.13. The simulated and measured energy width at the end of the linac for the (a) electron and (b) positron beams. 168

Figure 4.3.14. The measured energy distribution at the end of the linac when the compressor voltage is 36 MV and the phase of the linac is adjusted (a) -2 degrees, and (b) +2 degrees from the alleged minimized energy width. 169

Figure AP1.1. A circuit diagram for the input signal from the laser photodiode signal. The light chopper is used in the set-up to reduce the overall laser intensity hitting the photocathaode of the streak camera. 174

Figure AP1.2. A schematic of the feedback circuit. 175

Figure AP1.3. A plot of the laser frequency as a function of the bias voltage of the Burleigh amplifier driver. 176

Chapter 1. Introduction

1.1 Particle Physics and Particle Accelerators

The goal of particle physics is to answer the question "What is matter made of ?". Experimental research in this field uses particle accelerators and detectors to answer this question. To produce elementary particles, high energy accelerators are needed for two reasons: (i) To create heavy particles, and (ii) To probe small distances because of the uncertainty principle $\Delta x \Delta p \geq \frac{h}{4\pi}$.

The usefulness of an accelerator for production of elementary particles is determined by the reaction rate. The reaction rate is given by

$$R = \sigma L$$

where σ is the interaction cross section and L is the luminosity. The luminosity is a measure of the event rate for a unit cross section of the beam, whereas the cross section depends on the transition rate and phase space density for going from the initial state to the final state.

Accelerators are used in particle physics experiments in two different configurations. In the fixed target configuration an accelerated beam strikes a stationary target, while two accelerated beams interact with each other in a collider. The beams can be accelerated by a linear accelerator or a circular accelerator for either configuration, and it is possible to accelerate a variety of particles including electrons, protons, and light and heavy ions. Protons and electrons, as well as their antimatter twins, are almost always used in particle physics experiments because electrons are point particles and protons are almost point particles and both have infinite lifetimes. Point particles (electrons) are preferred for particle detection due to low background rates. Protons and electrons are used for fixed target and circular collider configurations, whereas electrons are exclusively used for linear colliders.

In a linear accelerator, particles travel through the accelerating structure once and are accelerated by either RF accelerating or electrostatic fields. In a circular accelerator, particles circulate the accelerator for many revolutions, and they accumulate energy every time they pass the accelerating structure. A more detailed description of the various types of accelerator configurations is made below.

Fixed Target Accelerators

A fixed target accelerator accelerates particles (electrons or protons) to energy E which collide with a target with particles of mass m. The center of mass energy available $\sqrt{s}$ for particle production for a fixed target experiment rises by the square root of the energy

$$E_{cm} = \sqrt{s} \approx \sqrt{2Em}\cdot$$

The luminosity of a fixed target accelerator is given by

$$L = N_b N_t$$

where N_b is the beam flux, N_t is the target density. As an example, a proton beam with flux of $N_b = 10^{12}$ protons/sec that traverses a liquid-hydrogen ($N_t = 9x10^{-5}\ g\ cm^{-3}$) target 1 meter long gives a luminosity of $L \approx 10^{37}\ cm^{-2}\ \sec^{-1}$. Fixed target accelerators have the advantage of delivering high luminosity, but the center of mass energy available for heavy particle production makes a fixed target accelerator of limited use in comparison to colliders.

Circular Colliders

A circular collider has two counter rotating beams which collide at the particle detector. If the two beams are of equal mass and energy the center of mass energy rises linearly with the beam energy

$$\sqrt{s} \approx 2E$$

allowing a large center of mass energy for the creation of new particles. The luminosity for a circular accelerator is given by

$$L_s = \frac{N^2 f_{rev} B}{4\pi\sigma_x\sigma_y}$$

where B is the number of bunches, N is the number of particles (electrons or protons) in the bunch, f_{rev} is the revolution frequency, and σ_x and σ_y are the rms horizontal and vertical beam dimensions, respectively, at the interaction point.

Proton Circular Collider: The proton circular collider has proton and either proton or anti-proton beams counter rotating which collide at the detector regions. The absence of synchrotron radiation has made them the most successful and affordable collider to reach

the highest possible center of mass energies in the world today. Presently, the Tevatron collider at Fermilab has the largest center of mass energy $\sqrt{s} = 2{:}0\ TeV$ and there are plans to build the Large Hadron Collider (LHC) at CERN which will have a center of mass energy of $\sqrt{s} = 16.0\ TeV$.

Protons consist of three valence quarks, two u quarks and one d quark, held together by gluons. A hard collision between two quarks rarely happens, but when it does it results in final states with a large transverse momentum. There are also large backgrounds from the remaining debris, the quarks and gluons not involved in the primary collisions. The collision between two quarks tends to have an energy that is usually much smaller than the center of mass energy of the two protons. As an example, the total proton-antiproton cross section is given by [L. Montanet, 1994]

$$\sigma_{total}(p\bar{p}) = 21.70s^{0.0808} + 98.39s^{-0.4525}$$

where $\sigma_{total}(p\bar{p})$ is in units of mb, and s is in units of GeV^2. The total cross section for the center of mass energy $\sqrt{s} = 1.8\ TeV$ for the Fermilab $p\bar{p}$ Tevatron is $\sigma_{total}(p\bar{p}) = 73\ mb$. The measured cross section ($\sqrt{s} = 1.8\ TeV$)of the top quark at the Tevatron is [F. Abe, 1995]

$$\sigma(q\bar{q} \rightarrow t\bar{t}) = 6.8^{+3.6}_{-2.4}\ pb.$$

The ratio of total cross section to top quark cross section is 10^{10}, which results in a large background to signal ratio. The top quark event rate for the Tevatron for the luminosity of $L = 7x10^{30}\ cm^{-2}\ \sec^{-1}$ is $R = 4.8x10^{-5}\ \sec^{-1}$ which results in 4.1 top quarks events per day, but the Tevatron has only detected 39 top quark pairs using the $67\ pb^{-1}$ data sample of $p\bar{p}$ collisions [Particle Data Group, 1994]. The measured mass of the top quark by the Tevatron is [F. Abe, 1995]

$$m_t = 176 \pm 8(stat.) \pm 10(sys.)\ GeV / c^2,$$

and yet the beam energy for the production of top quarks with protons needs to be $900\ GeV$ in order to provide a useful luminosity.

Despite the large background, the proton circular colliders are attractive for many experiments because the highest quark-quark center of mass energies can be reached. Until recently, the only competition was the electron circular colliders, and these have severe energy limitations due to synchrotron radiation.

Electron Circular Collider: Positrons and electrons are used in electron circular colliders. The interaction cross-section for an electron collider is proportional to the point-like particle production which is the electromagnetic process of muon pair

production. This cross section is important because it sets the scale for all processes, leptonic or hadronic, in electron colliders. The muon pair production cross-section is

$$\sigma(e^+e^- \to \mu^+\mu^-) = \frac{4\pi\alpha^2}{3s} = \frac{21.7nb}{s(GeV^2)}. \qquad (1.1.1)$$

The cross section for production of hadrons has two characteristic regions, a threshold region where strong interactions play a dominant role and a continuum region where the cross section is proportional to the muon pair production cross section. The ratio of hadron production to muon pair production

$$R = \frac{\sigma(e^+e^- \to hadrons)}{\sigma(e^+e^- \to \mu^+\mu^-)}.$$

as a function of center of mass energy is plotted in figure 1.1.1.

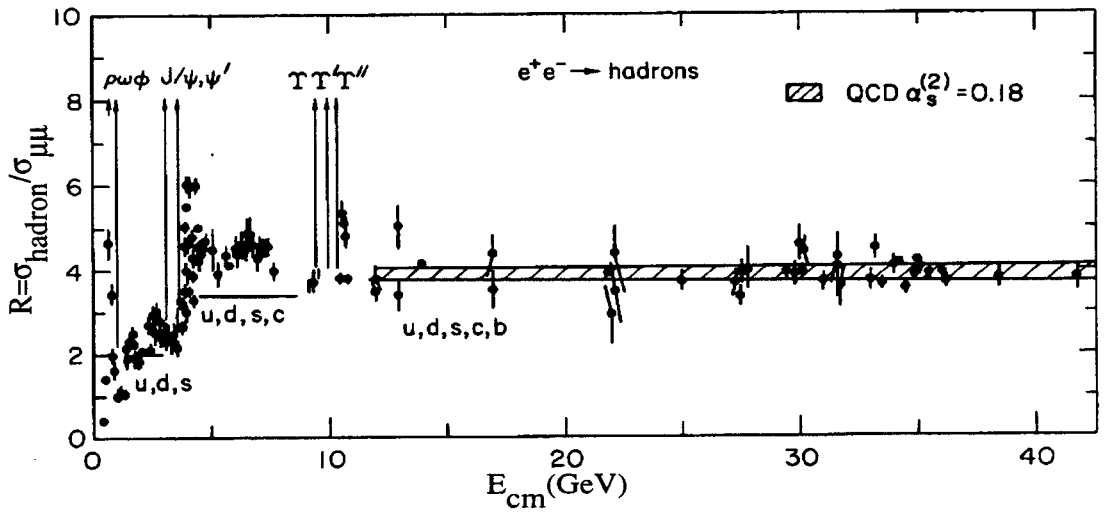

Figure 1.1.1. The experimental ratio of the cross section of hadron production and muon pair production for electron colliders [Hollebeek, 1984].

The cross section as a function of energy for electron colliders (eq. 1.1.1) varies inversely proportional to the center of mass energy squared as seen in figure 1.1.2. The cross section increases at the threshold region, as noted by the peaks of $\rho, \omega, \phi, \psi, \mathrm{T}, Z$ production, and there is a slight increase when W pair production occurs.

As an example, top quark production for electron accelerators is proportional to the muon pair production and is given by

$$\sigma(e^+e^- \to t\bar{t}) = 3\sum_q e_q^2 \sigma(e^+e^- \to \mu^+\mu^-) = \frac{108.5nb}{s(GeV^2)}$$

where the sum counts the fractional charge of the quarks e_q. The cross-section is proportional to the center of mass energy squared and because electrons are point particles the energy of the electron is the effective collision energy. For the center of mass energy of the Tevatron ($\sqrt{s} = 1.8\ TeV$) the top quark cross section is $\sigma(e^+e^- \to t\bar{t}) = 33.5\ fb$, which is small, therefore the luminosity for electron circular accelerators needs to be large to provide a useful event rate.

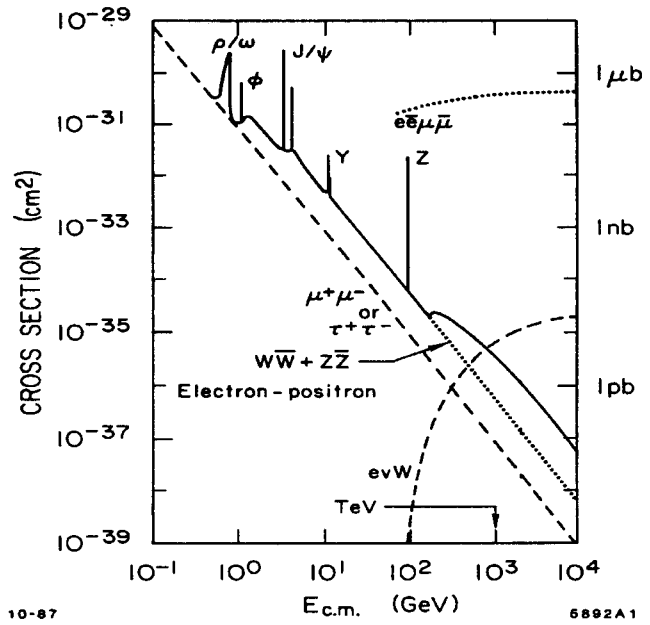

Figure 1.1.2. The cross section as a function of center of mass energy for electron colliders [Richter, 1987].

The center of mass energy $\sqrt{s}$ for an electron circular accelerator is limited by synchrotron radiation. The energy loss per turn due to synchrotron radiation is given by

$$U_0 = C_\gamma \frac{E^4}{\rho}$$

where E is the beam energy, $C_\gamma = 8.85x10^{-5} m\ GeV^{-3}$, and ρ is the bending radius [Sands, 1970]. The synchrotron radiation energy loss makes the electron circular colliders with energies above $100\ GeV$ too large and expensive. As an example, the LEP circular accelerator when upgraded to $95\ GeV$ will lose $2.31\ GeV / turn$ in energy due to synchrotron radiation [LEP Design Report, 1984]. This is why there are no larger electron circular accelerators planned beyond LEP.

Linear Collider

The electron linear collider was proposed by Maury Tigner in 1965 [Tigner, 1965]. The idea of a linear collider is to take two linear accelerators and have their beams collide head on resulting in a high center of mass energy without synchrotron radiation energy loss. The luminosity for a linear collider is given by

$$L_c = \frac{N^2 f_{rep} P}{4\pi\sigma_x\sigma_y}$$

where we have all the same factors as in the storage ring case except f_{rep} is the repetition rate of collisions, and the term P is the pinch term which is due to the two beams being focused by the electromagnetic interaction between them. From the point of view of particle physics, the electron linear collider has the same advantages as its circular counterpart.

Table 1.1.1 summarizes the most up to date main parameters for luminosity for the SLC and LEP. It is evident from table 1.1.1 that circular collider have two distinct advantages in delivering high luminosity: frequency of collisions and charge per bunch. The luminosity for a linear collider is increased by reducing the rms beam sizes at the interaction point. Unlike the circular collider, where the beam size at the interaction point is limited by the beam-beam blow-up, reducing the beam size for a linear collider can be done since the beams collide once and are then discarded. The luminosity of $10^{33}\,cm^{-2}\,s^{-1}$ for a linear collider with $\sqrt{s} = 1\,TeV$ will produce 9.4 top quark events/day.

The electron linear collider is the collider of the future. The advantages of low

	SLC	LEP
Energy (GeV)	45.6	45.6
N_e+/N_e- (particles per bunch)	$3.3-3.6x10^{10}\,/\,e^-$ $3.3-3.6x10^{10}\,/\,e^-$	$6.93x10^{11}$
$f_{rep}\,(Hz)$	120	$11.3x10^3$
P/B	~ 1.15	8
$\sigma_x(\mu m)$	2.0 – 2.6	312
$\sigma_y(\mu m)$	0.6 – 1.2	12.49
$L(cm^{-2}\,sec^{-1})$	$0.4-0.8x10^{30}$	$24x10^{30}$

Table 1.1.1. The present performance for the SLC [Emma, 1995] and LEP [Myers, 1995 and LEP Design Report, 1984].

backgrounds, no synchrotron radiation, and point-like particles make it the collider of choice for the next step in elementary particle physics research.

1.2 The Stanford Linear Collider (SLC)

The SLC is the first linear collider. It is shown in figure 1.2.1. The first and most striking feature is that it is not a true linear collider. Instead both beams are accelerated in the same linear accelerator and brought into collision through two beam transport lines, the arcs. A true linear collider would have two separate linear accelerators which collide the beams at the detector. The SLC energy is low enough that radiation effects in the arcs are small, and, therefore, the underlying beam dynamics of linear colliders can be studied.

The main components of the SLC are: 1) the electron source that produces bunches of electrons, 2) the pre-linac that accelerates them to 1.19 GeV for injection into the damping rings, 3) two damping rings, the NDR (North Damping Ring) and SDR (South Damping Ring), which increases beam brightness through radiation damping, 4) two bunch compressors which compress the bunch length, 5) the linac that accelerates the bunches to their final energy, 6) the positron target where positrons are produced, 7) the positron return line which transports the positrons back to the start of the pre-linac, 8) the collider arcs which transports the electrons and positrons to the final focus and 9) the final focus where the bunches are focused to the collision point. A more detailed description of these components is made simpler by a discussion of the SLC operating cycle.

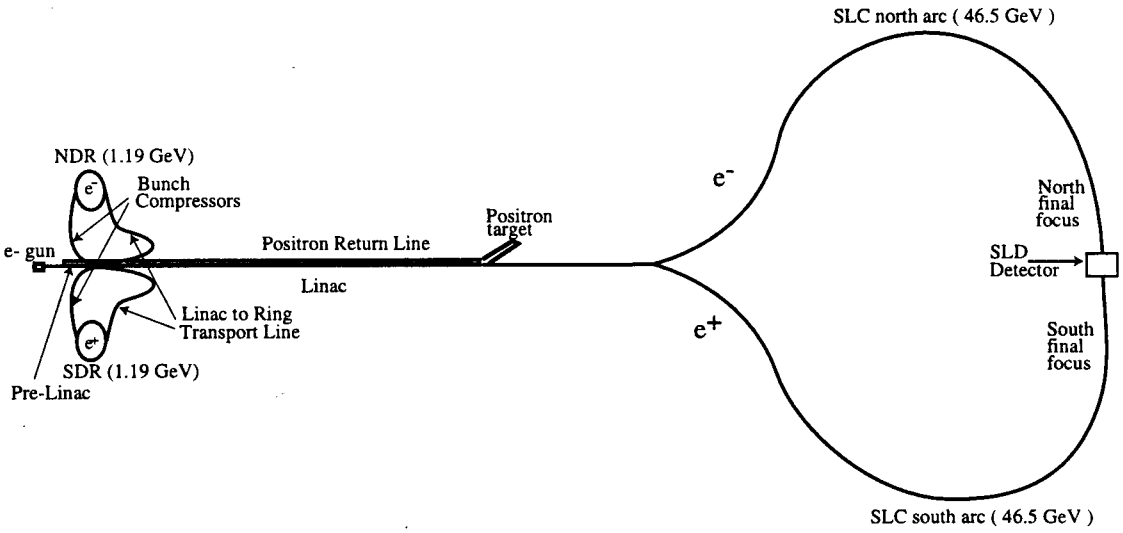

Figure 1.2.1. The layout of the Stanford Linear Collider.

Following is a series of snap shot pictures of the operating cycle of the SLC. In the figures, the dark circles are the electron bunches and the open circles are the positron bunches. The SLC runs at a repetition rate of 120 Hz and we start with two bunches in each damping ring.

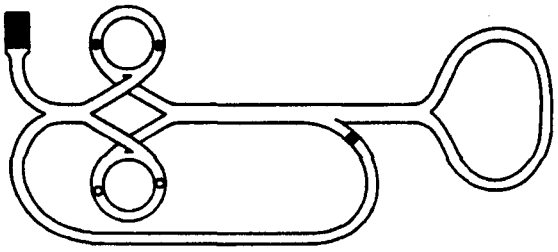

Figure 1.2.2. At time $t \approx 0\,\mu$sec, there are two electron bunches and two positron bunches in their respective damping rings. The electron bunches have been damping for approximately 8 msec and one positron bunch has been damping for approximately 16 msec, and the other for 8 msec.

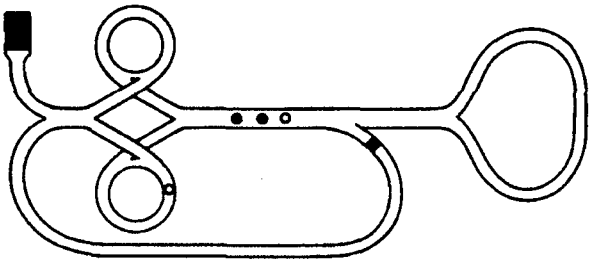

Figure 1.2.3. At time $t \approx 3\,\mu$sec, both electron bunches and one positron bunch (the one that has damped for 16 msec) are extracted from the damping rings, are compressed, and injected into the linac. The spacing between each subsequent bunch is 60 nsec. The positron bunch and the first electron bunch, called the production bunch, will collide later in the cycle. The second electron bunch, called the scavenger bunch, is used to produce the positrons for a subsequent cycle.

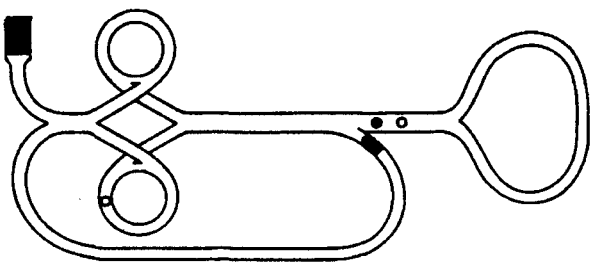

Figure 1.2.4. At time $t \approx 7\,\mu$sec, the scavenger electron bunch is deflected to the positron target approximately two thirds of the way down the linac. The production and positron bunches continue traveling toward the end of the linac.

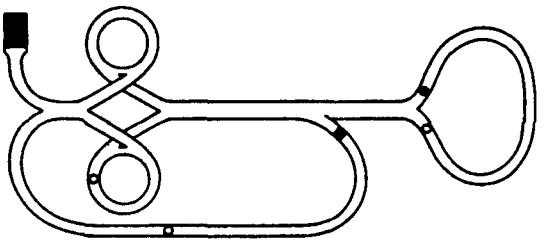

Figure 1.2.5. At time $t \approx 10\,\mu$sec, the production and positron bunches enter the arcs and the new positron bunch travels to the beginning of the pre-linac.

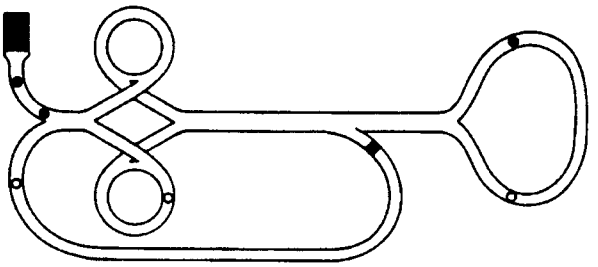

Figure 1.2.6. At time $t \approx 12\,\mu$sec, the production and positron bunches are traveling through the arcs. The electron gun produces two new electron bunches which are accelerated in the pre-linac and are injected into the electron damping ring. The new positron bunch is injected into the pre-linac, accelerated, and injected into the positron damping ring.

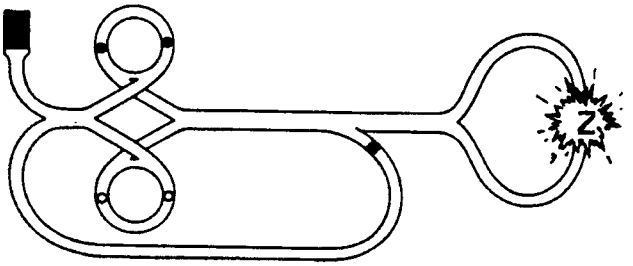

Figure 1.2.7. At time $t \approx 15\,\mu$sec, the production and positron bunches collide at the detector and the new positron and two electron bunches are at the beginning of the damping cycle in their respective rings.

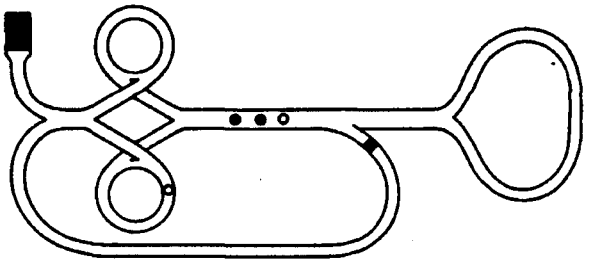

Figure 1.2.8. At time $t \approx 8\,msec$ the three bunches are extracted again from the damping rings and the process repeats.

Following is a brief description of the major sections of the SLC with some comments about longitudinal dynamics which is the subject of this thesis.

Electron Source: The polarized electron gun produces $5x10^{10}$ or more polarized electrons per bunch with a longitudinal polarization of 80%. Two bunches are separated by approximately 60 ns, and the repetition rate of the gun is 120 Hz. Following the gun the electrons are accelerated to 200 MeV for injection into the pre-linac section. This is the same energy as the positrons as they are injected into the pre-linac from the positron return line.

Pre-Linac: The pre-linac section consists of four high power linac sections that are used to accelerate two electron bunches and one positron bunch from 200 MeV to 1.19 GeV. After the pre-linac the production, scavenger, and positron bunches are transported to their respective damping rings through the LTR (linac to damping ring) transport lines.

The Damping Rings: The main purpose of the damping rings is to reduce the transverse emittance of the bunches by radiation damping. The SLC has two damping rings, one for electrons and one for positrons; although they are similar, they are operated in different manners. The production and scavenger bunches are damped for 8 ms after which they are extracted. The difference in the positron damping ring is that the positrons need to be damped longer, 16 $msec$, due to their larger transverse emittance when injected. During this period the "other" positron bunch is extracted and a new bunch is injected into the ring. It is in the damping ring where RF accelerating fields, radiation damping, and collective effects determine the longitudinal parameters (bunch and energy distribution) for the rest of the SLC.

The Compressor Line: The bunch length in the damping ring is approximately 5 mm which is too long to be accelerated in the linac. Between the damping ring and the linac there is a transport line where the bunch compressor is located. The compressor consists of two parts: 1) An acceleration section and 2) a non-isochronous transport line from the damping ring to the linac. This compressor system rotates the beam in longitudinal phase space thereby compressing the bunch length to approximately 1 mm at the expense of the energy spread. Both the electron and positron bunches have their own separate bunch compressors.

Linac: After the bunches have been compressed they enter the main part of the linear accelerator called the linac. The production and positron bunches are accelerated from $1.19\,GeV$ to $46.5\,GeV$ in the linac. This energy is determined by the mass of the Z^0 boson and radiation losses in the arcs. The scavenger bunch is accelerated up to $\sim 33\,GeV$, through approximately two-thirds of the linac, and is extracted at the positron target region. The acceleration in the linac by means of disk loaded wave guide accelerating structure powered by high power RF klystrons. The energy gain per klystron is $\sim 250\,MeV$ and there are 232 klystrons in the main section of the linac.

The bunch distribution is constant in the linac. The energy distribution changes due to the phase location on the RF accelerating wave and due to the energy loss from longitudinal wakefields.

Positron Source: The positron source was designed to produce equal production and positron bunch charge densities. That requires a large yield from the source. Positrons are produced by slamming the electron scavenger bunch into a tungsten target whereby a shower of electron-positron pairs is created, and the positrons are then collected by focusing elements. They are accelerated to $200\,MeV$ and transported back to the beginning of the linac and injected into the pre-linac. The transverse emittance of the positron bunch is large which results in needing damping twice as long ($16\,m\text{sec}$) as the electron bunch.

Collider Arcs: The purpose of the collider arcs is to transport the high energy positron and electron bunches to the final focus interaction region without introducing an emittance growth other than that due to quantum fluctuations. The arcs follow the contour of the SLAC site. Magnets are combined function with bend, quadrupole and sextupole components.

The bunch distribution change in the collider arcs is due to the dispersion and energy distribution in the bunch. The energy spread changes due to synchrotron radiation losses in the arcs.

Final Focus : The final focus is located after the collider arcs and is designed to transform the beam to a small spot at the interaction point. Small beam spots are achieved by reducing misalignments and errors and correcting the chromatic and geometric aberrations. The chromatic effects can be controlled by reducing the energy spread at the final focus. The energy spread at the final focus depends upon the energy spread at the end of the linac and emission of synchrotron radiation in the collider arcs.

1.3 Scope of the Thesis

This thesis consists of theoretical description, simulations, and measurements of the longitudinal dynamics of the SLC. The longitudinal dynamics relates to the performance of the accelerator in longitudinal phase space, bunch length and energy spread. Performance issues such as the bunch lengthening due to current intensity in the damping ring and the energy spread dependence on the bunch length in the linac will be presented.

The theoretical description of the longitudinal dynamics of the SLC begins in the damping ring, where the initial longitudinal phase is determined for the downstream sections of the SLC, and through the rest of the SLC, ending at the final focus. The measurements of longitudinal phase space were made using a 500 femto-second resolution streak camera to measure the bunch length and distribution and wire scanners to measure the energy spread. These measurements were made at both damping rings and at the end of the linac. Computer simulations of the longitudinal phase space will follow the evolving longitudinal phase space from the damping ring to the end of the linac.

Two final remarks should be made about this thesis: First, the references are ordered by first author and the year of the publication. Secondly, I will be using MKS units throughout the thesis unless otherwise noted.

Chapter 2.
Longitudinal Dynamics for Linear Colliders

2.1 Longitudinal Dynamics in Damping Rings

Introduction

The longitudinal dynamics for both the electron and positron damping rings depends on the interaction of particles with the electromagnetic fields in the accelerator. Single particle motion results when only externally imposed electromagnetic fields, fields from magnets and RF cavities are considered. In section 2.1 the single particle motion that gives rise to energy oscillations, radiation damping and quantum fluctuations for the electrons in the SLC damping rings will be presented [Sands, 1970]. A section which describes the longitudinal dynamics as a function of the bunch store time in the damping ring is included. Collective or coherent behavior results when beam induced as well as externally imposed fields are taken into account. The collective behavior of the bunch pulse in the damping rings will be presented in section 2.3.

Single Particle Motion for Damping rings

The damping rings (figure 2.1.1) consist of one klystron which produces RF power for the two RF accelerating cavities, dipole magnets (labeled B) which bend the beam in a circular orbit, quadrupole magnets (labeled Q followed by D or F for defocusing or focusing quadrupoles) for focusing the beam, and sextupole magnets (labeled S followed by D or F for defocusing or focusing sextupoles) for chromatic corrections. The figure also provides details of the location of corrector magnets, beam position monitors, and beam diagnostic devices.

As the electrons circulate around the damping ring they lose energy due to synchrotron radiation (U_{rad}), and the two RF accelerating cavities replace this lost energy. An electron which is on-axis, has the nominal energy E_0, and the nominal revolution period T_0 is called a synchronous electron. The time deviation of an electron from the synchronous electron is given by τ. The dipole magnets bend the electrons around the ring, and their path length depends on their energy deviation $\varepsilon = E - E_0$. The energy and time deviations give rise to a stable oscillation in time and energy about the synchronous

electron. The energy loss due to synchrotron radiation increases with the energy of the electron which results in damping of the oscillation.

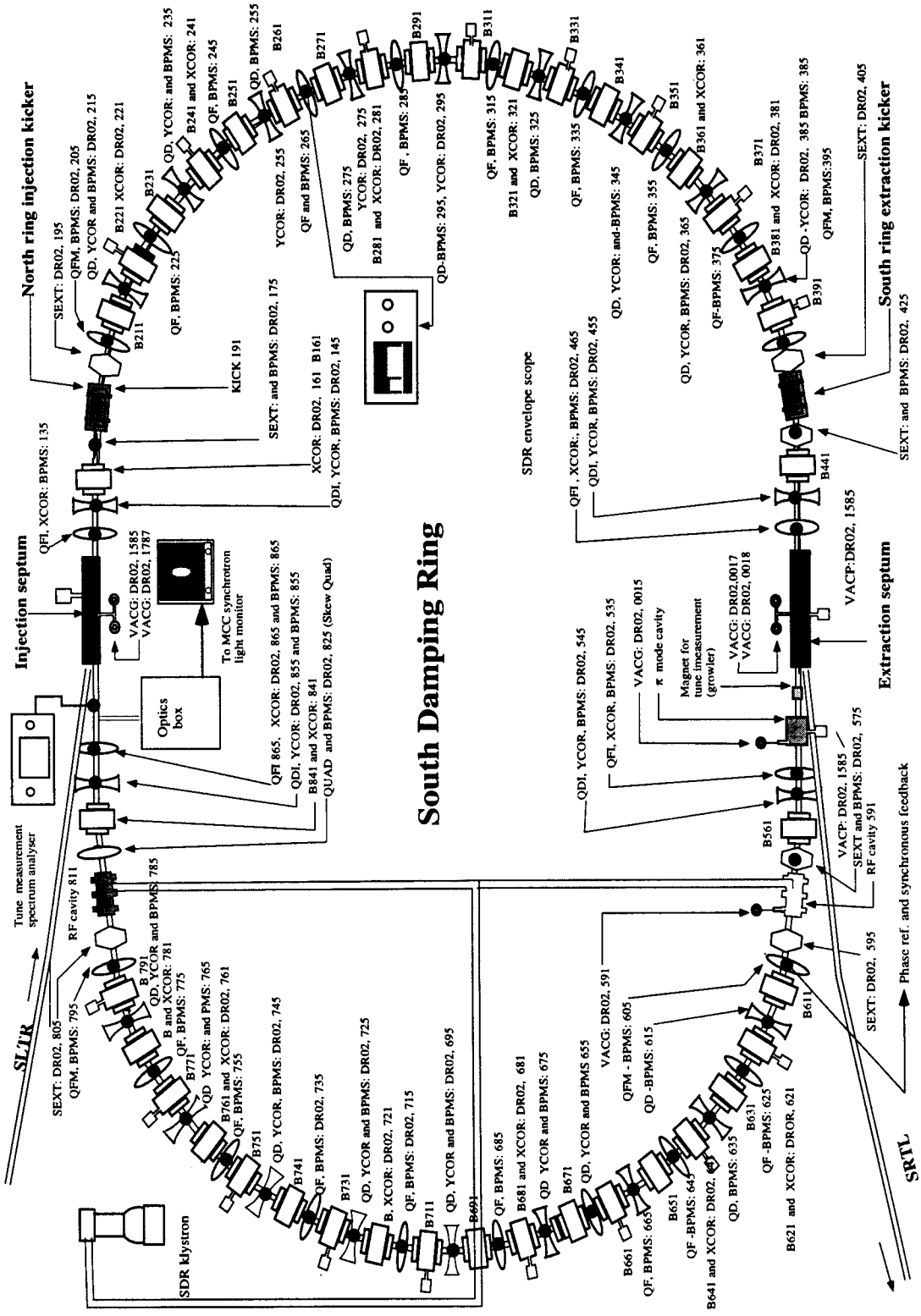

Figure 2.1.1. Layout of the positron (south) damping ring.

The differential equations for energy and time deviation for small oscillations are given by.

$$\frac{d^2\tau}{dt^2}+2\alpha_E\frac{d\tau}{dt}+\Omega_s^2\tau=0 \qquad \frac{d^2\varepsilon}{dt^2}+2\alpha_E\frac{d\varepsilon}{dt}+\Omega_s^2\varepsilon=0 \tag{2.1.1}$$

where $\alpha_E=\frac{1}{2T_0}\frac{dU_{rad}}{d\varepsilon}$ is the damping term and $\Omega_s=\sqrt{\frac{h\alpha e\omega_{rev}^2V_{rf}\sin\phi_S}{2\pi E_0}}$ is the synchrotron frequency. The term α is the momentum compaction, ω_{rev} and ω_{RF} are the revolution and RF frequencies, respectively, $h=\frac{\omega_{RF}}{\omega_{rev}}$ is the harmonic number, $\phi_s=\cos^{-1}\left(\frac{U_0}{eV_{rf}}\right)$ is the synchronous phase, U_0 is the energy loss per turn for a synchronous particle, and V_{rf} is the RF accelerating voltage. The solutions to the differential equations are

$$\varepsilon(t)=A\exp(-\alpha_E t)\cos(\Omega_s t-\varphi) \tag{2.1.2}$$

and

$$\tau(t)=\frac{-\alpha}{E_0\Omega_s}A\exp(-\alpha_E t)\sin(\Omega_s t-\varphi) \tag{2.1.3}$$

where A and φ are constants. Equations 2.1.2 and 2.1.3 describe the longitudinal motion (time and energy deviation) of a single particle in the damping ring. Neglecting the damping term α_E the electron will oscillate in time and energy with a fixed amplitude and synchrotron frequency Ω_s (figure 2.1.2). If damping is included, the electron will spiral toward the orbit of a synchronous electron.

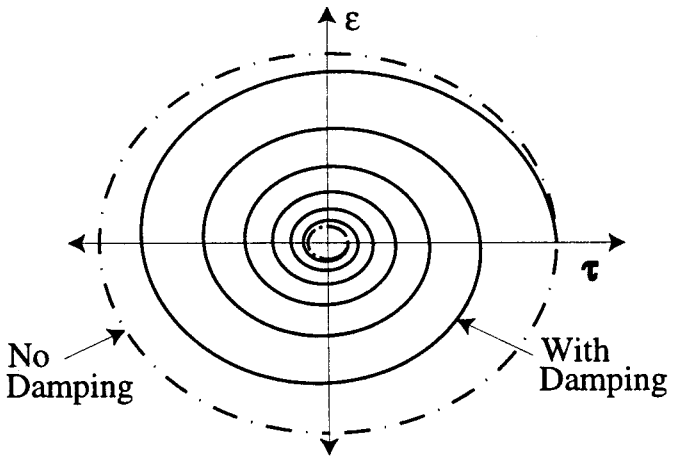

Figure 2.1.2. The electron longitudinal phase space with and without damping.

The damping term α_E is calculated from the rate of change of energy loss with energy. When the energy deviates from the nominal energy, E_0, the energy loss per turn changes in three different ways: 1) Synchrotron radiation power is dependent on the energy; 2) The path length is dependent on the energy; and 3) The magnetic fields depend on the deviation from the nominal orbit. The damping term α_E is given by

$$\alpha_E = \frac{1}{\tau_E} = \frac{C_\gamma E_0^2}{4\pi T_0}(2I_2 + I_4)$$

where $C_\gamma = 8.85x10^{-5}\ m\ GeV^{-3}$, and τ_E is the longitudinal damping time. The synchrotron integrals I_2 and I_4 are

$$I_2 = \oint \frac{ds}{\rho_0(s)} ds \qquad I_4 = \oint \left(\frac{1}{\rho_0(s)} + 2K(s) \right) \frac{\eta(s)}{\rho_0(s)} ds$$

where $G_0(s) = \frac{1}{\rho_0(s)} = \frac{ecB_0(s)}{E_0}$ is the inverse of the radius of curvature for a dipole magnet, $\eta(s)$ is the dispersion, and $K(s) = \frac{ec}{E_0}\left(\frac{\partial B}{\partial x}\right)$ is proportional to the gradient of the field.

Radiation damping is related to the average loss of energy due to synchrotron radiation, and it does not take into account that the energy is lost in discrete "quanta" (photons) at random times and energies. This random quantum emission excites energy oscillations which cause growth of the electron oscillation. When combined with radiation damping the electron oscillation reaches a stable equilibrium. Including quantum excitation, differential equation 2.1.1 becomes

$$\frac{d^2\tau}{dt^2} + 2\alpha_E \frac{d\tau}{dt} + \Omega_s^2 \tau = \frac{\alpha \Delta u}{E_0 T_0}. \qquad (2.1.4)$$

The fluctuating energy loss per turn, Δu, can be expressed in terms of the total rate of emission of photons of all energies N, the rms energy of the photons emitted σ_u, and the instant of time that the photon is emitted $\xi(t)$, as

$$\Delta u = \sqrt{N}\sigma_u \xi(t).$$

The impulse distribution $\xi(t)$ has the following properties:

$$\langle \xi(t) \rangle = 0 \text{ and } \langle \xi(t)\xi(t') \rangle = \delta(t - t').$$

The solution to the differential equation 2.1.4 is

$$\tau = A_\tau \exp\left[(i\Omega_s - \alpha_E)t - \varphi_0\right] + \frac{\alpha\sqrt{N}\sigma_u}{T_0 E_0 (i\Omega_s + \alpha_E)} \int_0^t \xi(t') \exp\left[(i\Omega_s - \alpha_E)(t - t')\right] dt'$$

which gives the following results:

$$\langle \tau \rangle = 0$$

$$\sigma_\tau = \left\langle \tau^2 \right\rangle^{1/2} = T_0 \sqrt{\frac{\alpha E_0}{2\pi h e V_{rf} \sin\phi_s}} \left(\frac{\sigma_\varepsilon}{E_0}\right) = \frac{\alpha}{\Omega_s} \sqrt{C_q E^2 \left(\frac{I_3}{2I_2 + I_4}\right)} \qquad (2.1.5)$$

The energy spread of the damping ring is dependent on the energy and bending radius. The energy fluctuations depend on the bending radius and do not change as the bunch distribution changes, so the bunch remains Gaussian in energy. The energy spread can be determined from the bunch length to give

$$\frac{\sigma_\varepsilon}{E_0} = \frac{\Omega_s}{\alpha} \sigma_\tau = \sqrt{C_q E_0^2 \left(\frac{I_3}{2I_2 + I_4}\right)} \qquad (2.1.6)$$

where the constant $C_q = 3.84x10^{-13} m$, and $I_3 = \oint G^3 ds$. The relationship between σ_τ and $\frac{\sigma_E}{E_0}$ depends on the local slope of the RF wave form and beam induced fields can distort the bunch shape even while the energy spread remains Gaussian.

The rms emittance of the injected bunch is the area in phase space that the bunch occupies and is given by

$$\varepsilon_l = \sigma_\tau \sigma_\varepsilon$$

where σ_τ is the rms length of the bunch and σ_ε is the rms energy deviation of the bunch.

It should be noted that the energy spread and bunch length from equations 2.1.5 and 2.1.6 are their equilibrium values at low currents. As the intensity of the bunch increases collective effects have to be included which modify there expressions.

SLC Damping Ring Longitudinal Dynamics

The bunch store time for the damping rings is 8.3 msec for electrons and 16.6 msec for positrons. The bunch is injected into the damping ring from the pre-linac with an energy of 1.19 GeV, a bunch length of $\sigma_\tau \approx 7.4$ $p$sec, and an energy spread of $\frac{\sigma_E}{E_0} = 0.3\%$. The bunch is extracted from the damping ring with a bunch length and

energy spread that depends upon the current. The range of these values is $\sigma_\tau \approx 15-21\ p\text{sec}$ and $\frac{\sigma_\varepsilon}{E_0} \approx 8.0-9.2x10^{-4}$.

The longitudinal dynamics of the damping ring begin with the bunch being injected into an RF bucket. The RF bucket is described by the Hamiltonian which can be determined from the two coupled longitudinal equations of motion in the damping rings [Sands, 1970]:

$$\frac{d\tau}{dt} = -\alpha\frac{\varepsilon}{E_0} \quad \text{and} \quad \frac{d\varepsilon}{dt} = \frac{qV(\tau)}{T_0}$$

where $qV(\tau)$ is the energy gain/lost due to synchrotron radiation, RF accelerating voltage, longitudinal wake potential, or any internally or externally applied voltage which increases or decreases the energy of the electron. Considering only the RF accelerating voltage and synchrotron radiation energy loss, the function $qV(\tau)$ is expressed as

$$qV(\tau) = qV_{rf}\cos\left(\omega_{rf}\tau\right) - U_{rad}$$

and substituting $qV(\tau)$ back into the second equation gives

$$\frac{d\varepsilon}{dt} = \frac{1}{T_0}\left[qV_{rf}\cos\left(\omega_{rf}\tau\right) - U_{rad}\right].$$

The two differential equations can be used to find the Hamiltonian $H = H(\varepsilon, \tau; t)$ which describes the longitudinal motion of the bunch. The differential equations can be written in terms of the Hamiltonian as

$$\frac{\partial H}{\partial \tau} = -\frac{d\varepsilon}{dt} = -\frac{1}{T_0}\left[qV_{rf}\cos\left(\omega_{rf}\tau\right) - U_{rad}\right] \tag{2.1.8}$$

$$\frac{\partial H}{\partial \varepsilon} = \frac{\partial \tau}{\partial t} = -\alpha\frac{\varepsilon}{E_0}. \tag{2.1.9}$$

and integrating the above equations gives the Hamiltonian

$$H(\varepsilon,\tau) = -\frac{\alpha\varepsilon^2}{2E_0} + \frac{U_{rad}\tau}{T_0} - \frac{qV_{rf}}{T_0\omega_{rf}}\sin\left(\omega_{rf}\tau\right) \tag{2.1.10}$$

where the RF acceleration is given by $qV_{rf}(\tau) = qV_{rf}\sin\left(\omega_{rf}\tau\right)$. The potential, $V(\tau)$, for the RF bucket is

$$V(\tau) = \frac{1}{T_0}\left(U_{rad}\tau - \frac{qV_{rf}}{\omega_{rf}}\sin\left(\omega_{rf}\tau\right)\right)$$

and is asymmetric due to the radiation damping (figure 2.1.3).

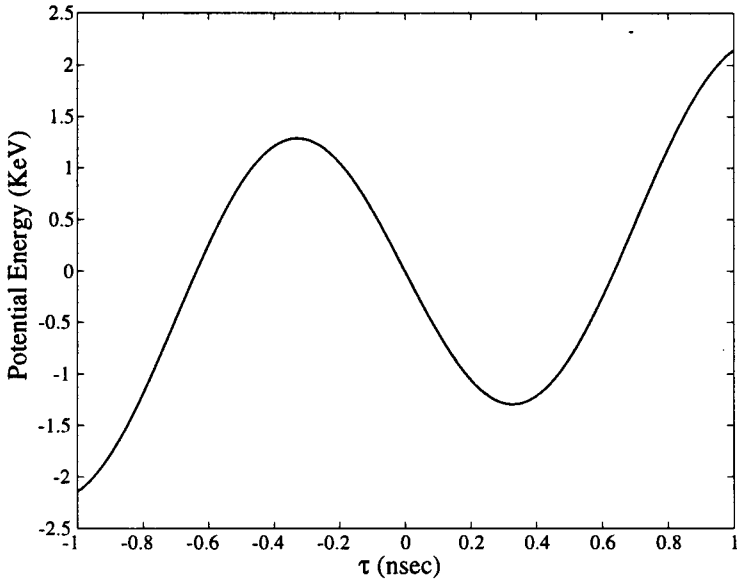

Figure 2.1.3. The potential energy term for the RF bucket.

The shape of the RF bucket is derived by varying the energy deviation and bunch length with the Hamiltonian fixed. The RF bucket is plotted in figure 2.1.4 and it contains several interesting features: 1) The dashed lines represent the separatrix of the RF bucket. The separatrix is the maximum amplitude of a captured particle. 2) The dot-dashed lines represent the particles that will not be captured in the RF bucket. These particles will travel around the ring and will be eventually lost. 3) The solid lines represent a constant Hamiltonian phase space trajectory (labeled H_1, H_2, and H_3 in figure 2.1.4). A particle that is injected on one of these trajectories will remain on that trajectory as it moves in phase space.

The maximum energy spread captured in the RF bucket can be determined from the Hamiltonian. For the SLC parameters and an RF voltage of 800 KV, the RF bucket has a maximum energy deviation acceptance of $\varepsilon_{\max} = \pm 19.6\, MeV$ which corresponds to an energy spread of $\delta = \pm 1.65\,\%$. The synchronous time in the damping ring is given by

$$\tau_s = \frac{1}{\omega_{rf}} \cos^{-1}\left(\frac{U_{rad}}{qV_{rf}}\right) = 0.329\, n\sec \cdot$$

The center of the RF bucket is the location where the energy acceptance is maximum.

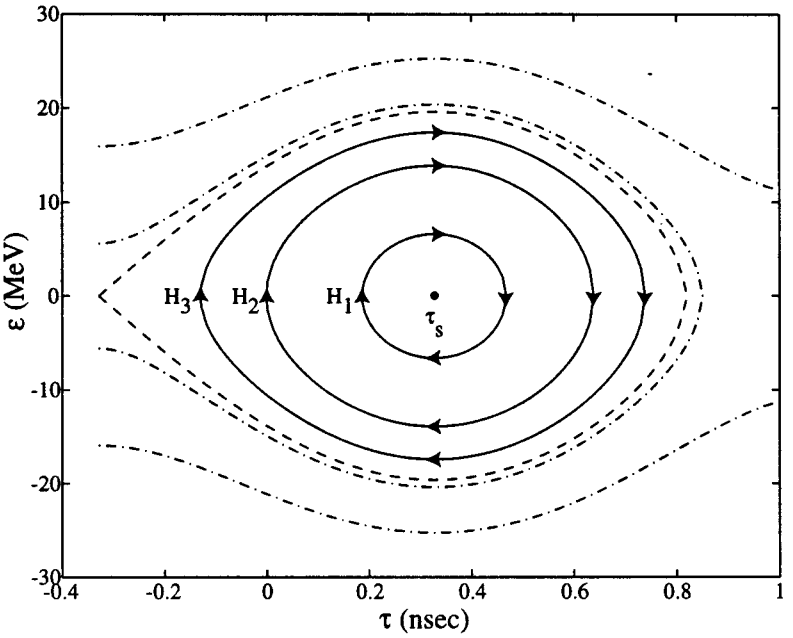

Figure 2.1.4. A plot of the longitudinal phase space for the SLC damping ring RF bucket.

A bunch injected into the damping ring occupies an area in phase space, and the location of the bunch in the RF bucket depends on the match between the pre-linac and the damping ring. In figure 2.1.5a, a bunch is injected into the damping ring RF bucket where the bunch is centered on the synchronous time, and the maximum amplitude of the bunch resides on the phase space trajectory H_1. The bunch travels around the ring with a period of 117.65 $n$sec and oscillates in time (length) and energy spread with the synchrotron frequency $2\Omega_s$.

Ignoring damping, the equation of motion for time deviation is

$$\frac{d^2\tau}{dt^2} + \frac{\Omega_s^2}{\omega_{rf}}\sin\left(\omega_{rf}\tau\right) = 0 \qquad (2.1.11)$$

where the RF wave form is not approximated by its linear form. Due to the non-linearity of the RF wave form, the synchrotron frequency is amplitude dependent. This results in filamentation in phase space. The approximate solution to the equation of motion when the RF is included shows that the frequency depends on the amplitude of the oscillation as [R. Siemann, 1989]

$$\tau(t) = \tau_0 \sin\left[\left(\Omega_s + \Delta\omega(\tau_0)\right)t - \varphi\right]$$

where

$$\Delta\omega(\tau_0) = -\frac{\Omega_s}{2}\left[1 - \frac{2J_1(\omega_{rf}\tau_0)}{\omega_{rf}\tau_0}\right].$$

Filamentation of phase space is illustrated by two examples. In figure 2.1.5, the bunch is injected into the damping ring RF bucket with the mean of the bunch centered on the synchronous time (figure 2.1.5 a) will oscillate in phase space where its maximum amplitude is trajectory H_1. The bunch will begin to filament because the particles with large amplitudes will rotate slower until eventually the bunch will occupy the whole phase space contained by the trajectory H_1 (figure 2.1.5b).

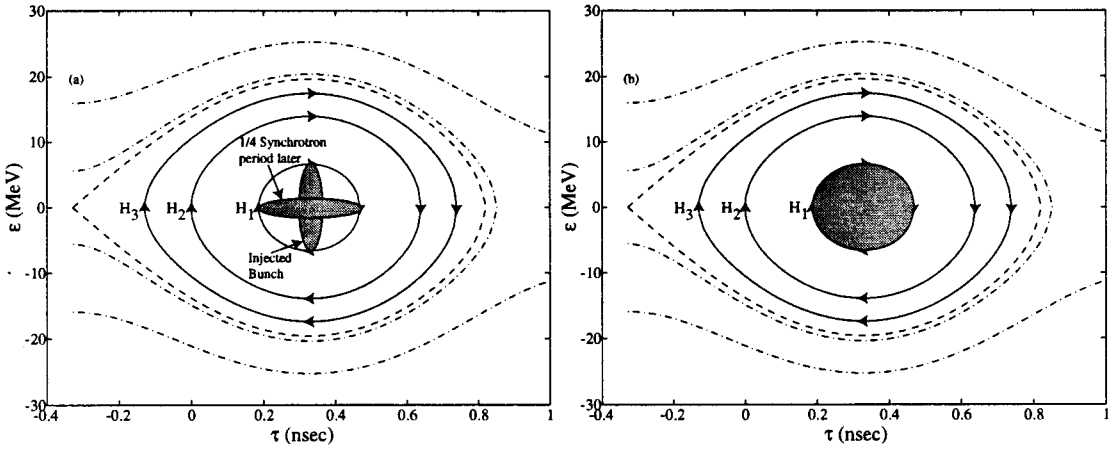

Figures 2.1.5. (a) The injected bunch and bunch after one-quarter of a synchrotron period later in the damping ring RF bucket. (b) The phase space after the bunch has been fully filamented.

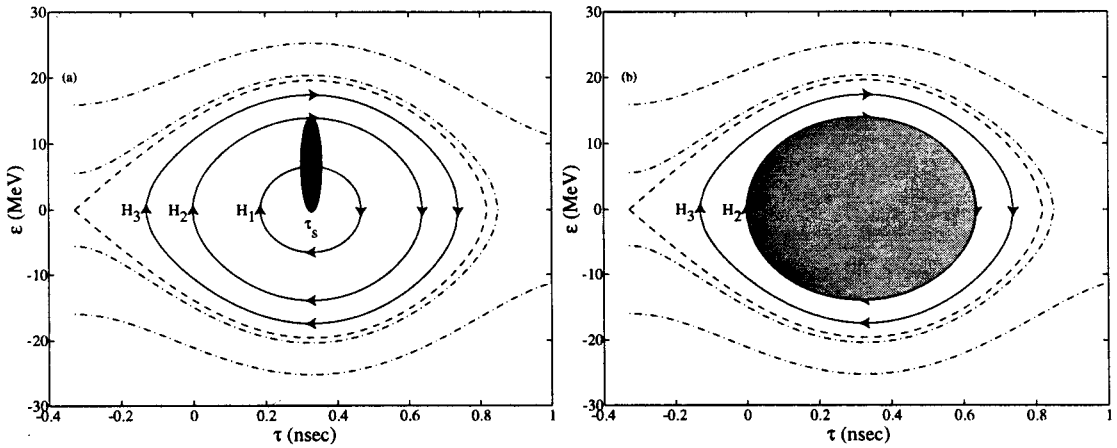

Figures 2.1.6. (a) The bunch is injected into the RF bucket with its mean offset in energy. (b) The longitudinal phase space of the bunch after filamentation.

In figure 2.1.6 the bunch, with the same total amplitude, is injected into the RF bucket where its longitudinal mean is not centered in energy. The maximum trajectory amplitude is H_2 and after the beam has been fully filamented the beam's longitudinal emittance will be the phase space occupied by the trajectory H_2 (figure 2.1.6b).

The initial longitudinal emittances for the two examples are identical, but after filamentation the emittance in example 2 is larger than example 1. When the bunch has fully filamented the bunch length can be measured to observe radiation damping of the bunch length. The equilibrium bunch length will be determined by radiation damping and quantum excitation (figure 2.1.7). The bunch length as a function of time can be determined by the longitudinal emittance equation which can be expressed as [Wiedemann, 1981]

$$\sigma^2(t) = {\sigma_{eq}}^2 + \exp\left(-\frac{2t}{\tau_E}\right)\left({\sigma_{inj}}^2 - {\sigma_{eq}}^2\right)$$

where σ_{eq} is the equilibrium bunch length, and σ_{inj} is injected bunch length. The bunch after being fully damped will remain in this state until the bunch has been extracted from the damping ring at $t = 8.3$ or $t = 16.6\, m\text{sec}$.

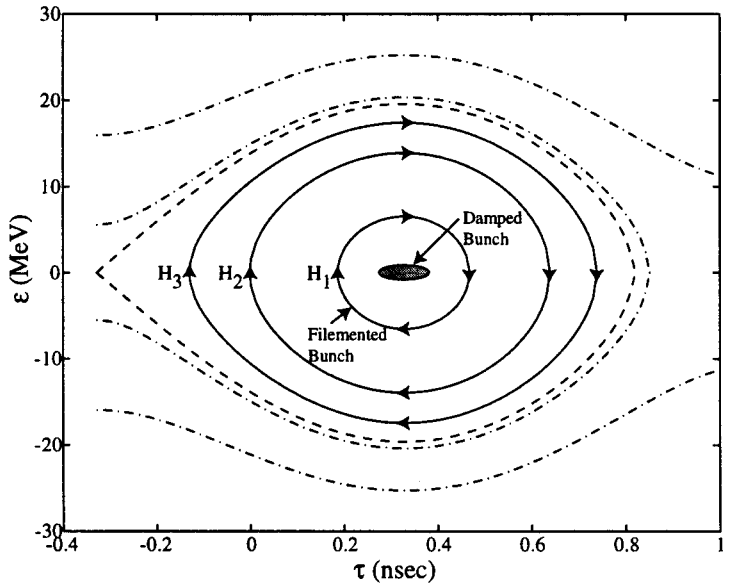

Figure 2.1.7. The bunch before and after filamentation. At $t \approx 4.5\, m\text{sec}$ the longitudinal phase space for the bunch has fully damped.

The bunch length and energy spread is current dependent and this will change the size of the phase ellipse and this will be presented in section 2.3.

SLC Damping Ring Parameters

General Parameters

Energy E_0	1.19 Gev
Circumference	35.270 m
Revolution Frequency	8.5 MHz
RF Frequency	714 MHz
Harmonic Number	84
Energy loss/Turn U_0	78.63 KeV
Bending Radius ρ_0	2.0372 m
Bending Field	19.484 Kgauss
Typical Operating Current	95 mA
Synchrotron Power (at operating current)	8.303 kWatts
Critical Energy ε_c	1.84 KeV

Synchrotron Integrals For the SLC Damping Rings (Calculations made by R. Early, 1994)

$\alpha = \frac{1}{L}\oint G\eta ds$	0.016
$I_2 = \oint G^2 ds$	2.785 m^{-1}
$I_3 = \oint G^3 ds$	1.347 m^{-2}
$I_4 = \oint (G^2 + 2K) G\eta ds$	-0.029 m^{-1}

Longitudinal Parameters

Equilibrium Bunch Length σ_z	5.34 mm
Equilibrium Energy Spread $\frac{\sigma_E}{E_0}$	7.11×10^{-4}
Synchrotron Period T_s	9.834 μsec
RF Voltage	800 kV
Synchronous Phase	84.36°
Longitudinal Damping time τ_E	1.79 msec
Synchrotron tune ν_s	11.969×10^{-3}

2.2 Wakefields

Introduction

The single particle longitudinal dynamics we have discussed thus far have not included the interaction between particles. The dynamics of individual particles and the collective dynamics of the beam are modified by the electromagnetic interaction between particles. This interaction changes the motion of the beam in the SLC. An introduction to longitudinal and transverse wakefields will be presented in this section [A. Chao, 1993, and R. H. Siemann, 1985]. Subsequent sections will show how the dynamics of the beam changes due to wakefields.

Wakefield Effects

The inter-particle interaction arises through the interaction of the beam with its environment. When a beam passes through an RF cavity, disk loaded wave guide, transitions in the vacuum chamber, or other accelerator component, it radiates electromagnetic fields. These fields, called wakefields, can act back on the beam to produce generally undesirable effects such as energy loss, energy transfer from head to tail of the bunch, energy transfer between bunches, and the head of the bunch can transversely

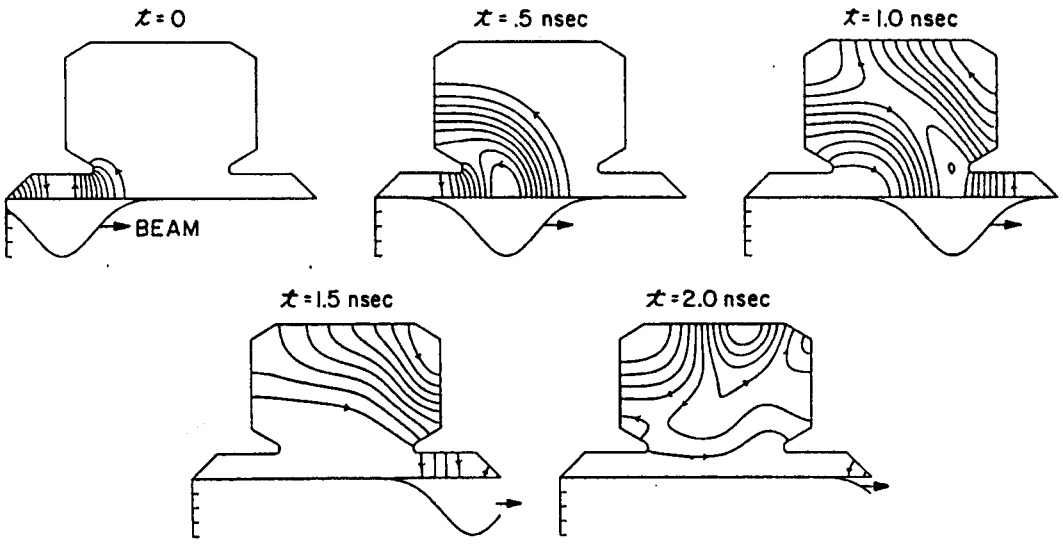

Figure 2.2.1. Simulation of the wakefield lines from a Gaussian bunch traveling through a LEP RF cavity [T. Weiland, 1980].

deflect the tail of the bunch. In figure 2.2.1, the beam enters a cavity and the fields penetrate the cavity. As the bunch travels through the cavity, the normal modes of the cavity are excited and the wakefields produced can interact with the bunch as it propagates through the cavity. When the beam leaves the cavity 2.0 $n$sec later it has left energy in the cavity which must be replaced by the RF system.

Longitudinal Wake Potential

Consider two ultra relativistic point charges q_1 and q_2 traveling parallel to the axis of a rotationally symmetric beam pipe as shown in figure 2.2.2.

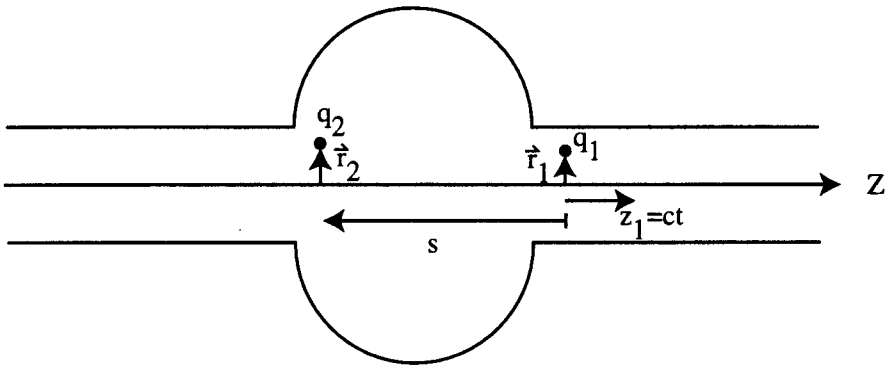

Figure 2.2.2. A source charge q_1 passes through a rotationally symmetric cavity followed by a test charge q_2.

In the case when the unit source charge q_1 is displaced a distance $\vec{r}_1$ from the z axis and moves according to $z_1 = ct$ and the unit test charge q_2 has displacement $\vec{r}_2$ and at a distance $s = ct_0$ behind the source charge, then energy change that charge q_2 receives is

$$\frac{dE}{dt} = \frac{dP_z}{dt} = E_z(\vec{r}_1, \vec{r}_2, t)$$

where $E_z(\vec{r}_1, \vec{r}_2, t)$ is the longitudinal electric field produced by the source charge q_1. The delta function longitudinal wake potential which test charge q_2 receives from source charge q_1 is derived by integrating the energy transfer over time and over the full length of the structure to give

$$\Delta E = V_L(\vec{r}_1, \vec{r}_2, t_0) = \int_{-\infty}^{\infty} dz \int_{-\infty}^{\infty} dt' E_z(\vec{r}_1, \vec{r}_2, t') \delta\left(t' - \left(t_0 + z/c\right)\right). \qquad (2.2.1)$$

where the wake potential has units of volts per Coulomb.

A general plot of the time dependence of the longitudinal wake potential (figure 2.3.3) is used to illustrate some important properties of longitudinal wake potential.

1) $V_L(\vec{r}_1,\vec{r}_2,t_0)$ must be negative as $t_0 \to 0$ because the source charge q_1 loses energy into the accelerator component.

2) As a consequence of causality, there is a lack of action occurring ahead of the source charge so that $V_L(\vec{r}_1,\vec{r}_2,t_0)=0$ for $t_0<0$.

3) $V_{self}=\frac{1}{2}V_L(\vec{r}_1,\vec{r}_2,t_0\to 0)$ is the fundamental theorem of beam loading which states that the self-voltage which the source charge sees is equal to half the induced voltage which the particle leaves [P. Wilson, 1981]

4) At large values of t_0, the wake potential depends on the geometry of the cavity.

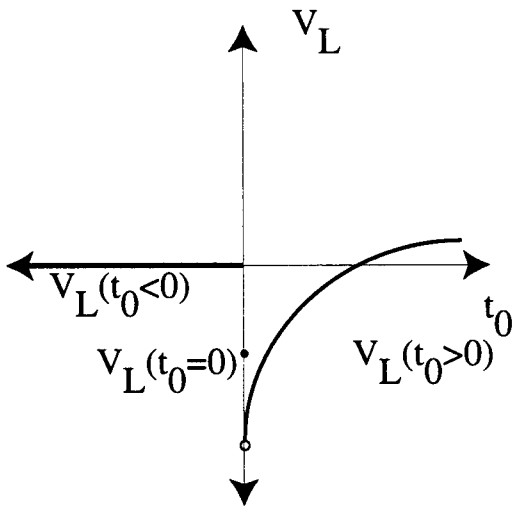

Figure 2.3.3. The longitudinal wake potential as a function of time.

Wake potential has been described as a function of time, but it is often useful to examine the frequency content of the wake potential. In the frequency domain the wake potential is called the impedance, and the longitudinal impedance is obtained by Fourier transforming the wake potential to give

$$Z_L(\omega)=-\int_{-\infty}^{\infty} dt V_L(t)\exp[-i\omega t]\cdot$$

One of the results of the longitudinal wake potential is the particles in the bunch will lose energy as a function of their location in the bunch. The energy loss due to longitudinal wakefields for a beam is calculated by integrating the longitudinal wake potential over the bunch current

$$\Delta E = \int_{-\infty}^{\infty} I(t) V_L(t) dt \cdot$$

The longitudinal wakefield effects the longitudinal dynamics in the SLC in three important areas. 1) The wake potential in the disk loaded wave guide accelerating structure in the main linac changes the energy profile of the beam. The wake potential for the SLC linac is presented in section 2.5. 2) The impedance of various accelerator components in the damping ring change the bunch distribution. This is called the potential well distortion and is presented in section 2.3. 3) The wake potential can lead to instabilities in the damping ring that can make the distribution unstable. This will be further discussed in section 2.3.

Transverse Wake Potential

If in figure 2.2.2, the charge q_1 is displaced from the z-axis by a distance $\vec{r}_1$ the charge q_2 can be deflected transversely by the fields produced by q_1. The momentum transfer that charge q_2 receives is

$$\frac{d\vec{P}_\perp}{dt} = \left[\vec{E}(\vec{r}_1, \vec{r}_2, t) + \beta c \hat{z} \mathrm{x} \vec{B}(\vec{r}_1, \vec{r}_2, t)\right]_\perp$$

where $\perp$ refers to the component in the transverse direction. The transverse wake potential is derived by integrating the momentum transfer to give

$$\Delta\vec{P}_\perp(\vec{r}_1, \vec{r}_2, t_0) = \int_{-\infty}^{\infty} dz \int_{-\infty}^{\infty} dt' \left[\vec{E}(\vec{r}_1, \vec{r}_2, t_0) + c\vec{z} x \vec{B}(\vec{r}_1, \vec{r}_2, t_0)\right]_\perp \delta\left(t' - \left(t_0 + z/c\right)\right).$$

The transverse wake potential has several interesting properties:

1) There is a coupling between the transverse and longitudinal wake potential is given by the Panofsky-Wenzel theorem [Panofsky and Wenzel, 1956]. This theorem relates the wake potentials by

$$V_\perp(\vec{r}_1, \vec{r}_2, t_0) = -\vec{\nabla}_\perp \int_{-\infty}^{t_0} V_L(\vec{r}_1, \vec{r}_2, t) dt$$

where $\vec{\nabla}_{\perp}$ is the gradient with respect to the test particle's coordinates.

2) The transverse wake potential is non-zero only if the test particle q_1 is off the z-axis. If test charge q_1 is off the z-axis then the tail particle q_2 is always deflected away from the z-axis in the direction of the head particle. This can cause the tail of the bunch to oscillate and can cause the emittance of the beam to increase in the main linac. The transverse wakefields need to be controlled to minimize transverse emittance growth in the SLC linac. The method used to control the emittance growth is BNS damping [V.E. Balakin, 1983], and this will be presented in section 2.3.

3) The general form of the transverse wake potential is shown in figure 2.3.4. It follows from the Panofsky-Wenzel theorem that the particular behavior at $t_0 > 0$ is dependent on the geometry of the cavity.

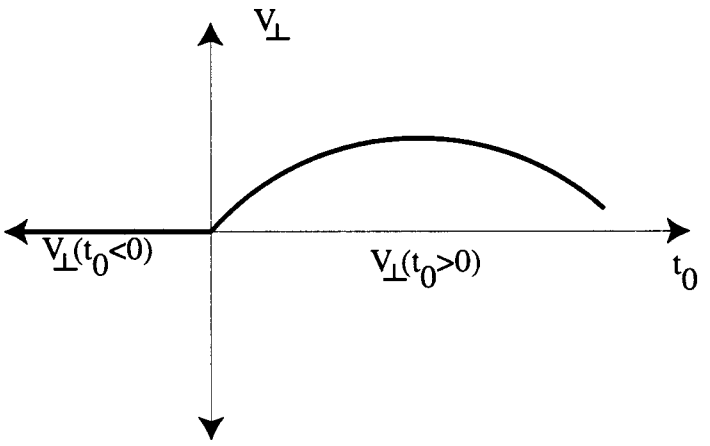

Figure 2.3.4. The transverse wake potential as a function of time.

2.3 Potential Well Distortion and Instabilities in the Damping Ring

Introduction

From the single particle motion described in section 2.1, the bunch distribution in the damping ring in equilibrium has a Gaussian distribution, and the length depends upon the RF accelerating voltage. In the same manner that the RF accelerating fields affect the bunch distribution, the longitudinal wakefields also influence the shape of the bunch distribution. There are several ways wakefields influence the longitudinal dynamics of the SLC beam in the damping ring; these will be examined in this section.

Hamiltonian for Longitudinal Dynamics with Wakefields

The Hamiltonian can be modified to include the longitudinal wake potential. Now the term $qV(\tau)$ includes the energy gain/lost due to synchrotron radiation, RF accelerating voltage but also the longitudinal wake potential. While ignoring the damping term, the function $qV(\tau)$ can be expanded for small oscillation amplitudes to give

$$qV(\tau) = q\left(\frac{dV_{rf}}{d\tau}\right)\tau + qV_L(\tau)$$

where $qV_L(\tau)$ is the longitudinal wake potential. The differential equations 2.1.8 and 2.1.9 in section 2.1 are modified to included the wake potential and can be written in terms of the Hamiltonian as

$$\frac{\partial H}{\partial \tau} = -\frac{d\varepsilon}{dt} = -\frac{1}{T_0}\left[q\left(\frac{dV_{rf}}{d\tau}\right)\tau + qV_L(\tau)\right] \tag{2.3.1}$$

$$\frac{\partial H}{\partial \varepsilon} = \frac{\partial \tau}{\partial t} = -\alpha\frac{\varepsilon}{E_0}. \tag{2.3.2}$$

Integrating equations 2.3.1 and 2.3.2 gives the Hamiltonian

$$H(\varepsilon,\tau;t) = -\frac{\alpha}{2E_0}\varepsilon^2 - \frac{\Omega_s^2 E_0}{2\alpha}\tau^2 + \int_0^{\tau}\frac{qV_L(\tau')}{T_0}d\tau'.$$

With potential well distortion the bunch is static but distorted from a Gaussian distribution by wakefields [J. Haissinski, 1973]. What we observe in the SLC damping rings is the higher the beam intensity the greater the distortion. There is another possibility,

that the distribution is not static but instead performs a collective oscillation. This is discussed later.

The stationary state particle distribution can be determined by solving Vlasov's equation where $\psi(\varepsilon,\tau)$ is the phase space distribution normalized to unity [Chao,1993]. Vlasov's equation is used to describe a multiparticle system which is influenced by electromagnetic fields. In our case, Vlasov's equation is

$$\frac{\partial\psi}{\partial t}+\dot{\tau}\frac{\partial\psi}{\partial\tau}+\dot{\varepsilon}\frac{\partial\psi}{\partial\varepsilon}=0$$

where

$$\dot{\tau}=\frac{\partial H}{\partial\varepsilon}=-\alpha\frac{\varepsilon}{E_0}$$

and

$$\dot{\varepsilon}=\frac{\partial H}{\partial\tau}=q\frac{V_L(\tau)}{T_0}-\frac{\Omega_s^2E_0}{\alpha}\tau.$$

The system we are dealing with is conservative because we are ignoring the damping term in the Hamiltonian. For a stationary distribution $\frac{\partial\psi}{\partial t}=0$ and Vlasov's equation becomes

$$\dot{\tau}\frac{\partial\psi}{\partial\tau}+\dot{\varepsilon}\frac{\partial\psi}{\partial\varepsilon}=0.$$

When dealing with a Hamiltonian with no explicit time dependence the particles will rotate in longitudinal phase space along constant contours described by the Hamiltonian. This allows the particle distribution to be expressed as any function of the Hamiltonian, and so I have chosen

$$\psi(\tau,\varepsilon)=\exp[-CH(\tau,\varepsilon)]$$

where C is an arbitrary constant. By choosing $C=\frac{1}{\alpha\sigma_E^2E_0}$ to give the correct result in the limit of zero wakefield, the resulting expression for the phase space distribution is

$$\psi(\tau,\varepsilon)=\exp\left[-\frac{\varepsilon^2}{2\sigma_E^2}-\frac{\tau^2}{2\sigma_\tau^2}+\frac{q}{\alpha T_0\sigma_E^2E_0}\int_0^\tau V_L(\tau')d\tau'\right]. \qquad (2.3.3)$$

There are three interesting points that can be made about the stationary state distribution:
1) At low current, the wakefield potential $V_L\approx 0$, which results in the distribution being Gaussian in τ.
2) The distribution will always be Gaussian in the energy deviation ε.
3) As the current increases the distribution remains Gaussian in ε but does not stay Gaussian in τ.

Equation 2.3.3 can be separated into two terms, one involving the energy spread and the other involving the bunch length. The stationary state solution can be written as

$$\psi(\tau,\varepsilon)=\exp\left[-\frac{\varepsilon^2}{2\sigma_E^2}\right]\exp\left[-\frac{\tau^2}{2\sigma_\tau^2}+\frac{q}{\alpha T_0\sigma_E^2E_0}\int_0^\tau V_L(\tau')d\tau'\right]=A(\varepsilon)B(\tau).$$

The charge density distribution is calculated by integrating over the phase space distribution

$$\rho(\tau)=N\int_{-\infty}^{\infty}\psi(\tau,\varepsilon)d\varepsilon$$

where N is the number of particles in the bunch. The charge density $\rho(\tau)$ is given by

$$\rho(\tau)=\rho(0)\exp\left[-\frac{\tau^2}{2\sigma_\tau^2}+\frac{q}{\alpha T_0\sigma_E^2E_0}\int_0^\tau V_L(\tau')d\tau'\right] \qquad (2.3.4)$$

where the term $\rho(0)$ is the normalization factor. Following are two examples of the bunch distribution changes due to the wake potential. These examples illustrate the bunch distribution changes due to the potential well distortion.

Inductive Wakefield

If the wake potential is modeled after a pure inductive impedance, the wake potential is proportional to the derivative of the charge density and is expressed as

$$V_L(\tau)=-L\frac{dI}{d\tau}$$

where L is the inductance, and I is the bunch current. The accelerator components that cause inductive wakefields are bellows, transitions in vacuum chamber walls, and masks. Substituting the wake potential into equation 2.3.4, the charge distribution after integration is

$$\rho(\tau)=\rho(0)\exp\left[-\frac{\tau^2}{2\sigma_\tau^2}-\frac{Lq^2N\rho(\tau)}{\alpha E_0T_0\sigma_\varepsilon^2}\right] \qquad (2.3.5)$$

where N is the number of particles in the bunch. The transcendental equation for $\rho(\tau)$ has the form

$$a(\tau)=C\exp\left(-\frac{\tau^2}{2}-a(\tau)\right)$$

which can be differentiated with respect to τ to give

$$\frac{da(\tau)}{d\tau} = \frac{-\tau a(\tau)}{1+a(\tau)}. \tag{2.3.6}$$

Equation 2.3.6 can be examined in the low and high current limits.

1) In the limit of low current ($a(\tau) << 1$) equation 2.3.6 can be approximated as

$$\frac{da(\tau)}{d\tau} = -\tau a(\tau)$$

which when integrated gives

$$a(\tau) = \exp\left[\frac{-D\tau^2}{2}\right]$$

where D is an integration constant. In this low current limit, the charge distribution is Gaussian as expected.

2) In the limit of high current ($a(\tau) >> 1$) equation 2.3.6 can be approximated as

$$\frac{da(\tau)}{d\tau} = -\tau$$

and integrated to give

$$a(\tau) = a_0 - \frac{1}{2}\tau^2 \tag{2.3.7}$$

where a_0 is an integration constant. As the current increases the bunch distribution deviates from a true Gaussian distribution and becomes parabolic in the high current limit. The bunch distribution, equation 2.3.5, can be plotted versus intensity using the Newton-Raphson method. The particle distribution after some manipulation is the stable iteration of the equation

$$\eta_{new}(x) = \eta_{old}(x) + \frac{B\exp\left[-\frac{x^2}{2} - \eta_{old} + B\right] - \eta_{old}}{B\exp\left[-\frac{x^2}{2} - \eta_{old} + B\right] + 1} \tag{2.3.8}$$

where the redefined terms are $A = \frac{LqN}{T_0 E_0 \alpha \sigma_E^2}$, $B = A\rho(0)$, $\eta(x) = A\rho(x)$, and $x = \frac{\tau}{\sigma_\tau}$.

In figure 2.3.1, the intensity term B has been varied and when B is small the distribution is Gaussian. As B increases the particle distribution peaks at its center which exhibits its parabolic behavior.

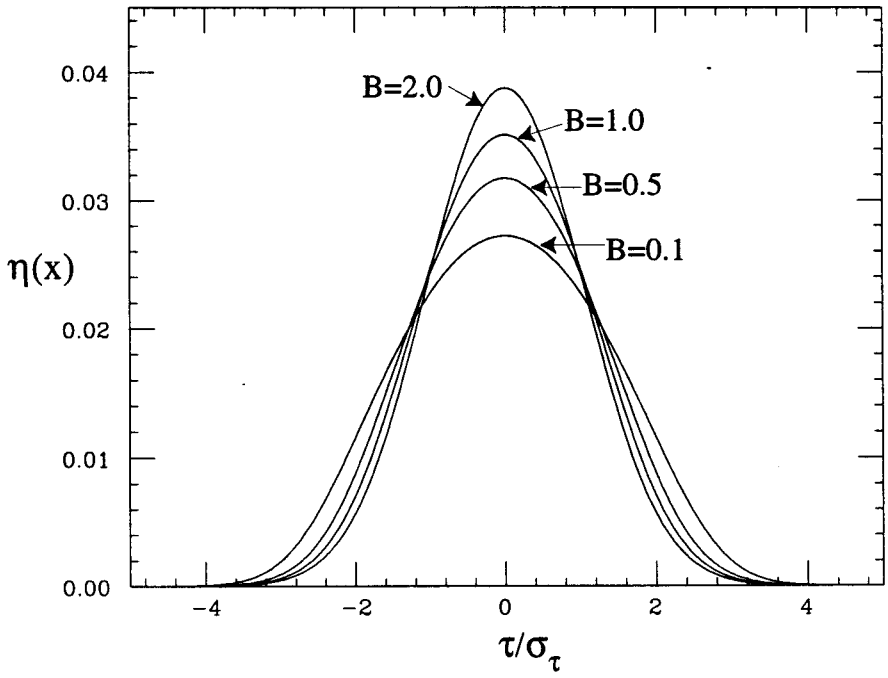

Figure 2.3.1. The bunch distribution as a function of the current for a purely inductive impedance where the nominal bunch length is the same in all cases and B is proportional to current.

The bunch distribution energy lost due to a purely inductive wakefield (ignoring any resistive part) is given by

$$\Delta u = \int_{-\infty}^{\infty} V_L(\tau) I(\tau) d\tau = -L\left(I^2(\infty) - I^2(-\infty)\right) = 0.$$

This means the beam loses no energy passing an accelerator component which produces an inductive wakefield.

Resistive Wakefield

The wake potential for a pure resistive impedance is proportional to the charge density and is given by given by

$$V_L(\tau) = RI(\tau)$$

where R is the resistance. The charge distribution for a resistive wakefield is

$$\rho(\tau) = \rho(0)\exp\left[-\frac{\tau^2}{2\sigma_\tau^2} + \frac{qR}{\alpha T_0 \sigma_E^2 E_0}\int_0^\tau I(\tau')d\tau'\right]. \qquad (2.3.9)$$

Equation 2.3.9 can be solved exactly to give [A. Ruggiero, 1977]

$$\rho(x) = \frac{\exp\left(-\frac{x^2}{2}\right)}{A\left(\coth\left(\frac{AN}{2}\right) - erf(x)\right)} \tag{2.3.10}$$

where $x = \frac{\tau}{\sigma_\tau}$, $A = \frac{q^2 R \sigma_\tau}{\alpha T_0 E_0 \sigma_E^2}$, and $erf(x) = \frac{2}{\sqrt{\pi}} \int_0^x \exp\left(\frac{-x'^2}{2}\right) dx'$. The charge density can be written as

$$\varphi(x) = \frac{\exp\left(-x^2\right)}{\coth(D) - erf(x)} \tag{2.3.11}$$

where $D = \frac{AN}{2}$ is dependent on the intensity and $\varphi(x) = \frac{\rho(x)}{A}$. A plot of equation 2.3.11 (figure 2.3.2) illustrates the resistive wakefield shifts of the bunch distribution as intensity (D in the figure) increases.

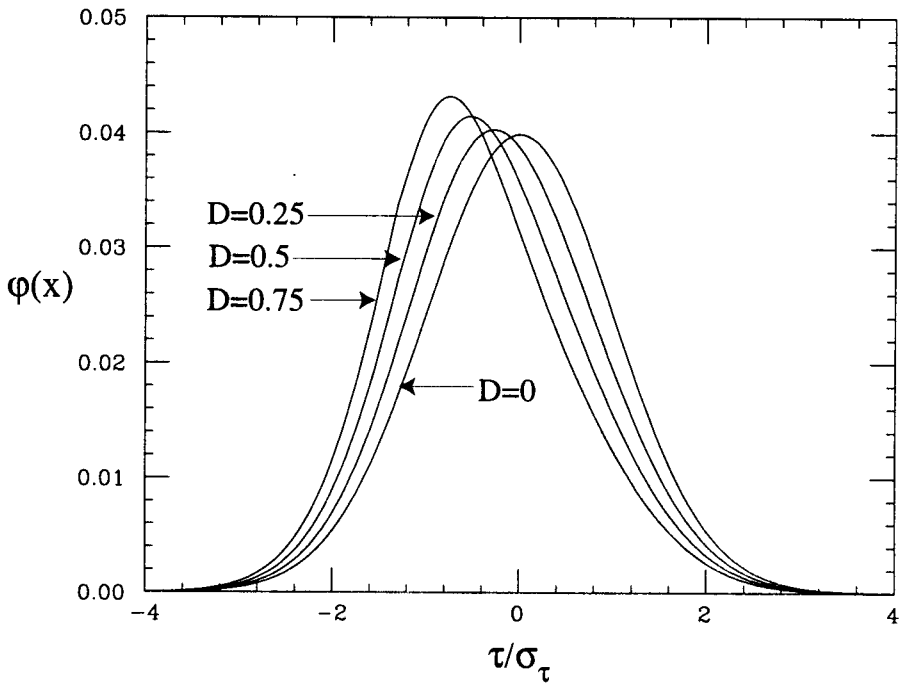

Figure 2.3.2. The bunch distribution as a function of the current for a purely resistive impedance. The factor D is proportional to the current.

The energy lost due to resistive impedance depends on the bunch length assuming a Gaussian distribution it is given by

$$\Delta u = R\frac{q^2N^2}{2\pi\sigma_\tau^2}\int_{-\infty}^{\infty}\exp\left[\frac{-\tau^2}{2\sigma_\tau^2}\right]d\tau = \frac{Rq^2N^2}{2\sqrt{\pi}\sigma_\tau}. \qquad (2.3.12)$$

By equating the energy lost to the RF energy gain, the average position of the bunch is

$$\bar{\tau} = \tau(N=0) + \frac{eNR}{2\sqrt{\pi}\sigma_\tau\frac{dV_{rf}}{d\tau}}.$$

The first term is due to the synchrotron radiation energy loss. The second term describes the shift of the distribution up the RF wave due to energy losses from the wakefield. This shift is proportional to intensity and inversely proportional to bunch length.

The above examples illustrate how the longitudinal wakefields change the distribution in damping rings. In reality, the wakefield in the SLC damping rings consist of resistive, inductive and capacitive parts. In principle, the particle distributions measured in the damping rings can be used to measure the dominant components of the impedance in the damping ring and this will be presented in chapter 4.

Longitudinal Instabilities

The discussion above has assumed that a stationary state of the beam exists and is stable. This cannot be taken for granted when wakefields are considered. What usually happens is that the beam becomes unstable above some threshold current. An enormous amount of literature is available which describes the instabilities which result in circular accelerators [F. Sacherer, 1972, R. Siemann, 1983, and A. Chao 1993].

The general methods of analysis of instabilities are to linearize Valsov's equation for small perturbations or to use computer simulations. One result is that the energy spread no longer remains constant as it does with potential well distortion. An increase in the energy spread is the signature of an instability and is a better method than measuring the bunch length to determining a current threshold for an instability.

The longitudinal phase space can be described by "rectangular" coordinates τ and ε or by polar coordinates $\hat{\tau}$ and ϕ (R. Siemann, 1989) and the beam distribution can be Fourier analyzed in ϕ. Usually an instability affects only a few Fourier components, and analysis of beam generated signals can identify the affected Fourier components. Longitudinal profile data can be used as an alternative to analysis of beam generated signals. These show variations of the bunch shape time intensity (K. Bane et al, 1995).

As will be discussed in the experimental results there is an instability in the SLC damping ring, but it does not dominate performance. Potential well distortion is the dominate effect. Details about this instability and its effects on the SLC will be discussed in the experimental chapter 4.

2.4 Bunch Compression

Introduction

The electron and positron bunch lengths after the damping ring are too large (~5-7mm) for acceleration in an S-band accelerating structure so they must be compressed. There are two bunch compressors at the SLC, one for positrons and one for electrons. They are both located in the transport line from the damping rings to the linac. In this section the dynamics of bunch compression will be presented [H. Wiedemann, 1981].

Bunch Compressor

The bunch compressor consists of two parts, the first part is an RF accelerating

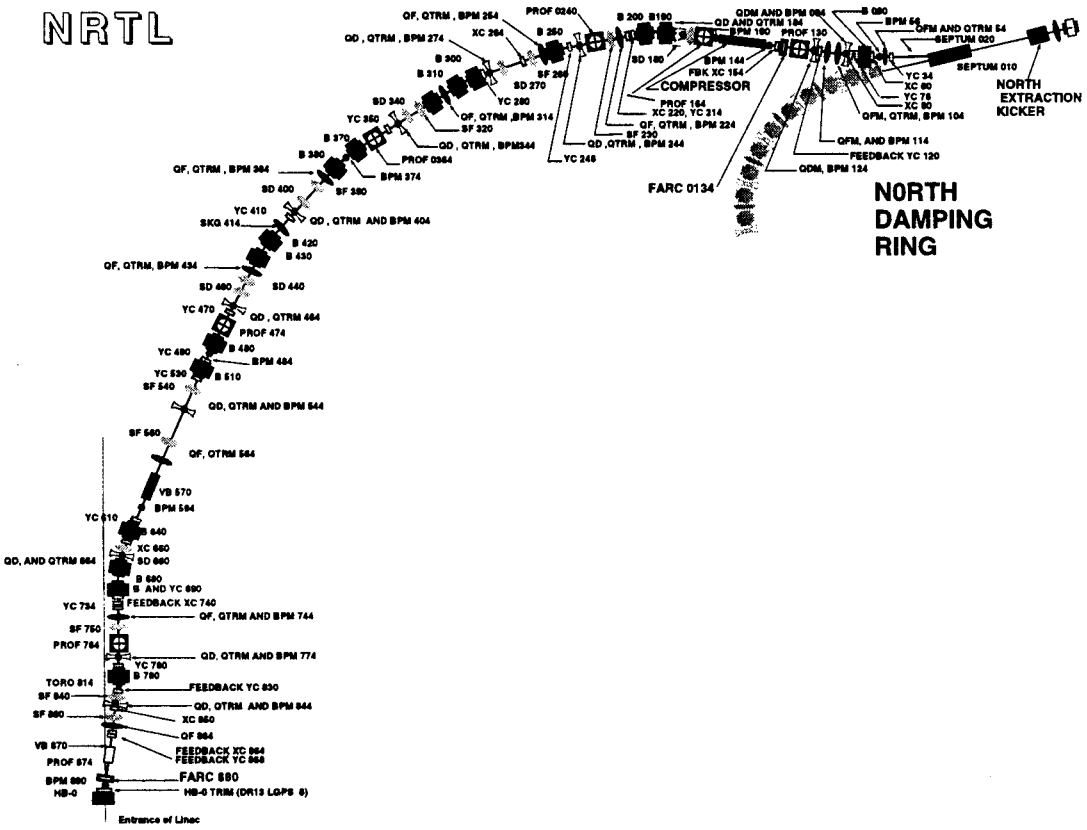

Figure 2.4.1. The electron bunch compressor, the North Ring to Linac (NRTL) transport line.

section that is just after the exit of the damping ring, and the second part is a nonisochronous transport section after the accelerating section. The layout of a bunch compressor is shown in figure 2.4.1.

The longitudinal phase space of the extracted bunch from the damping ring is shown in figure 2.4.2a. After the damping ring, the bunch enters the RF accelerating section. The RF accelerating section is phased such that the mean of the bunch is positioned at the zero crossing of the RF wave. The phase is also chosen to give the head of the bunch an energy gain while the tail of the bunch is decelerated. In essence, the RF section gives the bunch a correlated energy spread (figure 2.4.2b). Following the accelerating section the bunch is bent through a transport line with momentum compaction α_{comp} . Because of their higher energy the particles in the head of the bunch will travel over a longer path than the particles at the center of the bunch. The particles in the tail of the bunch will travel over a shorter distance than the center particles with a net result of a compressed bunch. The degree of compression (rotation in phase space) depends upon the amplitude of the RF voltage and the energy spread of the beam exiting the damping ring. The amplitude of the voltage can be adjusted to give a fully compressed (figure 2.4.2c), an under compressed (figure 2.4.2d) or an over compressed bunch (figure 2.4.2d).

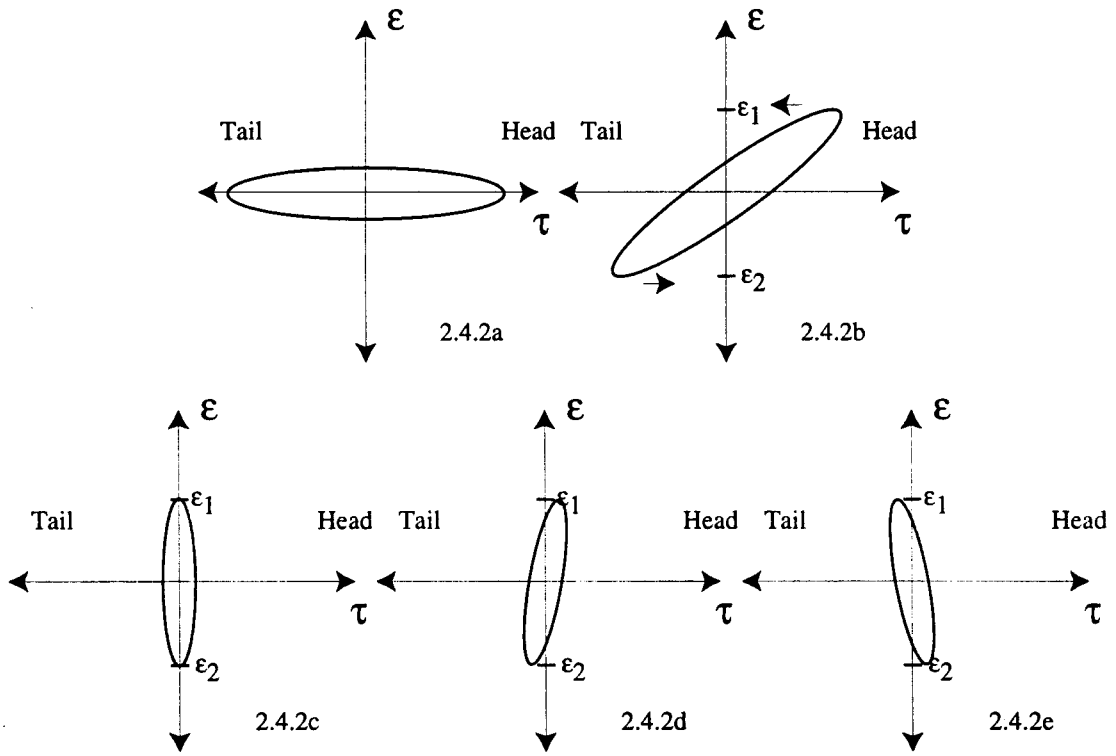

Figure 2.4.2. The longitudinal phase space of the beam entering the RF accelerating section (a), after the RF accelerating section (b), entering the linac fully compressed (c), under compressed (d), and over compressed (e).

Following is a more quantitative discussion of the method of compression. If the Gaussian energy spread and bunch length coming out of the damping ring are σ_ε and σ_τ the equation for a phase ellipse in longitudinal phase space is

$$\sigma_{\varepsilon_0}^2 \tau^2 + \sigma_{\tau_0}^2 \varepsilon^2 = \varepsilon_{l_i}^2$$

where τ is the time of the particle from the center of the bunch, ε is the energy deviation of the particle, and ε_{l_i} is the initial longitudinal emittance. After the damping ring the bunch goes through the compressor cavity and each particle's energy will be changed by an amount

$$\Delta E_{rf} = eV_{rf} \sin(\omega_{rf}\tau) \approx \gamma\tau \text{ where } \gamma = eV_{rf}\omega_{rf}$$

where ω_{rf} is the RF frequency, and V_{rf} is the compressor voltage. The energy of each particle is changed depending upon its location in the bunch, and the energy deviation after the acceleration section is $\varepsilon \rightarrow \varepsilon + \Delta E_{rf}$. Substituting the energy deviation into the equation of the ellipse gives

$$\left(\sigma_{\varepsilon_0}^2 + \sigma_{\tau_0}^2 \gamma^2\right)\tau^2 + \sigma_{\tau_0}^2 \varepsilon^2 + 2\sigma_{\tau_0}^2 \gamma\tau\varepsilon = \varepsilon_{l_f}^2$$

where ε_{l_f} is the final longitudinal emittance.

After the acceleration section the bunch travels through the transport line. The transport line has a momentum compaction factor of α_{comp} and length L. The travel time difference for a particle that does not have the ideal momentum (P_0) is given by $\Delta\tau = \frac{\Delta s}{c}$ where Δs is the change in the path length. The time shift in position through the transport line can be expressed in terms of the momentum compaction factor as

$$\Delta\tau = \frac{\alpha_{comp} L\varepsilon}{P_0} = \beta\varepsilon \text{ where } \beta = \frac{\alpha_{comp} L}{P_0}.$$

The shift in time is $\tau \rightarrow \tau - \beta\varepsilon$, and substituting it into the phase ellipse equation gives

$$\begin{aligned}&\left(\sigma_{\varepsilon_0}^2 + \sigma_{\tau_0}^2 \gamma^2\right)\tau^2 + 2\left(\sigma_{\tau_0}^2\left(\gamma - \beta\gamma^2\right) - \beta\sigma_{\varepsilon_0}^2\right)\varepsilon\tau \\ &+\left(\sigma_{\tau_0}^2 (1-\gamma\beta)^2 + \sigma_{\varepsilon_0}^2\beta^2\right)\varepsilon^2 = \varepsilon_{l_f}^2.\end{aligned} \tag{2.4.1}$$

The bunch length and energy spread after the bunch compressor are

$$\sigma_{\tau f} = \sqrt{\sigma_{\tau_0}^2\left(1 - \left(\frac{L\alpha_{comp}}{cP_0}\right)\left(eV_{rf}\frac{2\pi}{\lambda_{rf}}\right)\right)^2 + \left(\frac{L\alpha_{comp}}{cP_0}\right)^2 \sigma_{\varepsilon_0}^2} \tag{2.4.2}$$

and $$\sigma_{\varepsilon_f} = \sqrt{\sigma_{\varepsilon_0}^2 + \left(eV_{rf}\omega_{rf}\right)^2 \sigma_{\tau_0}^2}\,. \qquad (2.4.3)$$

The longitudinal emittance entering the linac when the bunch length is minimized is $\varepsilon_{l_f} = \sigma_\varepsilon \sigma_\tau = \sigma_{\varepsilon_0}\sigma_{\tau_0} = \varepsilon_{l_i}$. It is interesting to note that the initial longitudinal emittance is equal to the final emittance because Liouville's theorem states that the longitudinal phase space must be preserved for conservative forces [Wiedemann, 1993].

The bunch length and energy spread can be plotted versus the RF voltage to illustrate the effects of the initial beam parameters on the final bunch distribution. The final bunch length is plotted using the constants in the table at the end of this section versus RF voltage.

From figure 2.4.3, several interesting features are evident:

1) The minimum bunch length is dependent on the initial energy spread and is given by $\sigma_\tau = \left(\frac{L\alpha_{comp}}{cP_0}\right)\sigma_{\varepsilon_0}$.

2) Moving away from the minimum bunch length, the bunch length is determined by the initial bunch length, and the final bunch length is not dependent upon the initial energy spread in this regime.

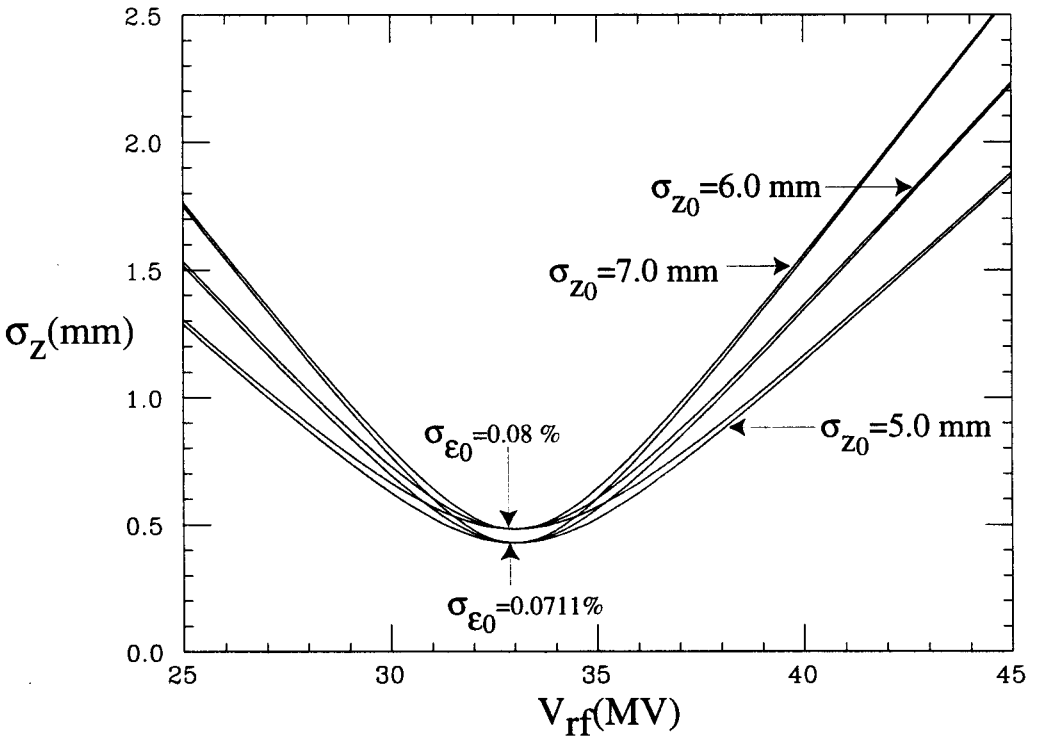

Figure 2.4.3. The bunch length versus RF voltage for various initial bunch lengths and energy spreads for the SLC bunch compressor.

The final energy spread is plotted versus RF voltage for different initial bunch lengths and energy spreads. Several interesting features are evident in figures 2.4.3 and 2.4.4:

1) The initial energy spread is determined by the SLC damping rings and its equilibrium value is 0.0711%. A turbulent instability has been observed in the damping rings and when the current is raised the energy spread increases which will effect the minimum bunch length achieved in the linac.

2) The two energy spreads overlap one another which illustrates the final energy spreads independence from the initial energy spread.

3) The energy spread of the beam entering the linac is solely dependent upon the initial bunch length. For each bunch length two energy spreads (0.0711% and 0.080%) are plotted.

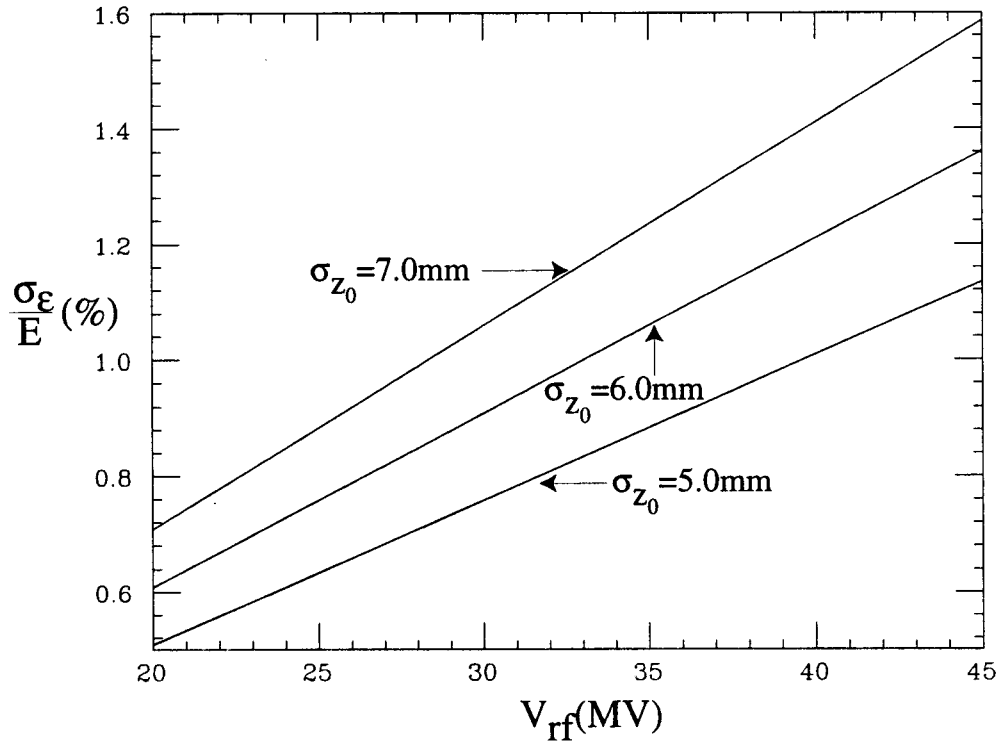

Figure 2.4.4. The energy spread of the beam entering the linac as a function of the RF voltage.

The minimum bunch length occurs when the phase ellipse is up right, and occurs when the cross term in equation 2.4.1 is zero. The RF voltage necessary to minimize the bunch length is

$$eV_{rf} = \frac{1}{\omega_{rf}}\left(\frac{P_0}{L\alpha}\right) \approx 33MV.$$

The minimum bunch length and corresponding energy spread are

$$\sigma_{\tau f} = \frac{\sigma_{\varepsilon_0}}{eV_{rf}\omega_{rf}}$$

and

$$\sigma_{\varepsilon f} = eV_{rf}\sigma_{\tau_0}\omega_{rf}.$$

This section presented the longitudinal phase space changes in the compressor for a Gaussian beam's distribution. In reality, the bunch distribution in the damping ring is not Gaussian due to potential well distortion and second order compression should also be included. In section 2.6, a tracking method will be presented which takes any bunch distribution from the damping ring and tracks the longitudinal phase space through the compressor region to second order.

Beam loading

Beam loading refers to the effects induced when the beam passes through an RF cavity structure. The effect of a beam passage is to excite additional fields in the cavity which change the accelerating voltage of the cavity. The passing bunch extracts energy from the cavity which results in less energy to accelerate the bunch. Beam loading is not only important for the main linac accelerating structure but it can also affect the performance of the compressor accelerating section. Normally the total energy gain, neglecting beam loading, for a linear structure is

$$E_{RF} = N_{SLED}\, x\, \sqrt{R_s L P_0 (1-\exp(-2\tau))}\cos(\varphi_s) \qquad (2.4.4)$$

where φ_s is the phase off the RF crest, P_0 is the RF power delivered to the section, R_s is the shunt impedance per unit length of the cavity, L is the length of the cavity, N_{SLED} is the SLED multiplication factor, and the attenuation factor $\tau = \frac{\omega L}{2v_g Q}$. For the compressor RF accelerating section there are two differences that will change equation 2.4.4. 1) The bunch length is longer in the compressor RF section but this turns out to be a negligible effect. 2) The bunch in a compressor RF section is centered on the zero crossing of the RF wave. The expression for the voltage delivered to the beam in the compressor RF section is

$$V_{beam} = \sqrt{\frac{8}{(1+\beta)^2}(\beta R_s P_o) + (kNq)^2} \qquad (2.4.5)$$

where β is the cavity coupling coefficient, N is the number of particles in the beam, and $k = \frac{\omega R_s}{4Q} = 0.7\ V/\ pc \cdot m$ for the SLC accelerating structure. The second term in equation 2.4.5 is due to beam loading. As an example, for a beam current of $N = 4\text{x}10^{10}$ particles per bunch the beam loading voltage is

$$V_{BL} = kNq = 9.72\ kV \cdot$$

When compared to a compressor's generated voltage of 30 MV, the beam loading voltage is negligible and does not need to be included in the simulations of longitudinal dynamics.

Compressor Phase stability

In the compressor accelerating section the mean of the bunch distribution is positioned on the zero crossing of the RF accelerating wave and the change in energy for the bunch is given by

$$\Delta E_{rf} = eV_{rf} \sin\left(\omega_{rf}\tau + \varphi\right)$$

where φ is the phase offset. The phase offset has been measured with a phase detector and is stable to $\pm\frac{1}{2}$ of a degree of the RF accelerating waveform [P. Krejcik, 1995]. The stability of the phase offset will be discussed in the simulation section of chapter 4.

SLC Bunch Compressor Parameters

Incoming Beam Parameters	
Energy E_0	1.19 Gev
Initial Energy Spread $\frac{\sigma_E}{E_0}$	$7.11x10^{-4}$
Initial Bunch Length σ_{z_0}	5-7mm
Compressor Transport Line	
RF Frequency	2856 MHz
RF Wavelength	10.497 cm
RF Voltage Range	0.0-44.0 MV

Transport $R_{56} = L\alpha_{comp} = \int \frac{\eta(s)}{\rho(s)} ds$	$-0.60261m\ \%^{-1}$
Transport $T_{566} = \frac{dR_{56}}{d\delta}$	$-1.076m\ \%^{-2}$

Compressor S-band Accelerating Structure Parameters

Length	2.170 m
Power	Variable
Shunt Impedance R_s	53 MΩ/m
Attenuation Factor τ	0.57

2.5 Longitudinal Dynamics for the SLC Linac

Introduction

The electron and positron beams both pass through the same accelerating structure in the SLC linac where they are accelerated from 1.19 GeV to 46.5 GeV. The longitudinal bunch distribution in the linac is fixed, however, the energy spread at the end of the linac is a result of phasing the bunch on the RF accelerating wave and longitudinal wakefield energy loss. In this section, single particle longitudinal dynamics in a linear accelerator, the accelerating structure of the SLC linac, and BNS damping will be presented.

Single Particle Longitudinal Motion for the SLC Linac

The capture of particles and the resulting energy at the end of the accelerating section depend greatly on the relative synchronism of the particle and wave motion. The particles injected in the main linac have an energy of 1.19 GeV so that their velocity is $v_p \approx c$. The difference in the distance traveled between the particle and the accelerating RF wave can be expressed in terms of a phase shift

$$\frac{d\varphi}{dz} = -\frac{2\pi c}{\lambda_{rf}}\left(\frac{v_{ph} - v_p}{v_p v_{ph}}\right)$$

where v_{ph} is the phase velocity of the RF accelerating electromagnetic wave. To keep the phase constant the accelerating structure for the SLC is a disk loaded wave guide which reduces the phase velocity v_{ph} to equal the particles' velocity v_p. The proper choice of dimensions of the disk assures the velocities are equal. For the SLC (figure 2.5.1), the spacing between disks is given by

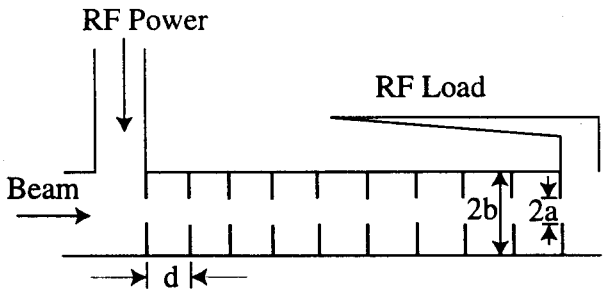

Figure 2.5.1. A cross section view of the accelerating structure for the SLC linac.

$$d = \frac{2\pi}{3}\left(\frac{c}{\omega_{rf}}\right) = 3.50cm$$

which results in φ, the phase shift, equal to a constant.

The particle's energy at the end of the linac is determined from the RF amplitude in the linac, the phase of the bunch on the RF accelerating wave, and the energy loss due to longitudinal wakefields. The bunch (figure 2.5.2) has a longitudinal distribution in z ($z = 0$ is the mean location of the bunch) and the energy of a particle, ignoring longitudinal wakefields, at the end of the linac is

$$E(z) = E_0(z) + \sum_i^N E_i \cos(\frac{2\pi z_i}{\lambda_{rf}} + \varphi_{linac} + \varphi_{BNS})$$

where N is the number of accelerating sections, $E_0(z)$ is the initial energy of the particle entering the linac, E_i is the maximum RF amplitude from an accelerating section, φ_{linac} is the overall adjustable linac phase with respect to the crest of the RF wave, φ_{BNS} is the phase used to BNS damp the beam and will be discussed later, and λ_{rf} is the S-band RF wavelength.

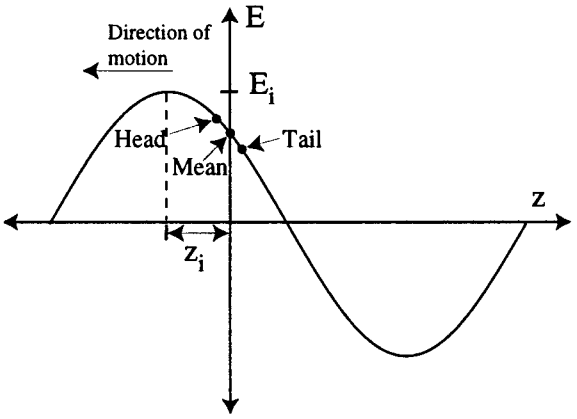

Figure 2.5.2. The spacing of three particles in the bunch traveling on the RF accelerating wave.

The longitudinal wakefields change the energy of a particle by decelerating the particles in the tail of the bunch. The analytic expression for the voltage for a particle (figure 2.5.3) due to the longitudinal wakefield for the SLC structure is given by [K. Bane, 1980]

$$W_l(z_j - z_i) = -7\left(\frac{\mathrm{V}}{\mathrm{pC}}\right)N_c \exp\left[-\sqrt{\frac{z_j - z_i}{1.62}}\right].$$

where $z_i - z_j$ is the distance, in millimeters, between the *i*th source particle and the *j*th test particle, and the units are volts per picocoulomb per cell with N_c the total number of cells in the SLC linac.

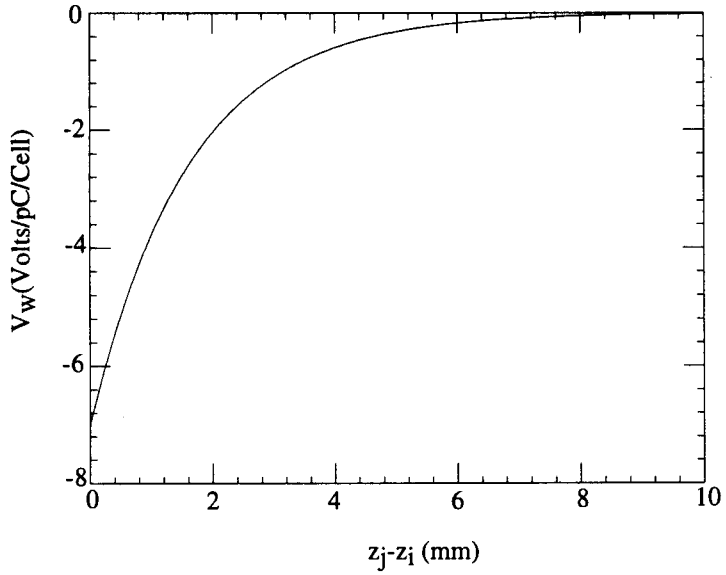

Figure 2.5.3. The longitudinal wake voltage per accelerating cavity for the accelerating structure in the SLC linac.

The total energy gain for the particle *j*th in the linac including the wakefield energy loss is

$$E_j(z) = E_0(z) + \sum_i^N E_i \cos\left(\frac{2\pi z}{\lambda} + \varphi_{linac} + \varphi_{BNS}\right)$$
$$-\sum_{k=1}^{j} 7\left(\frac{V}{pC}\right)N_c \exp\left(-\sqrt{\frac{z_k - z_j}{1.62}}\right) - \frac{1}{2}7\left(\frac{V}{pC}\right)N_c\Big) \qquad (2.5.1)$$

where the sum for the wakefield is over all particles in front of the *j*th particle, and the last term is the self-field energy loss. The maximum energy gain, E_i, depends on the shape of the pulse from the klystron. The SLC klystron pulse shape will be presented in the next section.

The energy spread of the beam at the end of the linac is given by

$$\frac{\sigma_E}{E} = \frac{\sqrt{\sum_{j=1}^{N_{total}} \left(E_j(z) - \overline{E}\right)^2}}{\overline{E}}.$$

where $\overline{E}$ is the mean energy and the sum is over all particles in the bunch. Minimizing the energy spread is done by shaping the initial distribution with the bunch compressor and by adjusting the bunch phase φ_{linac}. The distribution which gives the minimum energy spread will be shown to be a bunch distribution that is over-compressed.

The Accelerating Structure

The SLC linac accelerating structure is shown in figure 2.5.4.

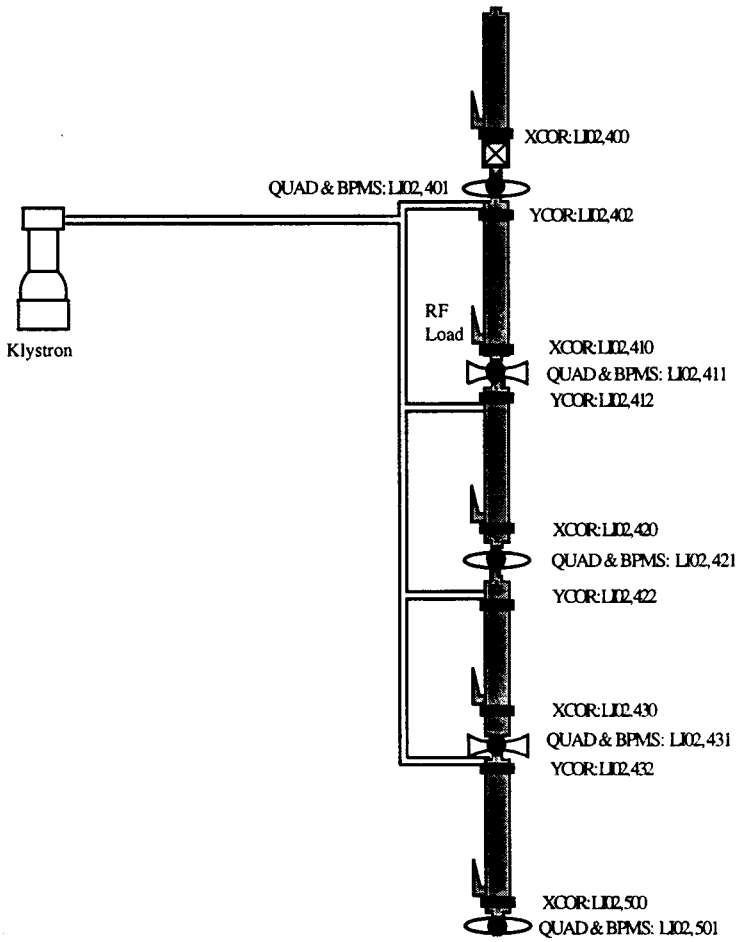

Figure 2.5.4. One girder of the SLC linac accelerating structure at the beginning (sector 2) of the linac. There are four quadrupole magnets per girder in this region to tightly focus the beam at low energy.

The basic components of the accelerating structure are: klystrons which produce RF power for the accelerating structure, corrector magnets which give local corrections to the beam's orbit, quadrupole magnets for focusing the beam, beam position monitors, and other beam diagnostics. The beam position monitors are located at the center of the quadrupole magnets and are used with the correctors to minimize the orbit oscillations. There are several types of quadrupole magnets used in the main linac. The higher field quadrupoles are used in the last 20 sectors where the beam is at high energy. Typically, each klystron feeds power to a 12.5 m girder which supports four 3.05 m accelerating sections. There are 240 klystrons in the main linac, and their specifications are listed at the end of this section. Each linac sector, of which there are 29 in the main linac, has 8 acceleration girders and the quadrupole and corrector magnets reside at the end of each girder.

Now for a more quantitative discussion of the linac. The SLC linac accelerates the beam with accelerating RF fields. The linac is a traveling wave structure, where the RF power is fed in at one end and propagates through the structure with some attenuation; the balance of the power is absorbed in the load. The accelerating RF fields are produced by klystrons and are transported to the accelerating structure by a rectangular wave guide. The fields enter the accelerating structure with the longitudinal electric field E_z propagating in the direction of the beam. The longitudinal electric field for a disk loaded traveling wave structure with an infinite periodic structure shown in figure 2.5.1 is

$$E_z = \sum_{n=-\infty}^{\infty} E_n(\vec{r}) \exp\left[\frac{-2\pi i n z}{d}\right] \exp\left(i\left(\omega_{rf} t - \beta_n z\right)\right) \exp(-\alpha z) \qquad (2.5.2)$$

The first term in the electric field is the space harmonics, the second term is the periodic structure of the disk loaded wave guide, the third term is due to the RF being a traveling wave, and the fourth term is due to the attenuation in the wave guide structure. In equation 2.5.2, β_n is the wave number for space harmonics n, d is the spacing between disks, α is the attenuation, and ω_{rf} is the frequency.

The phase velocity v_{ph}, is the velocity of a point of constant phase and is given by

$$v_{ph} = \frac{\omega}{\beta_n} = \frac{\omega}{\beta_0 + \frac{2\pi n}{d}}$$

where $\beta_n = \beta_0 + \frac{2\pi n}{d}$ is the wave number. The phase velocity is dependent of n and is generally greater than the speed of light. By loading the wave guide with disks the phase velocity can be slowed down to equal the particles velocity and thus accelerate the particle.

The group velocity v_g, is the velocity at which the energy of the RF wave propagates and it is given by

$$v_g = \frac{d\omega}{d\beta_n} = \frac{d\omega}{d\beta_0}$$

and is independent of n.

The SLC linac accelerating section is a constant gradient type. The constant field is achieved by tapering the cross section dimensions of the wave guide. The dimensions of the beam iris in one accelerating section varies from $2a = 2.622\ cm$ to $1.9093\ cm$ and the cylinder diameter varies from $2b = 8.3462\ cm$ to $7.9572\ cm$. There are 84 cavities in each accelerating section and the phase shift per cavity is $2\pi/3$.

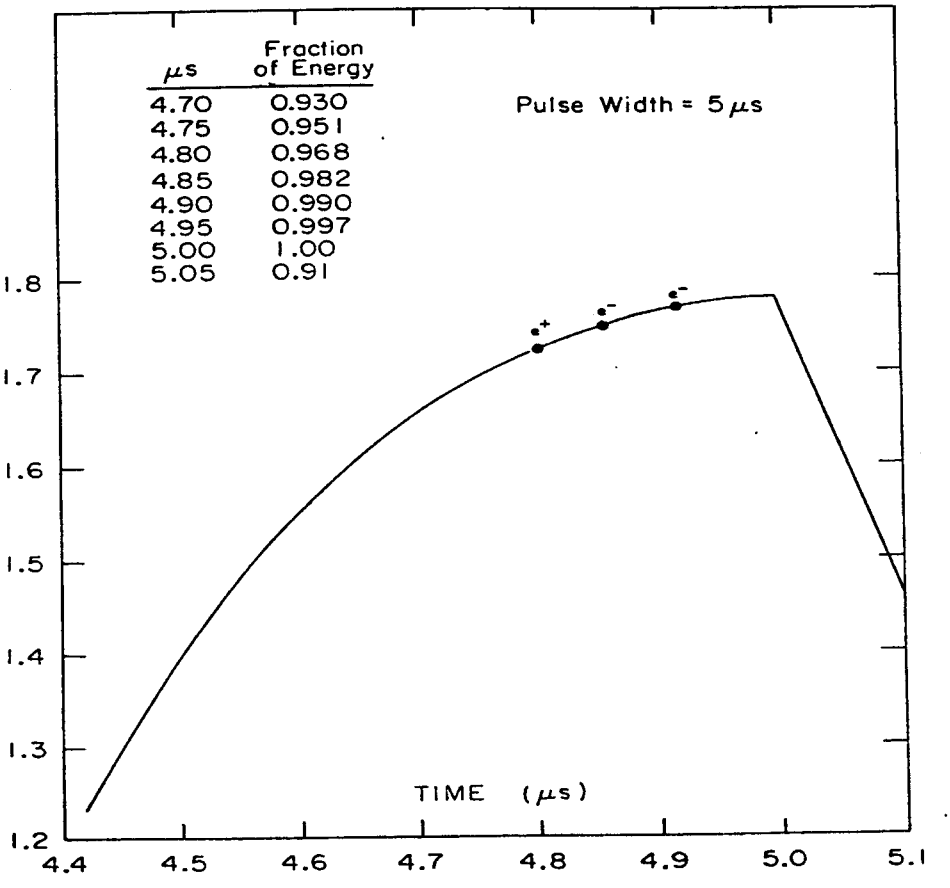

Figure 2.5.5. The energy gain as a function of time for the SLED II klystron pulse [SLAC Report 229, 1980].

The klystrons in the main linac have a peak output power of 50 MW and are able to put out a pulse width of 5 μsec at a repletion rate of 120 Hz. The energy gain and pulse shape are enhanced by operating the klystron in SLED mode [Z.D. Farkas et al, 1974]. The RF frequency from the klystrons is 2856 MHz, and the unloaded energy gradient from each klystron is approximately 21.66 $^{MeV}/_{m}$ or 264 MeV.

To reach a center of mass energy of 93 GeV, the bunches must have an energy of 47.5 GeV at the end of the linac (there is a 1 GeV synchrotron radiation energy loss in the arc region). The energy gain profile for the three pulses as a function of time for the SLED II pulse as it progressively fills the accelerator is shown in figure 2.5.5. The available maximum energy, E_i, for the three pulses in the linac are the following (ignoring the phasing of the klystrons for BNS damping):

$$E_i = N_{SLED}\ x\ f_{slope}\ x\ \sqrt{R_s L P_o (1-\exp(-2\tau))} \qquad (2.5.3)$$

where $N_{SLED} = 1.78$ is the SLED multiplier, f_{slope} is the energy adjustment for the SLED pulse shape shown in figure 2.5.5, $\sqrt{R_s L P_o (1-\exp(-2\tau))}$ is the energy gain for one girder, and τ is the attenuation factor.

The positron bunch is injected in the linac and receives 0.968 of the SLED II maximum energy gain and it removes approximately 300 Joules of the energy available for the remaining pulses (assuming a current of $4x10^{10}$ particles per bunch). When the subsequent electron pulse comes along 58.8 nsec later, it acquires an energy of 0.983 of the maximum energy gain (about 700 MeV higher than the positrons) but the positron bunch removed 258 MeV of available energy. The second electron bunch has an energy gain of 0.992 of the SLED pulse and reduced by another 300 MeV but since this pulse is used to create positrons it is not necessary to be equal to the other pulses. On average, each klystron supplies an energy gain of $E_i = 235$ MeV and energy gradient of 19.28 MeV/m.

Transverse Instability-BNS Damping

Transverse effects are outside the scope of this thesis, but to counteract the effects of transverse wakefields is one of the dominant considerations in the longitudinal dynamics.

If the bunch is injected into the linac off axis the particles at the head of the bunch will produce transverse wakefields that affect the tail of the bunch. The tail particles will be deflected in the direction of the oscillating head particles, and the amplitude of the oscillation will increase for the tail particles, as they travel down the linac (the tail particles will be deflected and the bunch will have the shape shown in figure 2.5.6). The increase in

beam size has a big detrimental effect on the attainable luminosity and produces large backgrounds and therefore must be minimized as much as possible.

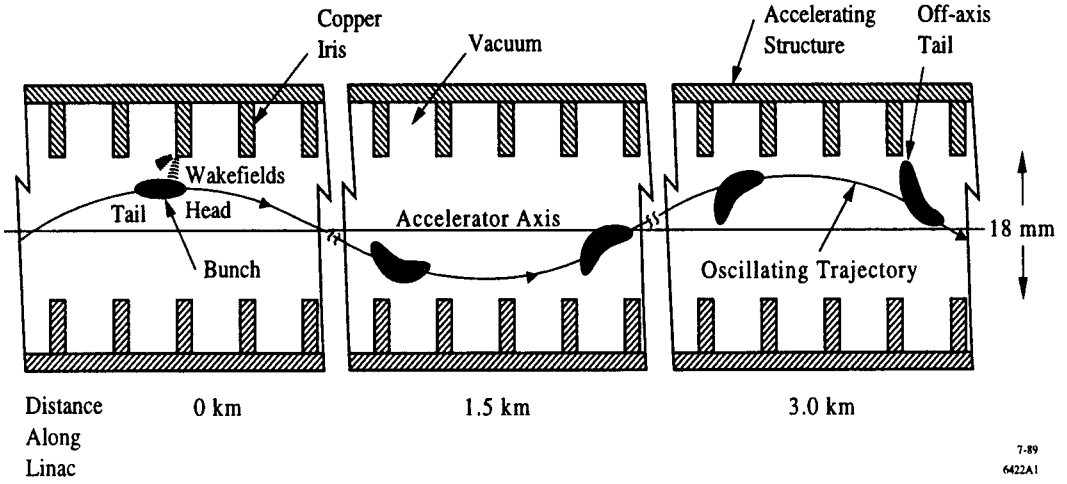

Figure 2.5.6. An illustration of beam blow up in the SLC due to transverse wakefields [J. Seeman, 1991].

A technique to control this resonant growth is called BNS damping, named after V. Balakin, A. Novokhatsky, and V. Smirnov [V. Balakin, 1983]. BNS damping lowers the energy of the back of the bunch by accelerating the bunch behind the crest of the RF accelerating wave early in the linac. The wakefield forces which act to defocus particles are counterbalanced by the increased quadrupole focusing for the low energy particles at the back of the bunch.

A quantitative discussion of beam breakup in the linac can be illustrated with a two particle model of the bunch. Consider two macro particles traveling down the linac in the vacuum chamber pipe and the particles are executing betatron oscillations. The two particles, x_1 and x_2, are spaced by a distance z_0 and each one has a charge $N/2$, where N is the total charge. The transverse equation of motion of the two macro particles, neglecting acceleration is

$$\frac{d^2x_1}{ds^2} + k_\beta^2 x_1 = 0$$

$$\frac{d^2x_2}{ds^2} + k_\beta^2 x_2 = -\frac{q^2 N V_\perp(z_0)}{2l_c E_0} x_1 \qquad (2.5.4)$$

where k_β is the betatron wave number, l_c is the cavity period, and $V_\perp(z_0)$ is the transverse wakefield for a particle traveling a distance z_0 behind the lead particle. The driving term in

the second differential equation is due the transverse wakefield produced by the lead particle as it travels through the linac accelerating structure. Taking the initial conditions to be $\frac{dx_1(0)}{ds} = \frac{dx_2(0)}{ds} = \hat{x}k_\beta$ and $x_2(0) = x_1(0) = 0$ the solutions to the differential equations are

$$x_1(s) = \hat{x}\sin\left(k_\beta s\right)$$

$$x_2(s) = \hat{x}\left[1 - \frac{qNV_\perp(z_0)}{4k_\beta^2 l_c E}\right]\sin\left(k_\beta s\right) + \frac{qNV_\perp(z_0)\hat{x}}{4k_\beta l_c E} s\cos\left(k_\beta s\right).$$

There are several interesting conclusions that can be made by the above derivation. 1) The tail particle is driven by the wakefield from the head particle. The amplitude of the first term depends on the size of $V_\perp(z_0)$. In the second term the response to the wakefield and is linear in s. 2) The solution is linear to the initial amplitude $\hat{x}$. 3) The tail will grow in size and particle loss is what limits the growth. 4) The dependence of the amplitude of the tail is proportional to the current.

When BNS damping is included the differential equation 2.5.4 becomes

$$\frac{d^2x_2}{ds^2} + \left(k_\beta + \Delta k_\beta\right)^2 x_2 = -\frac{q^2NV_\perp(z_0)}{2l_cE_0}x_1$$

where there is slightly stronger betatron focusing for the tail particles. The solution to the differential equation is

$$x_2(s) = \frac{q^2NV_\perp(z_0)\hat{x}}{2l_cE\left[\left(k_\beta + \Delta k_\beta\right)^2 - k_\beta^2\right]}\left[\frac{k_\beta}{k_\beta + \Delta k_\beta}\sin\left[\left(k_\beta + \Delta k_\beta\right)s\right] - \sin\left[k_\beta s\right]\right]$$

$$+ \frac{\hat{x}k_\beta}{\left(k_\beta + \Delta k_\beta\right)}\sin\left[\left(k_\beta + \Delta k_\beta\right)s\right].$$

The condition for the head and tail particles to oscillate together, which gives $x_1(s) = x_2(s)$ is

$$\left(\frac{\Delta k_\beta}{k_\beta}\right) = -\frac{q^2NV_\perp(z_0)}{4l_ck_\beta^2E} \qquad (2.5.5)$$

where the approximation of $\frac{\Delta k_\beta}{k_\beta} << 1$ is used. From equation 2.5.5, the BNS force for complete damping requires that the energy spread introduced needs to be adjusted

according to the current of the bunch. To achieve no beam blow up requires that the energy spread over the bunch must be carefully controlled and monitored.

In the SLC linac, the phasing of the klystrons assumes a bunch current of $3.5x10^{10}$ particles per bunch. The first 48 klystrons are back phased at -22 degrees, and the remaining klystrons have a forward phase of +16.5 degrees. The overall linac phase is adjusted so that the energy spread at the end of the linac is minimized. In practice, BNS damping is applied at the beginning of the linac at low energy where the instability is strongest. At the end of the linac, at high energies, the beam break up effect becomes small, and the bunch is forward phased on the RF accelerating wave to reduce the energy spread in the beam.

SLC Linac Parameters

General Parameters

Injected Energy E_0	1.19 Gev
Extracted Energy E_f	46.5 GeV
Main Linac Length	2900 m

Klystron Specifications

Klystron Peak Output Power	50 MW
Frequency	2856 MHz
Peak Beam Voltage	315 kV
Peak Beam Current	354 Amps
Peak Beam Power	111.5 MW
Average Beam Power	120.3 kW
RF Pulse Width	5 μsec
Repetition Rate	120 Hz
Klystron Efficiency	0.45
dc Power	141.6 kW
ac Power	157.5 kVA

Accelerating Structure Specifications

Length	3.048 m
Shunt impedance R_s	53 $M\Omega/m$
Q	15,000
Attenuation factor τ	0.57

Phase shift per cavity	$2\pi/3$
Number of cavities per section	84
Wave guide inside diameter 2b	8.3462-7.9527 cm
Disk hole diameter 2a	2.622-1.9093 cm
Disk thickness t	0.5842 cm
Filling time t_f	0.83 μsec

2.6 Longitudinal Simulations

Introduction

In this section, I will describe the computer model of the longitudinal dynamics for the SLC. In the simulation, longitudinal dynamics result from externally applied and beam generated fields. The longitudinal beam dynamics simulated here begins with the bunch being extracted from the damping ring and traveling through the bunch compressor and the main linac. The simulation can be compared to the measurements done with the streak camera in the damping ring and linac, as well as the wire scanner measurements in the compressor transport line and at the end of the linac.

Initial Longitudinal Phase Space

The longitudinal phase space of the SLC is initially determined by the damping rings. Due to the damping ring impedance being predominately resistive, the bunch distribution is best described by an asymmetric Gaussian distribution. An asymmetric Gaussian is two Gaussian distributions with different widths connected at the origin. The charge density expressed as an asymmetric Gaussian is given by

$$\rho(z) = B\exp\left\{-\frac{1}{2}\left(\frac{z-C}{(1+sgn(z-C)A)D}\right)^2\right\}.$$

where A, B, C, and D are the fitting parameters. The area, mean, and rms width of the asymmetric Gaussian are

$$Area = \sqrt{2\pi}DB$$

$$\langle z\rangle = C + 2\sqrt{\frac{2}{\pi}}AD$$

$$\sigma_z = \left\langle (z-\langle z\rangle)^2\right\rangle^{\frac{1}{2}} = \left[1+\left(3-\frac{8}{\pi}\right)A^2\right]^{\frac{1}{2}}D.$$

The asymmetry parameter A is used to characterize the deviation due to potential well distortion from a true Gaussian (figure 2.6.1).

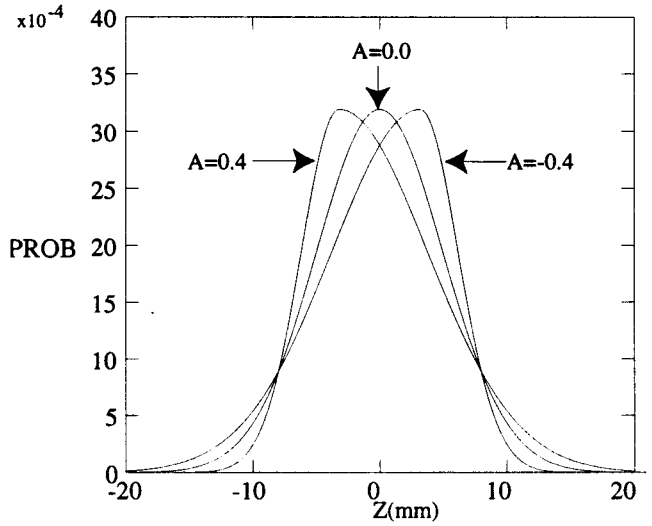

Figure 2.6.1. An illustration of the asymmetric Gaussian with $D = 5.00\ mm$ and three different asymmetry factors A.

The initial longitudinal phase space is described by an asymmetric Gaussian in length and symmetric Gaussian in energy. The phase space is created by 7000 random macro particles. The seed for the random number generator depends upon the clock of the computer and gives a different initial distribution every time the simulation is run. Histograms of the energy and length distribution are shown in figures 2.6.2a and b.

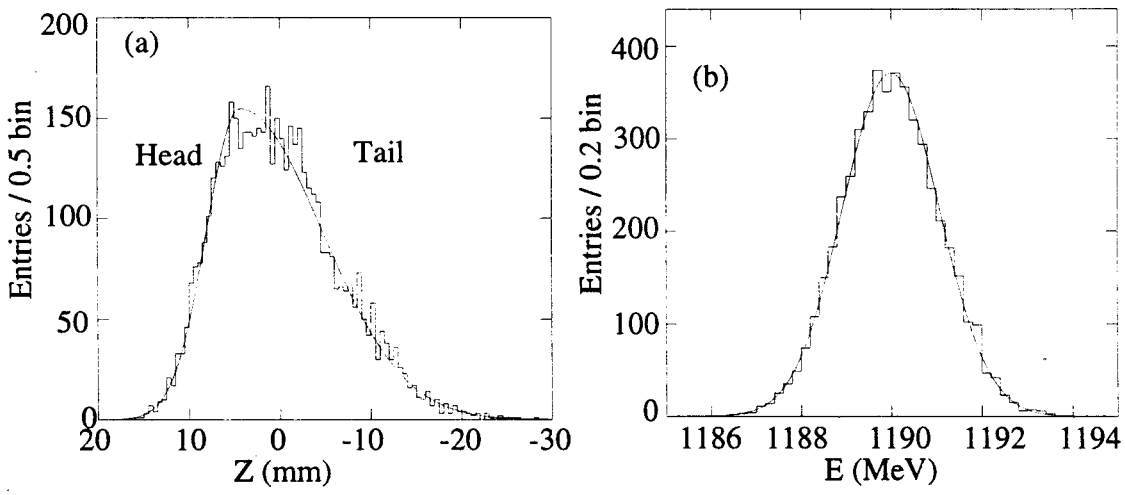

Figure 2.6.2. (a) A histogram of the bunch distribution described by an asymmetric Gaussian with $\sigma = 6.60$ mm and A=0.41. (b) A histogram of the energy distribution with an initial mean energy of $\langle E \rangle = 1190$ MeV and energy spread of $\frac{\sigma_E}{\langle E \rangle} = 9.0\text{x}10^{-4}$.

The initial conditions of each macro particle have been determined. Each macro particle has an energy E_i, and longitudinal coordinate z_i associated with it. The phase space distribution is shown in figure 2.6.3. The longitudinal phase space for the bunch exiting the damping ring has now been determined, and it can now be tracked through the rest of the SLC. Initial bunch parameters that will be used for tracking the macro particles through the SLC (unless denoted) are: bunch length is $\sigma = 6.60\ mm$, an asymmetry parameter of $A = 0.41$, a mean energy of $\langle E \rangle = 1190 MeV$, and an energy spread of $\frac{\sigma_E}{\langle E \rangle} = 9.00x10^{-4}$.

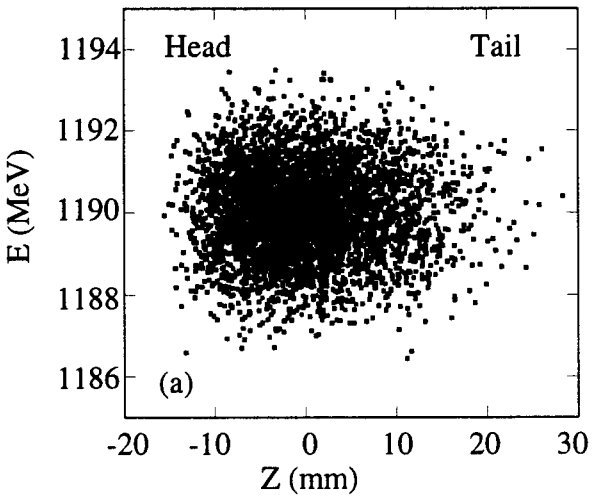

Figures 2.6.3. The initial longitudinal phase space of the bunch in the damping ring.

Single Particle Motion through the Compressor

The compressor has two parts: the RF accelerating section, and the nonischronous bend section. The RF accelerating section will give each macro particle an energy gain of

$$E_f = E_i + eV_{rf} \sin\left(\frac{2\pi z_i}{\lambda_{rf}} + \varphi_{offset}\right)$$

where V_{rf} is the RF voltage amplitude, λ_{rf} is the RF wavelength, and φ_{offset} is the phase offset of the mean of the distribution. The mean of the distribution entering the RF section usually is centered on the zero crossing of the RF wave, i.e. $\varphi_{offset} = 0$. The effect of the RF section is to give the bunch a correlated energy spread (figure 2.6.4)

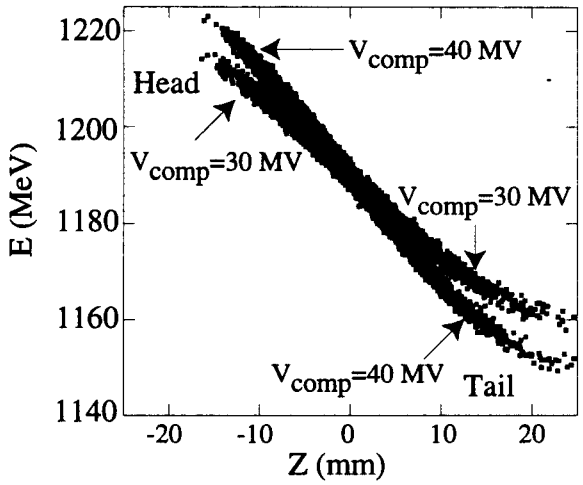

Figure 2.6.4. The phase space of the bunch after the RF accelerating section for the compressor amplitudes of 30 and 40 MV.

After the RF accelerating section the bunch travels through a transport region where the tails of the distribution are compressed. The change in the longitudinal position for a macro particle is given by

$$z_f = z_i + R_{56}\left(\frac{E_i - \overline{E}}{\overline{E}}\right) + T_{566}\left(\frac{E_i - \overline{E}}{\overline{E}}\right)^2$$

where z_i, z_f are the initial and final longitudinal positions, $\overline{E}$ is the mean energy, E_i is the energy, $R_{56} = \alpha_{comp} L$, and $T_{566} = \frac{dR_{56}}{d\delta}$ for the transport line.

Figure 2.6.5a is a plot of the longitudinal phase space after the bunch compressor

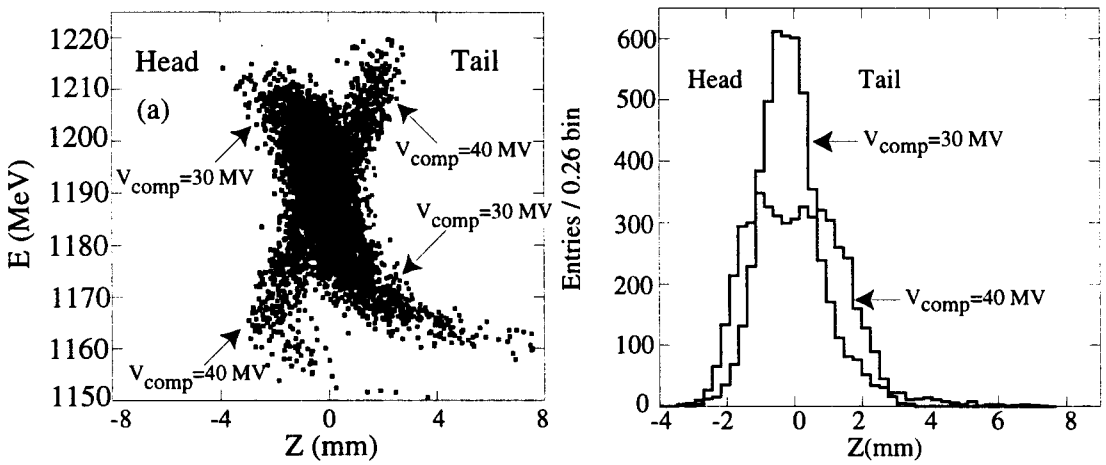

Figure 2.6.5. (a) The longitudinal phase space after the bunch compressor. (b) Histograms of the bunch distributions after the compressor.

for the RF voltage settings of 30 and 40 MV. The bunch distribution can be under compressed (30 MV), fully compressed (35 MV not shown), or over compressed (40 MV). A histogram of the bunch distribution is shown in figure 2.6.5b.

The transmission of particles through the compressor transport line is reduced due to an aperture. This reduction in particles is dependent on the initial bunch length and RF acceleration in the compressor. The transport line has a beam pipe with a radius of $r = 2.25\ cm$, and a peak dispersion of $\eta_x = 0.9\ m$, which allows passage of particles that are $\pm 2.5\%$ within the mean energy of the bunch. Figure 2.6.6a illustrates the current transmission for various bunch lengths and RF acceleration in the compressor line. Figure 2.6.6b is a plot of the simulated transmission loss in the compressor region after the energy cut of $\pm 2.5\%$ and $\pm 2.1\%$ as a function of compressor voltage.

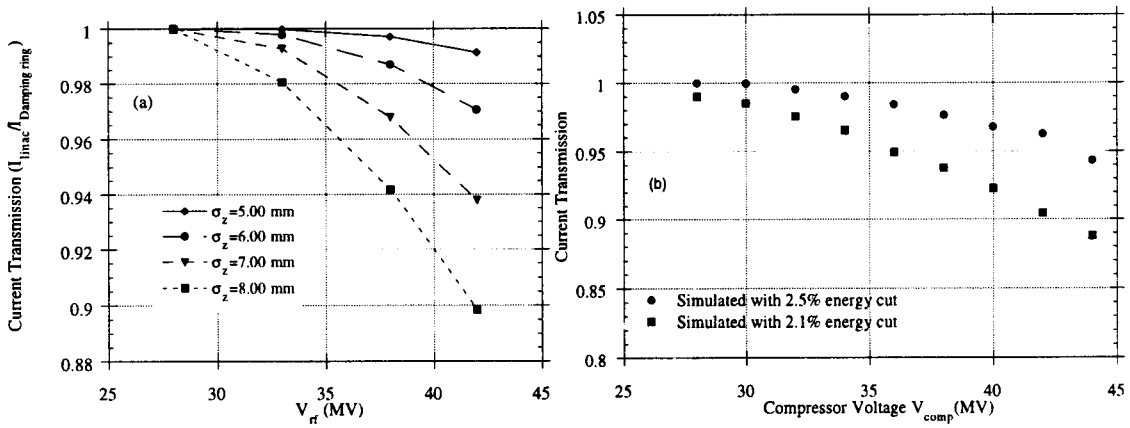

Figure 2.6.6. (a) Current transmission from simulation for various compressor voltages and initial bunch lengths. (b) The simulated transmission loss in the compressor transport region for two different energy apertures.

After the bunch has been compressed, it enters the main linac where is accelerated to 46.5 GeV.

Linac

The energy of the bunch in the linac changes due to RF acceleration and longitudinal wakefields. The macro particles travel through the main linac accelerating structure where each section has a peak energy gain and wakefield energy loss which is

dependent on the number of disk loaded cavities. The net energy gain/loss in the linac is a culmination of the 240 accelerating structures and is written as:

$$E_{particle} = E_i + \sum_{k=1}^{240}\left(E_k \cos\left(\frac{2\pi z_i}{\lambda_{rf}} + \varphi_{linac} + \varphi_{BNS} \right) - E_{wake,k}(z_i) \right)$$

where E_k is the peak klystron energy gain for the 240 klystrons, E_i is the initial energy of the macro particle entering the linac, φ_{linac} is the overall linac phase, φ_{BNS} is the BNS phase, and $E_{k,wake}(z_i)$ is the longitudinal wakefield energy loss for the accelerating structure. The BNS phase in the linac and used in the simulation is 22 degrees for sectors 2-8 and -16.5 degrees for sectors 9-30. The longitudinal phase space without longitudinal wakefield energy loss is plotted in figure 2.6.7. The linac phase was chosen to minimize the energy spread at the end of the linac.

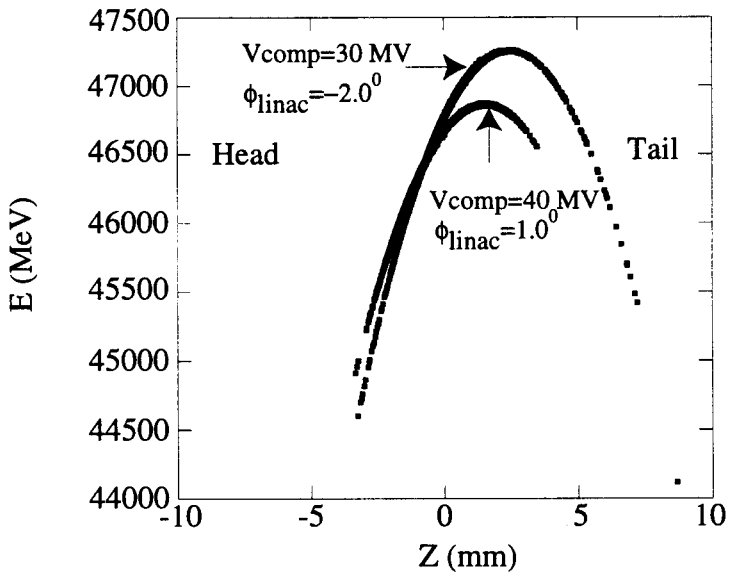

Figure 2.6.7. The longitudinal phase space at the end of the linac for two different compressor setting and linac phases without the longitudinal wakefield energy loss.

The longitudinal wakefield energy loss is calculated over the whole bunch for one disk loaded cavity and is scaled by the number of cavities in a given accelerating structure to give the total energy loss. The longitudinal wakefield energy loss for one cavity is given by

$$E_{wake}(z_i) = \left(\frac{L_s}{l_c} \right) \left[\sum_{j>i} (N / N_{Macro}) W_l(z_j - z_i) - \frac{1}{2}(N / N_{Macro}) W_l(0) \right] \quad (2.6.1)$$

where L_s is the accelerating structure length, l_c is the individual cavity length, N is the total charge in the bunch and N_{Macro} is the number of macro particles (after cut in the compressor line). The first term is due to interaction of the macro particles and the second term is the self field energy loss. The longitudinal wake potential $W_l(z_j - z_i)$ is given by

$$W_l(z_j - z_i) = -7\left(\frac{\mathrm{V}}{\mathrm{pC}}\right)\mathrm{N_c}\exp\left[-\sqrt{\frac{z_j - z_i}{1.62}}\right].$$

The wakefield energy loss from equation 2.6.1 is plotted as a function of location in the bunch for two compressor settings (bunch lengths). In figure 2.6.8, the energy loss for a bunch that travels through the linac after a compressor voltages of 30 and 40MV. The wakefield energy loss can be shaped by adjusting the bunch compressor amplitude.

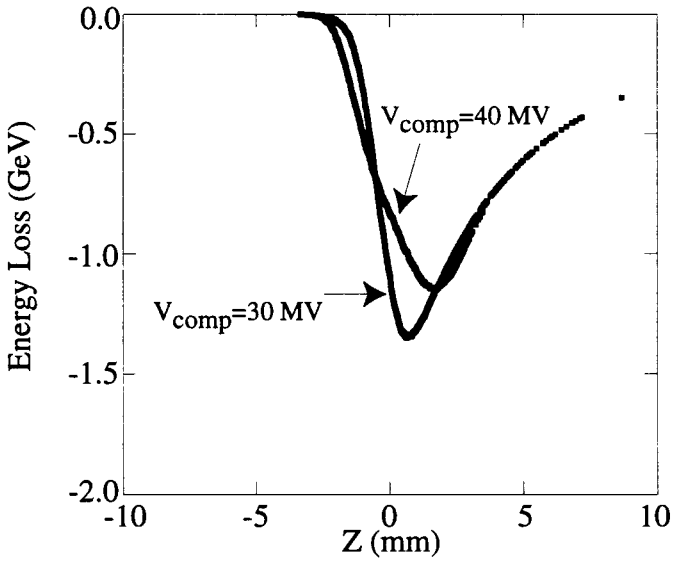

Figure 2.6.8. The wakefield energy loss as a function of current and bunch location in the SLC linac.

The energy spread of the bunch changes as it travels down the linac. The energy spread at the beginning of the linac is determined by the bunch compressor amplitude and as it travels down the linac the energy spread comes from the phase of the bunch on the RF and the longitudinal wakefield energy loss. The energy spread reaches it maximum value at the BNS phase transition location and it reaches its minimum (when phases properly) at the exit of the linac. A simulation of the energy spread of the bunch as it travels down the linac is shown in Figure 2.6.9.

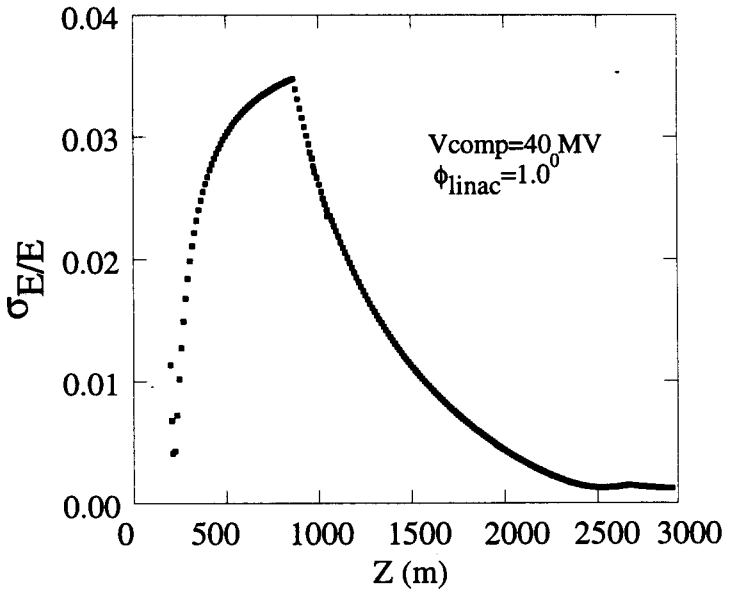

Figure 2.6.9. A simulation of the energy spread of the bunch plotted at each quadrupole in the linac. The initial energy spread of the bunch is 1.1% and at the end of the linac is 0.12%.

Combining the RF acceleration in figure 2.6.7 and the wakefield energy loss in figure 2.6.8 gives the simulated longitudinal phase space at the end of the linac (figure 2.6.10a).

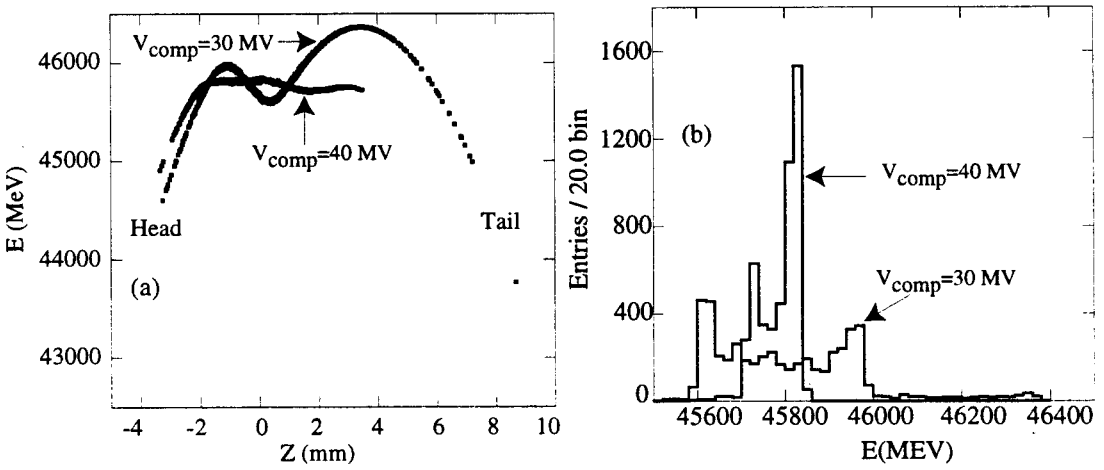

Figure 2.6.10. (a) The macro particle longitudinal phase space at the end of the linac for three different RF phases. (b) A histogram of the energy distribution at the end of the linac for three different RF phases.

In order to minimize the bunch distribution it is important to cancel out the curvature of the RF accelerating wave with the longitudinal wakefield energy loss. This

can be achieved by shaping the bunch distribution with the compressor so that the RF accelerating wave and the beam generated wakefield energy loss cáncel each other and greatly reducing the energy spread at the end of the linac [G.A. Loew et al, 1985 and F.J. Decker et al, 1994]. This has been shown experimentally and will be presented in chapter 4.

Chapter 3.
Apparatus for Measurements

3.1 Streak Camera

Introduction

The longitudinal distribution of the bunch in the SLC was measured using a streak camera at the end of the linac and in the electron and positron damping rings. In this section I will describe how the streak camera uses the synchrotron light produced by the beam to measure the beam distribution.

Streak Camera

The streak camera is a device to measure ultra-fast pulsed light intensity versus time. The streak camera used in this thesis was a Hamamatsu model N3373-02 streak camera made by Hamamatsu Photonics. The basic components of the streak camera are shown in figure 3.1.1, and they are the variable input slit, input optics, photo cathode, accelerating mesh, deflection plate, micro-channel plate, phosphor screen, output optics, CCD camera, and analog to digital read-out system. The parameters of the streak camera components are listed at the end of this section.

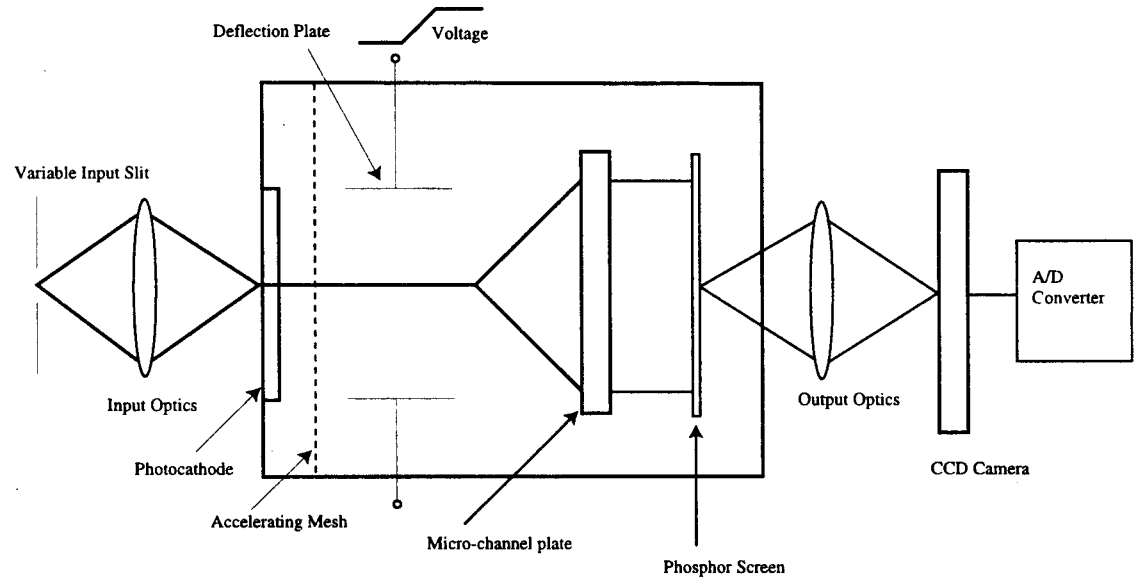

Figure 3.1.1. The layout of the various components of the Hamamatsu streak camera.

The streak camera measures the bunch distribution in the following manner. Consider a pulse of light that consists of four photons that are separated in time as they enter the streak camera (see figure 3.1.2a,b). These four photons can be tracked through the camera to illustrate its basic operations.

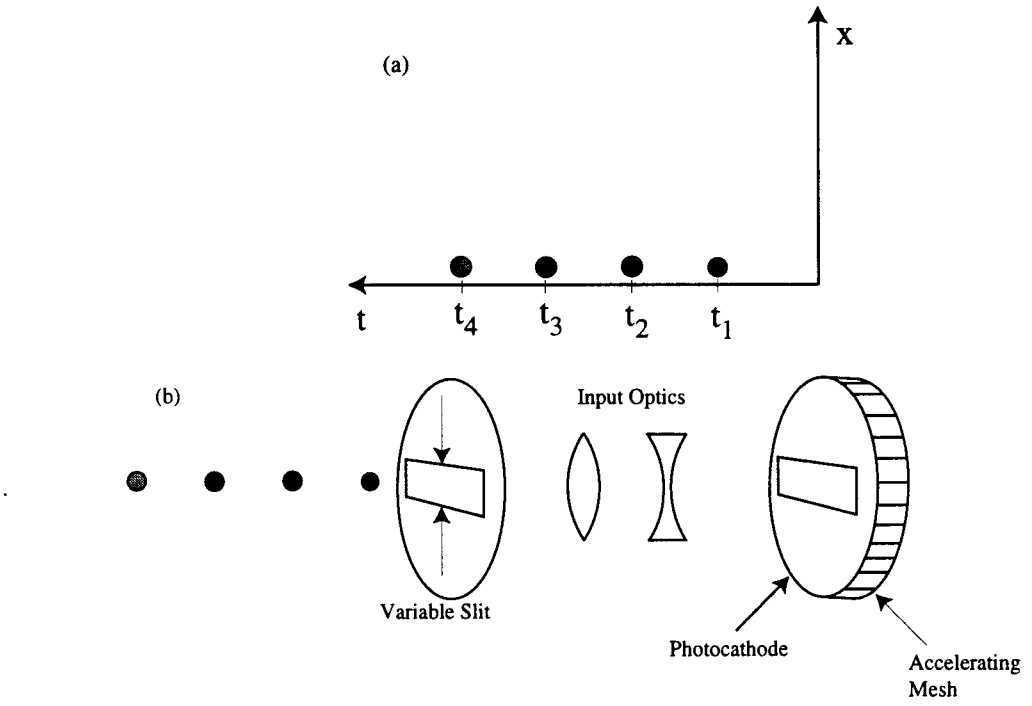

Figure 3.1.2. (a) The four photons that make up the pulse of light that enter the streak camera are separated in time. (b) The four photons entering the streak camera.

The four photons enter the streak camera through a variable vertical slit that is typically 100 μm wide. The photons are transported through the streak camera input optics. The input optics form an image of the variable slit onto a photocathode. The photons hit the photocathode of the streak tube where they are converted photoelectrons. The number of photoelectrons produced is proportional to the number of the photons. The photoelectron pulses are again spaced by the arrival time of the photons. The emitted photoelectron pulses are accelerated by an accelerating mesh which pulls the photoelectrons away from the photocathode and keeps the pulses separated in time. The electrons pass between deflecting plates where a high voltage is applied at a timing synchronized to the incident light (figure 3.1.3). The timing of the incident pulse initiates a very high speed sweep of the high voltage. During the high speed sweep, the electrons are deflected at different angles depending upon there arrival time at the deflection plates. After deflection the electrons enter the micro-channel plate.

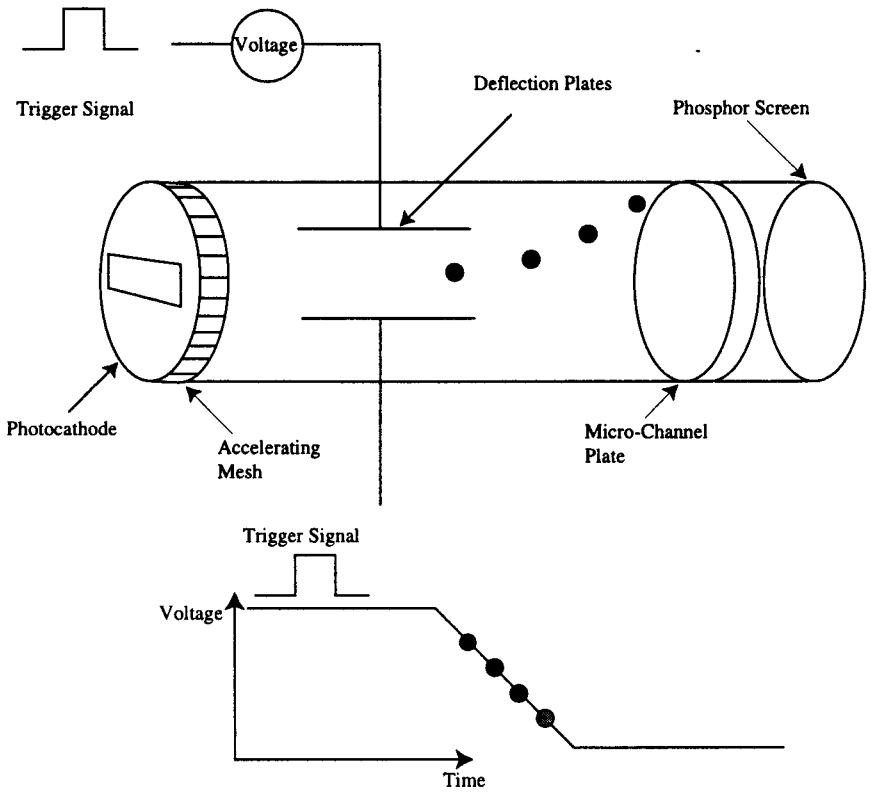

Figure 3.1.3. The trigger signal is synchronized with the arrival of the photoelectrons at the deflecting plate.

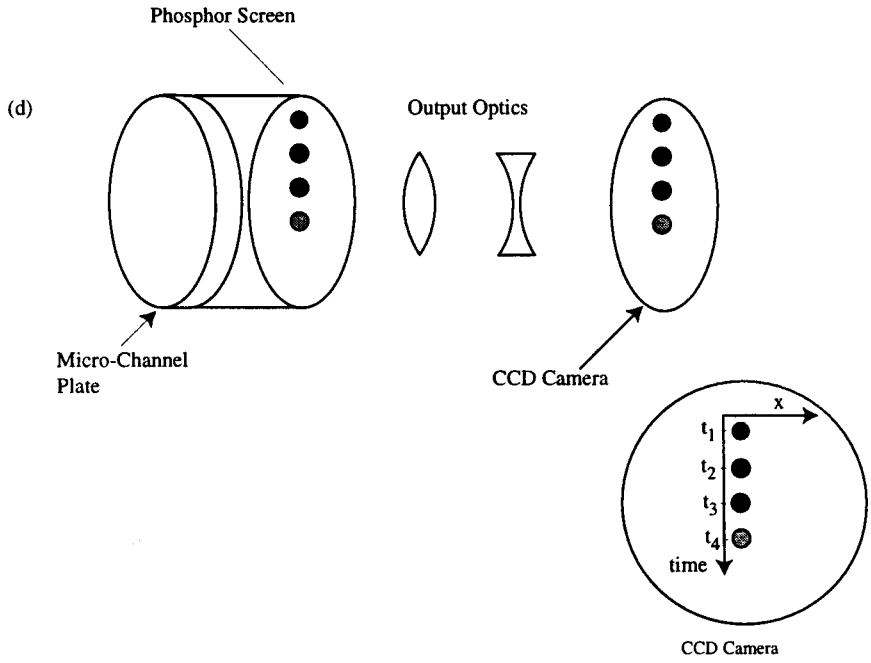

Figure 3.1.4. The output of the streak camera.

The micro-channel plate multiplies the electron pulse by several thousand times. After the micro-channel plate, the photoelectrons strike a phosphor screen where they are converted into light again. The brightness of the phosphor screen is proportional to the intensity of the pulse. The vertical axis on the phosphor screen is the time axis (figure 3.1.4). The image on the phosphor is transported by the output optics to a cooled CCD camera where the image is then digitized and processed by a computer.

A more detailed description of the photocathode, micro-channel plate, phosphor screen, and CCD camera for the streak camera:

Photocathode:

When struck by light, the energy is absorbed and electrons (called photoelectrons) are emitted. The quantum efficiency from photons to electrons and the wavelength range of the photons which produce the electrons depend on the material makeup of the photocathode. The photo cathode used in this camera is an S-20 multi-alkali photo cathode constructed of Sb, Na, K, and Cs, and is 500 angstroms thick. The quantum efficiency of the photocathode is 9% at 532 nm wavelength.

Micro-channel plate (MCP):

The MCP consists of many thin glass capillaries which are tightly bundled together. The walls of the capillaries are coated with a secondary emitting material that when impacted by an electrons causes them to multiply in number. The MCP is biased between the plates to accelerate the electrons through the MCP. The micro channel plate used in this camera has individual channels which are 10 microns in diameter, 0.5 mm in length and are coated with aluminum. The gain of a MCP can be as high as $5x10^3$ at 900 Volts.

Phosphor screen:

The phosphor screen is used turn the electron pulse back into a light pulse. A phosphor screen produces light when electrons bump against it. The phosphor screen consists of layers of fluorescent materials on the surface of a glass plate. The kinetic energy of the electrons which strike the phosphor screen determines the amount of light generated by the fluorescent material. The phosphor screen used in this camera is a P-20 phosphor and its peak emission is 560 nm. The gain for the P-20 phosphor screen at its peak emission is 50 γs per incident electron.

Cooled CCD Camera:

The camera has CCD chip which is cooled to reduce dark current noise and enables higher detection sensitivity because a longer exposure time can be used with the reduced dark current noise. A cooled CCD camera also allows a wider dynamic range and higher image quality. The C3640-60 CCD camera uses the Texas Instruments TC-215 CCD chip. The CCD camera has a quantum efficiency of 40% at a wavelength of 510 nm.

Streak Camera Image Acquisition

The image acquisition begins with the read-out from the CCD camera. The CCD elements are arranged in a two dimensional array of rows and columns. These elements are called picture elements or pixels, and are square in shape. There are 1000 by 1018 pixels on the CCD camera and they are binned two at a time (500 by 509 pixels) to smooth the image and to reduce the data acquisition time. The entire surface of the CCD camera forms a sensitive area, so that incoming light has to be obstructed while the electrical charges accumulated by the CCD are being transmitted. With this camera, a mechanical shutter is employed to obstruct the incident light, and the exposure time of the CCD is controlled by the opening and closing of this mechanical shutter. The shutter interval can be set between 10 msec and 1 hour.

Light incident on the CCD chip surface, or the optical image, is converted into a pattern of electrical charges that matches the optical image. These charges can be read out as CCD output signals. The electrodes arranged on the CCD are used to transmit the charges to the final output amp stage. The charges sent to the output stage amp are output one pixel at a time as voltage values proportional to the charge in that pixel. The cycle is repeated until all lines of the image have been transferred, and all of the charges accumulated on the CCD have been output. The data is digitized pixel by pixel as they are readout from the CCD. The digitized data is then sent to a computer and is plotted out all 500 by 509 pixels.

Streak Tube

Model	N3373-02
Photo cathode Type	S-20
Photo cathode diameter	3 mm
Spectral Response	200-900 nm
Phosphor Screen Type	P-20
Phosphor Screen diameter	15 mm

Micro-Channel gain	3000 Minimum
Time resolution	<700 fsec

Output Optics

Image magnification	1:1 (50:50mm)

Electric Properties

Sweep time	60 ps/10 mm
	200 ps/10 mm
	500 ps/10 mm
	1200 ps/10 mm
Sweep repetition frequency	1 kHz maximum
Streak trigger input signal:	
Amplitude	+5-40 Volts
Pulse width	2-100 ns
Frequency	1 kHz maximum
Jitter	<20 psec for 60 ps rate

CCD Camera Head

Number of pixels	1000 (hor.) by 1018 (vert.)
Pixel size	$12\mu m \times 12\mu m$
Frame rate	4 seconds (full readout)
Exposure time	10 msec to one hour
Spectral response	400-1000 nm
Cooling method	Thermoelectric air cooling
Operating temperature	0^0 C to 40^0 C
Frame rate	4 sec (full frame readout)

3.2 Synchrotron Light Optics in the Damping Ring and Linac

Introduction

The streak camera uses synchrotron radiation produced by the accelerator bend magnets. The synchrotron light is transported from the source out of the vacuum chamber to a safe location shielded from ionizing radiation where the streak camera measurements can be performed. There are three different locations where the bunch distribution was measured: 1) The electron damping ring, 2) the positron damping ring, and 3) the end of the linac. In this section I will describe the experimental set-up used to produce and transport the synchrotron radiation to the streak camera.

Synchrotron Radiation

Synchrotron radiation is emitted from the positrons and electrons as they are bent by a bend magnet. The radiation is emitted tangentially from the particles orbit with a characteristic angle of $\pm\gamma^{-1}$ where

$$\gamma = \frac{E}{mc^2}. \tag{3.2.1}$$

The radiation is emitted over a wide spectrum of photon frequencies characterized

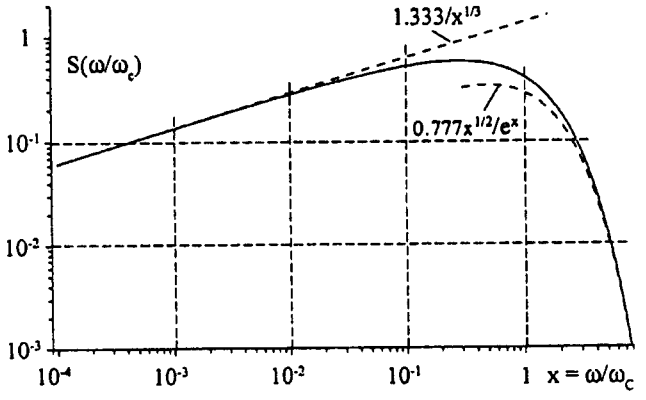

Figure 3.2.1. The synchrotron radiation spectrum as a function of frequency. $S\left(\omega/\omega_c\right)$ is the normalized synchrotron radiation spectrum [H. Wiedemann, 1995].

by the critical frequency of the bunch given by [Sands, 1970]

$$\omega_c = \frac{3c\gamma^3}{2\rho}$$

where ρ is the radius of curvature of the magnet, c is the speed of light, and γ is given by equation 3.2.1. The intensity, $S\left(\omega/\omega_c\right)$ of photons with the frequencies above the critical frequency starts to drop significantly as can be seen in figure 3.2.1. The synchrotron radiation used for the streak camera is visible light with a wavelength of 500 nm (green light) which is well below the critical frequencies ($x = \omega/\omega_c = 1.3\text{x}10^{-3}$ and $1.3\text{x}10^{-6}$ for the damping rings and linac respectively) in all cases. Therefore, the camera uses radiation from the flat portion of the spectrum. The parameters of the light sources in the damping ring and linac are listed at the end of this section.

Damping Ring Synchrotron Light Optics

The electron and positron damping rings have identical synchrotron radiation sources and transport lines. The bend magnet and optics used to transport the light out of the damping ring vacuum chamber is shown in figure 3.2.2.

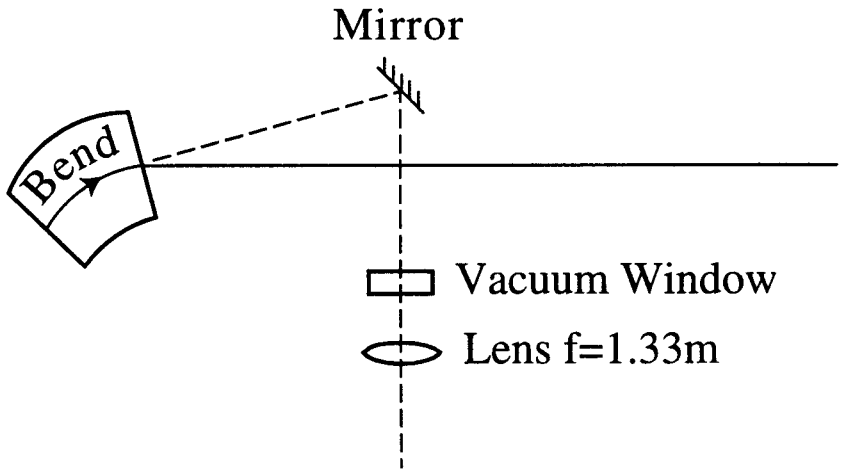

Figure 3.2.2. The general layout of the synchrotron light set up in the damping ring.

The synchrotron light is emitted by the beam traveling through a bending magnet adjacent to the straight injection section. The synchrotron light is reflected by a molybdenum mirror inside the vacuum chamber and passes through a synthetic fused silica window. The mirror position in the vacuum chamber is remotely controlled, and the mirror is water

cooled to dissipate the large incident synchrotron radiation power. The light is transported outside the damping ring vault by a succession of mirrors, and passes through an evacuated pipe that is terminated on both ends by two synthetic fused silica windows (figure 3.2.3). The evacuated pipe ends at the damping ring power supply building were an optics table is located for the streak camera measurements.

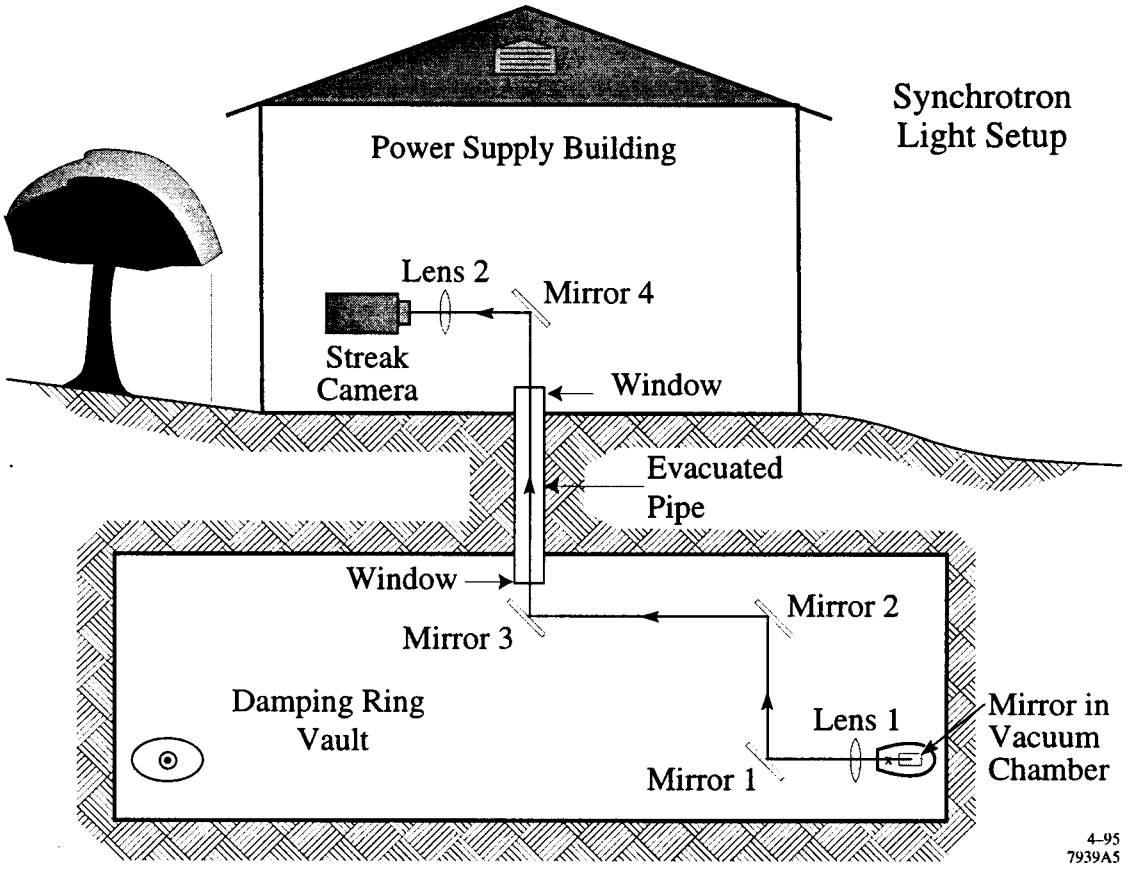

Figure 3.2.3. The damping ring optics set up used to transport the visible synchrotron radiation to the streak camera.

Two lenses are used to focus the light on the streak camera slit. The first lens, with a focal length 1.33 m, is positioned right after the vacuum window, and the second lens, with a focal length of 0.5 m, focuses the light on the slit of the streak camera and is positioned just before the streak camera slit (figure 3.2.4).

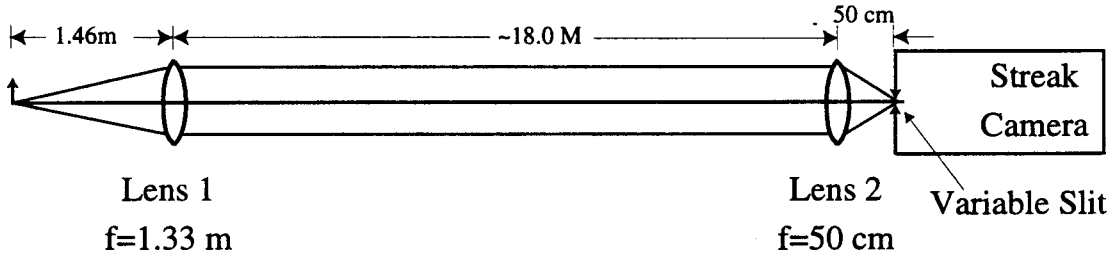

Figure 3.2.4. The location of the lenses in the damping ring optics line used to focus the synchrotron light onto the streak camera slit

Linac Synchrotron Light Optics

The same optics transport line can be used to measure the positron and electron bunch distributions at the end of the linac. The synchrotron light is produced by a bend magnet (50B1) which deflects the electron and positron bunches into their respective arcs. The synchrotron light emitted by the bunch is reflected by a mirror located just before profile monitor 50PR2 (figure 3.2.5). The mirror reflects the synchrotron light from the electron and positron bunch. The mirror is cut with a notch which allows it to fit around the fixed target beam pipe.

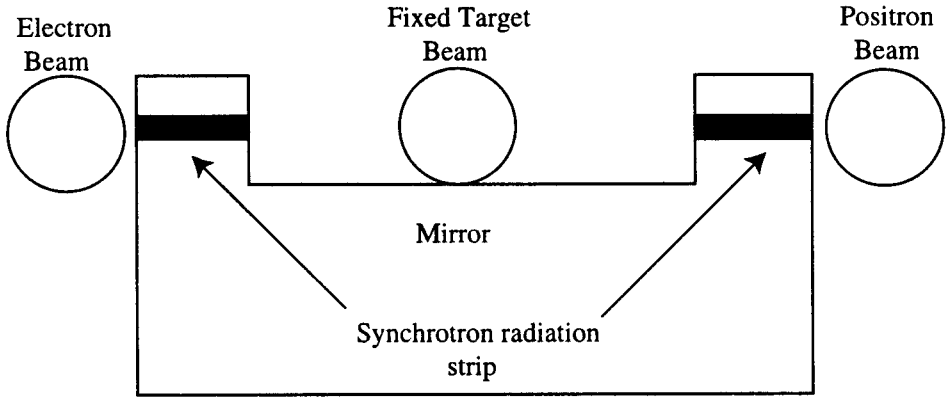

Figure 3.2.5. The first mirror used to transport the synchrotron light out of the vault at the end of the linac. The bend magnet which deflects the electrons and positrons is located upstream of this mirror. The mirror is tilted to deflect the synchrotron light out of the plane of the beam and onto the second mirror. The beams are about 30 cm apart at the mirror.

The synchrotron light from the two beams is transported to the streak camera by the optics shown in figure 3.2.6. The light then passes through a synthetic fused silica window and is reflected off two mirrors. The third mirror can be adjusted to guide the light through the penetration hole. The penetration hole ends in building 136 were there is an optics table for the streak camera measurements.

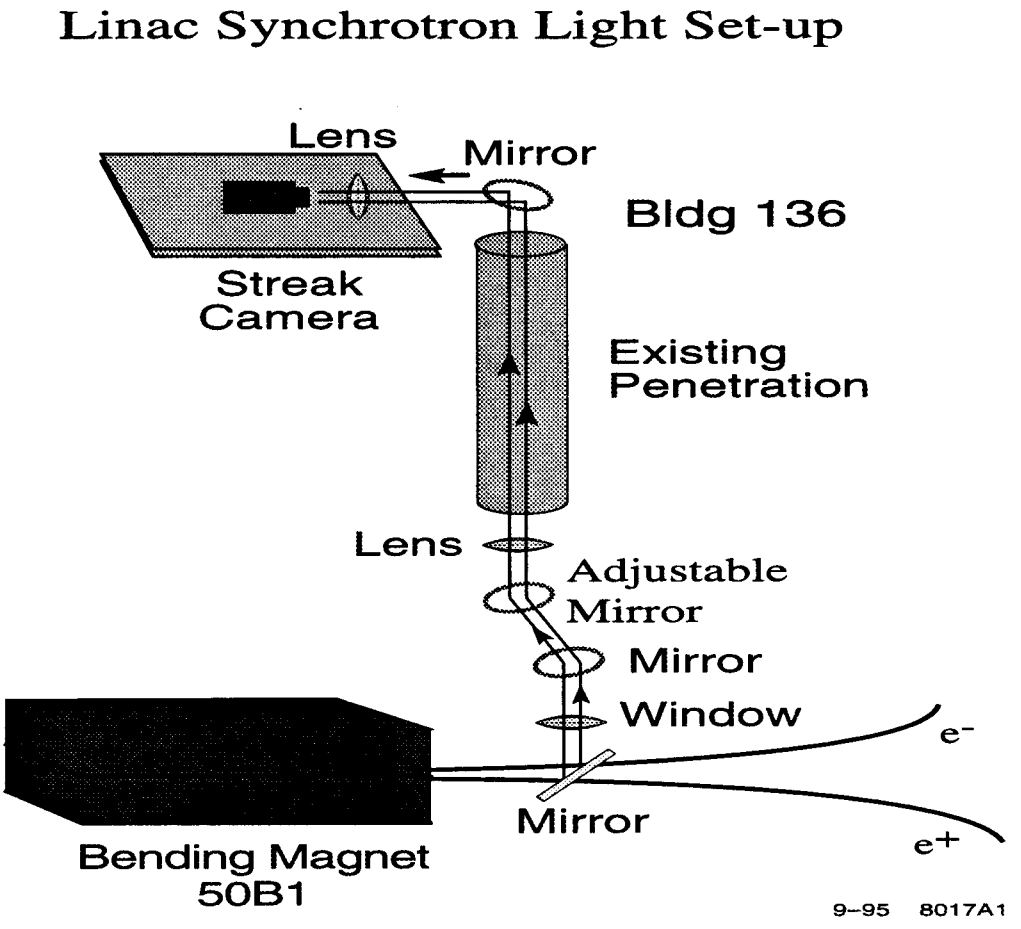

Figure 3.2.6. The optics layout for the streak camera at the end of the linac.

Two lenses are used to focus the light on the streak camera slit. The first lens has a focal length of approximately 2.0 m and the second lens has a focal length of 0.5 m. The distance between lenses and focal lengths are shown in figure 3.2.7.

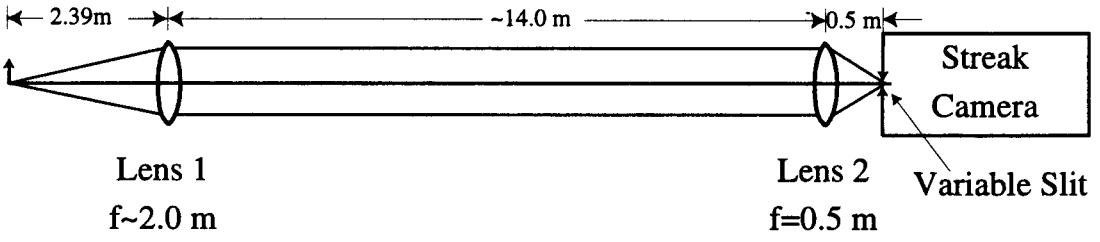

Figure 3.2.7. The location of the lenses in the linac optics line used to focus the synchrotron light onto the streak camera slit.

Optical Path Length correction to the Streak Camera resolution

When the electrons travel through a bend magnet, synchrotron light is produced over the path length of the magnet. If the path length is large the streak camera resolution is degraded. In this section the correction to the camera resolution will be calculated. Consider an electron which moves through a bend magnet and a mirror located a distance l from the center of the optical path. The electrons emit photons tangent to the electron trajectory and some of these photons are reflected off the mirror and are transported to the streak camera. The horizontal width of the mirror, denoted as 2W, is the aperture of the optical length seen by the streak camera. For a mirror of width 2W, the total angle 2δ and

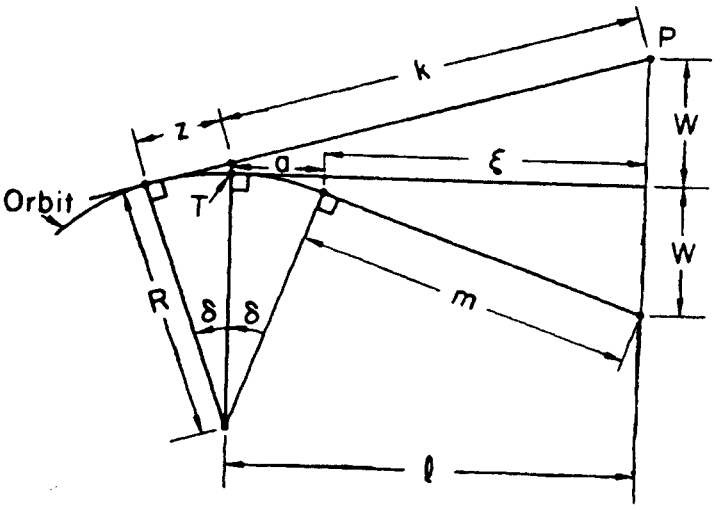

Figure 3.2 8. The geometry of the optical path length for the bend magnet which produces the synchrotron light for bunch length measurements [Munro and Sabersky, 1980].

path length P of the bend magnet path of the photons observed is

$$2\delta = \tan^{-1}\left(\frac{2W}{l}\right) \text{ and } P = 2R\delta \cdot$$

The time arrival difference between two photons emitted at $\pm\delta$ is given by [Munro and Sabersky, 1980]

$$\Delta t = \frac{2R\delta^3}{3c}$$

and this time difference is the correction to the resolution of the camera. It should be noted that this correction is due to the first optics aperture in the system, however this is not the only aperture. The slit width of the streak camera is another aperture and is a much tighter constraint but this calculation will give the correction to first order.
The resolution correction is done for both the damping ring and linac optical systems. The parameters for the damping ring and linac systems are listed below:

Parameter	Damping Ring	Linac
l	0.78 m	1.94 m
2W mirror width	1.41 cm	1.65 cm
δ path angle	$9.03x10^{-3}$ rad	$4.26x10^{-3}$ rad
R radius of curvature	2.0372 m	117 m
P path length	3.7 cm	0.997 m
Δt resolution correction	26.7 fsec	20.1 fsec

The resolution correction for the streak camera due to the optical path difference for the damping ring and linac measurements are insignificant compared to the resolution of the camera and can be ignored.

Damping ring Synchrotron Light Parameters:

Bend Magnet

Length	0.32 m
Pole Tip field	19.7 kG
$\int \bar{B} \cdot d\bar{l}$	6.304 kG-m
Bend	176.56 mrad
Radius of curvature	2.0372 m

Synchrotron light parameters

Opening Angle	0.429 mrad
ε_c	1.84 keV
λ_c	0.67 nm

Linac Synchrotron Light Parameters:

Bend Magnet

Length	2.264 m
Pole Tip Field	11.9 kG
$\int \bar{B} \cdot d\bar{l}$	26.94 kG-m
Bend angle	19.3 mrad
Radius of curvature	117 m

Synchrotron light parameters

Opening Angle	0.011 mrad
ε_c	1.92 MeV
λ_c	0.65 pm

3.3 Experimental Technique for the Streak Camera

Introduction

In this section I will describe the experimental technique used for measurements with the streak camera, how to eliminate space charge effects associated with streak camera measurements, and the linearity and resolution of the streak camera.

(i) Experimental Techniques for the Streak Camera

The Hamamatsu streak camera manual describes the operation of the streak camera in more detail than will be described here. The goal here is to point out some of the experimental operating techniques and set-up requirements used when measuring the bunch dynamics for the SLC, as well as some precautions which should be used when operating the camera. The steps in the section on "Turning on the Camera" need to be followed each time the camera is used to assure the synchrotron light is properly optimized for taking data.

Streak Camera Components

The streak camera input optics, filtering, sweep unit, CCD camera, vacuum pump, and data acquisition system, are shown in figure 3.3.1. The additional optics located before

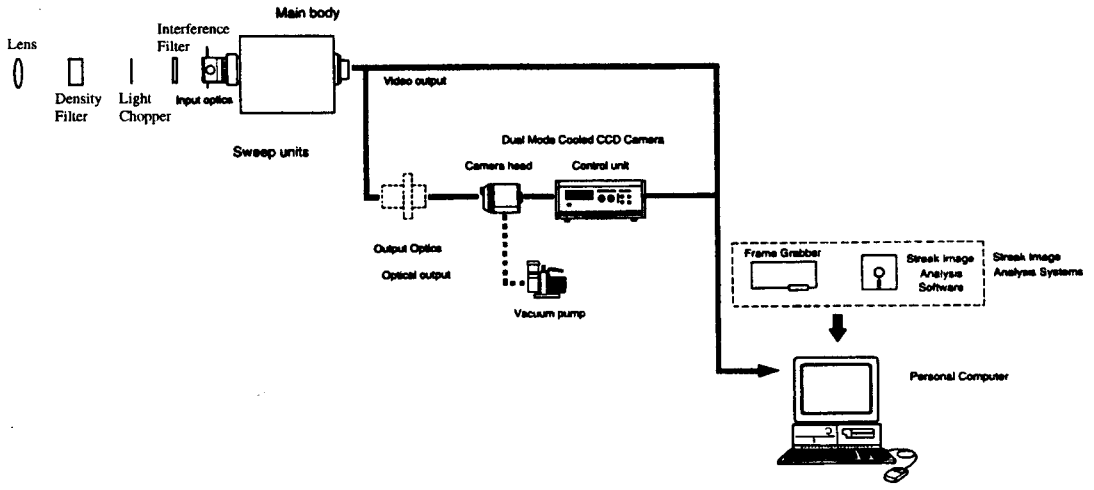

Figure 3.3.1. The experimental set-up for taking data with the Hamamatsu Streak Camera.

the main sweep unit consist of: 1) A lens to focus the synchrotron light on the slit of the camera, 2) a neutral density filter wheel, 3) an interference filter, and 4) a light chopper. The need for the additional input optics elements will be described in the following sections.

When the Camera is not in use

When the streak camera is not being used several precautions must be observed to assure that it will not be damaged. 1) The input shutter should be closed, and it is advisable to make sure the light chopper or the input plug is in place so light does not enter the camera. 2) The power supply for the sweep unit should remain off. 3) The CCD camera cooler **must** be turned off. If the vacuum pump fails or is turned off the CCD camera will be damaged if cooled. The vacuum pump for the CCD camera is left on in the event that if the cooler is turned on the camera will not be damaged.

Initial Precautions

The streak camera has two operation modes: streak mode and focus mode. In streak mode, the streak voltage is turned on to one of four possible streak speeds. In focus mode the streak voltage is turned off which allows the full power of the incident light to strike a small area on the micro channel plate. There are different light intensity requirements depending on the mode of operation. Running in focus mode the light needs to be filtered significantly more than in the streak mode because the gate in focus mode is greater than 5 msec. In addition to filtering, the micro channel plate needs to be set at its lowest voltage level to avoid damage.

Before operating the streak camera, a power meter is used to check the light power levels to determine if filtering is needed to protect the camera. The maximum peak level of input light for the streak camera is $4x10^{-7}\ W / mm^2$ when the incident light has a 500 nm wavelength and the camera is in streak mode. Filtering is almost always needed to keep the camera from being damaged.

Trigger Requirements

The streak camera trigger needs to be between 5 and 50 volts with a width of 10-100 nsec and jitter less than 20 psec. The jitter requirement is important when taking data at the fastest streak speed of 60 psec full width.

Damping Ring and Linac Trigger Signals

The trigger signal for the streak camera is derived from the 476 MHz linac master oscillator located in sector 0 (at the beginning of the linac). In the linac, the trigger signal is a NIM signal from the PL01 trigger (used for the fixed target experiment gun) which is timed off of the master oscillator. The NIM trigger is converted to a 10 V, 100 nsec signal which is put through a 0.5 nsec phase shifter and a 32 nsec delay box (with 1 nsec intervals). The PL01 trigger is a reference signal which can be adjusted in 1 nsec steps and along with a phase shifter, with 0.5 nsec range, the trigger signal can be adjusted until the beam pulse is observed by the streak camera. When running on the fastest streak speed (60 psec screen width and bunch lengths of 4 psec) BNC elbows are used to give another 0.5 nsec range for the phase shifter. The PL01 trigger was set to -638.00 nsec for positrons and -571.00 nsec for electrons.

The repetition rate of the PL01 trigger can be varied between 120 to 1/30 Hz. Under normal running conditions the trigger rate is 10 Hz, but correlating the streak camera with other devices requires a trigger rate of 1/30 Hz because the camera can only acquire and save beam profiles every 30 seconds.

The damping ring trigger does not need the jitter tolerance of the linac trigger because a slower streak speed is used in the damping ring. The same trigger is used in the

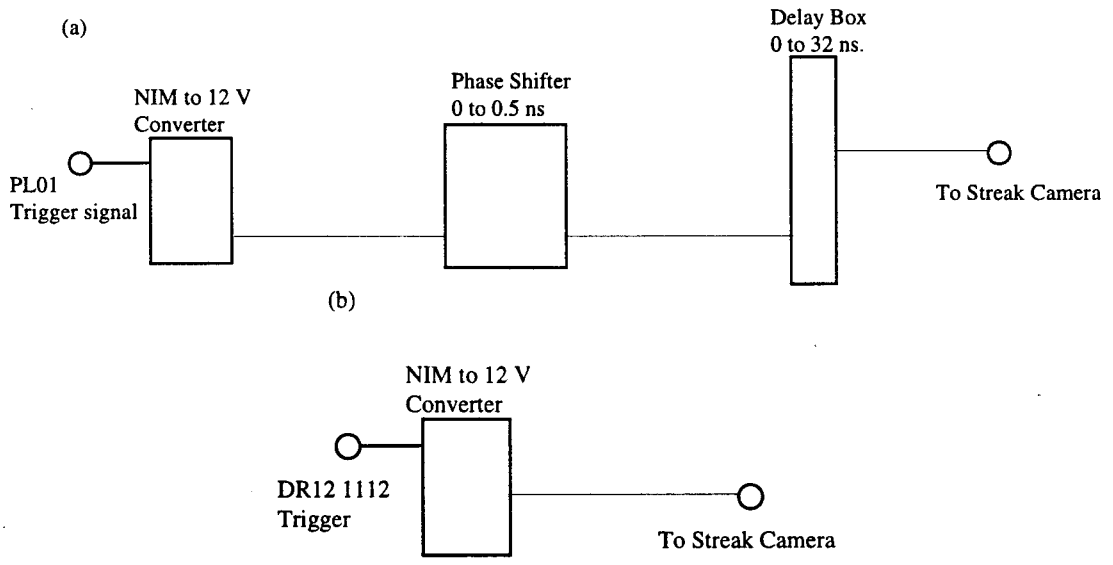

Figure 3.3.2. (a) The linac trigger system for the streak camera. (b) The damping ring trigger system for the streak camera.

north and south damping ring by patching the signal from the north to the south. The trigger signal is DR12 1112 and it has a step delay of 8.3 nsec. A finer delay is controlled by a variable delay unit (VDU) and its smallest delay is 0.1 nsec and so the phase shifter is not required in the damping ring. The DR12 1112 trigger signal is a NIM signal and is again converted to a 10 V, 100 nsec signal which is connected to the streak camera. A computer program has been written to increment the VDU delay time in time steps of 1.0 and 0.1 nsec so that finding the beam can be automated. A schematic of the linac and damping ring trigger signals is shown in figure 3.3.2 a and b.

Light chopper

Beam related background at the damping ring is associated with its high repetition rate (8.5 MHz). If the synchrotron light strikes the photocathode at the full repetition rate, stray photoelectrons accumulate at the photocathode and produce unacceptable background levels for data taking. A light chopper, model #300 manufactured by Palo Alto Research, is used to lower the background signal by lowering the average light intensity entering the camera. The chopper is triggered on the same trigger pulse as the streak camera but with a TTL trigger signal. Two chopper wheels with two gaps, typically a 10 degree gap is used; are placed on top of each other and one is rotated to allow the gap width to be adjusted.

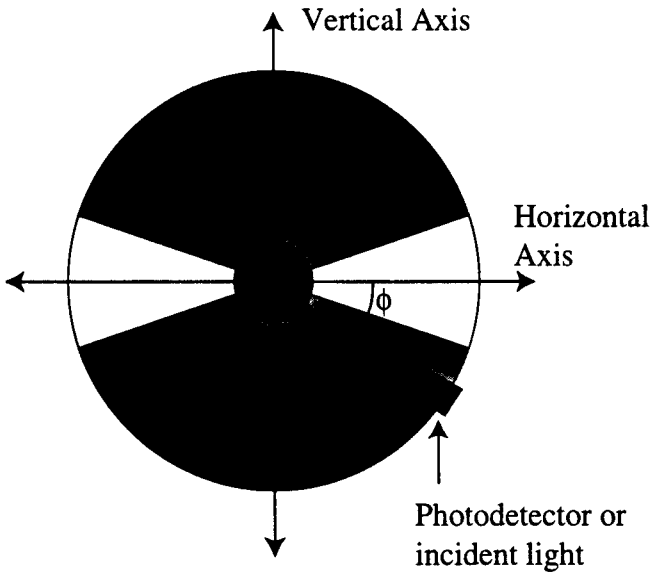

Figure 3.3.3. Two chopper wheels placed together allows the opening angle to be varied. The phase calibration was done with a photo detector mounted at three different angles. A positive angle for this orientation is below the horizontal axis.

The phase of the gap can be adjusted by the chopper controller, and it has been calibrated to allow the phase to be measured from the horizontal axis of the chopper axis (figure 3.3.3).

The calibration of the light chopper phase was done in the following manner:

1) A function generator running at 10 Hz triggered a pulser which delivered a TTL pulse to the chopper controller and a trigger to the photodiode-detector unit (see figure 3.3.4)

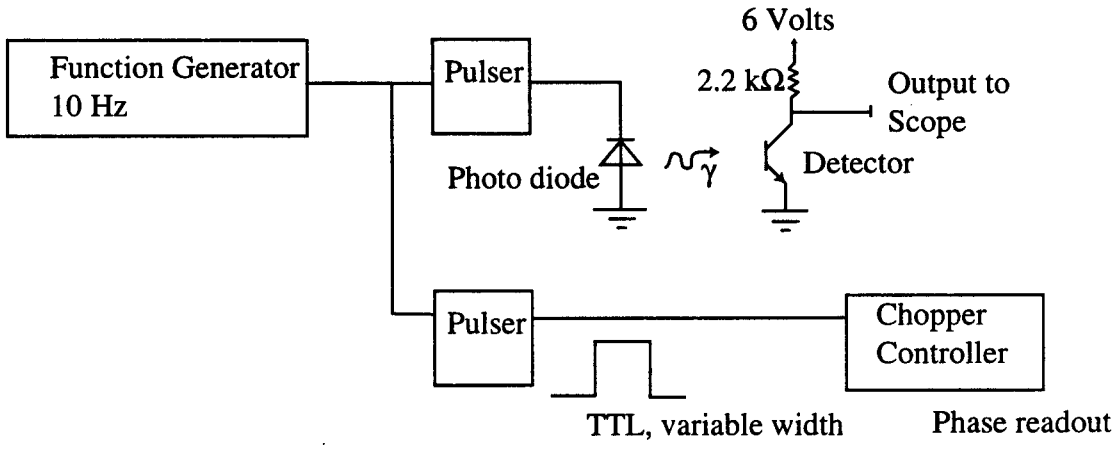

Figure 3.3.4. A schematic of the calibration electronics for the light chopper.

2) The TTL pulse width was varied from 1-10 msec, and the chopper phase was varied. The phase range for a detectable photodiode signal did not depend on the pulse width.

3) The photo diode-detector unit was mounted at three different angles with respect to the horizontal axis (figure 3.3.3), and the phase of the chopper was adjusted until a signal

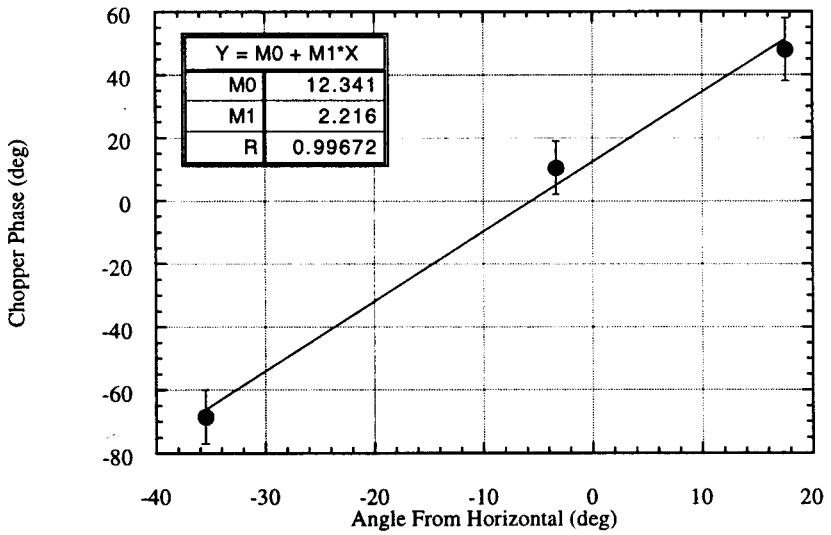

Figure 3.3.5. The calibration of the phase of the chopper. Measuring the angle of the incident light from the horizontal axis gives the chopper phase needed for measurement.

from the detector is registered. The angle from the horizontal axis to the location of the LED was measured with a protractor. The calibration curve can then determine the phase at which the chopper needs to be set to assure that the beam pulse will be transported through the chopper gap. The range of the signal was measured and plotted versus the angle from the horizontal axis of the chopper wheel (see figure 3.3.5).

Turning on the Camera

This process should be followed in the sequence below each time the camera is turned on to make sure the experimental set-up is optimized.

1) Turn on the Personal Computer (PC) which controls the data acquisition. If there is an ethernet connection to the PC, make sure that it has the proper address to connect to the Main Control Center (MCC) VAX.

2) Once the PC and windows are up and running, start up the Hamamatsu Streak Camera software. The software runs the camera, acquires the data, and gives the status of the camera.

3) Check the CCD camera temperature by looking at the status display. If the CCD camera cooler is turned off (as it should be if shut-off properly) than the temperature should be ~27°C.

4) Before cooling the CCD camera, make sure the vacuum pump is connected and turned on. When turned on, the cooling process can begin by pressing the cooler button on the CCD power supply unit.

5) While the camera is cooling, turn on the streak camera power supply unit as well as the read out monitor.

6) It is wise to make sure everything is working properly. This can be achieved by loading an old image or streaking the camera to make sure that all of the devices are connected properly. Before doing this, make sure the shutter to the input optics is closed.

7) Make sure the input optics have the synchrotron light focused on the slit of the streak camera. This is best done with the slit of the camera closed to allow the light to be centered on the slit vertically and horizontally. Make sure the light entering the camera is not at an angle vertically or horizontally to 2-3 degrees accuracy.

8) The aligned synchrotron light needs to be focused on the camera in focus mode. This step must be taken with great care because the amount of light entering the camera can easily damage it. In focus mode the streak camera does not streak the light and the gate of the camera is large (it can vary between 5 msec to one hour) which makes it possible to over expose the multichannel plate. The first step is filtering the light. There is no

prescription as to how much filtering is needed in focus mode, but it is always better to over filter than damage the camera. At the damping ring, I used a narrow band interference filter (± 10 *nm* centered at 500 nm) and at least 5.0 neutral density filtering. If the light is visibly entering the camera after setting up this filtering scheme, then more filtering is needed. The next step is to set the micro channel plate to its lowest setting (that includes the vernier knob). Set the trigger to internal on the data acquisition software with a gate width of 5 msec. The slit to the camera needs to be opened to greater than 1 mm to make sure all the light enters the camera. Set the streak speed to focus mode and start the camera (with the shutter closed). Open the input shutter and, if properly aligned, the image of the light should appear on the readout monitor. The light should not be saturating the camera (saturation is red on the read-out), but if it is, more filtering is needed. Center the image on the readout monitor by adjusting the input optics. Once centered, the slits can be closed to their desired size and the image should be at the center on the monitor. Now the image can be streaked.

9) Finding the streaked image depends on the trigger delay between the streak camera and the arrival time of the bunch. Discussion of the trigger set-up was mentioned earlier so I will assume that it has already been set-up. To find the bunch it is easiest to find it on the slowest streak speed (1.2ns / 10 mm) with the method described in the next section. Once it has been found on the slow streak speeds, the following recipe (table 3.3.1) will get you close to the location with the faster streak speeds, and using the phase delay or VDU will allow you to locate the bunch. When streaking the bunch, the neutral density filter of the beam can be reduced and the micro channel plate voltage can be turned up.

Speed (ps/10 mm)	Delay time (ns)	Phase shift (deg.)	# of BNC elbows
1200	0	0	0
500	1	150	0
200	-10	40	0
60	2	160	2

Table 3.3.1. The trigger delay time for the four speeds of the streak camera. The delay time is the change in time from the previous time setting.

Finding the beam

Finding the beam with the streak camera has been semi-automated so that the search does not need to be time consuming and frustrating. A photomultiplier tube (PMT) in conjunction with the streak camera trigger is used to find the beam. The schematic for the photo multiplier tube beam finder is shown in figure 3.3.6 .

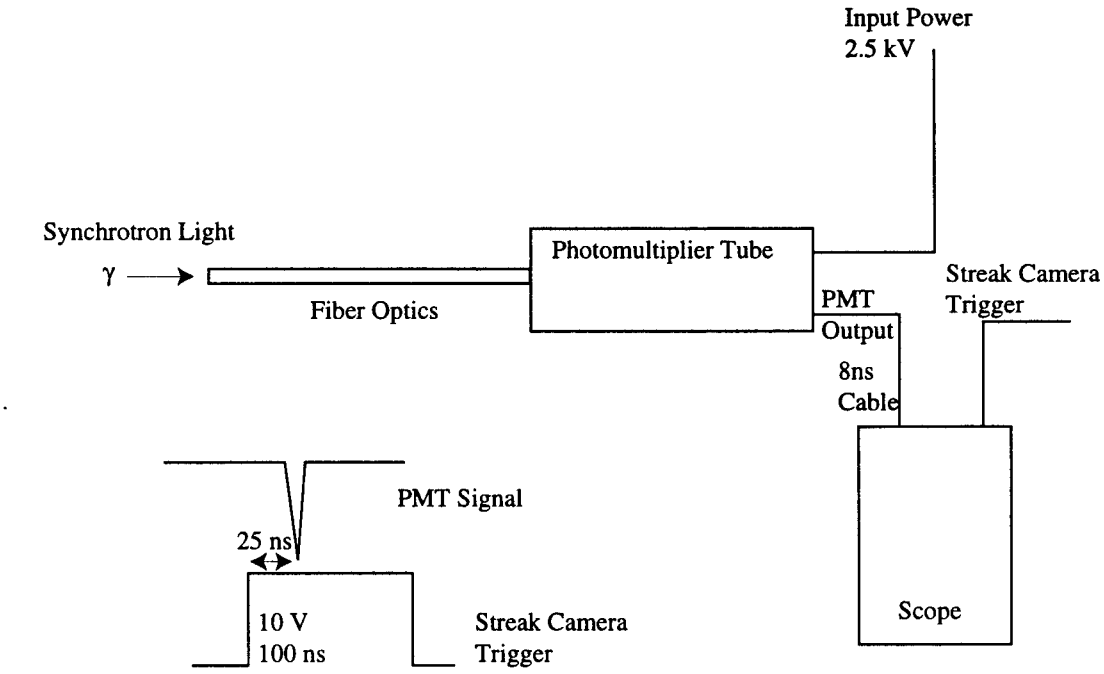

Figure 3.3.6. A schematic of the experimental set-up for the beam finder.

The method is to trigger an oscilloscope off the streak camera trigger and measure the time difference between the beam arrival and the trigger signal. The delay in the PMT is approximately 80 nsec and the delay in the streak camera is approximately 100 nsec,

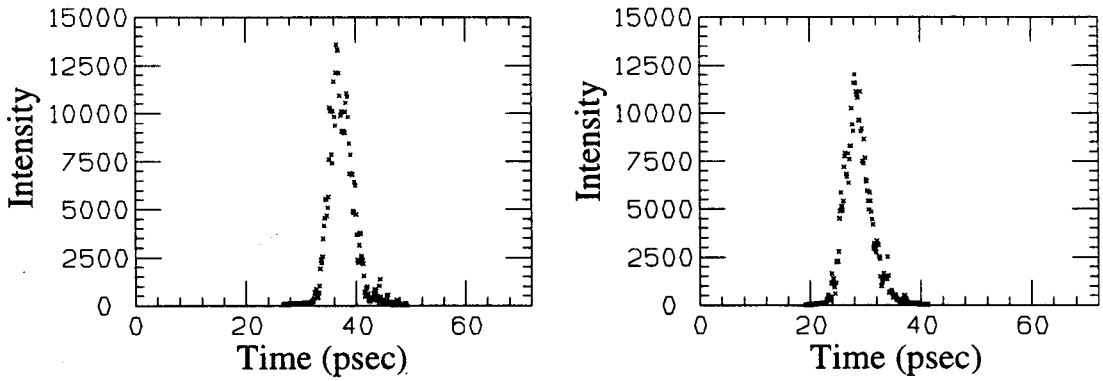

Figure 3.3.7. Two bunch length profiles at the end of the linac taken by the streak camera.

therefore, triggering the oscilloscope with streak camera trigger and adjusting the delay to approximately 25 nsec where the beam was found. In the future, a solid state photodiode will be used in place of the PMT. This will eliminate the high voltage dependence of the PMT delay.

Examples of bunch length profiles taken by the streak camera at the end of the linac are shown in figure 3.3.7.

(ii) Space Charge Effects in the Streak Camera

Space charge effects can occur when the intensity of the synchrotron light incident on the photo cathode is too high. This causes the photoelectrons to interact and leads to a systematic error in the bunch length measurement. The measured length is larger than the actual length. To eliminate the space charge effects, the multichannel plate gain was set to its maximum setting and the incident light was filtered until the bunch length measurement was stable over a range of light intensities. The height of the distribution is also measured to illustrate the signal for saturation of the CCD camera. Figure 3.3.8 exhibits the effect of light intensity on bunch length measurement for the damping ring, and, in this example, the light is filtered by 50% to eliminate this effect in subsequent measurements. Measurements were also conducted at the end of the linac to quantify the effect of systematic errors in the bunch length measurement due to space charge.

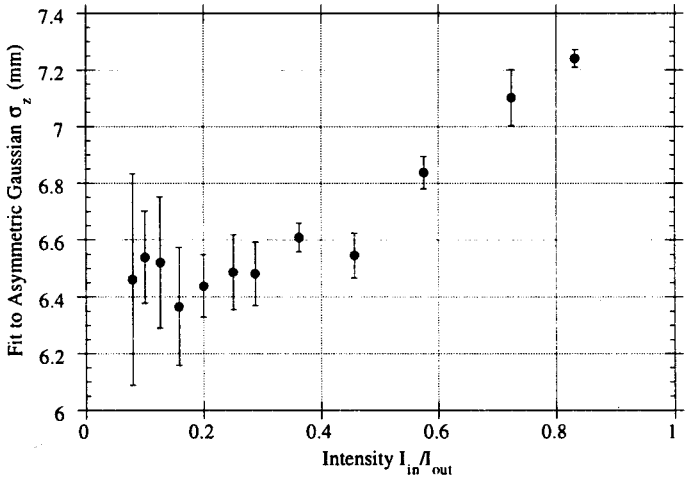

Figures 3.3.8. The measured bunch length dependence on light intensity at the south damping ring (positron) with a current of I=3.6x10^{10}. The measurement consists of taking 5 streak camera profiles at each density filter setting. The figure is a plot of the mean and rms error of each density filter setting.

(iii) Linearity and Resolution of Streak Camera

Hamamatsu Linearity Results

A measurement of the linearity of the streak camera tube was done at the Hamamatsu Corporation, and the linearity curves for the four different streak speeds is shown in figure 3.3.9 a-d. The calibration data was fit to polynomial curves which were used in the analysis of the data.

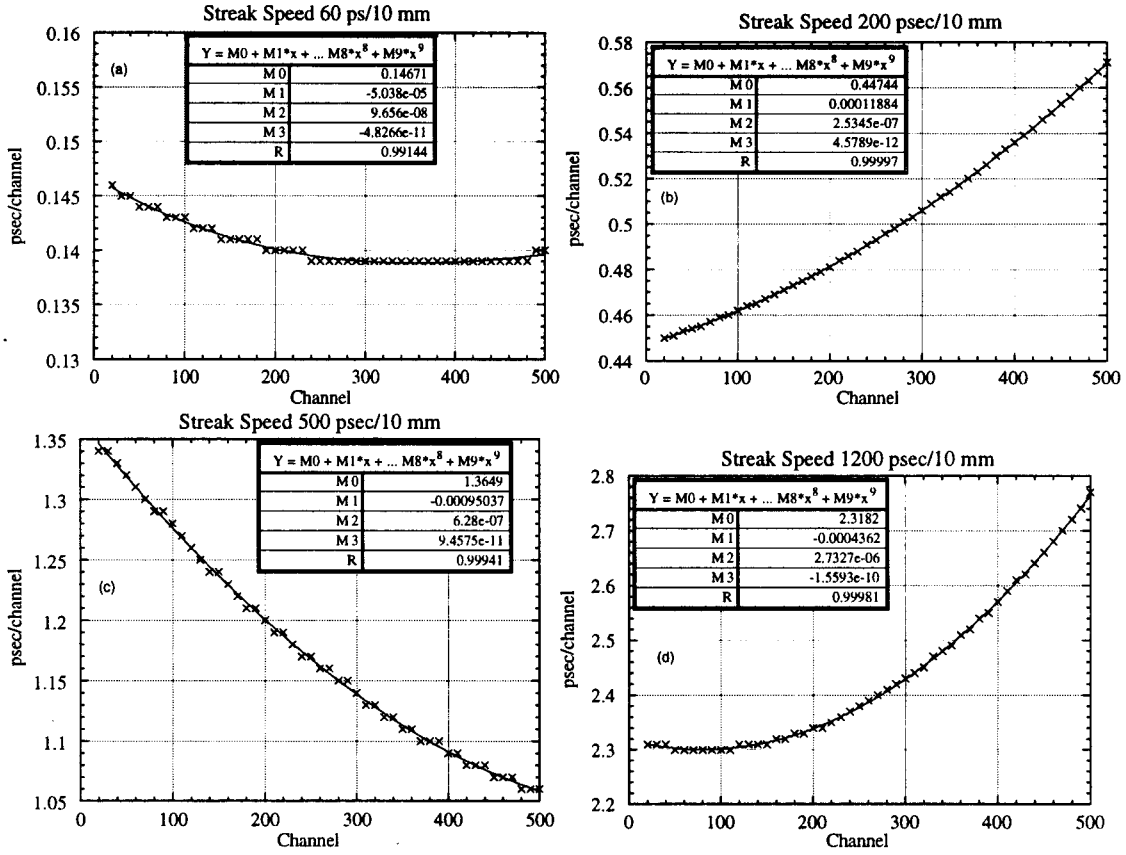

Figure 3.3.9. The calibration curve for the streak camera for the streak speeds of: (a) 60 psec/10 mm, (b) 200 psec/10 mm, (c) 500 psec/10 mm, and (d) 1200 psec/10 mm.

Resolution

The major factors which can limit the resolution of the streak camera are:

1) Dispersion in the glass optics t_1.

2) Photoelectrons having a transit time spread within the streak tube t_2.

3) The slit image at the photo cathode gives a temporal width t_3.

The time resolution including all of these factors is given by adding these in quadrature

$$t_{res} = \sqrt{t_1^2 + t_2^2 + t_3^2}\,. \qquad (3.3.1)$$

The actual bunch length can be written in terms of the camera resolution and the measured bunch length as

$$t_{actual} = \sqrt{t_{measured}^2 - t_{res}^2}\,.$$

The slit width and dispersion effects have been studied for the measurements with the Hamamatsu streak camera at the damping ring and linac. For the damping ring measurements, by choosing a slit width of 200μm or less this contribution is negligible (figure 3.3.10). For the linac, a slit width of 100μm or less is needed to avoid a significant contribution to the resolution.

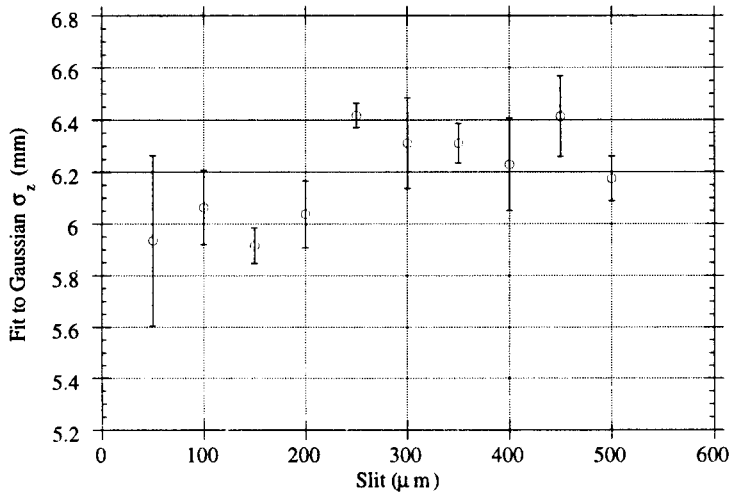

Figures 3.3.10. The dependence of the measured damping ring bunch length on the streak camera slit width. The measurement consists of taking 7 streak camera profiles at each slit width. The mean and rms error is plotted at each setting. The light intensity is adjusted at each slit width to avoid systematic errors.

Dispersion in the glass elements of the optics can be minimized by using a narrow band interference filter (figure 3.3.11). The peak spectral response of the streak camera is

500 nm, and the interference filter used is centered at 500 nm with a 10 nm full width half maximum acceptance for linac measurements, 40 nm full width half maximum acceptance for damping ring measurements.

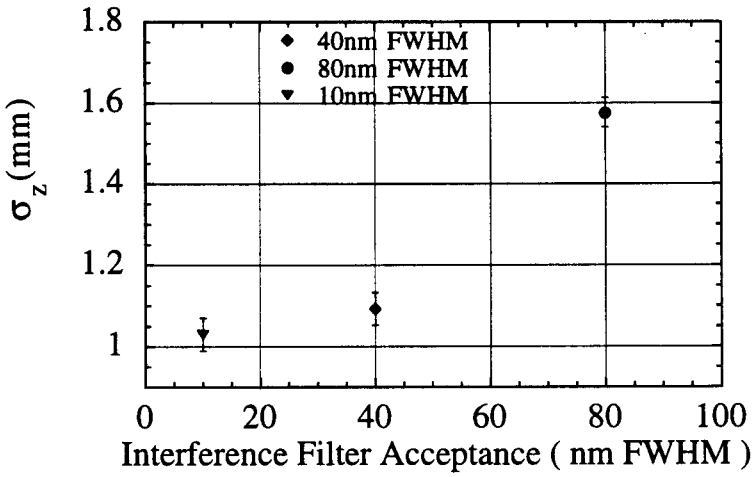

Figures 3.3.11. The measured electron bunch length at the end of the linac as a function of interference filter acceptance. The measurement consists of taking 10 streak camera profiles and plotting the mean and rms error for each filter acceptance. The light intensity is adjusted at each setting to avoid systematic errors caused by light.

Resolution Measurement

The resolution of the streak camera was measured with a titanium sapphire pulsed laser. The laser puts out a 200 femtosecond full width at half maximum (FWHM) pulse at 800 nm wavelength. The details of the experimental set-up is described in appendix A.

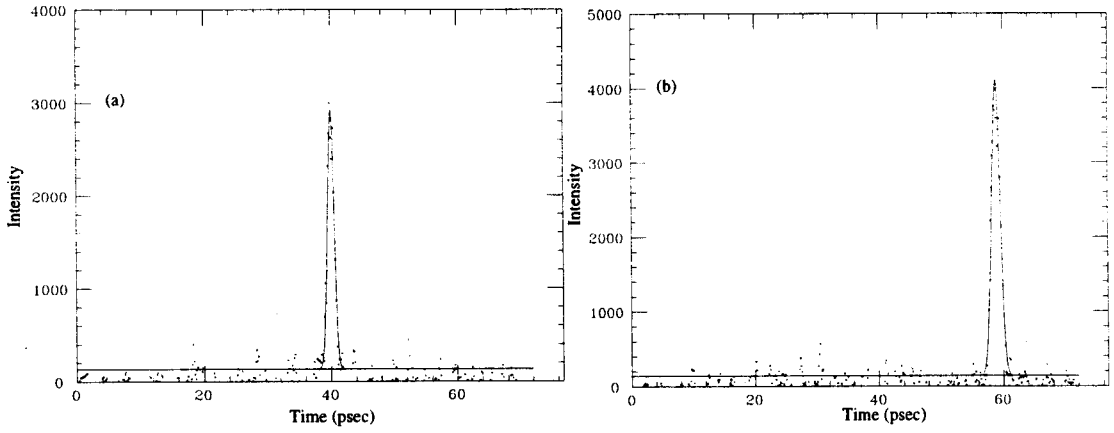

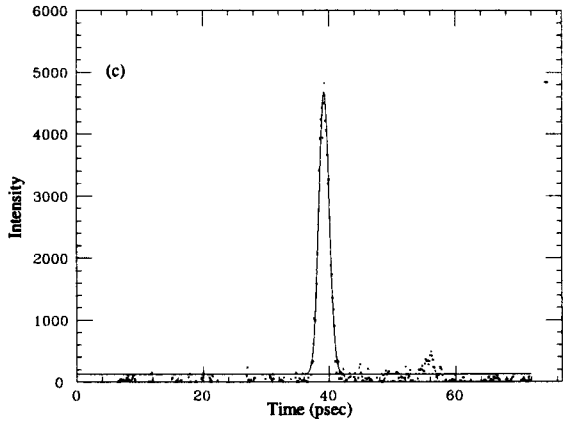

Figure 3.3.12. Streak camera images of the titanium sapphire laser pulse at the 60 ps/10mm setting for the slit width of: (a) 20 μm, (b) 50 μm, (c) 100 μm.

The resolution of the streak camera was measured as a function of slit width and streak speed. Typical profiles are shown in figures 3.3.12a-c and 3.3.13a-d. Table 3.3.2 is a summary of the measurements.

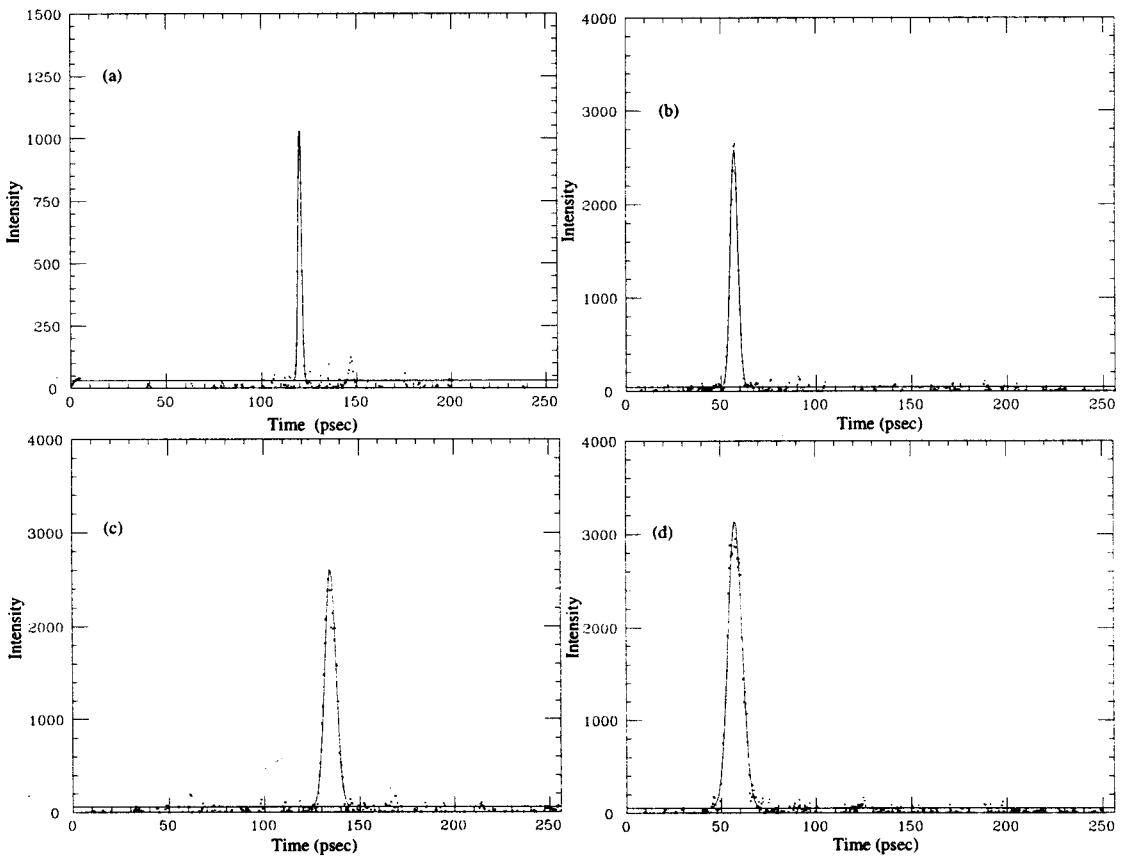

Figure 3.3.13. Streak camera images of the titanium sapphire laser pulse at the 200 ps/10mm setting for the slit width of: (a) 30 μm, (b) 100 μm, (c) 150 μm, (d) 200 μm.

Streak Speed (ps/10 mm)	Slit Aperture (μm)	Number of profiles	σ_t(ps) from Gaussian fit	Standard Deviation (ps)
60	20	24	0.561	0.064
60	50	24	0.676	0.055
60	100	25	0.874	0.042
200	30	19	0.952	0.066
200	100	17	2.213	0.079
200	150	21	3.071	0.136
200	200	26	3.927	0.180

Table 3.3.2. The streak camera resolution results.

Correcting the data in table 3.3.2 for the laser pulse width, 200 fs subtracted in quadrature, allows the resolution of the streak camera at zero slit width to be determined. Determining the zero slit width resolution for a laser pulse (meaning virtually no dispersion) allows the transit time contribution to the resolution to be determined from equation 3.3.1. The transit time contribution to the streak camera resolution (zero slit width) for the streak speeds of 60ps/10mm and 200ps/10mm streak speeds is 526 fs and 937 fs respectively (figures 3.14a and b).

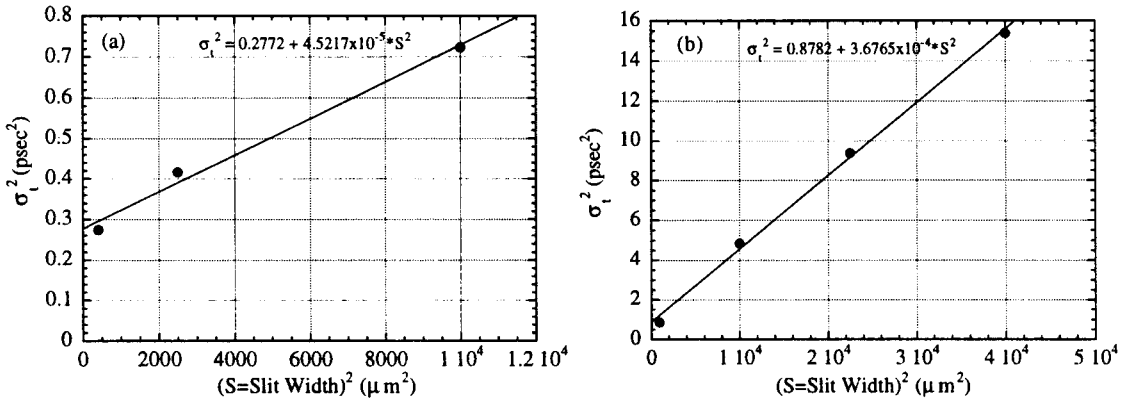

Figure 3.3.14. The measured resolution corrected bunch length squared as a function of slit width squared for the streak speeds of (a) 60 ps/10mm, and (b) 200 ps/10mm.

3.4 Bunch Length Cavity

Introduction

Another apparatus used to measure the bunch length in the linac is an RF bunch length cavity [A. Kulikov, 1985, E. Babenko, 1993]. The RF bunch length cavity can measure only relative changes in the bunch length so it must be calibrated with another device such as a streak camera. The RF cavity is an ideal diagnostic device for monitoring changes in the bunch length in the linac. In this section a theoretical description, the experimental set-up, and calibration of the RF bunch length cavity will be presented.

Theoretical description of the RF bunch length cavity

Consider a highly relativistic bunch traveling through a vacuum chamber. The bunch emits electric field lines which propagate radially from the bunch at an angle of

$$\varphi = \gamma^{-1} = \frac{mc^2}{E}.$$

Integrating the fields over the bunch distribution will give the power spectrum of the bunch, conversely if the power spectrum is measured the bunch distribution can be determined.

The RF cavity sits on top of the beam pipe and measures the power at one frequency, i.e., it samples the spectrum of the beam at this frequency. As an example, if the bunch is considered to be Gaussian in length, the line charge is

$$\lambda(z) = \frac{Q}{\sqrt{2\pi}\sigma_z}\exp\left[\frac{-z^2}{2\sigma_z^2}\right]$$

where Q is the charge of the beam and σ_z is the standard deviation of a Gaussian distribution. The electromagnetic fields produced by a passing bunch in the approximation of $\gamma \to \infty$ is

$$\vec{E} = \frac{Q\gamma\hat{r}}{(2\pi)^{3/2} r\sigma_z}\exp\left[\frac{-z^2}{2\sigma_z^2}\right] \text{ and } \vec{B} = \frac{Q\gamma\hat{\varphi}}{(2\pi)^{3/2} r\sigma_z}\exp\left[\frac{-z^2}{2\sigma_z^2}\right]$$

where γ is given above. The fields can be Fourier transformed using

$$E(\omega), B(\omega) = \int_{-\infty}^{\infty} E(t), B(t)\exp[i\omega t]dt$$

to get the frequency spectrum of the radiated fields. The Fourier transformed fields are given by

$$E(\omega) = \frac{Q\gamma}{2\pi rc}\exp\left[\frac{-\omega^2\sigma_t^2}{2}\right] \text{ and } \mathrm{B}(\omega) = \frac{Q\gamma}{2\pi rc}\exp\left[\frac{-\omega^2\sigma_t^2}{2}\right].$$

The cavity is narrowband and has a high Q mode at some resonant frequency. The cavity is shock excited by the passing beam, and the Q of the cavity is high enough so that the energy is radiated slowly through a wave guide and detected with a power detector. The energy lost into the high Q mode is

$$U(\omega) = QK_{loss}F(\omega)$$

where K_{loss} is a loss factor dependent on the cavity geometry and $F(\omega)$ is the bunch form factor given by

$$F(\omega) = \exp\left(\frac{-\omega^2\sigma_t^2}{2}\right).$$

The power received by the detector after traveling through the waveguide is given by

$$P \propto CQ^2\exp\left[-\omega^2\sigma_t^2\right]\exp(-\eta x)$$

where C is a constant, η is the wave guide attenuation constant and x is the distance along the wave guide. At low power $V \propto P$ and hence

$$V(\omega) \propto Q^2\exp\left(\frac{-\omega^2\sigma_t^2}{2}\right),$$

as the voltage increases $V \propto \sqrt{P}$ and hence

$$V(\omega) \propto Q\exp\left(-\omega^2\sigma_t^2\right).$$

Details about the two regimes are discussed below.

Experimental Set-up

The RF bunch length cavity is located at sector 25 of the linac. The cavity sits on top of a ceramic gap in the vacuum chamber. The electric fields from the electron or positron bunch can pass through the ceramic gap and enter the cavity through a small hole located on the bottom (figure 3.4.1).

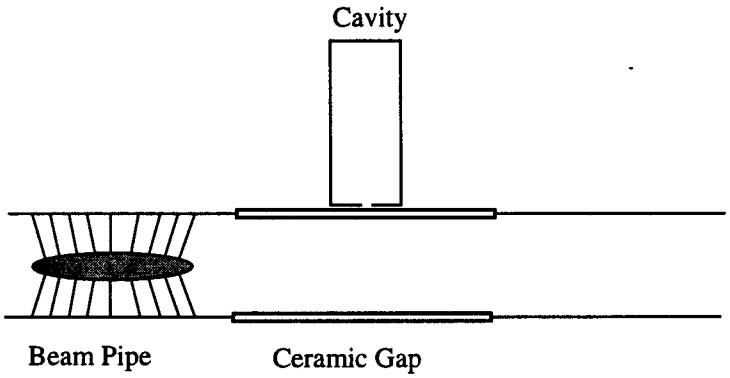

Figure 3.4.1. The bunch length cavity set-up at sector 25 of the linac.

The cavity radiates power out of a larger hole which is connected to a rectangular wave guide. The wave guide transports the power to a high frequency coaxial GaAs microwave power detector (figure 3.4.2). The detector is located in the klystron gallery in an insulated housing which is kept at a constant temperature to assure no variations of the output of the detector due to temperature. The detector voltage is amplified and integrated by a gated analog to digital converter (GADC). The output signal of the GADC depends on the bunch charge and bunch length. The output signal from the GADC is

$$\left(\frac{G-G_0}{Q}\right) \propto \exp\left[\frac{-\omega_0^2\sigma_t^2}{2}\right]$$

where G_0 is the GADC pedestal. Relative changes of the bunch length can be detected during constant current running. When the current varies there are several toriods that have been used as well as a gap current monitor near the bunch length cavity to determine the current Q of the passing bunch. The GADC signal is sent to the main control center (MCC) VAX so that the bunch length signal can be monitored and history buffered for SLC operations.

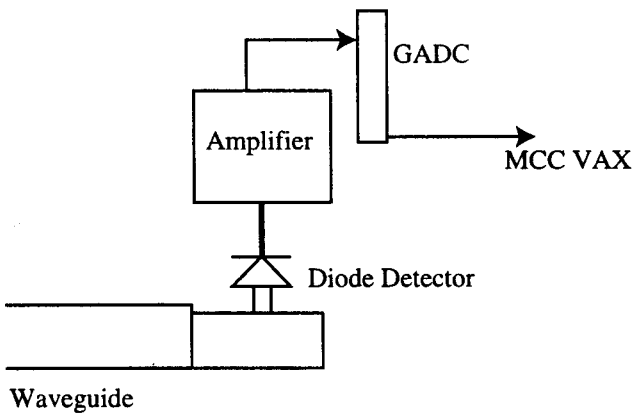

Figure 3.4.2. The bunch length cavity readout system for the bunch length cavity signal.

Detector Calibration

The detector is a nonlinear device, and to account for that it was calibrated in the laboratory to characterize its operating regimes.

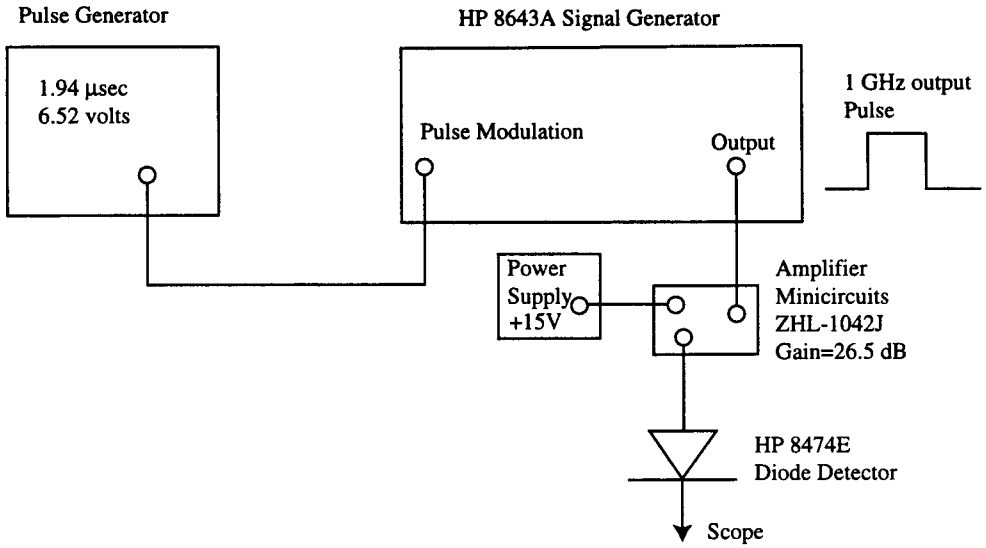

Figure 3.4.3. The laboratory set-up for calibrating the diode detector.

The calibration set-up is shown in figure 3.4.3. The pulse generator was set to put out a 6.52 volt signal that has a 1.94 µsec width. This signal is fed into a signal generator that puts out a 1 GHz signal modulated by the pulse. The signal is amplified and connected to the diode detector. The diode output signal is read by a scope and is terminated into 50

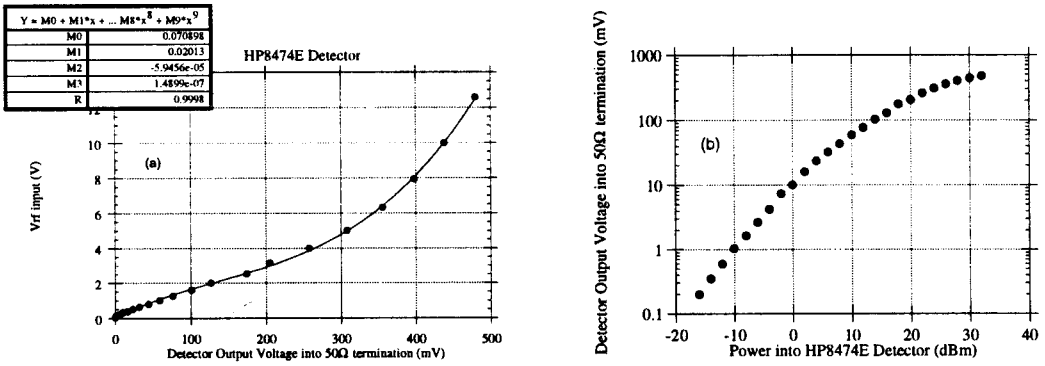

Figure 3.4.4. (a) The diode detector output voltage as a function of the input voltage. (b) The diode detector output voltage as a function of the input power.

Ω (the linac signal also terminates into 50 Ω). The characteristics of the detector are determined by varying the signal generator output and measuring the detector output. The detector output is nonlinear, as expected, and its voltage and power characteristics are plotted in figures 3.4.4 a and b.

Bunch length cavity calibration

Before the RF cavity can be calibrated, the sensitivity to transverse motion of the beam must be examined. Moving the beam with a corrector magnet upstream of the bunch length cavity by 1 mm introduced no change in the bunch length cavity signal. The SLC beam electron in the linac is stable to 200 μm, therefore, transverse motion will not effect the cavity signal.

The RF bunch length cavity calibration for the electron bunch was done in the following steps:

1) Keeping the current constant (current jitter was about 1-2%), adjust the electron compressor voltage and measure the detector signal for electrons.

2) Keeping the electron bunch compressor voltage constant, adjust the current and measure the detector signal.

3) Repeat steps 1 and 2 with the signal being measured by the GADC.

The results are plotted in figures 3.4.5 and 3.4.6.

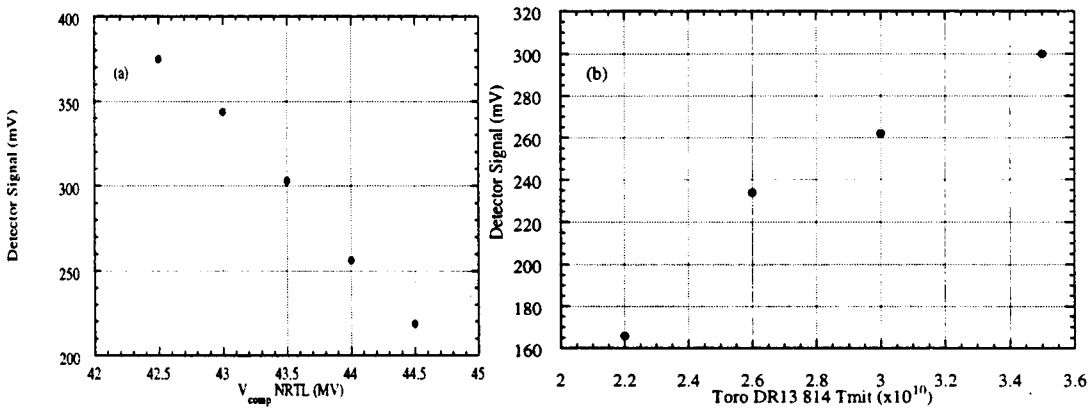

Figures 3.4.5. (a) The detector signal as a function of the compressor voltage at a current of 3.5×10^{10} particles per bunch. (b) The detector signal as a function of current with the compressor set at 43.5 MV.

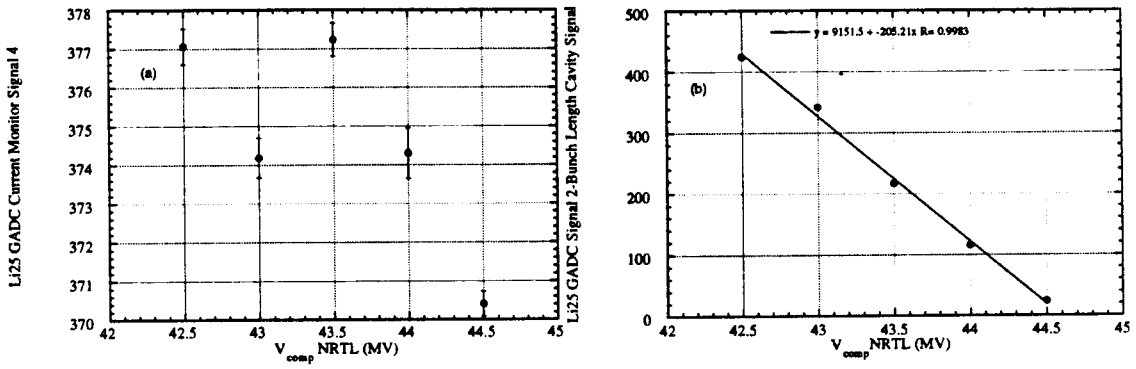

Figures 3.4.6. (a) The current signal at the detector as a function of compressor voltage. This indicates that the current was constant during calibration. (b) The GADC signal as a function of compressor voltage at a current of $3.4\text{x}10^{10}$. A linear fit to the data is shown in the figure.

The electron bunch length from the cavity signal can be determined for small deviations around the normal operating point. The GADC bunch length signal can be written in terms of the current and the bunch length as

$$\text{GADC} = A'\left(\frac{I}{I_0}\right)\sigma\cdot$$

The term A' has been determined for the central compressor value of 43.5 MV and a current of $3.5\text{x}10^{10}$ particles per bunch to be

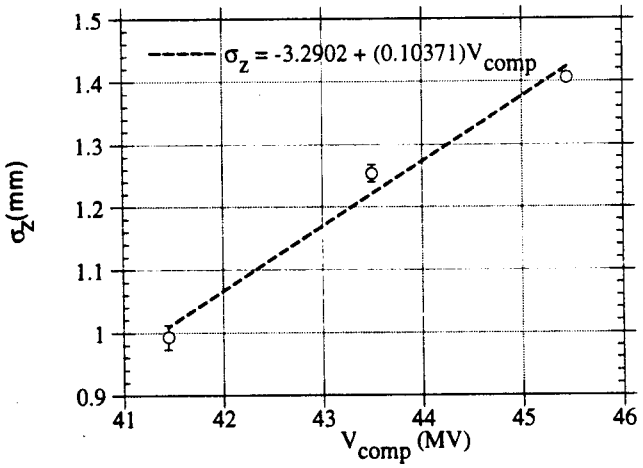

Figure 3.4.7. The electron bunch length as a function of the compressor voltage using the streak camera. The streak camera measurement is used to calibrate the RF cavity signal.

$$A' = \frac{\frac{d(GADC)}{dV_{comp}}}{\frac{d\sigma}{dV_{comp}}} = \frac{205.21 MV^{-1}}{0.1037 \frac{mm}{MV}}.$$

The value for the bunch length dependence on the compressor voltage is from the streak camera data (figure 3.4.7). The electron bunch length measurement from the RF bunch length cavity and current monitor is expressed as

$$\sigma(mm) = \frac{\text{GADC}}{(\text{Current signal})\left(\frac{A'}{375}\right)}.$$

The calibration of electron bunch length measurement from the RF cavity was done with the positron beam turned off. The calibration will change when the positrons are turned on because of the cross talk between the two beams due to a 60 nsec separation between bunches. In principle this calibration for the electron beam is valid for the positron beam because the signal from the positron beam is uncoupled from the electron signal. The calibration for the electron signal with a positron signal present was not done but this does not deter from the principle use of the RF cavities in this dissertation which was to correlate the bunch length signal with the streak camera measurements in order to detect pulse to pulse jitter.

Cavity Parameters

Frequency	36 GHz
Excited mode	TM_{020}
Radius	0.73 cm
Height	0.67 cm
Distance to beam	3.8 cm
Output hole diameter	0.35 cm
Input hole diameter	0.30 cm

Wave Guide Parameters

Type	WR-28
Frequency range	26.5-40 GHz
Length	13 m
Wide Wall	0.71 cm
Narrow Wall	0.36 cm
Attenuation constant	0.42 m^{-1}

3.5 Wire Scanner

Introduction

The wire scanners for the SLC provide accurate non-invasive transverse beam size measurements at various locations in the SLC. By measuring the beam size in a high dispersion region the energy spread can be determined. In the ring to linac transport line (RTL) where the bunch compressor is located the energy spread and bunch length are measured. In this dissertation, the energy spread and bunch length are measured at the exit of the north (electron) damping ring and the energy spread is measured at the end of the linac for both electron and positrons. In this section I will describe the design and uses of the wire scanners [M.C. Ross, 1991].

Overview

A schematic diagram of a wire scanner is shown in figure 3.5.1. The wire is made of gold plated tungsten (with a diameter of 120 μm in the arc and 75 μm in the RTL) and is strung around 1.5 mm stainless steel studs that are attached to a 3/16 inch thick aluminum fork. The wire is positioned to scan three different orientations of the beam, x,

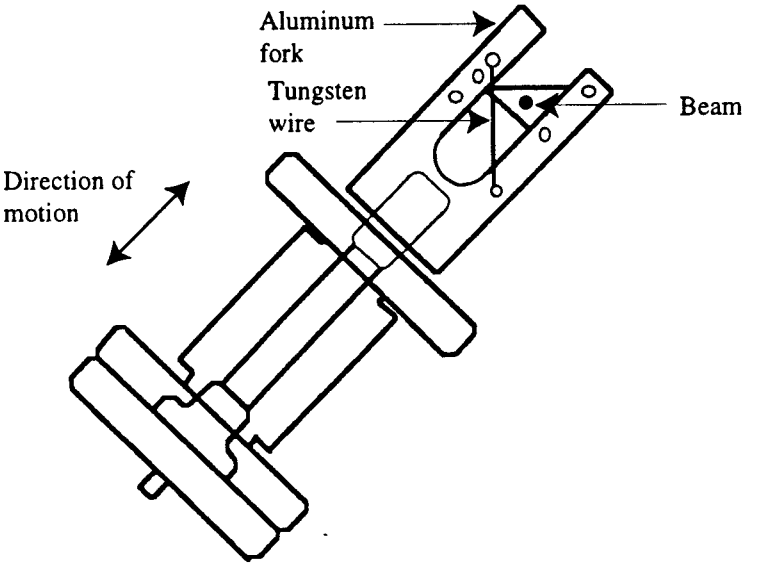

Figure 3.5.1. The SLC wire scanner support card. The fork is stepped across the beam and the wires measure the x, y, and u beam size [M.C. Ross, 1991].

y, and u (45 degrees to x and y). The wire is moved through the beam by a stepping motor with 200 steps where the step size can be varied (typical numbers are between 10-50 μm).

When the wire scans through the beam, low energy electrons are emitted at all angles. The ones emitted at 90 degrees are detected. A 125 μm thick stainless steel window positioned opposite the wire allows scattered electrons to exit the vacuum chamber. The radiation emitted from the wire is proportional to the amount of beam striking the wire and this gives a good signal to measure the transverse size of the beam. A photomultiplier located 30 cm from the wire amplifies this signal. Shielding is used to protect the PMT from beam losses upstream due to collimators and upstream wire scanners. In some cases fast ion chambers were installed downstream of the wire scanner to eliminate some of the background signal [D. McCormick, 1991].

The size of the wire contributes to the transverse measurement size of the beam. The rms wire size can be subtracted in quadrature to give the measured size [M.C. Ross, 1991]

$$\sigma_{xbeam} = \sqrt{\sigma^2_{xmeasured} - \sigma^2_{xwire}}$$

where the rms for a wire of radius a is given by $\sigma_{xwire} = a/2$.

Measurements

In this dissertation, wire scanners located in two different areas of the SLC are used to measure the transverse size of the beam, one at the exit from the north damping ring (the compressor line), and the other at the end of the linac.

In the compressor line, the energy spread of the beam is derived from measuring the transverse size of the beam in a high dispersion region with the compressor turned off. The energy spread is given by

$$\frac{\sigma_E}{E} = \frac{1}{\eta_x}\sqrt{{\sigma_{xwire}}^2 - \beta_x \varepsilon_x}$$

where σ_{xwire} is the transverse size of the beam measured by the wire, η_x is the dispersion, β_x is the betatron function at the location of the wire scanner, and ε_x is the emittance.

At the end of the linac, the transverse shape of the beam might not be Gaussian, so the full width half maximum (FWHM) divided by 2.345 can be used in place of σ_{xwire}.

The longitudinal bunch distribution can also be measured in the bunch compressor transport line with wire scanners. The RF accelerating section of the bunch compressor gives the bunch a correlated energy spread such that the energy spread at the wire is given by

$$\sigma_{xwire} \approx \eta_x \left(\frac{\Delta E}{E} \right) \tag{3.5.1}$$

where the contribution from the emittance is neglected due to the large energy spread from the bunch compressor RF. The energy deviation can be written as

$$\Delta E = V_{rf} \sin\left(\frac{2\pi z}{\lambda_{rf}} \right) \approx \left(\frac{2\pi z}{\lambda_{rf}} \right) V_{rf} \tag{3.5.2}$$

where the approximation is valid because the bunch is centered on the zero crossing of the RF wave and that allows the sine function to be approximated with its small angle approximation. Substituting equation 3.5.2 into 3.5.1 gives the bunch length as a function of the transverse size of the beam

$$\sigma_{xwire} = \frac{2\pi V_{rf} \eta_x \sigma_z}{E \lambda_{rf}}. \tag{3.5.3}$$

The problem with equation 3.5.3 is that the distribution is distorted by the nonlinearity of the compressor RF accelerating wave. To account for this distortion, the connection between the longitudinal position in the bunch z and the transverse position on the wire x is [K. Bane, 1989]

$$x - x_0 = \frac{\eta_x e V_{rf}}{E} \sin\left[\frac{2\pi}{\lambda_{rf}} (z - z_0) \right]$$

where x_0 is the position of the wire which corresponds to the zero crossing of the compressor RF z_0. The longitudinal charge distribution $\rho_l(z)$ can be determined from the transverse charge distribution $\rho_t(x)$ from

$$\rho_l(z) = \rho_t(x) \left| \frac{dx}{dz} \right|.$$

The longitudinal charge distribution can be written to include the nonlinearity of the RF accelerating wave as

$$\rho_l(z) = \rho_t(x) \frac{2\pi}{\lambda_{rf}} \sqrt{\left(\frac{\eta_x e V_{rf}}{E} \right)^2 - (x - x_0)^2}. \tag{3.5.4}$$

The expression of the longitudinal charge distribution $\rho_l(z)$ can be fit to an asymmetric Gaussian distribution to determine the bunch length.

A possible systematic error associated with wire scanner measurements is beam movement at the location of the wire. The measurement of the beam size is taken over many beam pulses and if the beam is moving transversely the measurement is incorrect. Correcting this problem is rather difficult because the beam movement can be smaller than the resolution of the beam position monitors so that a correction for this error is difficult. The minimum pulse to pulse beam movement observed by beam position monitors in the compressor line is $50\ \mu m$ with a rms of $15\ \mu m$. The rms can be used as an upper limit on the systematic error and can be subtracted in quadrature to give the correct transverse beam size.

Wire Parameters

NRTL Wire Scanner 364

Wire diameter	120 μm
Step size	Variable
Dispersion η_x	-0.5667 m
Betatron function β_x	5.4121 m
Emittance $\gamma\varepsilon_x$ (Typical)	$3x10^{-5}$ m · rad
Wire scan planes	x and y
Wire speed	Variable

Beam Switch Yard Wire CA11 62

Wire diameter	75 μm
Step size	Variable
Dispersion η_x	-0.0173 m
Betatron function β_x	2.2 m
Emittance $\gamma\varepsilon_x$ (Typical)	$4x10^{-5}$ m · rad
Beam energy	46.6 GeV
Wire scan planes	x, y, and u
Wire speed	variable

3.6 Measurement of the Resistive Impedance and Synchronous Phase in the Damping Ring

Introduction

As described in chapter 2 section 3, the circulating beam induces a wall image current that acts back on the beam and leads to an energy loss due to the resistive impedance of the vacuum chamber. This energy loss is called the parasitic mode energy loss, and the main source is the vacuum chamber components and RF accelerating cavities. The method of measuring the resistive impedance and the synchronous phase from the bunch distributions in the damping ring is described in this section.

Theory

The shape of the longitudinal bunch distribution in the damping ring changes as the intensity increases due to potential well distortion. In principle, measuring the distribution as a function of current, the resistive and reactive impedance can be determined. In practice determining both terms of the impedance is difficult if not impossible. In the SLC damping rings, it can be assumed that the reactive impedance is small in comparison to the resistive impedance. The resistive impedance is constant as a function of current and can be used to determine the parasitic energy loss and synchronous phase in the damping rings. The synchronous phase can be calculated from the measured bunch distribution in the damping ring as a function of current in the following manner:

1) Fitting the measured bunch distributions to the function given by equation 2.3.10 to determine the resistive impedance.

2) Integrating over the bunch distribution gives the parasitic energy loss given by (equation 2.3.12)

$$\Delta u = R \int_{-\infty}^{\infty} I^2(\tau) d\tau$$

where the current is given by $I(\tau) = \frac{qN}{\sqrt{2\pi}\sigma_\tau} \exp\left(-\frac{(\tau - c)^2}{2[1 + sgn(\tau - c)E]^2 D^2} \right)$.

3) The synchronous phase can be determined by the RF accelerating voltage and the synchrotron radiation energy loss and is given by

$$\varphi_s = \cos^{-1}\left(\frac{U_0 + \Delta u}{eV_{rf}}\right)$$

where U_0 is the synchrotron energy loss. The synchronous phase of function of current can now be plotted and compared to the measurement described below.

The synchronous phase as a function of beam current is measured by comparing the shift in phase at which the beam passes a fixed location in the ring (using a beam position monitor) with the RF accelerating cavity signal on a vector voltmeter. A set-up of the experiment is shown in figure 3.6.1.

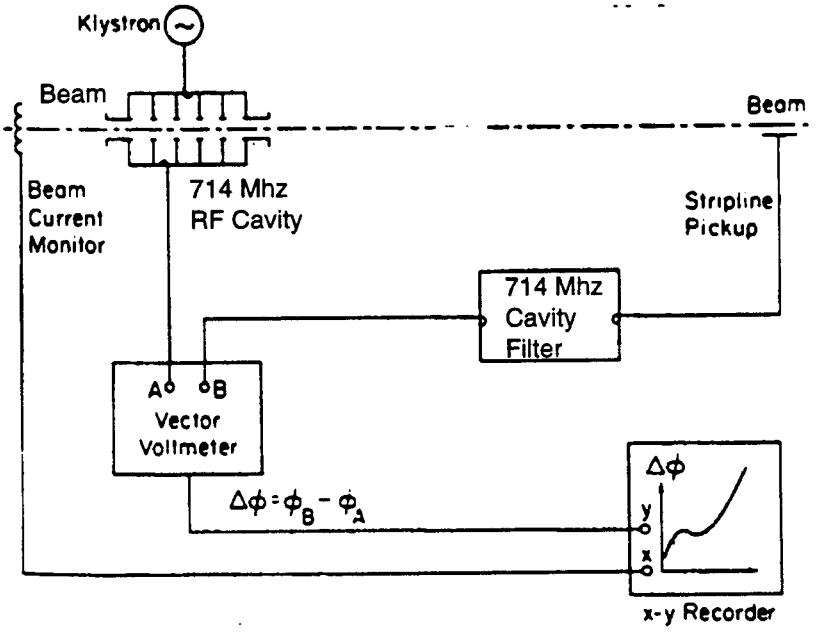

Figure 3.6.1. A schematic of the instrument used to measure the synchronous phase of the damping ring [M.A. Allen, 1975].

The signal from the beam position monitor is put through a 714 MHz transmission cavity. This cavity has a Q of 4400 which converts the beam signal to a sine wave signal which allows the phase difference between the beam and the RF cavity to be compared. The beam current monitor is also used to register the current.

The measurement was carried out by storing the beam in the damping ring and measuring the vector voltmeter signal as a function of current for a fixed RF accelerating voltage setting. The total voltage in the damping ring cavities comes from two different sources, the generator voltage and a beam induced voltage. The best way to represent these

two voltages in the cavity is by a phasor diagram in figure 3.6.2. The voltage induced by the beam is represented by the phasor $\vec{V}_b$ and the cavity and generator voltages are $\vec{V}_c$ and $\vec{V}_g$ respectively. The cavity voltage is the vector sum, $\vec{V}_c = \vec{V}_b + \vec{V}_g$, of the beam and generator voltage, and it needs to be regulated to make sure it is not affected by the voltage induced by the beam. During the measurement the cavity feedback loop is turned on. This feedback loop adjusts the generator voltage so that the cavity voltage is constant. This loop eliminates beam loading from affecting the synchronous phase measurement by keeping the cavity voltage V_c constant.

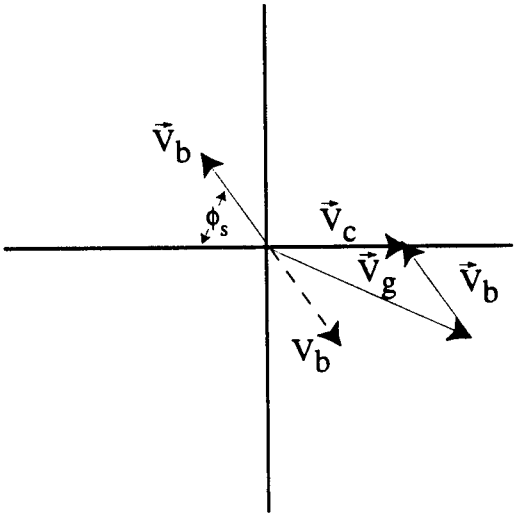

Figure 3.6.2. A phasor diagram of the voltages in the damping ring cavities. The dashed line shows the direction of the actual beam voltage. The beam voltage is measured at the synchronous phase ϕ_s from the crest of the RF voltage.

3.7 Method of Data Analysis

Introduction

The data acquired by the streak camera and wire scanners are analyzed in different ways depending on the location of the apparatus and the type of fit to the data required. In this section the analysis of the data will be discussed.

Streak Camera

The streak camera takes images of the bunch distribution which are 512 by 512 pixels in size. A selected area can be chosen such that the vertical columns in that area are projected on the horizontal axis. This creates a profile which can be fit to a function which characterizes the length of the bunch. Figure 3.7.1b is a profile of the selected area in figure 3.7.1a together with a fit to a Gaussian distribution.

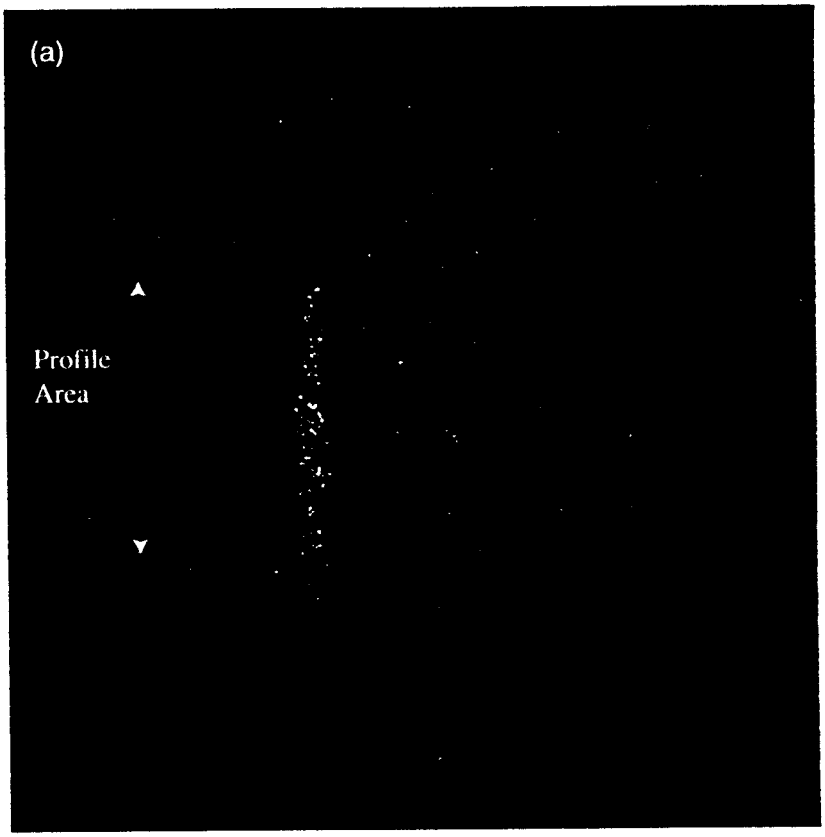

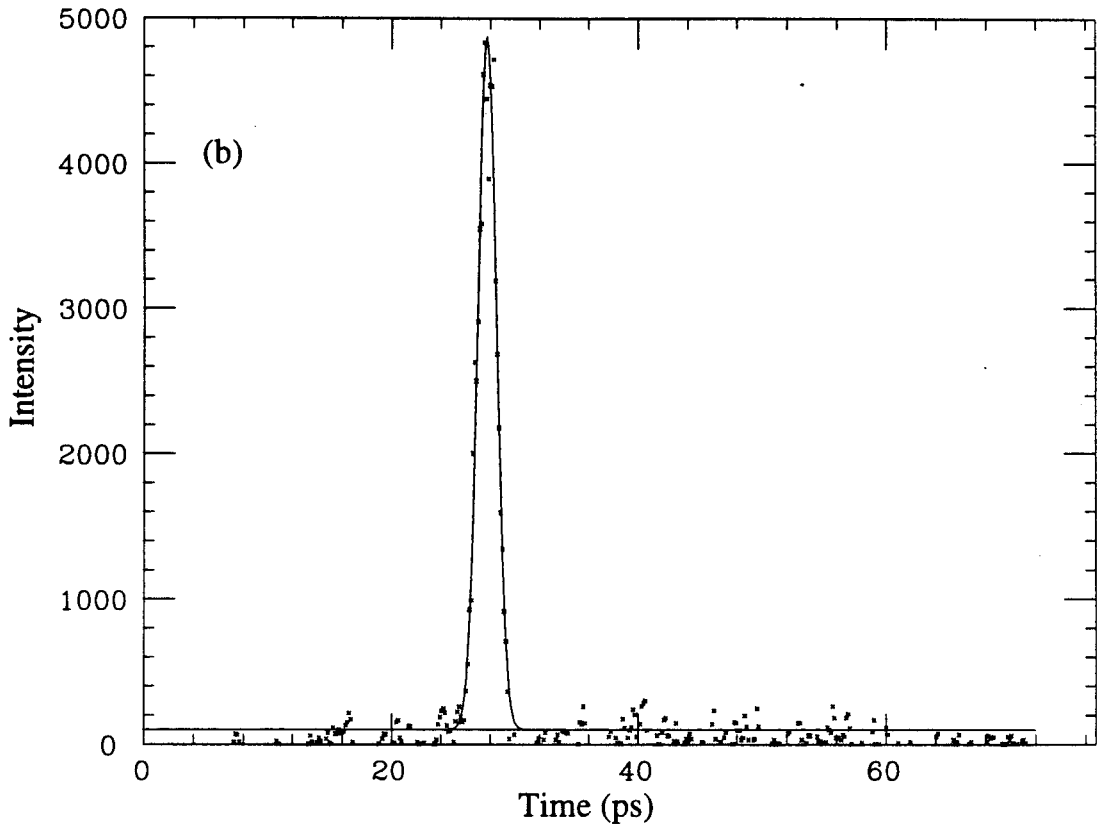

Figure 3.7.1. (a) A streak camera image. The horizontal lines mark the location where the vertical columns are summed. (b) A profile of the summed vertical columns.

The longitudinal profile of the beam distribution in the damping ring and at the end of the linac have different shapes and so the function that the profile is fit to differs. In both cases the function is χ^2 minimized using the minimization package Minuit [F. James, 1975].

(i) Damping rings

As discussed in chapter 2 section 3 the bunch distribution in the damping ring deviates from a pure Gaussian distribution due to potential well distortion. The function used to characterize the bunch shape is an asymmetric Gaussian distribution. The longitudinal profiles of the beam distribution are fitted to an asymmetric Gaussian function with a constant background given by

$$I(z) = I_0 + I_1 \exp\left\{-\frac{1}{2}\left(\frac{(z-\bar{z})}{(1+sgn(z-\bar{z})A)\sigma}\right)^2\right\} \qquad (3.7.1)$$

where I_0=pedestal, I_1=peak of the asymmetric Gaussian. The term $sgn(z-\bar{z})A$ is the asymmetry factor that parameterized the shape of the asymmetric Gaussian. A χ^2 minimization was performed on each streak camera picture

$$\chi^2 = \sum_i^n \frac{\left[I(z_i; A, I_0, I_1, \bar{z}, \sigma) - x_i\right]^2}{x_i}$$

where x_i is the digitized signal from the streak camera profile. The fit will return the mean $\bar{z}$, asymmetry factor A, background level I_0, and width σ of the distribution.

(ii) Linac

The bunch distribution in the linac depends on the initial conditions of the beam exiting the damping ring and the degree of compression in the ring to linac transport line. If the bunch is fully compressed it appears to be Gaussian in shape otherwise it has a much different shape. There are two methods used to characterize the bunch length, they are the root mean square (rms) width and the 10-90% width. To determine the rms width the mean and σ of the projections are estimated by χ^2 fitting the entire profile to an asymmetric Gaussian function (equation 3.7.1) and then making a cut about the mean of the distribution to eliminate background signal from effecting the measurement. The rms width is determined by calculating

$$\sigma_z = \sqrt{\frac{\sum_i^N (z_i - \bar{z})^2 I(z_i)}{\sum_i^N I(z_i)}}$$

where N is the number of CCD pixels within $\pm 3\sigma$ of the mean $\bar{z}$, z_i is the location of the pixel, and $I(z_i)$ is the projection height.

The 10-90% bunch width is measured by first fitting the distribution to a asymmetric Gaussian distribution with a straight line background (figure 3.7.2a). Each bin is then normalized

$$\mathrm{Bin}(t_j) = \frac{\left(y_j - Background\right)}{\sum_{i=1}^{N} \left(y_i - Background\right)} \qquad (3.72)$$

where N is the total number of bins (figure 3.7.2b). The width from 10% to 90% (80% of the beam) is calculated from

$$Width = t(bin = 0.90) - t(bin = 0.10)$$

The 10-90% width is then resolution corrected width by subtracting the width (wire width=1.3 times the wire size) in quadrature from the measured width.

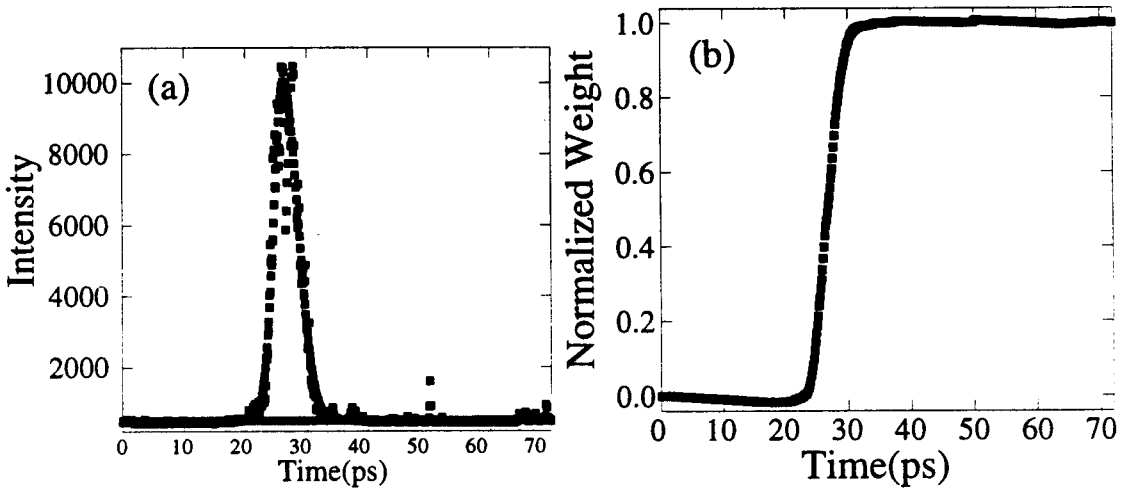

Figure 3.7.2. (a) A streak camera profile for a full compressed bunch (36MV) fit to a asymmetric Gaussian distribution with the background subtraction. (b) The normalized bin profile for the fully compressed distribution.

Wire Scanners

The wire scans the beam in discrete steps, and the signal from a photomultiplier tube or fast ion chamber is plotted as a function of step location. The signal is χ^2 fit to a function to determine the transverse beam size. Two different wire scanners were used; one in the RTL (ring to linac transport line) and the second in the BSY (Beam switch yard).

(i) RTL

The energy spread of the beam in the damping ring is measured by extracting the beam with the compressor off and measuring the transverse size of the beam. The beam size is fit to a Gaussian function, and the energy spread can be determined from the fit. Figure 3.7.3a is a typical measurement of the energy spread.

With the compressor turned on the bunch length can be measured using the same wire. The beam size is fit to an asymmetric Gaussian function, but to get the true bunch

distribution it needs to be unfolded from the compressor RF wave which requires using equation 3.5.1. Figure 3.7.3b is a typical measurement of the bunch distribution.

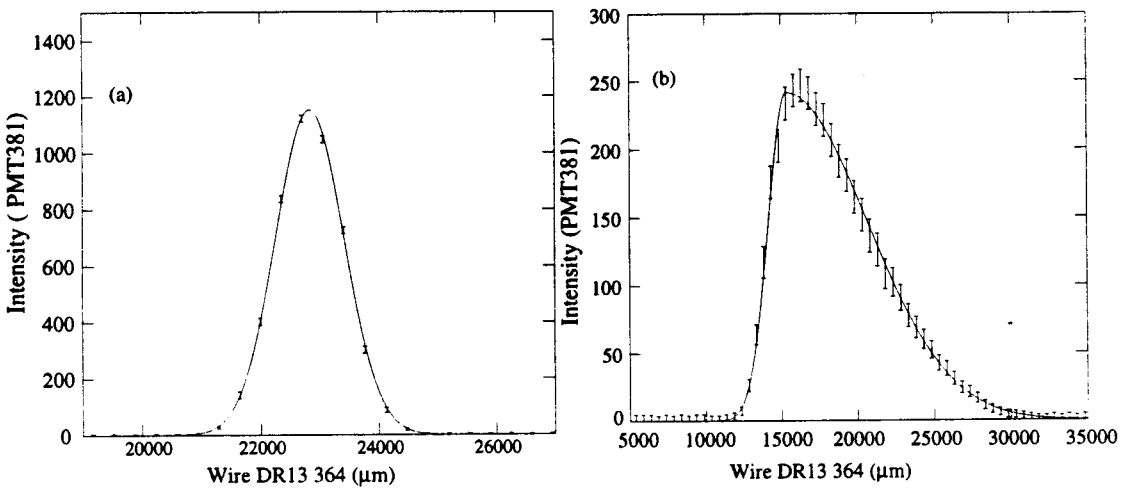

Figure 3.7.3. (a) Transverse measurement of the beam fit to a Gaussian distribution. The current of the beam is $3.5\text{x}10^{10}$ particles per bunch and $\sigma = 580\mu\text{m}$. (b) Transverse measurement of the beam fit to an asymmetric Gaussian distribution. The beam current for the figure is $3.8\text{x}10^{10}$ particles per bunch and the compressor voltage was 22 MV.

(ii) BSY

The wire scanner in the beam switch yard, unlike the scanner in the RTL, uses a fast ion chamber detector. Once again the transverse size of the beam is measured, however, the beam distribution is dependent upon parameters such as the compressor

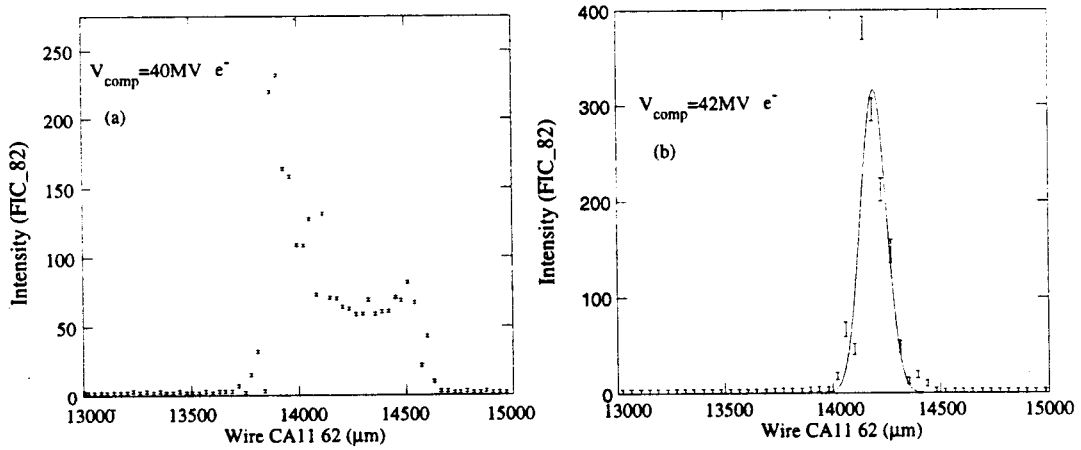

Figure 3.7.4. A measurement of the transverse size of the beam when the compressor is set to (a) 40 MV and (b) 42 MV. The distribution is fit to a Gaussian in the figure (b).

amplitude and phasing of the klystrons which in some cases make it impossible to fit to a function (figure 3.7.4a). Two methods employed to characterize the energy spread are: 1) Calculate the rms of the distribution, and 2) the 10-90% width The results will be presented in chapter 4.

The rms width is determined by calculating

$$\sigma_x = \sqrt{\frac{\sum_i^N (x_i - \bar{x})^2 h(x_i)}{\sum_i^N h(x_i)}}$$

where N is the number of wire steps, $\bar{x}$ is the location of the mean, x_i is the location of the wire, and $h(z_i)$ is the projection height. The cuts on the distribution are made to eliminate background from affecting the measurement.

The 10-90% energy width is calculated by fitting the horizontal beam sizes to a Gaussian distribution with a linear background to determine the background level. Subtracting the background and normalizing the distribution (equation 3.7.2), as in figures 3.7.5 a and b, the 10-90% horizontal bunch width can be determined.

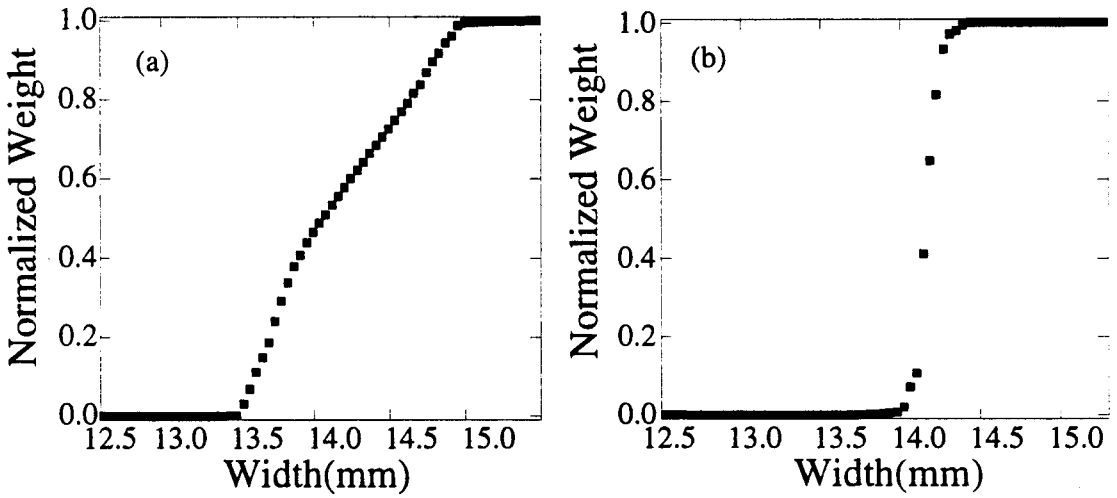

Figure 3.7.5. The normalized horizontal bunch width for the electron beam for a compressor setting of (a) 36MV (b) 42MV.

Chapter 4. Results

4.1 Damping Ring Results

Introduction

In this section the measurements of the longitudinal properties of the bunch in the damping ring will be described in direct sequence of production of a damped bunch starting with the injection into the damping ring through to extraction. The measurements were made during the 1994-1995 high current physics run on the SLC and were done when accelerator physics time was available. The results of the measurements of the resistive impedance and synchronous phase will also be presented.

Preface for Streak Camera Measurements

A table is included for each section where the streak camera was used. The table lists all necessary operating conditions of the camera and the damping ring during the measurement. The interference filters used in the measurement were centered at 500 nm and had a full width at half maximum (FWHM) acceptence of 40 nm or 10 nm (denoted by filter acceptance in the table by 40 or 10 nm). The number n which describes the neutral density filter setting refers to the amount of light transmitted and follows the equation

$$T = 10^{-n}$$

where T is the transmittance.

Injection

The longitudinal dynamics measurements begin with the electron or positron bunch being injected into the damping ring. The measurement of the longitudinal phase space of these injected bunches is presented in this section. The precision of the measurements does not reflect the day to day variations in longitudinal phase space, but it reflects the fluctuation of this single snap shot measurement.

The energy spread of the electron or positron beam entering the damping ring is measured with a wire scanner located in the linac to ring (LTR) transport line. The

horizontal beam size is measured with the wire in a high dispersion region (figures 4.1.1a and b), and the energy spread is calculated from the relation

$$\frac{\Delta E}{E} = \frac{1}{\eta_x}\sqrt{\sigma_x^2 - \beta_x \varepsilon_x} \qquad (4.1.1)$$

where the design optics parameters $\beta_x = 16.40\text{m}$ and $\eta_x = 0.6067\text{m}$ are used and the emittance ε_x is measured with a set of wires upstream of the energy spread wire scanners in a zero dispersion region. The energy spread at the location of measurement is large which makes the emittance contribution negligible. The current during the measurement was $I = 4.75\text{x}10^{10}$ particles per bunch for electrons and $I = 2.2\text{x}10^{10}$ particles per bunch for positrons.

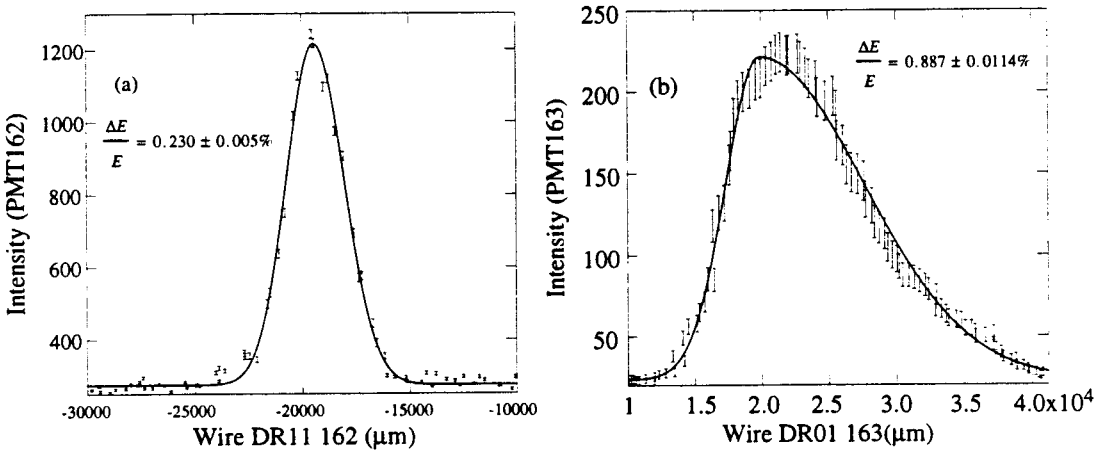

Figure 4.1.1. The (a) electron and (b)positron horizontal beam sizes measured with a wire scanner and fit to an asymmetric Gaussian distribution.

The initial energy spread for the electron or positron bunches is due to different methods of production. Electron production is by an electron gun after which the bunch travels through the pre-linac to the damping ring. The energy spread of the electron bunch is determined by its bunch length and the phasing of the bunch on the RF accelerating wave in the pre-linac. Positrons are produced by slamming a high energy electron bunch into a tungsten target. After the target, the positrons are collected, accelerated, and transported, through two trombones, back to the damping ring. The longitudinal phase space of the positrons after the tungsten target is quite large. Since there is no cooling mechanism, the energy spread of the positron bunch is large.

The injected bunch distribution was measured using the streak camera in the following manner. The streak camera needed to be triggered on the first turn of the damping ring store. When the beam image has been established with the camera, the first

turn is obtained by adjusting the streak camera trigger backwards by one revolution period until the image no longer appears then the first turn is located by moving the trigger forward one revolution to the first turn. The first turn can be verified by triggering a scope with the streak camera trigger and comparing it with a beam induced signal (from a BPM) which shows injection into the ring.

The measurement was made by taking twenty five streak camera profiles and fitting them to an asymmetric Gaussian distribution. The rms width of the profiles is histogramed in figure 4.1.2a and the conditions of the measurement are listed in table 4.1.1. The sum of the twenty five profiles where the means of the profiles are shifted to a common origin is shown in figure 4.1.2b.

The numbers quoted in the histogram have not been corrected for the resolution of the streak camera. The resolution corrected injected bunch length for the positron beam at a current of $I = 3.65\text{x}10^{10}$ is

$$\sigma_t = 8.04 \pm 0.09\,\text{psec.}$$

The first turn bunch distribution measurement was made only with the positron bunch. The injected electron bunch distribution was measured and displayed a peculiar behavior due to the gun and linac not being properly set up for the measurement.

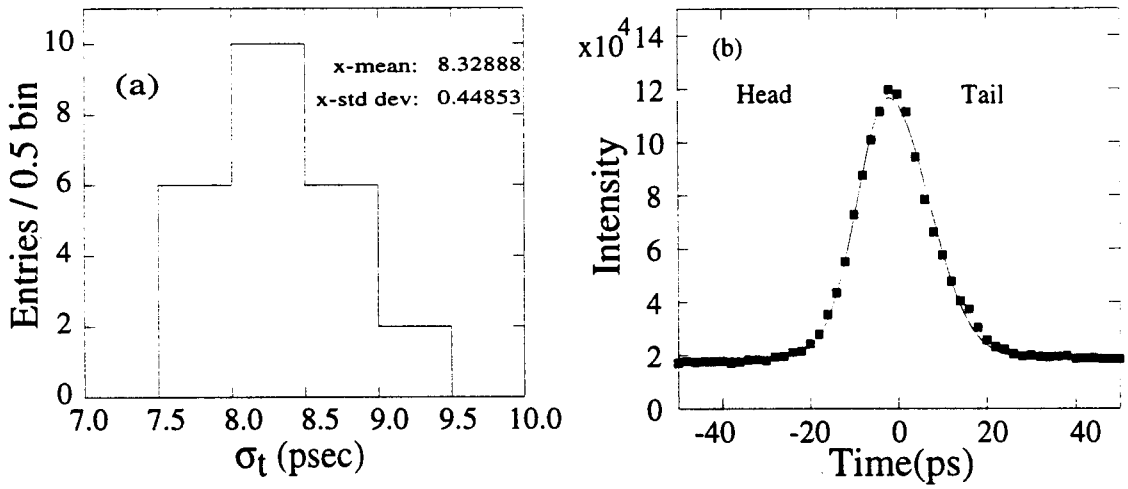

Figure 4.1.2. (a) A histogram of the 25 streak camera measurements of the bunch length of the beam injected in the south damping ring (positrons). (b) The bunch distribution of the injected positron bunch fit to an asymmetric Gaussian distribution.

In conclusion, the initial energy spread of the beam, when compared to the extracted beam, is large. This large energy spread, along with injection mismatches, leads to large fluctuations (filamentation) in the bunch length. Operationally, the large

fluctuations in the bunch length do not appear to affect the operation of the damping ring as long as injection into the rings RF bucket has been optimized.

Slit size (μm)	100
Density filter	0.44
Interference filter FWHM	40 nm
Damping ring RF Voltage (KV)	801
Current per bunch ($x10^{10}$)	3.65

Table 4.1.1. The damping ring and streak camera parameters for the injection measurements.

Single Particle Motion

A number of beam properties depend upon single particle motion in the damping ring. They are 1) synchrotron period, 2) filamentation of the longitudinal phase space, 3) longitudinal damping time, and 4) dependence of the bunch length on the RF gap voltage. In the next few sections I will present the single particle measurements with the streak camera.

The longitudinal equation of motion for a single particle dynamics in the damping ring is

$$\frac{d^2\tau}{dt^2} + 2\alpha_E \frac{d\tau}{dt} + \frac{\omega_s^2}{\omega_{RF}} \sin(\omega_{RF}\tau) = \frac{U_0 \alpha}{E_0 T_0} \qquad (4.1.2)$$

where all the terms are described in chapter 2 section 1. In the following sections, approximations to equation 4.1.2 in the regimes of interest are made to describe single particle motion in the damping ring.

(i) Synchrotron Motion

Just after injection into the damping ring, the differential equation (4.1.2) can be approximated as a harmonic oscillator given by

$$\frac{d^2\tau}{dt^2} + \omega_s^2 \tau = 0$$

$$\tau(t) = \tau_a \cos(\omega_s t + \varphi).$$

The above approximation is valid because the time range of interest is short compared to the damping time. The above equation describes the motion as rotation in longitudinal phase space at the synchrotron frequency.

The first measurement made with the streak camera was the synchrotron period. The streak camera was used to measure the bunch length oscillation by taking bunch profiles starting with the injected bunch. The bunch profiles are fit to an asymmetric Gaussian distribution. The condition of the streak camera and damping ring during the measurement are listed in table 4.1.3. The measurement consists of measuring the bunch length three times every tenth turn (1.17 μsec) starting from injection. Because the bunch length varies between 20 and 80 psec the light intensity entering the camera was adjusted using neutral density filters to reduce space charge effects on the camera photocathode. The mean bunch length and standard deviation are plotted as a function of store time as shown in figure 4.1.3. The data is then fit using χ^2 minimization to the curve

$$\sigma(t) = \sigma_0 + B\sin\left(\frac{4\pi t}{T_s} + \phi_0\right) \tag{4.1.3}$$

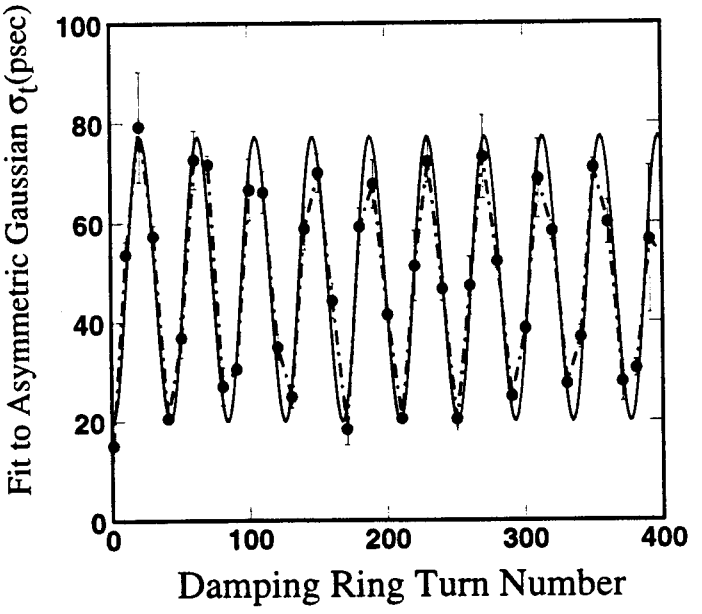

Figure 4.1.3. A plot of the mean bunch length as a function of damping ring turn number in the south damping ring. The solid line is the fit to the data. The dot-dash line is a connection of all the data points.

to determine the synchrotron period . The synchrotron period T_s is a fitting parameter as well as the amplitude B, phase ϕ_0, and offset σ_0. The fit parameters are shown in table 4.1.2.

B	28.7 ± 0.4 psec
ϕ_0	4.606 ± 0.019 radians
σ_0	48.6 ± 0.4 psec
T_s	9.835 ± 0.012 μsec

Table 4.1.2. The fitted parameters in equation 4.1.3.

The measured synchrotron period is $T_{s,meas} = 9.835 \pm 0.012\,\mu\text{sec}$ which is in good agreement with the calculated value of $T_{s,calc} = 9.834\,\mu\text{sec}$ (chapter 2 section 1). A more accurate measurement of the synchrotron period is made with a spectrum analyzer, but using the streak camera serves as a check on its usefulness in measuring the bunch length in the damping ring.

Slit size (μm)	200
Density filter	Variable 0.1-0.44
Interference filter FWHM	40nm
Damping ring RF Voltage (KV)	800
Current per bunch (x10^{10})	2.5

Table 4.1.3. The damping ring and streak camera parameters for the synchrotron period measurement.

(ii) Filamentation

The differential equation in the regime just after injection which includes the nonlinearity due to the RF wave form is

$$\frac{d^2\tau}{dt^2} + \frac{\omega_s^2}{\omega_{RF}} \sin(\omega_{RF}\tau) = 0$$

where the damping term is ignored because the time of interest is short compared to the damping time. The approximate solution to the nonlinear differential equation is [R. Siemann, 1989]

$$\tau(t) = \tau_a \cos\left((\omega_s + \Delta\omega_s(\tau_a))t + \varphi\right)$$

$$\text{where } \Delta\omega_s(\tau_a) = \frac{-\omega_s}{2}\left[1 - \frac{2J_1(\omega_{RF}\tau_a)}{\omega_{RF}\tau_a}\right].$$

The amplitude dependence of the synchrotron frequency will cause the beam to filament in phase space.

The measurement of filamentation was conducted by measuring the bunch length with the streak camera every 10 turns starting at turn 2101 (approximately 0.25 msec after injection), turn 3101, and turn 4101 for 100 turns. The results of fitting the data are shown in figures 4.1.4 a-c and the conditions of the measurement are listed in table 4.1.4. There are two interesting conclusions that can be inferred from these results: 1) The oscillation in the bunch length decreases as a function of store time (this is a signature of filamentation);

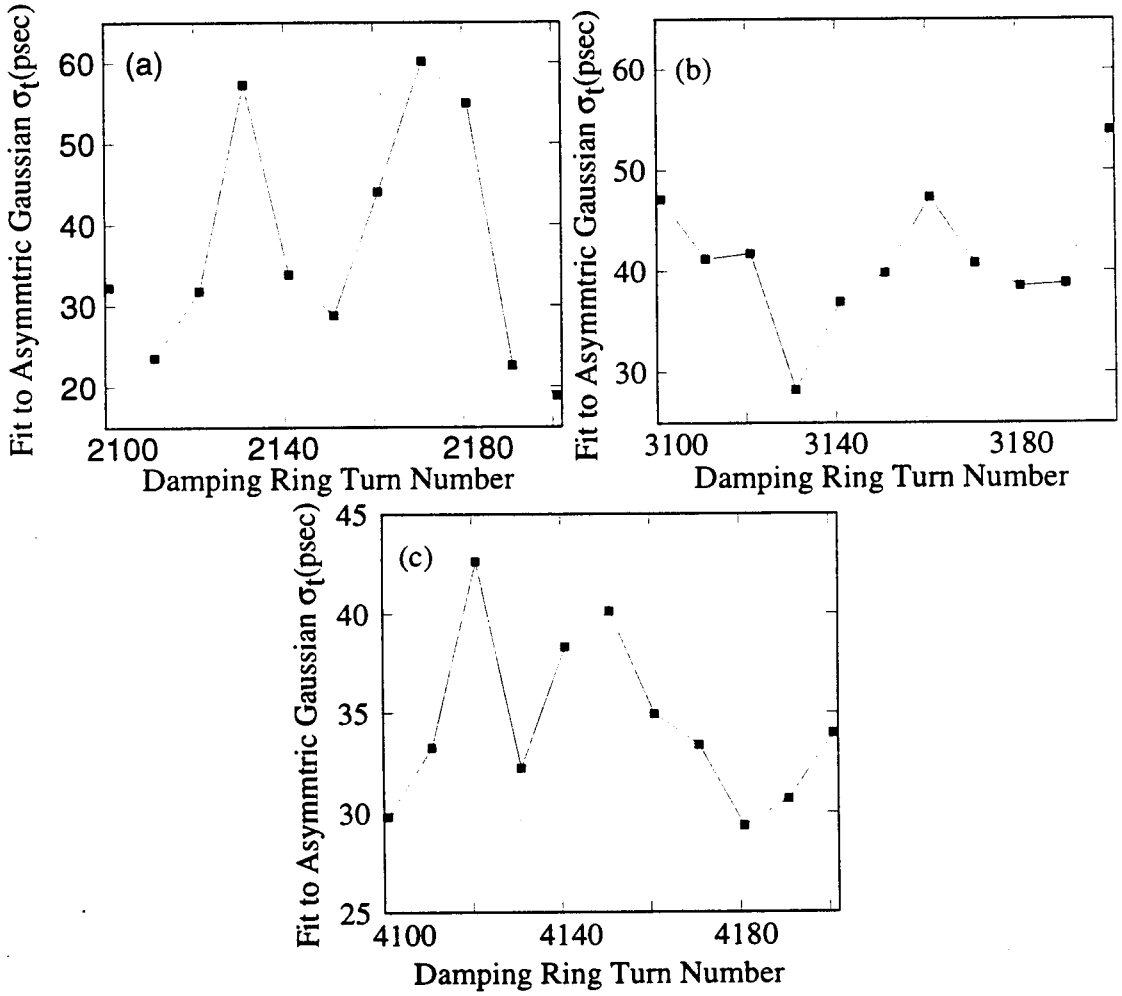

Figure 4.1.4. The bunch length as a function of turn number in the positron damping ring starting at turn (a) 2101, (b) 3101, and (c) 4101.

2) the average bunch length decreases as a function of store time which is caused by longitudinal damping. But the overall result is that filamentation is difficult to see from the data which points out one of the shortcomings of the streak camera, in that the streak camera takes a single shot of one pulse injected into the ring, it cannot track the pulse turn by turn. As a result, small variations in the damping ring, such as RF power, and operators optimizing injection affect the measurement.

Slit size (μm)	150
Density filter	Variable
Interference filter FWHM	40 nm
Damping ring RF Voltage (KV)	805
Current per bunch (x10^{10})	3.55

Table 4.1.4. The damping ring and streak camera parameters for the filamentation measurement.

(iii) Damping

When the longitudinal phase space has been fully filamented the process of radiation damping of the longitudinal emittance can be measured. The differential equation in this regime is given by:

$$\frac{d^2\tau}{dt^2} + 2\alpha_E \frac{d\tau}{dt} + \omega_s^2 \tau = 0,$$

and the solution is a damped harmonic oscillator which is given by

$$\tau(t) = \tau_a \exp[-\alpha_E t]\cos\left(\sqrt{\omega_s^2 - \alpha_E^2}\, t + \varphi\right).$$

The bunch length will reach its equilibrium size when the process of radiation damping and quantum fluctuations are at equilibrium.

The bunch length versus time elapsed since injection can be used to measure the longitudinal damping time. The streak camera trigger was set at turn 5000 (~0.6 msec) into the store time, and ten bunch length measurements are made every 1000 turns until the longitudinal phase space has been fully damped at turn 38,000 (~4.5 msec). The damping ring longitudinal feedback, which locks the 714 MHz phase of the damping ring with the 2856 MHz phase of the linac, was turned off during the measurement. If the feedback

loop is turned on the bunch receives a longitudinal kick 1.2 msec into the store. The mean is plotted for each point, and the data are fit by χ^2 minimization to the curve (figure 4.1.5)

$$\sigma^2(t) = \sigma_{eq}{}^2 + \exp\left(-\frac{2t}{\tau_\delta}\right)\left(\sigma_{inj}{}^2 - \sigma_{eq}{}^2\right) \qquad (4.1.4)$$

where each point is weighted by the inverse of the square of the rms error. The fitting parameters are the damping time τ_δ, the injected bunch length σ_{inj}, and the equilibrium bunch length σ_{eq}. The theoretical longitudinal damping time is $\tau_\delta = 1.79\ msec$ and is in good agreement with the measured value. The fit values are listed in table 4.1.5 and the conditions of the measurement are listed in table 4.1.6.

σ_{inj}	41.74 ± 1.58 psec
σ_{eq}	19.10 ± 0.23 psec
τ_δ	1.87 ± 0.13 msec

Table 4.1.5. The fitted parameters from equation 4.1.4 fit to the data in figure 4.1.5.

Measuring the damping time sets a rough time limit on filamentation of the beam in longitudinal phase space. For the positron damping ring the bunch filaments for approximately 0.5 msec.

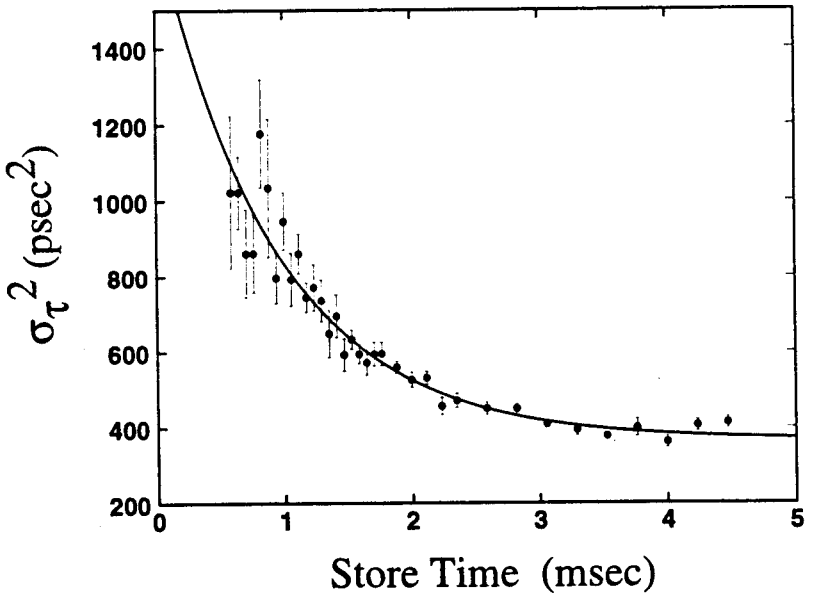

Figure 4.1.5. The bunch length as a function of store time. The curve is the fit to the data.

Slit size (μm)	150
Density filter	Variable
Interference filter FWHM	40 nm
Damping ring RF Voltage (KV)	800
Current per bunch ($x10^{10}$)	3.0

Table 4.1.6. The initial conditions for the injection measurements.

Combining the longitudinal damping time with its transverse counterparts provides a test of Robinson's partition theorem for the damping rings [K. Robinson 1958],

$$\frac{1}{\tau_x}+\frac{1}{\tau_y}+\frac{1}{\tau_z}=4\frac{\langle P_\gamma\rangle}{2E_0}.$$

The transverse damping time for the positron damping ring was measured with a gated camera [C. Simopoulos 1995]. As pointed out in table 4.1.7, the vertical damping time does not agree with the expected value, and as a result, Robinson's partition theorem does not hold for the positron damping ring. This means that the positron damping ring is either not modeled correctly, or the systematic errors associated with the transverse measurement are not fully understood. The systematic errors that should be studied in the future to explain the differences between the damping ring model and the measurements are: 1) The interaction between the two beams in the ring, 2) orbit changes in the ring, and 3) high vacuum chamber pressure in the damping ring.

Ring	τ_x msec	τ_y msec	τ_z msec
Electron	3.32 ± 0.28	4.11 ± 0.31	-
Positron	3.60 ± 0.15	4.17 ± 0.14	1.87 ± 0.13
Expected	3.52	3.56	1.79

Table 4.1.7. The results of the transverse and longitudinal damping time for the electron and positron damping rings.

(iv) Bunch Length versus RF Gap Voltage at Low Current

At low current collective behavior of the bunch is small, and as a result the equilibrium bunch length in a storage ring is inversely proportional to the square root of the RF accelerating gap voltage. At low current, the bunch length in the positron damping ring

was measured as a function of RF accelerating voltage. This was done by taking twenty-five streak camera pictures at RF voltages between 600 kV and 1 MV. The mean and root mean error were calculated at each RF voltage setting and plotted in figure 4.1.6 as well as the expected theoretical value. The condition of the streak camera and damping ring during the measurement are listed in table 4.1.8.

Fitting the data to the function $\sigma_z = A(V_{RF})^m$ gives a value of $m = -0.49 \pm 0.03$ which is in good agreement with the expected value. Ignoring collective effects of the beam, the theoretical bunch length is 5% larger then the measured bunch length. This 5% systematic offset in the bunch length is possibly due to an incorrect calibration of the sweep voltage for the streak camera and can be used as one limit on the size of that error.

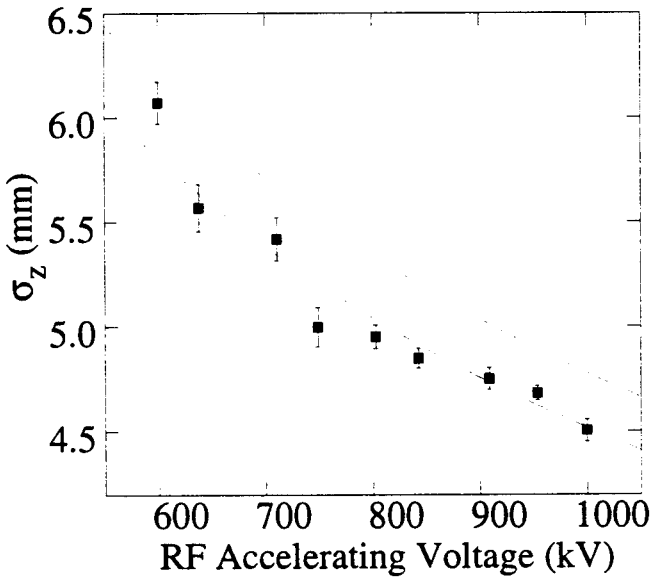

Figure 4.1.6. The bunch length as a function of RF accelerating voltage measured in the positron damping ring. The dot dash line is the theoretical bunch length.

Slit size (μm)	150
Density filter	Variable
Interference filter FWHM	40 nm
Damping ring RF Voltage (KV)	variable
Current per bunch ($x10^{10}$)	$0.6 \pm 0.1 x10^{10}$

Table 4.1.8. The conditions for the positron bunch length versus RF accelerating voltage at low current.

High Current Effects on Longitudinal Dynamics in the Damping Rings

In the following few sections the measurements on the damping ring which involve high current running will be presented. This includes: 1) the equilibrium bunch length at several times in the damping ring store, 2) the bunch length as a function of current, 3) the bunch length versus RF accelerating voltage at high current, and 4) the energy spread of the damping ring as a function of current.

(i) The Equilibrium Bunch length

After the longitudinal emittance has been fully damped the bunch length remains constant for the remainder of the store time in the damping ring. To verify this statement

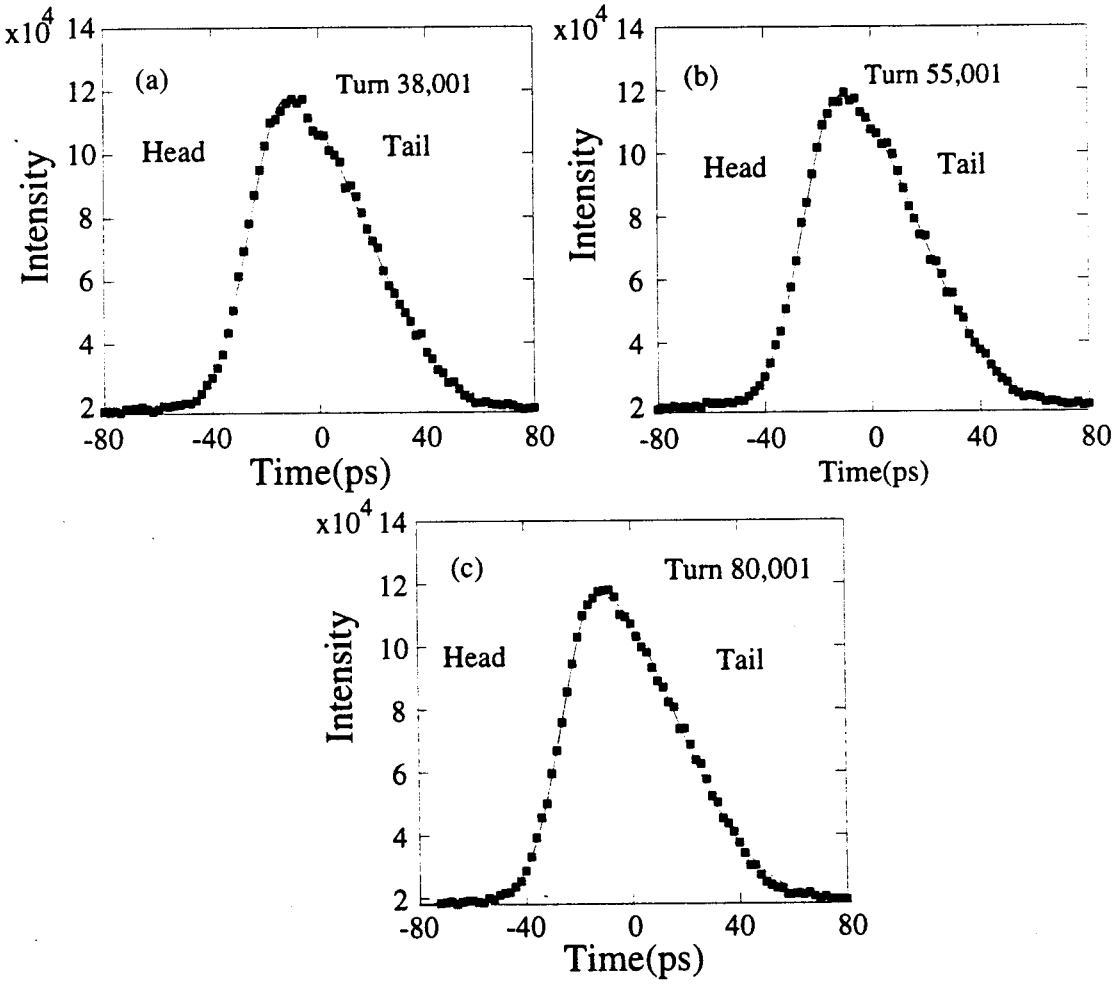

Figure 4.1.7. The sum of 25 streak camera profiles for turn: (a) 38,001, (b) 55,001, and (c) 80,001 in the positron damping ring.

the bunch length was measured at three different store times in the positron damping ring. Twenty-five streak camera profiles were taken at each trigger setting, and the profiles are fit to an asymmetric Gaussian distribution. Figure 4.1.6a-c is a plot of the bunch distributions at the various turn numbers. Table 4.1.9 lists the mean bunch length and asymmetry factor as well as the root mean error for each measurement, and table 4.1.10 denotes the condition of the streak camera and damping ring during the measurement.

The equilibrium bunch length measurement points out several interesting features. 1) No large (on the order of 1 mm or greater) bunch length instability is observed in the positron damping ring. 2) An upper limit on the bunch length growth during the damping ring store can be made from the data listed in table 4.1.9. The mean bunch length growth (or decay) is on the order of 0.1 mm with a rise or (fall time) on the order of 1 msec.

Time 4.5 msec	Turn 38,001	$\sigma_z = 6.43 \pm 0.06$ mm	$As = -0.363 \pm 0.016$
Time 6.5 msec	Turn 55,001	$\sigma_z = 6.33 \pm 0.06$ mm	$As = -0.355 \pm 0.018$
Time 9.5 msec	Turn 80,001	$\sigma_z = 6.39 \pm 0.08$ mm	$As = -0.375 \pm 0.018$

Table 4.1.9. The store time, bunch length, and asymmetry factor from the asymmetric Gaussian fit to the 25 streak camera profiles.

Slit size (μm)	150
Density filter	0.54
Interference filter FWHM	40 nm
Damping ring RF Voltage (KV)	830
Current per bunch ($x10^{10}$)	3.7

Table 4.1.10. The conditions for the equilibrium bunch length measurement.

(ii) Bunch Length as a Function of Current

The bunch distribution was measured as a function of current in both damping rings. In the electron damping ring, the measurement consisted of taking approximately 25 streak camera profiles at current settings between 0.63 to $3.83x10^{10}$ particles per bunch. The camera is triggered during the last 2 msec of the store time and so the equilibrium bunch distribution was measured. The bunch length and light intensity varies for each current setting so the neutral density filter setting also is varied to avoid saturation on the photocathode. The profiles are fit to an asymmetric Gaussian distribution. Three

distributions at different currents are shown in figures 4.1.8 a-c. Figure 4.1.9 a is a plot of the bunch length as a function of current. The data shows significant bunch lengthening due to potential well distortion. The asymmetry factor in the fitting function measures the departure from a Gaussian. Results are presented in figure 4.1.9b, and they exhibit a slight asymmetry at low current which increases steadily due to potential well distortion. Table 4.1.11 lists the results from the measurements, and table 4.1.12 lists the conditions of the measurement.

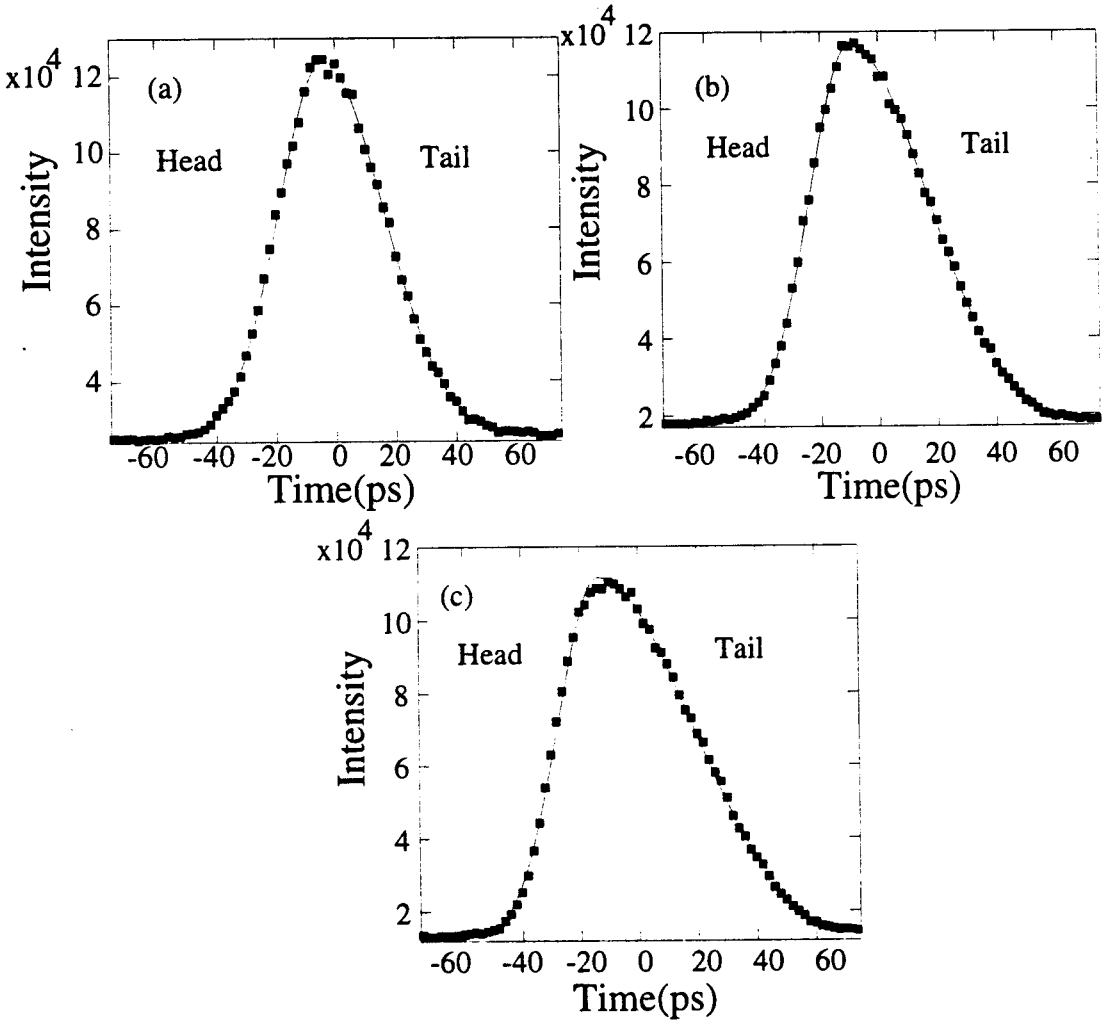

Figure 4.1.8. This plot is a sum of approximately 25 streak camera profiles of the electron bunch at three different currents of (a) 1.0×10^{10}, (b) 2.73×10^{10}, and (c) 3.83×10^{10} particles per bunch. The data are fit to an asymmetric Gaussian distribution.

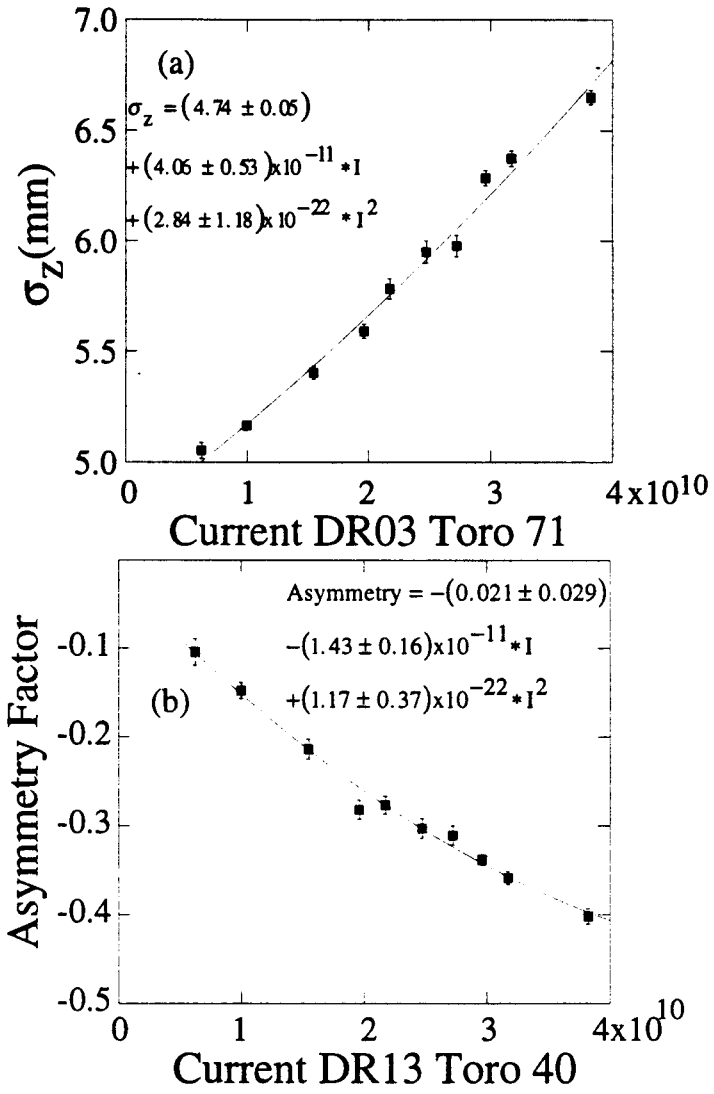

Figure 4.1.9. (a) The bunch length as a function of current in the electron damping ring. The data points are the mean bunch length and the rms error fit to a quadratic function. (b) The asymmetry factor as a function of current in the electron damping ring. The data points are the mean asymmetry factor and the rms error fit to a quadratic function.

Current ($\times10^{10}$)	σ_z(mm)	Asymmetry Factor
3.825 ± 0.150	6.650 ± 0.032	-0.402 ± 0.009
3.175 ± 0.150	6.376 ± 0.035	-0.359 ± 0.007
2.963 ± 0.125	6.287 ± 0.035	-0.338 ± 0.006
2.725 ± 0.100	5.978 ± 0.048	-0.311 ± 0.011
2.475 ± 0.150	5.951 ± 0.051	-0.303 ± 0.011
2.175 ± 0.150	5.783 ± 0.046	-0.276 ± 0.010

1.963 ± 0.125	5.591 ± 0.032	−0.282 ± 0.011
1.550 ± 0.100	5.404 ± 0.028	−0.214 ± 0.011
1.000 ± 0.100	5.165 ± 0.032	−0.148 ± 0.009
0.625 ± 0.050	5.052 ± 0.035	−0.104 ± 0.015

Table 4.1.11. The results from measuring the electron bunch length as a function of current.

Slit size (μm)	200
Density filter	Variable
Interference filter FWHM	40 nm
Damping ring RF Voltage (KV)	820
Current per bunch (x10^{10})	Variable

Table 4.1.12. The conditions for the electron bunch length versus current measurements.

The bunch length as a function of current was also measured for the positron damping ring under slightly different conditions (table 4.1.14). A plot of the summed distributions are shown in figure 4.1.10. The bunch length and asymmetry factor as a function of current is shown in figure 4.1.11 a and b. Table 4.1.13 lists the results of the measurements.

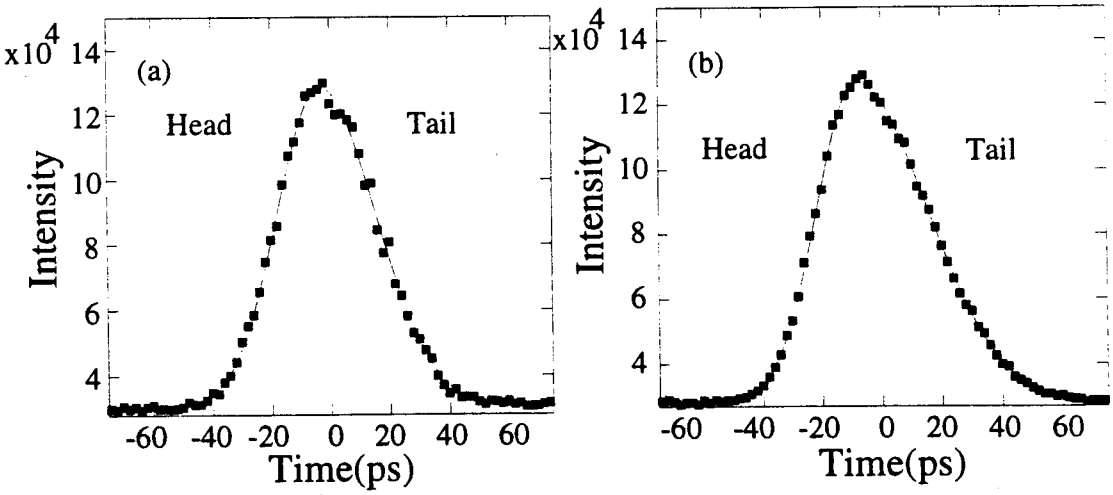

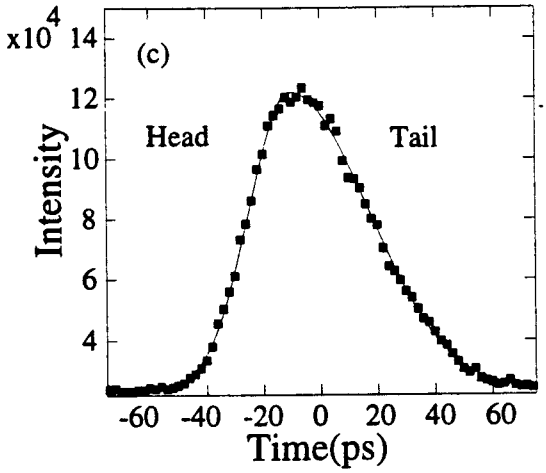

Figure 4.1.10. This plot is a sum of approximately 25 streak camera profiles of the positron bunch at three different currents of (a) $0.6\text{x}10^{10}$, (b) $2.3\text{x}10^{10}$, and (c) $3.3\text{x}10^{10}$ particles per bunch. The data is fit to an asymmetric Gaussian distribution.

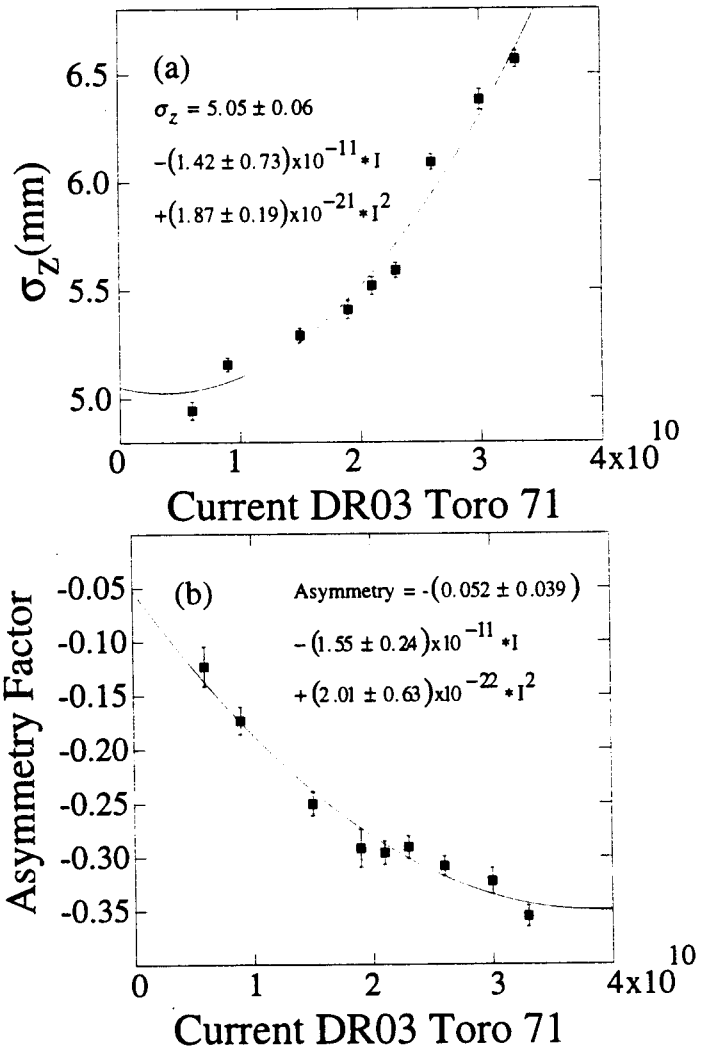

Figure 4.1.11. (a) The bunch length as a function of current in the positron damping ring. The data points are the mean bunch length and the rms error fit to a quadratic function. (b) The asymmetry factor as a function of current in the positron damping ring. The data points are the mean asymmetry factor and the rms error fit to a quadratic function.

Current ($x10^{10}$)	σ_z(mm)	Asymmetry Factor
3.300 ± 0.100	6.567 ± 0.039	-0.355 ± 0.010
3.000 ± 0.100	6.382 ± 0.048	-0.322 ± 0.012
2.600 ± 0.100	6.092 ± 0.036	-0.308 ± 0.009
2.300 ± 0.100	5.591 ± 0.035	-0.291 ± 0.010
2.100 ± 0.100	5.520 ± 0.041	-0.296 ± 0.011
1.900 ± 0.100	5.410 ± 0.043	-0.292 ± 0.018
1.500 ± 0.100	5.290 ± 0.032	-0.250 ± 0.011
0.900 ± 0.050	5.158 ± 0.032	-0.173 ± 0.013
0.600 ± 0.050	4.946 ± 0.040	-0.123 ± 0.018

Table 4.1.13. The results from measuring the positron bunch length as a function of current.

Slit size (μm)	150
Density filter	Variable
Interference filter FWHM	40 nm
Damping ring RF Voltage (KV)	805
Current per bunch ($x10^{10}$)	Variable

Table 4.1.14. The conditions for the positron bunch length versus current measurements.

There are several noteworthy features of the experimental data to point out. 1) The low current, ignoring collective beam effects, bunch length for the positron and electron damping ring with the damping ring design parameters is 5.33 and 5.28 mm respectively. There is a systematic difference between measurement and theory of 5% for positrons and 10% for electrons. 2) There is a jump in the asymmetry factor for both electrons and positrons at a current of approximately $2.0x10^{10}$ particles per bunch. 3) The bunch length and asymmetry factor is almost linear as a function of current for electrons unlike the positron case. 4) The bunch distribution at low current differs from a pure Gaussian distribution.

(iii) Bunch Length versus RF Gap Voltage at High Current

At high current the bunch length dependence on RF accelerating voltage changed due to the potential well distortion. The bunch length versus RF accelerating voltage experiment at high current was measured with the streak camera. The measurement was made by taking 25 streak camera profiles at each gap voltage and fitting the profiles to an asymmetric Gaussian distribution. The results of the measurements are shown in figures 4.1.12 a and b. Fitting the data to the function $\sigma_z = A(V_{RF})^m$ gives the value of

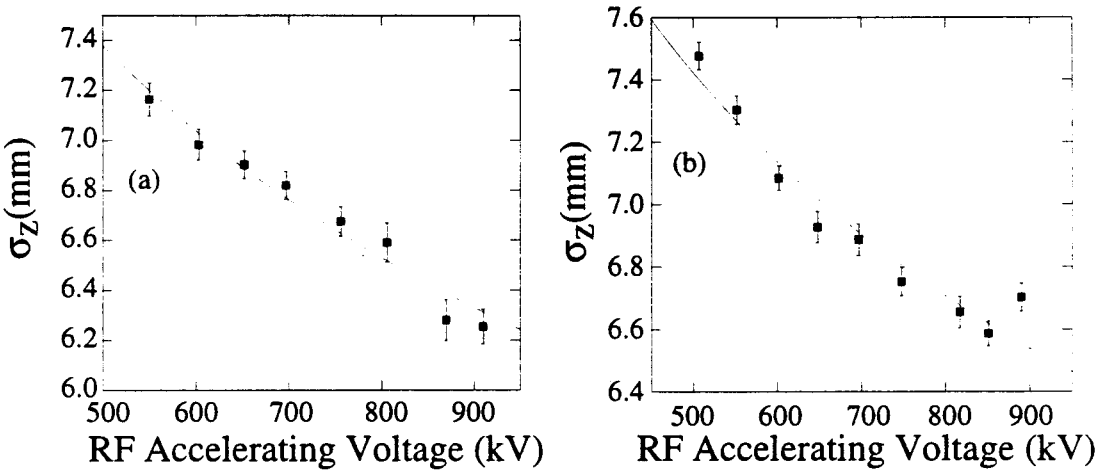

Figure 4.1.12. The bunch length as a function of RF accelerating voltage for the (a) positron and (b) electron damping rings.

	Electron Measurement	Positron Measurement
Slit size (μm)	200	150
Density filter	Variable	Variable
Interference filter FWHM	40 nm	40 nm
Damping ring RF Voltage (KV)	Variable	Variable
Current per bunch ($x10^{10}$)	$3.8 \pm 0.10 x10^{10}$	$3.2 \pm 0.2 x10^{10}$

Table 4.1.15. The conditions for the positron and electron bunch length versus RF accelerating voltage at high current.

$m = -0.260 \pm 0.024$ for the positron and $m = -0.216 \pm 0.011$ for the electron damping ring. The conditions of the experiments are listed in table 4.1.15. .

Comparing with the low current results, it can be concluded that the dependence of the bunch length on the RF accelerating voltage decreases as the current increases in the damping ring.

(iv) Energy Spread North Damping Ring

The energy spread was measured as a function of current using a wire scanner in the transport line of the extracted beam. The measurement was conducted at two different RF gap voltages in the damping ring. A representative of the horizontal beam size from the wire scanner for gap voltages of 765 and 900 kV are plotted in figures 4.1.13 a and b respectively. Given the dispersion, emittance, and beta function at the wire scanner the energy spread can be calculated from equation 4.1.1 where η_x=-0.5667m, β_x=5.41m, $\gamma\varepsilon_x$=4x10^{-5}m rad, and the energy is E=1.19GeV.

The design energy spread, ignoring collective beam effects, of the damping rings is 7.11x10^{-4} which disagrees with the zero current measurement of 8.1x10^{-4} by 14%. The measurement also shows an increase in energy spread (4.1.14a and b) at a current of I=1.5-2.0x10^{10}; this is due to the onset of a turbulent instability.

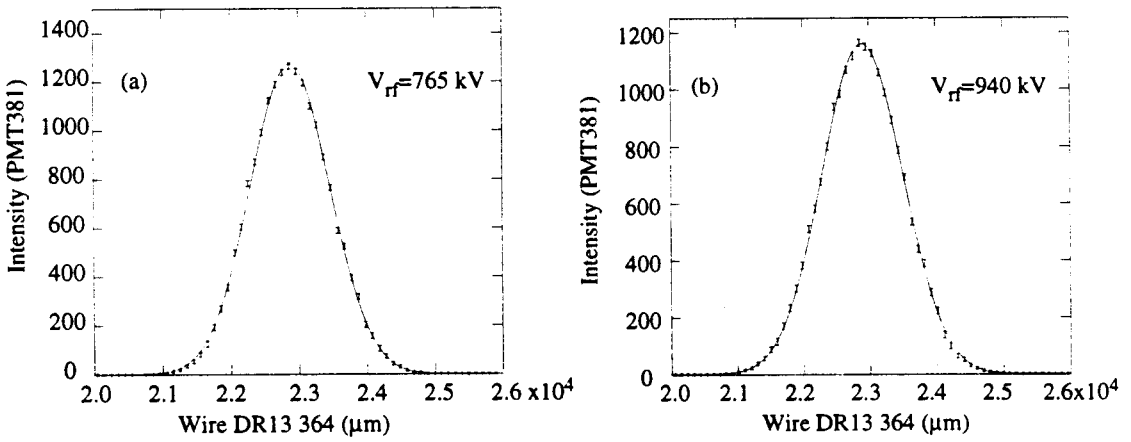

Figure 4.1.13. The horizontal beam size measured with a wire scanner for the beam exiting the damping ring for a current of (a) 3.8x10^{10} and (b) 3.7x10^{10}.

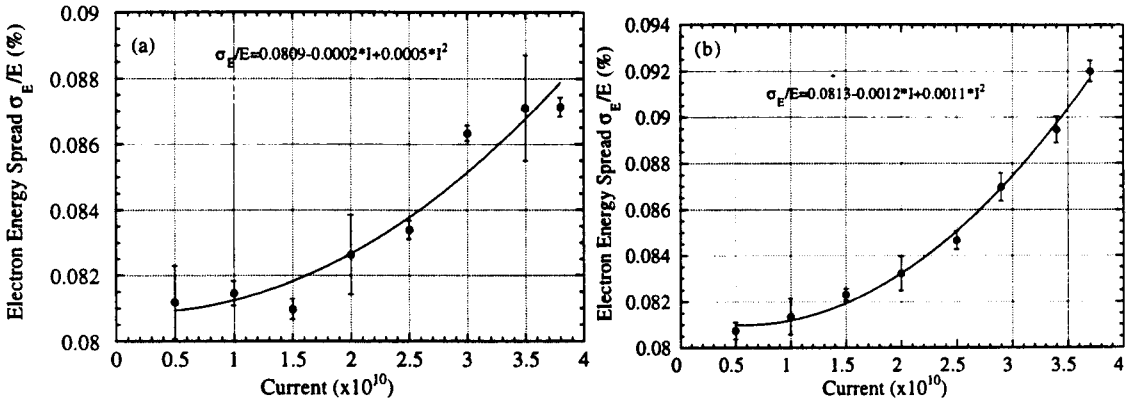

Figure 4.1.14. The energy spread of the electron damping ring as a function of current when the RF gap voltage was (a) 765 kV and (b) 940 kV.

(v) Wire Scanner Bunch Length Measurements

A wire scanner in the electron transport line was used to measure the bunch distribution in the damping ring. The method of measurement is described in chapter 3 section 5. The connection between the transverse size of the beam and the longitudinal position in the beam is determined from the equation

$$x - x_0 = \frac{\eta_x e V_{rf}}{E} \sin\left[\frac{2\pi}{\lambda_{rf}}(z - z_0)\right]$$

where x_0 is the position of the wire which corresponds to the zero crossing of the compressor RF z_0. The terms x_0, z_0, and $\frac{\eta_x e V_{rf}}{E}$ are determined by calibrating the compressor. The calibration is determined by measuring the bunch location on the wire as a function of bunch phase on the RF wave. The calibration curve for 22 MV is shown in figure 4.1.15. From the calibration curve, the connection between the transverse density and location is determined by the equation

$$\rho_l(z) = \rho_t(x)\frac{2\pi}{\lambda_{rf}}\sqrt{\left(\frac{\eta_x e V_{rf}}{E}\right)^2 - (x - x_0)^2}$$

and

$$z = \frac{\lambda_{rf}}{2\pi}\left[\sin^{-1}\left(\frac{E(x - x_0)}{\eta_x e V_{rf}}\right) - z_0\right].$$

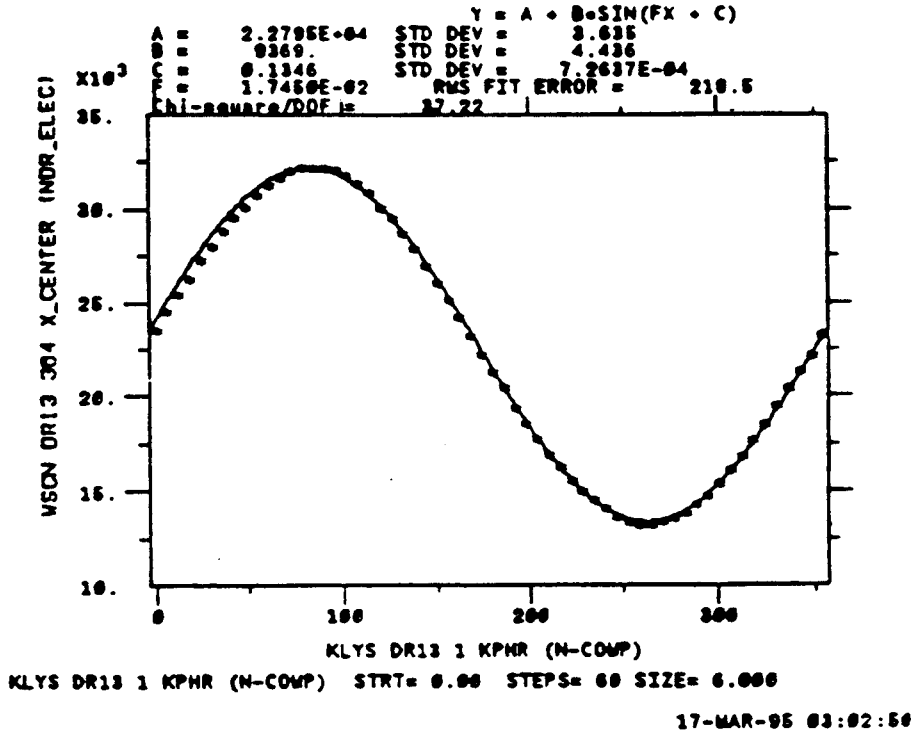

Figure 4.1.15. The calibration of the wire scanner with the RF accelerating wave. The constant terms are shown in the figure.

The bunch length was measured as a function of current and RF accelerating voltage with the wire scanner. The electron bunch distributions for three different currents fit to an asymmetric Gaussian function are plotted in Figure 4.1.16 a-c.

Two bunch length measurements were made at each current and RF voltage, and the bunch distributions are fit to an asymmetric Gaussian distribution and the resolution of the wire is subtracted in quadrature. In figure 4.1.17, the mean bunch length and error of the fit is plotted in figure 4.1.17 as a function of current along with the streak camera data.

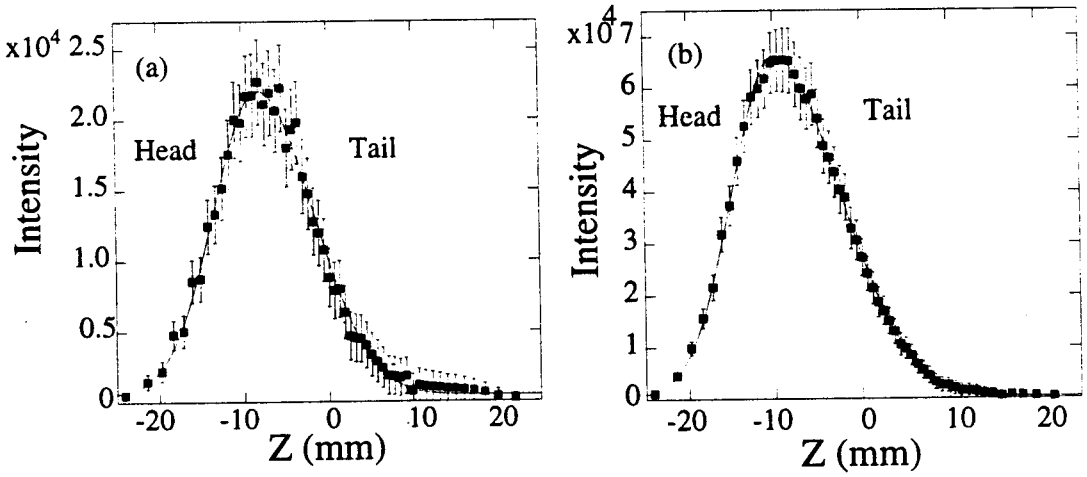

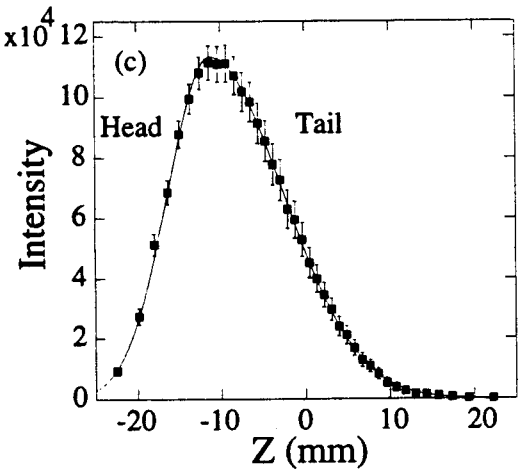

Figure 4.1.16. The electron bunch distribution measured by the wire scanner for the current of (a) $0.6\text{x}10^{10}$, (b) $2.0\text{x}10^{10}$, and (c) $3.8\text{x}10^{10}$ particles per bunch.

The bunch length growth as a function of current differs between the streak camera and wire measurements, at low current the difference is large (~14%) but at high current there is only a 2% difference.

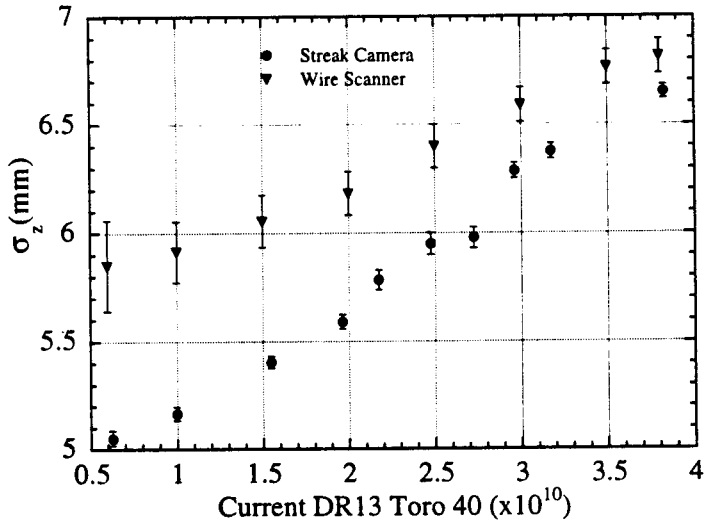

Figure 4.1.17. A comparison of the bunch length measurements with the streak camera and wire scanner for the electron damping ring. The RF accelerating voltage in the electron damping ring is 785 kV during the wire measurements.

Possible difference in the two measurements can be attributed to 1) The difference in the RF gap voltage of the damping ring during the measurement. The measured bunch length scaling at low current for the streak camera measurement is $\left(820/785\right)^{0.49} = 1.02$

and at high current it is $\left(820/785\right)^{0.216} = 1.01$. This is a rather small effect. 2) The wire scanner measures the bunch length over many pulses so if there is jitter of the compressor phase or large current the bunch length measurement will be effected. In the low current limit (no collective effects), the theoretical bunch length for the wire is 5.39 mm and differs from the measurement by 9%.

The bunch length was also measured twice as a function of RF voltage and the mean and fit error is plotted in figure 4.1.18. Fitting the data to the function $\sigma_z = A(V_{RF})^m$ gives the value of $m = -0.312 \pm 0.021$. The power dependence between the wire and streak camera measurements differs by 44% which is quite large. For both measurement it appears that at a high RF gap voltage (~900 kV) the bunch length starts to grow as the voltage increases.

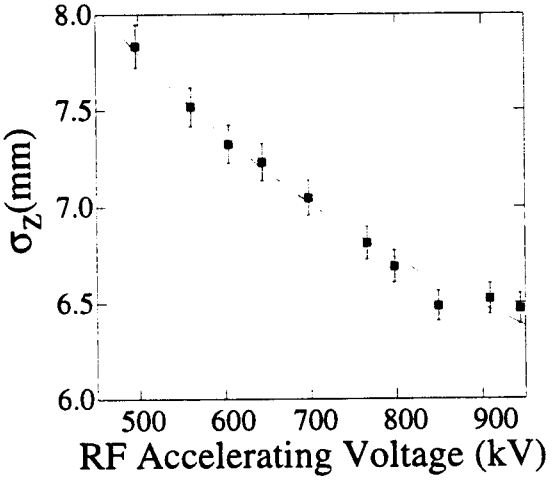

Figure 4.1.18. The bunch length versus accelerating voltage for electrons measured with the wire scanner. The current of the bunch is 3.8×10^{10} particles per bunch for this measurement.

(iii) New Vacuum Chamber

Prior to the 1994-1995 high current physics run for the SLC there was a single bunch instability in the damping rings [K. Bane et al, 1995]. The instability limited the SLC current to 3.0×10^{10} particles per bunch in the damping ring, and it was believed that by reducing the inductive impedance in the damping rings vacuum chamber that the instability would be at $5 - 6.0 \times 10^{10}$ particles per bunch. A new low inductive impedance vacuum chamber was installed in the SLC damping rings prior to the 1994-1995 run and the inductive impedance of the vacuum chamber elements are listed in table 4.1.16.

Element	Old Chamber (nH)	New Chamber (nH)
Synch. Radiation Masks	9.5	---
Bellows	---	1.1
Quadrupole to Dipole Chamber Transitions	9.3	2.4
Ion Pump Slots	0.2	0.05
Kicker Magnet Bellows	4.1	---
Flex Joints	3.6	---
Beam Position Monitors	3.5	0.2
Other	2.4	2.4
Total	33	6

Table 4.1.16. A table of the inductive impedance elements in the damping ring vacuum chamber [K. Bane et al, 1995].

With the new vacuum chamber the threshold of the instability was reduced to $1.5-2.0\text{x}10^{10}$ particles per bunch but the instability is less severe and the current in the

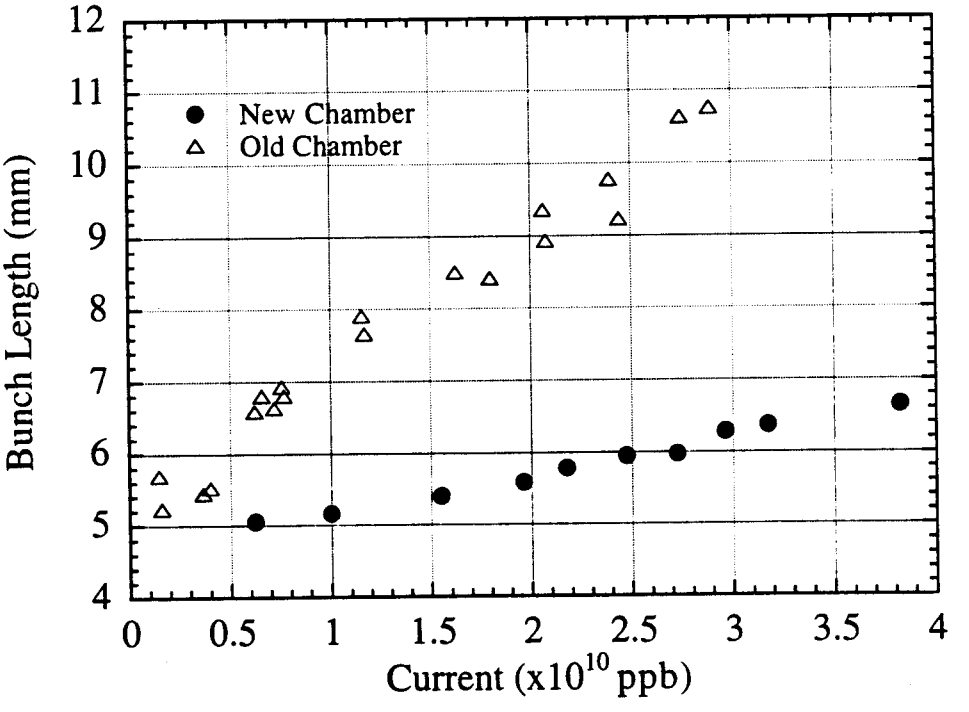

Figure 4.1.19. The bunch length as a function of current for the old vacuum chamber, measured with a wire scanner, and the new vacuum chamber, measure with the streak camera.

damping rings is not limited by the instability. The new vacuum chamber resulted in a significant reduction in the bunch length with the new chamber. Figure 4.1.19 is a comparison of the bunch length for the old and new vacuum chamber. The distributions for the old chamber are not Gaussian and so the FWHM values are quoted.

The bunch distribution in the damping ring with the old and new vacuum chamber is shown in figure 4.1.20. The bunch distribution for the old vacuum chamber is parabolic in shape and this is the signature of an inductive dominant vacuum chamber. The distribution in the electron damping ring is asymmetric in shape and which is the signature of a resistive dominant impedance.

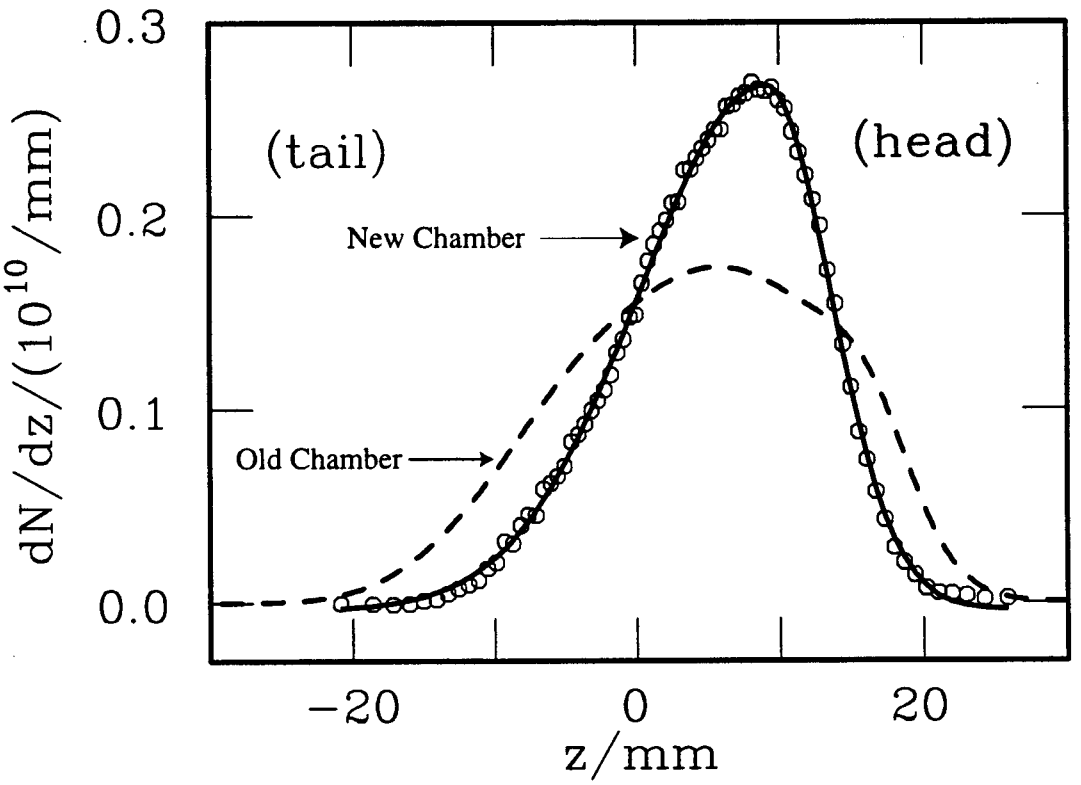

Figure 4.1.20. The bunch distribution in the electron damping ring at a current of 4.5×10^{10} particles per bunch for the old and new vacuum chambers [K. Bane et al, 1995].

(iv) Resistive Impedance in the Damping Rings

The measured bunch distributions shown in figures 4.1.8 and 4.1.10 a-c are used to determine the resistive part of the vacuum chamber impedance by fitting the distributions to equation 2.3.10

$$\rho(t) = \rho_{offset} + \frac{\rho_0 \exp\left(-\frac{t^2}{2\sigma_t^2}\right)}{\alpha'\left(\coth(\alpha') - erf\left(\frac{t}{\sqrt{2}\sigma_t}\right)\right)} \qquad (4.1.5)$$

where the fit variables are ρ_{offset}, ρ_0, and α'. The bunch length σ_t is the measured low current bunch length and is scaled by the measured energy spread. The resistive impedance, R, is determined by fitting α' and substituting into the equation

$$R = \frac{2\alpha'\gamma C\sigma_t^2\omega_s^2}{Nr_o c\alpha}$$

where $\gamma = E/mc^2$, C is the circumference of the damping ring, ω_s is the synchrotron frequency, N is the charge per bunch, c is the speed of light, and α is the momentum compaction. The term α' is derived by a χ^2 minimization of the distributions. The error of the distributions is adjusted so that χ^2 divided by the number of degrees of freedom is equal to one. Two of the fits are displayed in figure 4.1.21 a and b.

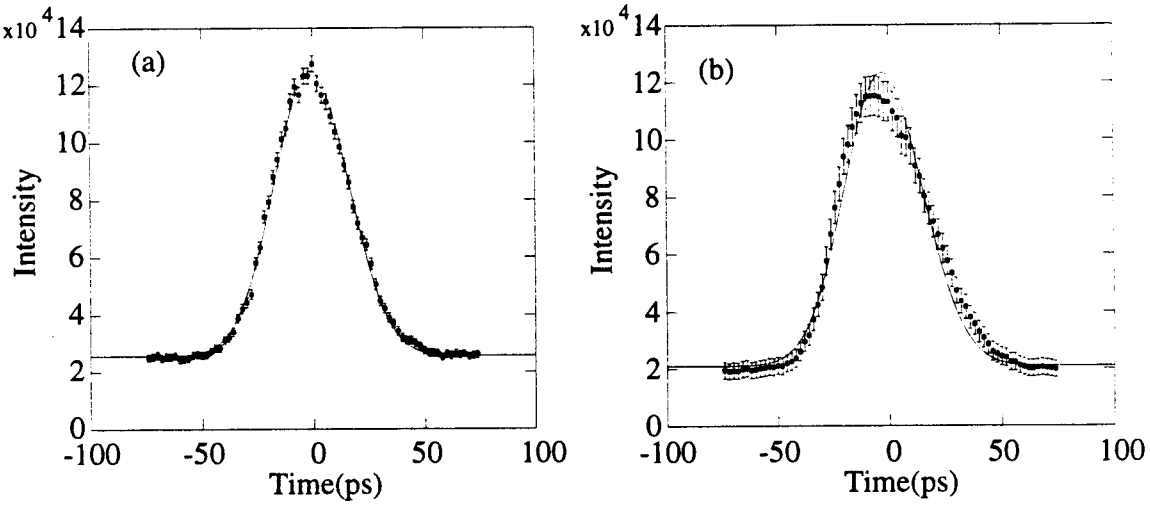

Figure 4.1.21. The electron damping ring distribution for a current of (a) $0.65\text{x}10^{10}$ ppb and (b) $2.2\text{x}10^{10}$ ppb fit to function 4.1.5 to determine the resistive impedance of the damping ring.

The resistance is derived from the fits to the data and is shown in figure 4.1.22. The mean and standard deviation of the resistance is $R_{e^-} = 237.4 \pm 9.7\,\Omega$ for the electron and $R_{e^+} = 265.8 \pm 23.6\,\Omega$ positron damping ring.

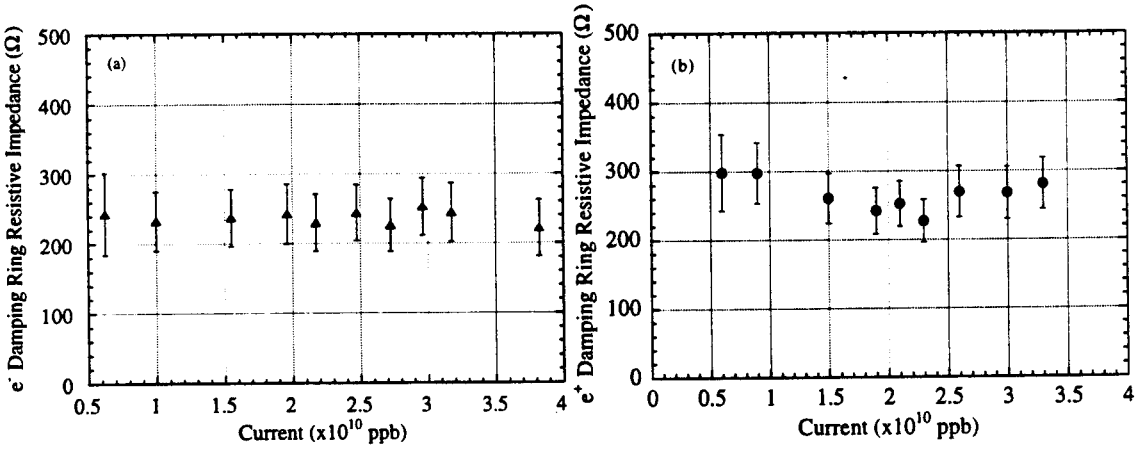

Figure 4.1.22. The resistance as a function of current for the (a) electron damping ring and (b) positron damping ring.

The energy loss per turn for a particle in the damping ring due to the resistive impedance is

$$u_R = R\int_{-\infty}^{\infty} I^2(\tau)d\tau,$$

and for an asymmetric Gaussian distribution the energy loss is

$$u_R = \frac{RqN}{2\pi D}\int_{-\infty}^{\infty} \exp\left[\frac{-(\tau - C)}{(1+sgn(\tau - C)E)^2 D^2}\right] = \frac{RqN}{2\sqrt{\pi}D}.$$

This additional energy loss is compensated by a shift in the synchronous phase. The synchronous phase which includes the resistive energy loss is

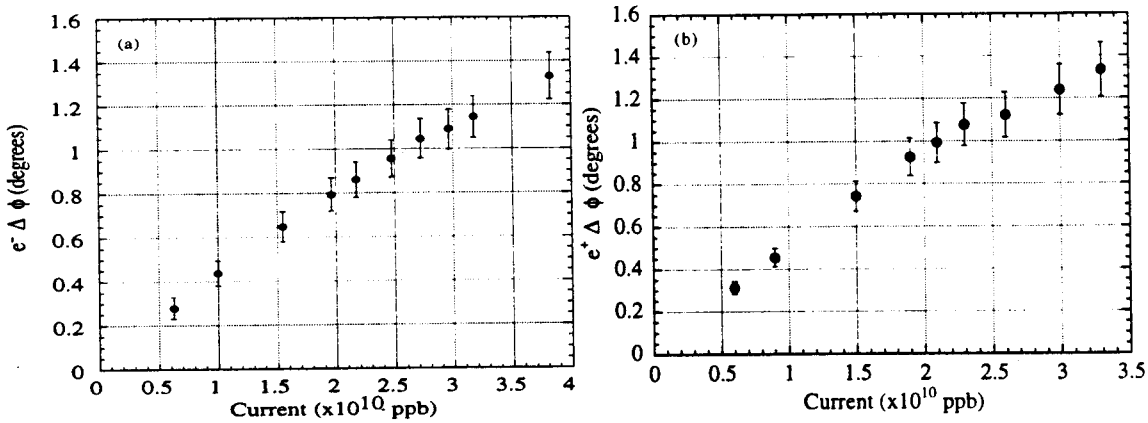

Figure 4.1.23. The synchronous phase as a function of current for the (a) electron and (b) positron damping ring.

$$\varphi_s = \cos^{-1}\left(\frac{u_R + u_\gamma}{eV_{rf}}\right)$$

where u_γ is the synchrotron radiation energy loss. The synchronous phase as a function of current using the measured resistance is plotted in figure 4.1.23.

Several remarks can be made about the results. 1) The resistance is constant as a function of current which is expected. 2) If the impedance in the damping ring is purely resistive, the bunch would not lengthen as a function of current. However, due to the turbulent instability the energy spread increases, and the bunch length should increase as well. Even with this modification, it is evident from figure 4.1.21b that as the current is raised the bunch length increases not only as a result of the turbulent instability but also due the inductive impedance in the damping ring. The synchronous phase of the electron damping ring was made during the 1994-95 run, but some of the necessary feedback loops were turned off. Therefore, a comparison between the synchronous phase from measurement and from the resistive impedance cannot be made.

4.2 Bunch Compressor and Linac Results

Introduction

The results of the measurements of current transmission in the compressor transport lines, the bunch distribution with the streak camera, and the energy spread with the wire scanners at the end of the linac will be presented in this section. The bunch distribution measurements were correlated with compressor voltage, current in the damping ring, and damping ring RF accelerating voltage. The results of these correlations will also be presented.

Particle Losses in the Bunch Compressor Transport Line

When the bunch compressor transport line (the transport line from the damping rings to the linac) was designed, bunch lengthening due to intensity in the damping ring was not expected and the advantages of over compressing the bunch were not realized. As a result, the transport line was designed with an energy aperture of ±2.5%, and this aperture results in significant particle losses when the damping ring is run at high intensities and in over compression mode. The particle transmission through the electron and positron transport lines was measured at high intensity by varying the compressor amplitude. Two toriods were used, at the entrance and exit of the transport line, to measure the current. The current (listed in table 4.2.1 a and b) was measured approximately 30 times at each compressor voltage. The mean transmission is determined from

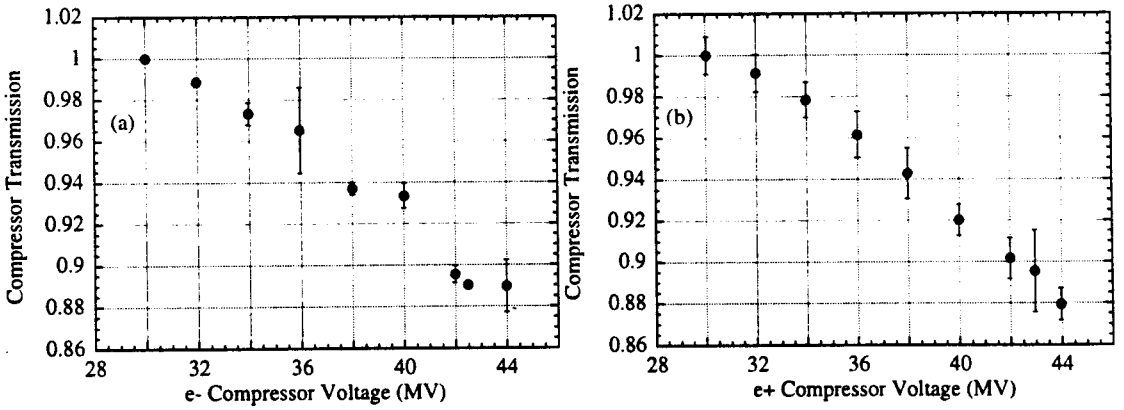

Figure 4.2.1. The particle transmission at high intensity through the (a) electron and (b) positron compressor transport lines as a function of compressor voltage.

$$T = \frac{1}{n}\sum_{i}^{n}\frac{I_{exit}}{I_{entrance}}$$

where n is the number of measurements, $I_{entrance}$ and I_{exit} are the measured currents at the entrance and exit of the transport line. Because there is a small amount of current lost in the transmission line when the bunch is under compressed the transmission is normalized to the compressor amplitude of 30 MV. The mean and rms error for both electron and positron transport lines is plotted in figures 4.2.1 a and b.

The particle loss for both the electron and positron compressor lines is 12% when the compressor is set to 44 MV (over compression) instead of 30 MV (under compression).

Determination of the Compressor Line Energy Aperture

The current transmission through the electron compressor transport line was measured to determine its energy aperture. Setting the phase of the compressor RF section to either $\pm\pi/2$ and varying the compressor RF amplitude, the current entering the linac as a function of compressor voltage is measured. The compressor voltage which gives 50% current transmission is considered the energy aperture. For the electron transport line at

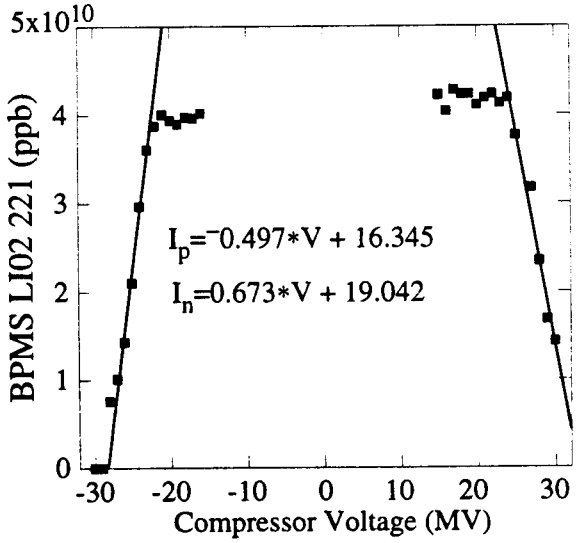

Figure 4.2.2. The results of the energy aperture measurement in the electron transport line. The data are fit to straight lines for positive and negative compressor voltages to determine the half current energy aperture. The fit I_n and I_p refer to the negative and positive compressor voltages. The current of the bunch was I=4.0x10^{10} ppb during the measurement.

high current (figure 4.2.2) the current loss is fit to a straight line to determine the half current voltage. From the fit to the data, the half current voltage was measured to be 27.2MV on the positive side and -24.7 MV on the negative side for the electron transport line. The measured 50% current transmission compressor voltages are used to simulated the particle losses in the compressor line in section 4.3.

Bunch Compression Measurements

As discussed previously, the bunch distribution in the linac is due to its intensity, the damping ring RF accelerating voltage, and the bunch compressor voltage. The bunch distribution at the end of the linac was measured as a function of compressor voltage with the streak camera. The measurement consists of taking approximately 30 longitudinal profiles at compressor settings 2 MV apart. During the measurements great effort was made to keep the current and damping ring RF voltage as stable as possible.

Two methods, the rms and 10-90% width, are used in determining the bunch length from the linac streak camera profiles. Both methods are described in chapter 3 section 7. The results of the measurement, listed in table 4.2.1, show the variations of the SLC during the measurement. The bunch length results include the resolution correction of $\sigma_{resolution} = 0.645 \pm 0.011 ps$ for the rms and $W_{resolution} = 1.3\sigma_{resolution}$ for the width. The resolution correction is subtracted in quadrature for the streak speed and camera slit size used in the measurement. The parameters of the measurement are listed in table 4.2.2. A plot of the bunch length for the various compressor voltage settings is in figures 4.2.3 a and b. The electron and positron bunch lengths are in good agreement considering the beam currents and ring parameters are different. The bunch distribution for three different compressor voltages for the electron and positron bunches is plotted in figures 4.2.4 a-c and 4.2.5 a-c. When the compressor is set to 30 MV this results in an under compressed bunch, 36 MV results in a fully compressed bunch, and 42 MV results in an over compressed bunch. During the 1994-95 SLC high current physics run the bunch compressor voltage was 42.5 MV for electrons and 43 MV for positrons.

Compressor Voltage (MV)	rms Bunch Length (mm)	Damping ring current ($x10^{10}$)	Linac Current ($x10^{10}$)	Damping ring RF voltage(kV)
30.01 ± 0.04	1.08 ± 0.02	4.04 ± 0.02	3.84 ± 0.02	828.9 ± 4.0
31.99 ± 0.04	0.78 ± 0.02	4.01 ± 0.04	3.77 ± 0.03	827.6 ± 4.1
33.99 ± 0.05	0.65 ± 0.01	4.02 ± 0.07	3.72 ± 0.06	828.5 ± 2.6

35.98 ± 0.04	0.58 ± 0.01	3.46 ± 0.30	3.18 ± 0.25	805.0 ± 10.0
38.01 ± 0.03	0.67 ± 0.01	4.01 ± 0.05	3.58 ± 0.04	827.6 ± 3.9
40.02 ± 0.04	0.91 ± 0.01	3.35 ± 0.10	2.97 ± 0.07	797.9 ± 2.9
42.00 ± 0.03	1.11 ± 0.01	4.01 ± 0.08	3.42 ± 0.06	829.2 ± 4.6
42.49 ± 0.03	1.21 ± 0.01	4.05 ± 0.03	3.43 ± 0.03	835.5 ± 4.3
43.99 ± 0.02	1.38 ± 0.01	3.49 ± 0.21	2.96 ± 0.16	802.9 ± 4.6

Table 4.2.1a. The electron compressor results. The errors quoted are the rms error except for the current measurement where the error listed is the standard deviation.

Compressor Voltage (MV)	rms Bunch Length (mm)	Damping ring current ($x10^{10}$)	Linac Current ($x10^{10}$)	Damping ring RF voltage(kV)
30.04 ± 0.13	1.01 ± 0.03	3.41 ± 0.10	3.62 ± 0.12	881.4 ± 2.3
32.01 ± 0.07	0.74 ± 0.02	3.44 ± 0.11	3.61 ± 0.11	881.0 ± 3.1
33.99 ± 0.02	0.67 ± 0.01	3.36 ± 0.10	3.48 ± 0.11	880.7 ± 3.9
36.02 ± 0.04	0.60 ± 0.01	3.33 ± 0.14	3.39 ± 0.14	880.2 ± 2.3
37.99 ± 0.01	0.69 ± 0.01	3.25 ± 0.15	3.25 ± 0.14	879.7 ± 2.2
40.00 ± 0.02	0.93 ± 0.02	3.36 ± 0.09	3.27 ± 0.10	879.7 ± 3.6
42.00 ± 0.02	1.16 ± 0.02	3.37 ± 0.13	3.22 ± 0.13	880.5 ± 2.3
42.96 ± 0.02	1.24 ± 0.02	3.20 ± 0.23	3.04 ± 0.21	880.3 ± 4.0
43.97 ± 0.03	1.33 ± 0.2	3.44 ± 0.11	3.21 ± 0.10	880.4 ± 2.4

Table 4.2.1b. The positron compressor results. The errors quoted are the rms error except for the current measurement where the error listed is the standard deviation.

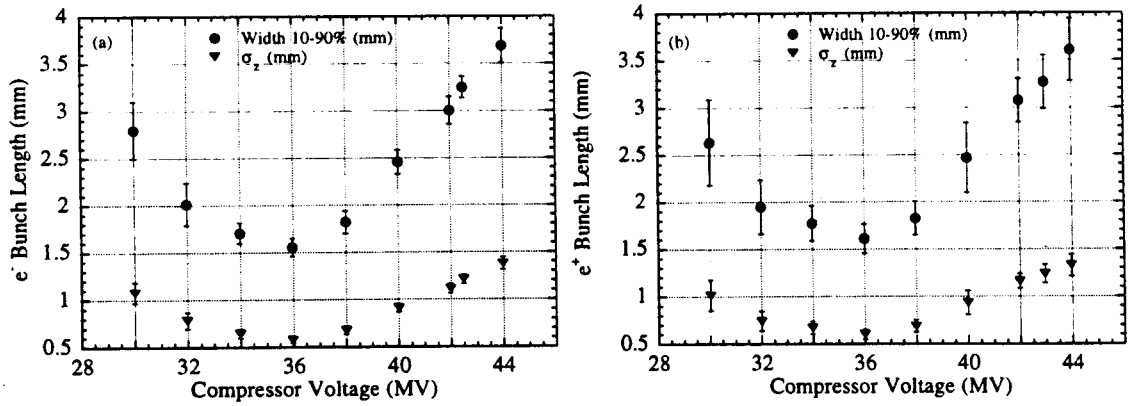

Figure 4.2.3. The (a) electron and (b) positron bunch length as a function of compressor voltage.

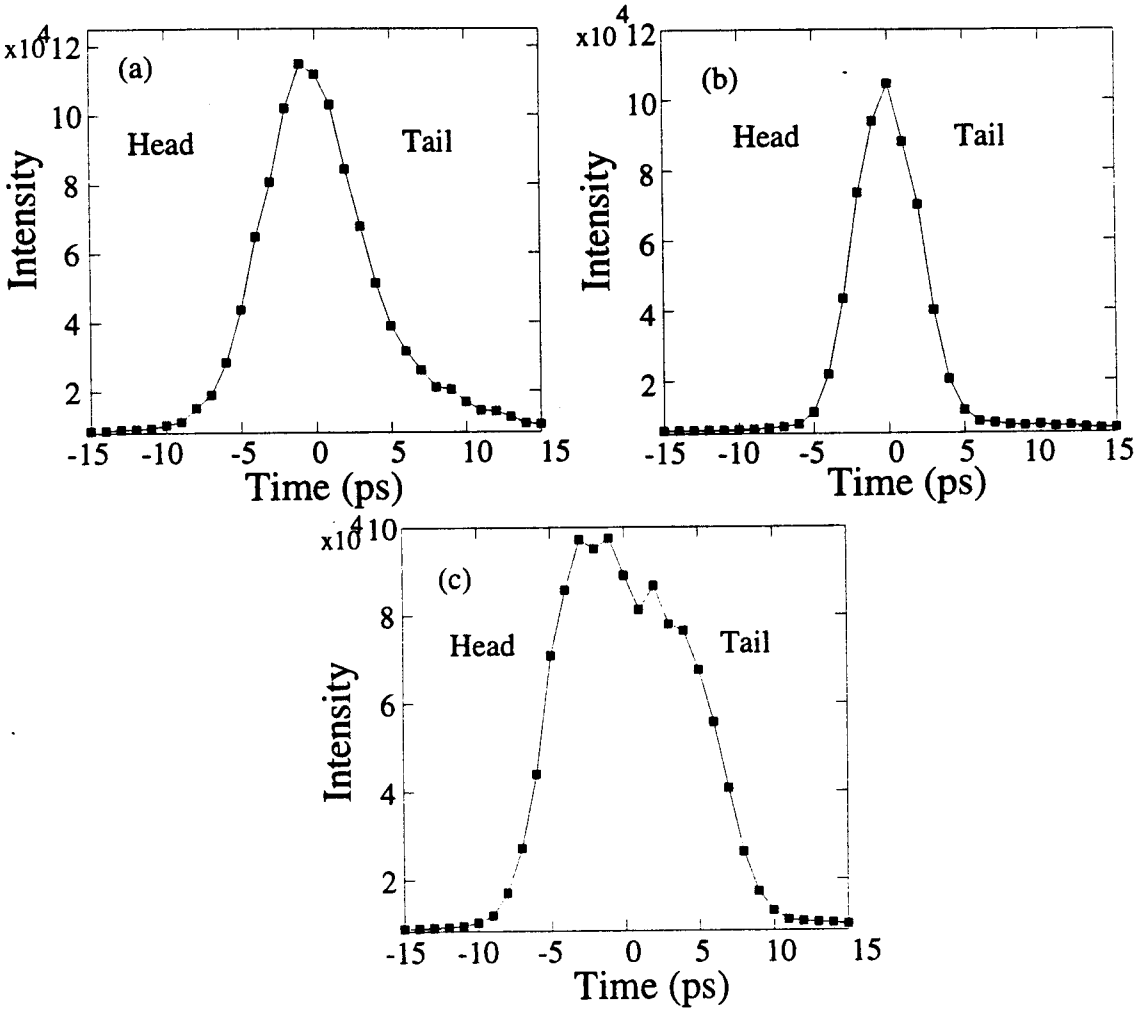

Figure 4.2.4. The electron distributions for the compressor settings of (a) 30 MV, (b) 36 MV, and (c) 42.5 MV.

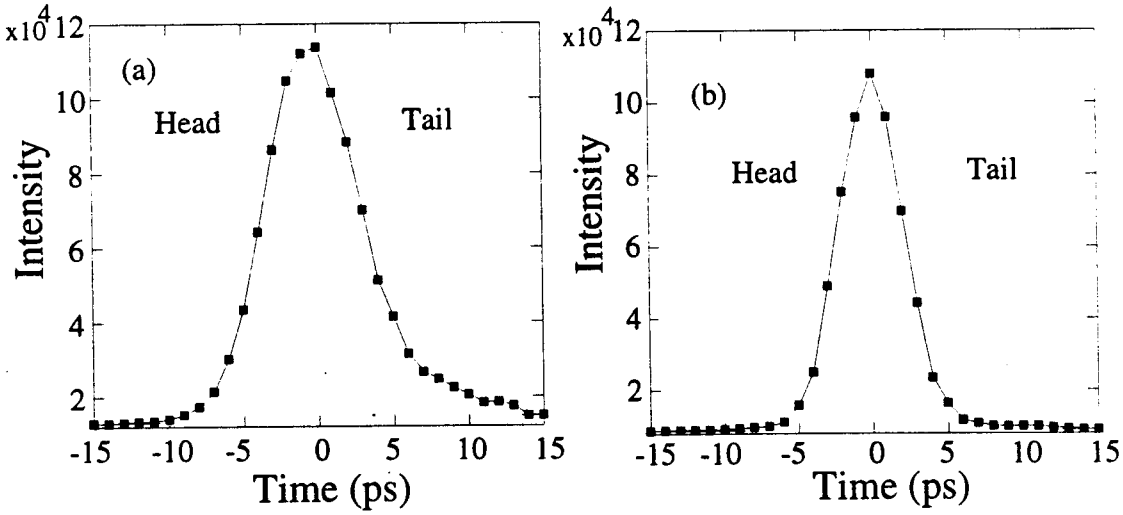

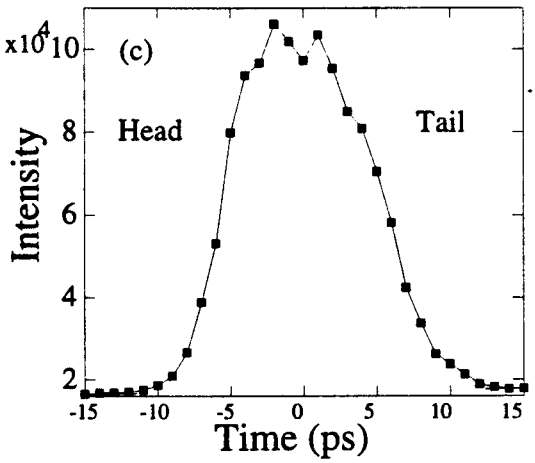

Figure 4.2.5. The positron distributions for the compressor setting of (a) 30 MV, (b) 36 MV, and (c) 43 MV.

Slit size (μm)	50
Density filter	Variable
Interference filter FWHM	10 nm
Damping ring RF Voltage (kV)	Listed in table 4.2.1
Current per bunch (x10^{10})	Listed in table 4.2.1

Table 4.2.2. The damping ring and streak camera parameters for the injection measurements.

Several conclusions can be made from the above data: 1) The minimum bunch length for an initial Gaussian distribution is given by

$$\sigma_\tau = \left(\frac{L\alpha_{comp}}{cP_0} \right) \sigma_{\varepsilon_0}$$

Using the energy and momentum compaction along with the measured energy spread the expected minimum bunch length is $\sigma_\tau = 0.55mm$. The minimum measured rms bunch length is $\sigma_z = 0.58 \pm 0.01mm$ (5% difference) for electrons and $\sigma_z = 0.60 \pm 0.01mm$ (8% difference) for positrons. The discrepancy between the expected and measured bunch lengths could be due to the bunch being asymmetric rather than Gaussian, the compressor setting for the minimum could be lower or higher than 36 MV, or a systematic offset in the streak camera calibration. An offset has been observed for both tests, low current limit in the damping ring in section 4.1 and full compression of the bunch, of the streak camera calibration. In both cases the calibration offset is at the 5-10% level. 2) The electron and

positron results are consistent with each other even though the current during the measurements is slightly different. 3) The bunch distributions for the under compressed cases have tails which are prominent in figures 4.2.4 and 4.2.5 a. The particles in the tail are scraped off in the over compressed case in the compressor transport line. The tail particles for the under compressed case are low in energy at the end of the linac, and they are either lost in the arcs or are background in the detector. 4) The rms and 10-90% bunch width follow the same trends as a function of compressor voltage.

Energy spread at the end of the Linac

The energy spread at the end of the linac is measured with a wire scanner at the start of the arc region of the SLC. The horizontal beam size is measured with the wire scanner in a high dispersion region. The energy spread is calculated from equation 4.1.1 where the design optics parameters of $\beta_x = 2.2\text{m}$, $\beta_x = 3.2\text{m}$ and $\eta_x = -0.071\text{m}$, $\eta_x = 0.083\text{m}$ are used for electrons and positrons respectively. The emittance ε_x is measured with a set of wires at the end of the linac.

The horizontal beam size at the end of the linac depends on the compressor voltage and the overall phase of the klystrons in the linac. To make sure that the minimum energy spread is measured for a given compressor setting, a synchrotron light monitor is used. The synchrotron light monitor is located after a vertical bend magnet in the arc region. The synchrotron light from the vertical bend magnet strikes a phosphorus screen which images the horizontal beam size. The light from the phosphorus screen is projected on a CCD camera which is viewed in the SLC control room. When the energy spread is minimized the synchrotron light strip is minimized. It should be noted that minimizing the synchrotron light strip does not always mean that the rms or 10-90% energy width is minimized. A distribution with large energy tails can have a small energy width but will not be optimized for colliding beams because these tail particles will be lost in the arcs, final focus, and detector.

For each compressor setting the overall linac phase is adjusted to minimize the energy spread and the wire scanner is then used to measure the energy spread. The energy spread was measured two to five times at each compressor setting.

Typical wire scans are shown in figure 4.2.7 a-c. Because the beam size is not easily fit to a closed form function, the rms beam size is calculated with the cuts shown in figures 4.2.7 a-c. Two interesting points can be noted about the horizontal beam size shown in figure 4.2.7: 1) When the bunch is under compressed, the rms width shown in figure 4.2.7 a does not include a rather large tail. If this tail is included, the energy spread is

substantially larger and these off energy particles are a problem in the arc and final focus of the SLC. 2) The over compressed horizontal bunch size does not have a tail and the beam size when fit to a Gaussian distribution has a width of $\sigma_x = 82.4\ \mu m$ which gives an energy spread of $\sigma_E/E = 0.03\%$.

The energy spread for the electrons and positrons at the end of the linac as a function of compressor voltage is shown in figures 4.2.6 a and b.

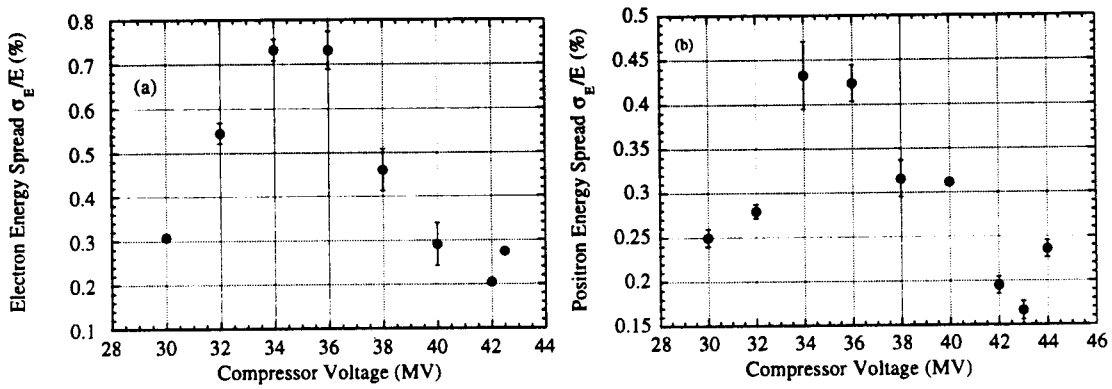

Fig 4.2.6. The energy spread at the end of the linac for (a) electrons and (b) positrons. Plotted is the mean energy spread, and the errors are the standard deviations of the measurements.

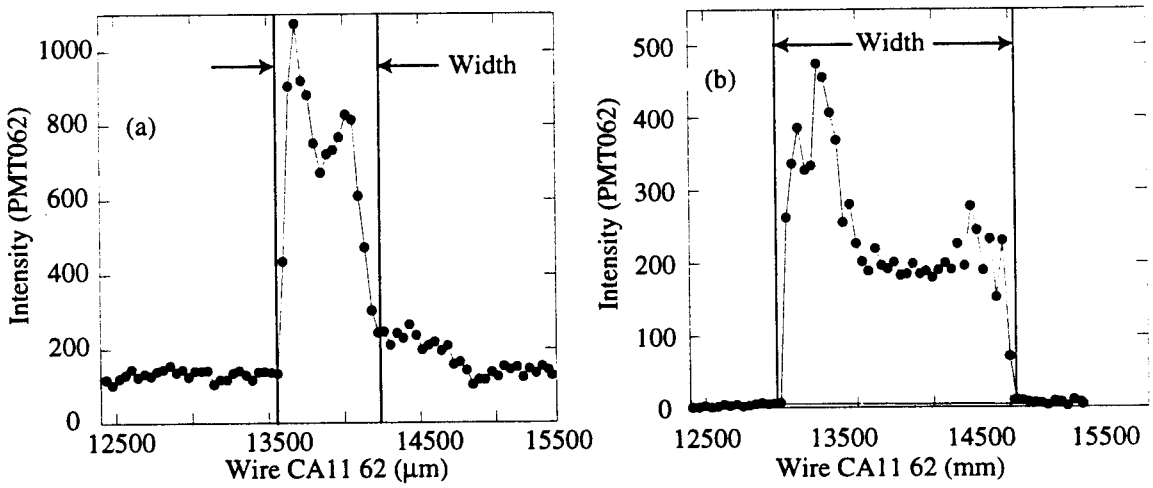

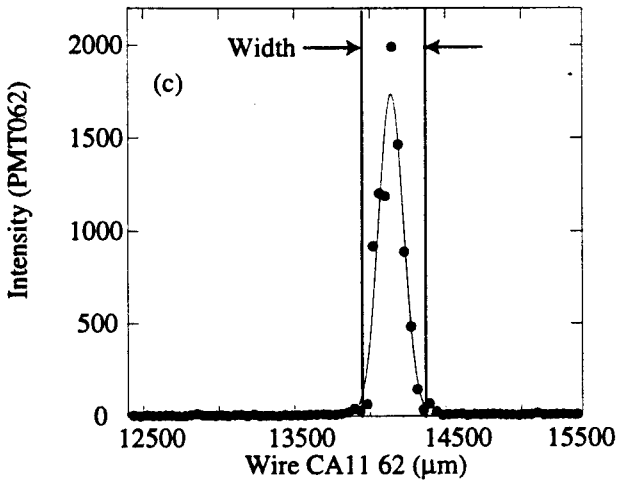

Figure 4.2.7. Typical horizontal beam size profiles for a compressor voltage of (a) 30 MV, (b) 36 MV, and (c) 42 MV.

Another method of characterizing the energy spread at the end of the linac is the 10-90% energy width. The energy width, described in chapter 3 section 7, can be determined from the equation

$$W_\varepsilon = E\sqrt{\frac{W_x^2 - \beta_x W_{\varepsilon_x}}{\eta_x^2}}$$

where W_x is the resolution corrected width and $W_{\varepsilon_x} = 1.3\varepsilon_x$ is the emittance width.

Figures 4.2.8 a and b are the minimized energy width at the end of the linac as a function of compressor voltage for the electron and positron bunches.

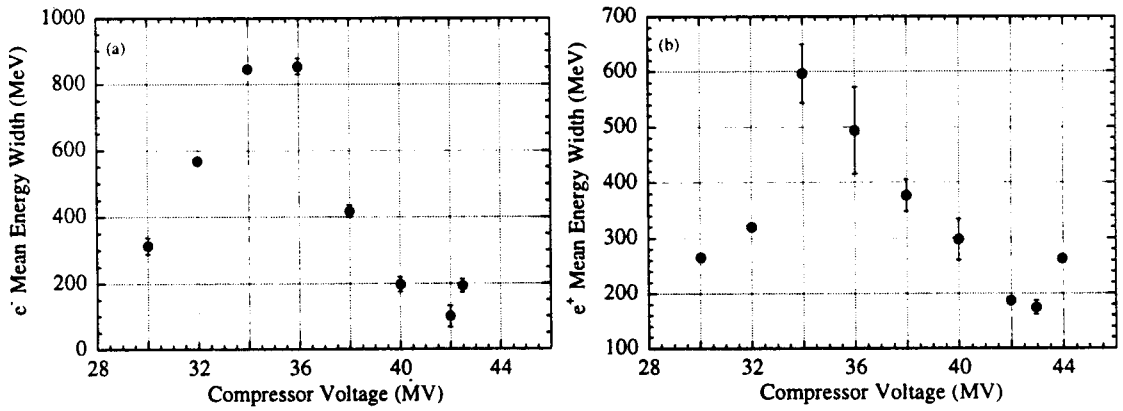

Figure 4.2.8. The (a) electron and (b) positron energy width at the end of the linac as a function of compressor voltage. Plotted is the mean energy width and standard deviation is denoted as the error.

Several conclusions can be made about the energy spread measurement. 1) The energy spread of a fully compressed bunch is a factor of 4 times larger than an over compressed bunch. 2) The energy spread of an over compressed bunch is a factor of 2-3 times smaller than an under compressed bunch. 3) Determining the energy spread for an under compressed bunch is difficult due to the large tails and background. 4) The electron energy spread (and width) is slightly higher than for the positron case. 5) The general trend of the energy spread for the width and rms measurements are in agreement.

Bunch Length Cavity Measurements

The bunch length cavity signal and current gap monitor (located at the cavity) were recorded as a function of compressor voltage during the streak camera measurement. The cavity sensitivity due to current fluctuations is removed by dividing the signal by the current. This gives an easily calibratable measurement of relative changes in the bunch length when the power detector for the cavity is operated in its linear regime (see chapter 3 section 4). Unfortunately, in order to run the detector in the linear regime a variable attenuation must be used and that was not done for this measurement. None the less, the cavity signal will still give a useful signal that follows the streak camera measurement of the bunch length. The cavity signals mean and rms error are plotted as a function of the compressor voltage in figure 4.2.9 a and b. As expected, the cavity curve in both cases is inverted to the bunch length measurement from the streak camera.

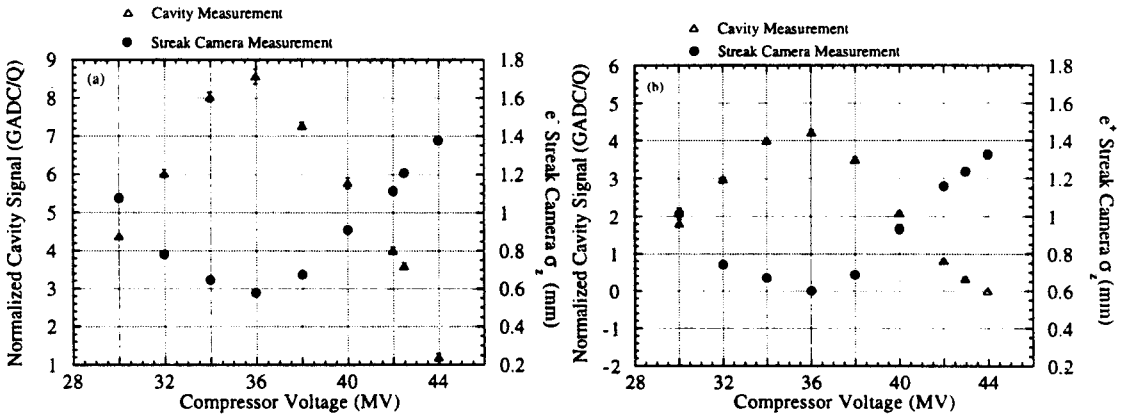

Figure 4.2.9. The normalized bunch length cavity signal is plotted on the left y axis and streak camera bunch length is plotted on the right y axis as a function of compressor voltage for the (a) electron, and (b) positron bunch. The units of the cavity signal is GADC counts per current counts. The current counts are proportional to the particles per bunch. These units will be denoted by GADC/Q.

Correlation of Machine Parameters with Measurement

The stability of the SLC longitudinal beam parameters at the end of the linac begins with stability in the damping rings. As an example, the energy spread and bunch length at the end of the linac depend on the stability of the RF accelerating voltage, the beam current, the bunch compressor voltage and also the stability of the bunch itself. A measurement of the dependence can be done by correlating the machine parameters with the streak camera measurements. The correlation is done by triggering the streak camera every 30 seconds, a slow enough rate, to allow the profile to be saved, and taking data with the devices that affect the longitudinal parameters in the damping ring, bunch compressor, and linac on that same trigger pulse. This allows the streak camera and accelerator components to be correlated.

Correlation between parameters is determined by fitting the data to a straight line. The errors on the streak camera data points are determined from the χ^2 minimization of the fit to the data. The χ^2 minimization to the data is given by

$$\chi^2 = \frac{1}{\sigma^2}\sum_{i=1}^{n}\left(y_i - f(x_i)\right)$$

where the error on all the data points are taken to be equal. The error σ is determined from normalizing the χ^2 divided by the number of data points minus the number of fit variables (two in the case of a line). Therefore the error on each point is given by

$$\sigma = \sqrt{\frac{\chi^2}{n-2}}$$

where n is the number of data points. The degree of correlation is determined by the slope of the line and the error on the slope. The accelerator components that have been correlated with the streak camera are the current, compressor voltage, and damping ring RF.

Correlation Results

(i) Current Gap Monitor and Toriod Current

A correlation between the toriod at the exit of the damping ring and the gap current monitor located at the bunch length cavity can be used for two purposes. 1) To calibrate the gap current monitor with a toriod; 2) Verify that correlations between the linac and

damping ring can be made. The data is plotted in figure 4.2.10, and the data is highly correlated. A linear fit to the data gives the result of

$$Q_{gap} = -(96.26 \pm 8.45) + (122.65 \pm 2.47)\text{x}10^{-10} Q_{toriod} \qquad (4.2.1)$$

where Q_{gap} is the gap monitor reading and Q_{toriod} is the particles per bunch given by the toriod. Equation 4.2.1 can be used to determine the number of particles in a bunch for a given gap current monitor reading.

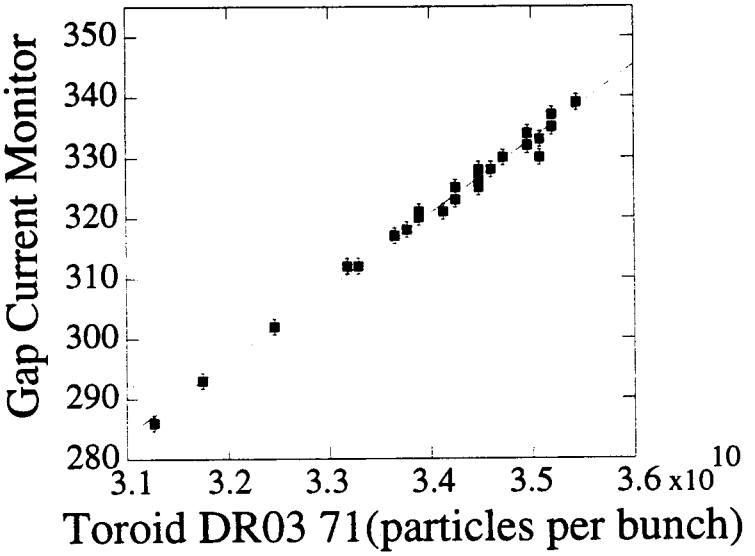

Figure 4.2.10. The correlation of the positron current entering the linac as measured by a toriod and the current measured by the gap current monitor located at the bunch length cavity. The compressor setting for the positron beam is 30 MV during this measurement. The error was determined by the χ^2 fit to the data.

(ii) Streak Camera and Damping Ring RF Accelerating Voltage

The bunch length dependence on the RF accelerating voltage in the damping ring was presented in section 1 of this chapter. The purpose of this section is to examine the effects of a fluctuating damping ring voltage on the bunch width in the linac. In figure 4.2.11 a and b the bunch width as a function of the positron damping ring voltage is plotted. Fitting the data to a straight line in figure 4.2.11 a gives

$$\text{Width(mm)} = 260.91 \pm 116.31 - (2.86 \pm 1.32)\text{x}10^{-1} * V_{RF}(\text{kV})$$

and figure 4.2.11 b gives

$$\text{Width(mm)} = -80.83 \pm 66.90 + (9.92 \pm 7.59)\text{x}10^{-2} * V_{RF}(\text{kV}).$$

In both cases the error on the slope is large which gives reason to doubt the relevance of the measurement, but several comments can be made: 1) For both cases the beam is under compressed in the linac and the slope of the dependence of the RF voltage on the bunch width has changed sign. This gives doubt to the data because it is expected that if the damping ring RF voltage goes up, the bunch length goes down and the bunch at the end of the linac should follow this trend. 2) The fluctuations of the RF voltage is approximately ±4kV corresponds to a bunch length change of approximately 0.05mm in figure 4.1.13b. But, according to figure 4.2.11 a, a bunch length change of 0.05mm in the damping ring leads to a bunch width change of approximately 2mm.

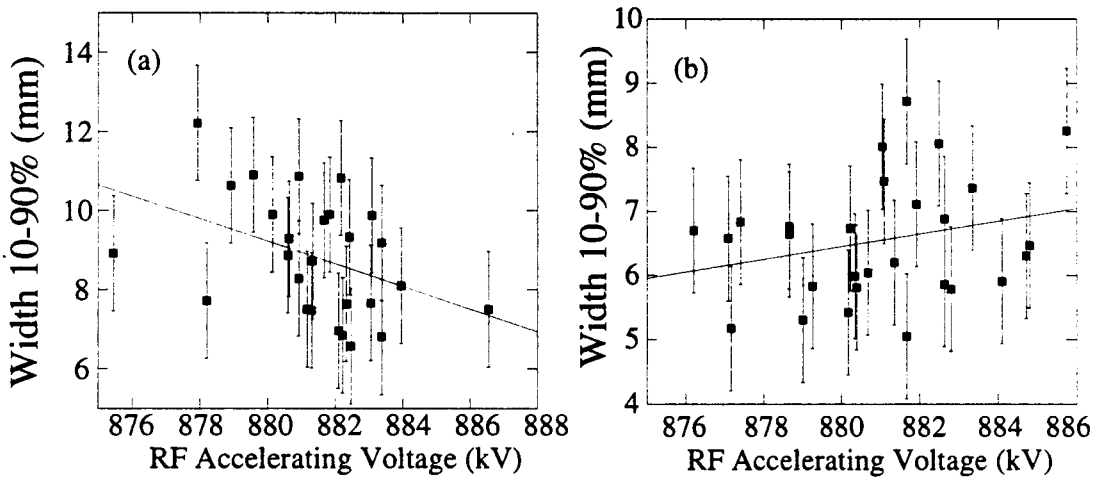

Figure 4.2.11. A correlation between the streak camera bunch width measurements and the positron damping ring RF accelerating voltage for the compressor voltage of (a) 30 MV, and (b) 32MV.

(iii) Streak Camera and Current

The bunch length dependence on intensity in the damping ring has been measured and presented in section 1 of this chapter. The pulse to pulse intensity jitter in the SLC is a probable source for pulse to pulse jitter of the bunch width in the linac. In figure 4.2.12 a and b the bunch width as a function of the current exiting the damping ring is plotted. Fitting the data to a straight line in figure 4.2.12 a gives

$$\text{Width(mm)} = 28.88 \pm 8.23 - (6.14 \pm 2.45)\text{x}10^{-10} * \text{I}$$

and figure 4.2.12 b gives

$$\text{Width(mm)} = 11.66 \pm 10.45 - (8.32 \pm 30.59)\text{x}10^{-10} * \text{I}.$$

Several comments can be made about the results. 1) As the current increases in the damping ring, the bunch length increases and this should result in a longer bunch width in the linac. Figure 4.2.12 a contradicts this result. 2) The error in the slope in figure 4.2.12 b is almost 4 times larger than the slope value, and therefore no correlation can be concluded. As a result of the two figures, the correlation between current and bunch length is inconclusive.

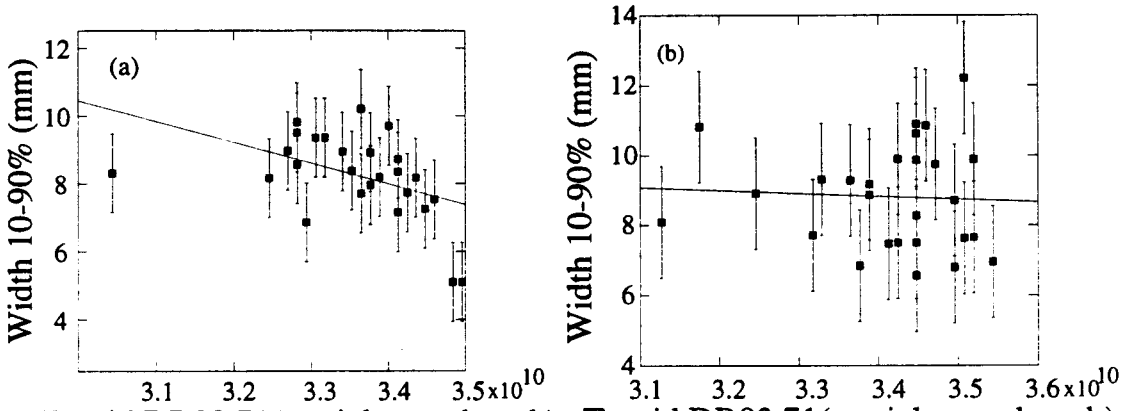

Figure 4.2.12. The correlation between the bunch width and current for the positron bunch when the compressor is set to (a) 40 MV and (b) 30MV.

(iv) Streak Camera and Compressor Voltage

The bunch length dependence on the compressor voltage has been presented previously in this section, but the pulse to pulse jitter of the voltage has not been mentioned. Because the compressor voltage is directly responsible for the bunch length in the linac, fluctuations of the compressor voltage will determine if the streak camera measurement fluctuations are due to the compressor, statistical, or other phenomenon. In figure 4.2.13 a and b the bunch length as a function of the current exiting the damping ring is plotted. Fitting the data to a straight line in figure 4.2.13 a gives

$$\text{Width(mm)} = -477.97 \pm 3.30 + (11.14 \pm 0.08) * V_{comp}$$

and figure 4.2.13 b gives

$$\text{Width(mm)} = 1153.04 \pm 2.87 - (24.26 \pm 0.07) * V_{comp}.$$

Several comments can be made about the results. 1) In figures 4.2.13 a and b the jitter in compressor voltage is approximately ±0.05 MV and ±0.03 MV respectively. This corresponds to a bunch width change of 1mm and 2 mm respectively. 2) The sign of the

slope of the linear fit to the data in figure 4.2.13 a makes physical sense because a lower compressor setting should result in a shorter bunch length, but the slope is in the wrong direction for figure 4.2.13 b. Since the data is not self consistent, correlating the compressor voltage and the bunch width is inconclusive.

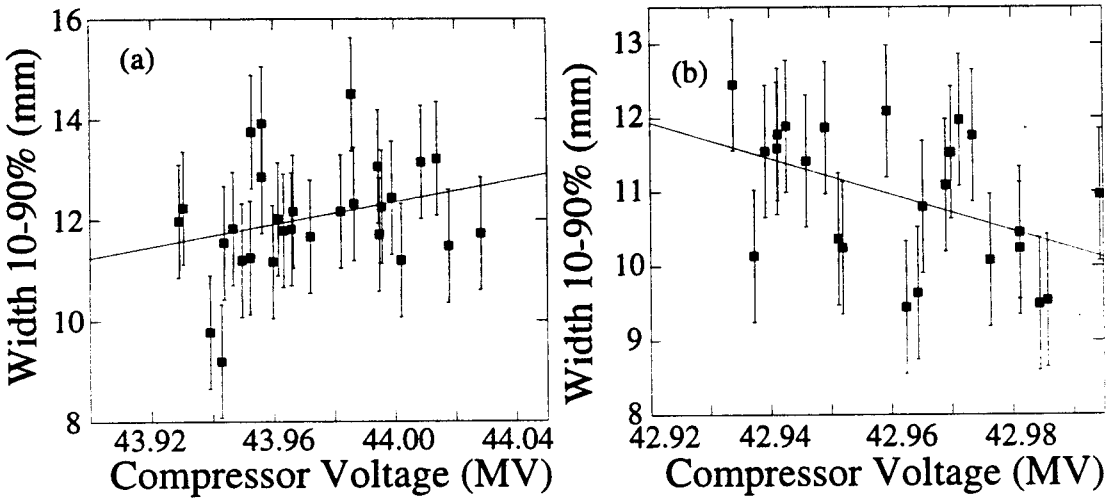

Figure 4.2.13. The correlation between positron bunch width and compressor voltage for compressor setting of (a) 44MV, (b) 43MV.

4.3 Simulation of Longitudinal Dynamics

Introduction

The basic features of the simulation code were described in chapter 2 section 6. In this section the results of computer simulation of the longitudinal dynamics of the SLC are compared with the measurements presented in the two previous sections.

Initial Beam Parameters

The simulation of the longitudinal dynamics of the SLC begins with the bunch being extracted from the damping ring. In order to simulate bunch compression, current losses in the transport line, and the energy spread at the end of the linac, the initial longitudinal phase space of the bunch exiting the damping ring is needed. The initial phase space, σ_z and σ_E/E, used in the simulation were determined from measurements on the damping ring presented in section 4.1 The initial electron and positron bunch distributions and electron energy spread are determined from the fits to the measured bunch length and asymmetry factor shown in figures 4.1.9, 4.1.11, and 4.1.14 a-b. Since the energy spread for the positron damping ring was not measured, the results from the electron damping ring are used. In table 4.3.1, for each compressor voltage and current setting, the corresponding measured energy spread, bunch length, and asymmetry factor used as initial conditions in the simulation is denoted.

Vcomp(MV)	I (x10^{10})	$\frac{\sigma_E}{E}(\%)$	$\sigma_{z(mm)}$	Asymmetry
30.14	4.04	0.094	6.85	-0.41
31.99	4.01	0.094	6.83	-0.41
33.97	4.02	0.094	6.84	-0.41
35.98	3.46	0.090	6.49	-0.38
38.01	4.01	0.094	6.83	-0.41
40.02	3.35	0.090	6.42	-0.37
42.00	4.01	0.094	6.83	-0.41
42.49	4.05	0.094	6.86	-0.41
43.99	3.49	0.091	6.51	-0.38

Table 4.3.1a. The initial conditions of the electron bunch

Vcomp(MV)	I (x10^{10})	$\frac{\sigma_E}{E}$(%)	$\sigma_{z(mm)}$	Asymmetry
30.04	3.41	0.090	6.74	-0.35
32.02	3.44	0.090	6.78	-0.35
33.99	3.36	0.090	6.69	-0.34
36.02	3.33	0.090	6.65	-0.34
37.99	3.25	0.089	6.56	-0.34
40.00	3.36	0.090	6.69	-0.34
42.00	3.37	0.090	6.70	-0.34
42.96	3.21	0.089	6.52	-0.34
43.97	3.44	0.090	6.78	-0.35

Table 4.3.1b. The positron bunch initial conditions.

Current Transmission in the Compressor Line

The measured current transmission in the electron compressor line is presented in section 4.2. The compressor voltage for 50% current transmission was measured to be 27.2 and -24.7 MV at a current of I=4.0x10^{10} ppb. For the simulation, the initial distribution in longitudinal phase space is determined from figures 4.1.9 and 4.1.14. For a current of I=4.0x10^{10} ppb, the bunch length is $\sigma_z = 6.82$ mm with an energy spread and

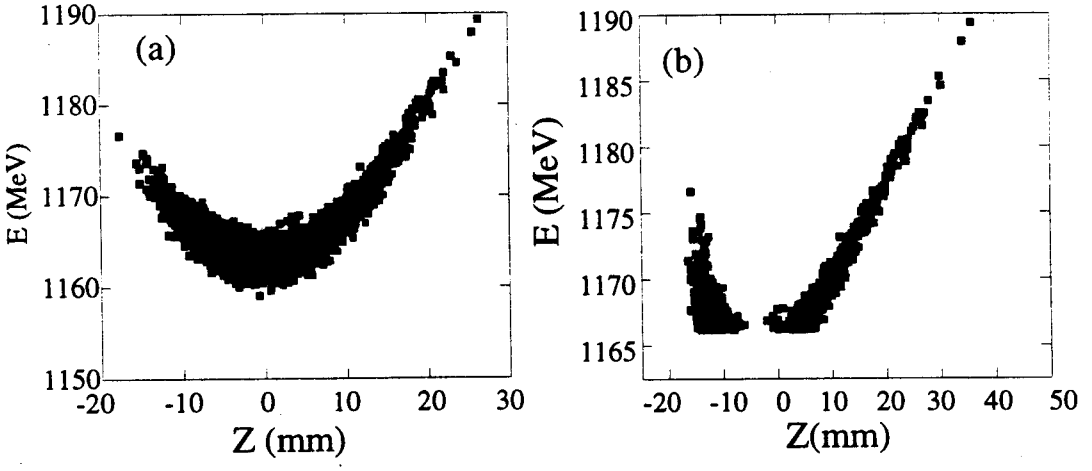

Figure 4.3.1. A simulation of the longitudinal phase space of the beam when the mean of the beam is put on the valley of the RF wave with an amplitude of 27 MV. (a) The phase space after the compressor RF section and (b) after an energy aperture of -2.0%.

asymmetry of $\sigma_E/E = 9.4\text{x}10^{-4}$ and Asymmetry = –0.41, respectively. The simulated bunch is placed on the crest or valley of the RF waveform and then sent through an energy aperture where the particles that are outside of the aperture are lost. Figures 4.3.1 a and b is a plot of the simulated beam longitudinal phase space before and after the energy aperture. In figure 4.3.2, the current losses as a function of compressor amplitude are plotted, and in this case there is an energy aperture of 1.8%.

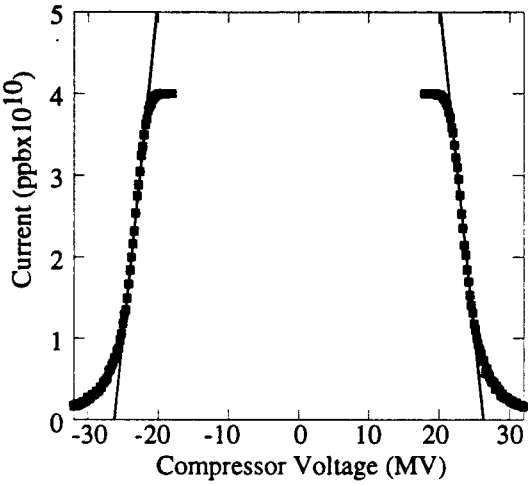

Figure 4.3.2. Simulation of the energy aperture at a current of $4.0\text{x}10^{10}$ ppb and an energy acceptance of 1.8 %. The current is fit to straight lines to determine the compressor voltages where half of the current is lost.

The simulation is repeated with energy acceptances ranging from 2.5% to 1.8% to

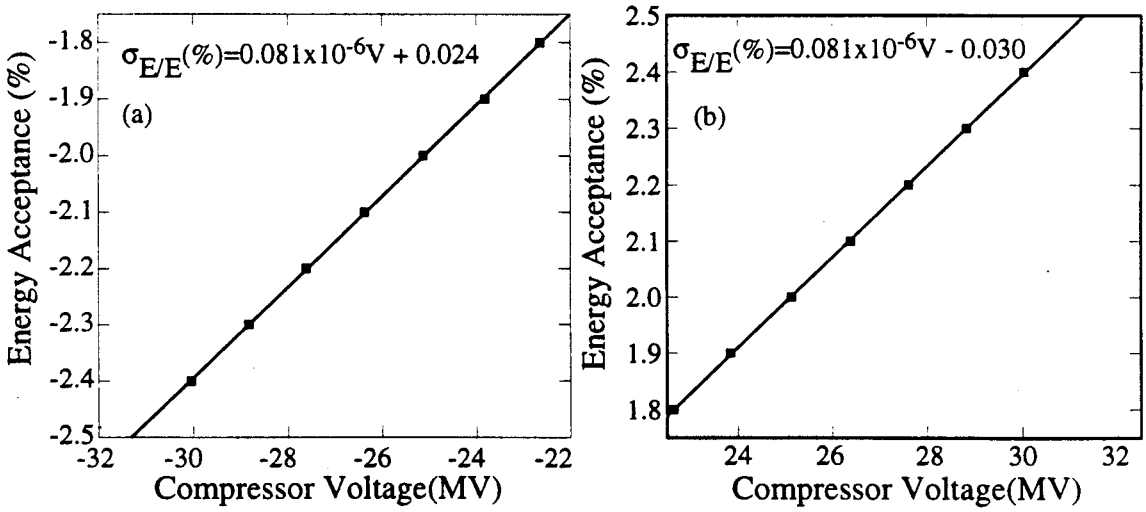

Figure 4.3.3. The half current RF amplitude at high current (I=$4.0\text{x}10^{10}$ ppb) for the electron transport line when the bunch is put on the (a) valley and (b) crest of the RF wave.

determine their half current amplitudes. Figure 4.3.3 a and b is a plot of the half current acceptance for the positive RF amplitude and negative amplitude. The curves are fit to a straight line and are used to determine the measured energy acceptance.
According to the simulation, the measured amplitudes of 27.2 and -24.7 MV gives an energy acceptance of +2.17% and -1.97%. Using this energy acceptance and the initial conditions listed in table 4.3.1 a simulation of the compressor line transmission can be made. The simulation was run ten times at each compressor setting and the results along with the measured values are plotted in figures 4.3.4 a and b.

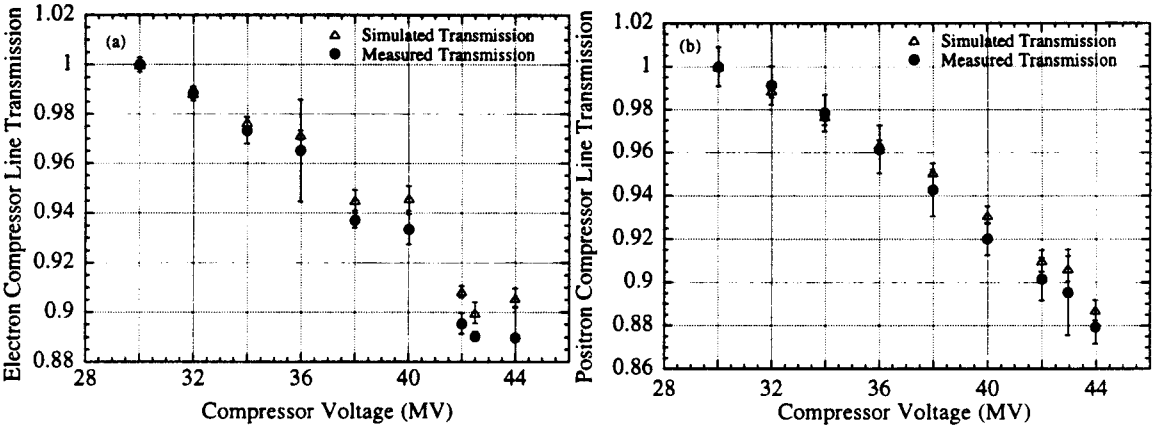

Figure 4.3.4. The measurement and simulation of the current transmission through the compressor transport line for the (a) electron and (b) positron beams.

The measured and simulated transmission curves have the same general shape, but there is a small offset between them. The offset between the measurement and simulation can be due to a systematic error in the initial bunch length measured in the damping ring. If the bunch length is increased by 4.5% the transmission curve align perfectly. Even though the positron energy aperture was not measured, the consistency between the electron and positron results gives reason to believe that the two transport lines have similar apertures.

Compression-Determination of R_{56} and T_{566} terms

For the bunch compressors, the degree of compression is determined from the R_{56} and T_{566} terms in the in the transport line and the compressor RF voltages. The R_{56} and T_{566} terms are given by

$$R_{56} = \alpha_{comp} L = \int \frac{\eta(s)}{\rho(s)} ds \text{ and } T_{566} = \frac{dR_{56}}{d\delta}$$

and are dependent on the dispersion and radius of curvature in the line, and are thus fixed, whereas the compressor voltage is adjustable. A measurement of the dispersion in the electron compressor transport line (figure 4.3.5) shows the difference between the design and actual dispersion [M. Minty, 1996]. The actual dispersion is lower by a few percentage points and will affect the bunch length.

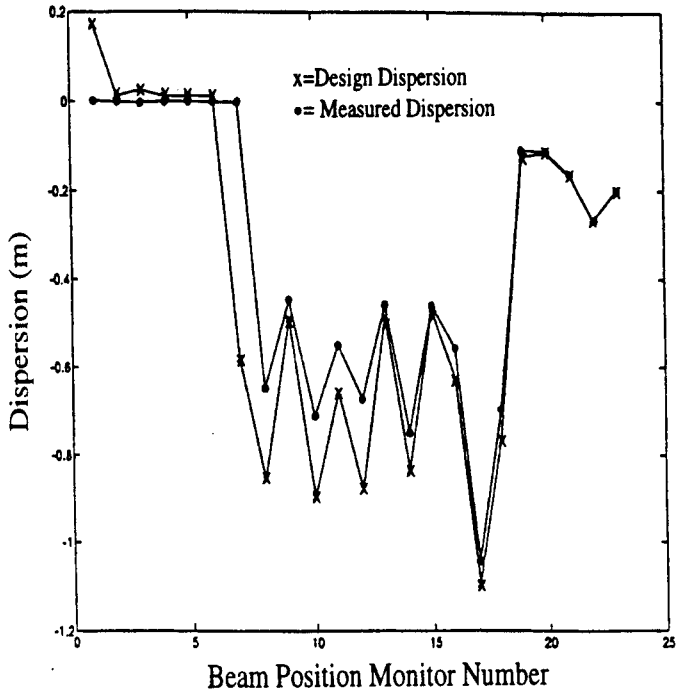

Figure 4.3.5. The measured and design dispersion for the electron transport line.

The R_{56} and T_{566} terms can be determined by calculating the χ^2 between the measured bunch distributions at the end of the linac and the simulated distributions. The χ^2 is given by

$$\chi^2 = \sum_{i=1}^{n} \frac{\left(S(t_i) - M(t_i)\right)^2}{S(t_i)}$$

where $S(t_i)$ and $M(t_i)$ are the simulated and measured bunch height at time t_i in the distribution. From χ^2, an R_{56} and T_{566} value for each compressor setting is calculated (figure 4.3.6). The mean value for the electron bunch is R_{56}=-586.9 mm/% and T_{566}=-1470 mm/%^{2} and for positrons R_{56}=-588.4 mm/% and T_{566}=-1490 mm/%^{2}.

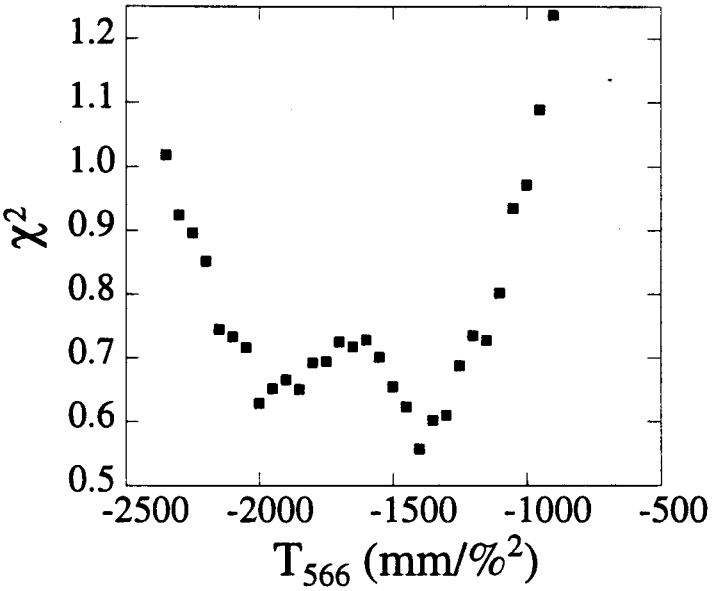

Figure 4.3.6. The χ^2 value as a function of T_{566} term with R_{56}=-582 mm/%. This simulation was done for the electron bunch with a compressor setting of 40 MV. For this particular simulation, χ^2 is at a minimum at -1450 mm/%^{2}.

A comparison between the measured RMS bunch length and width can now be made with simulation. The simulation was run ten times at each compressor setting and the results along with the measured values are plotted in figures 4.3.7 a and b. The errors denoted in the figure are the standard deviation of the simulation and measurement.

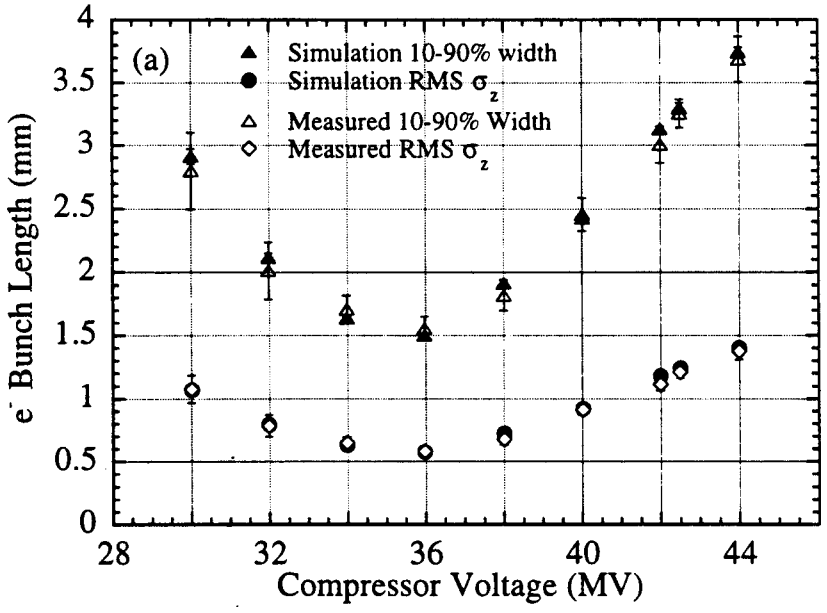

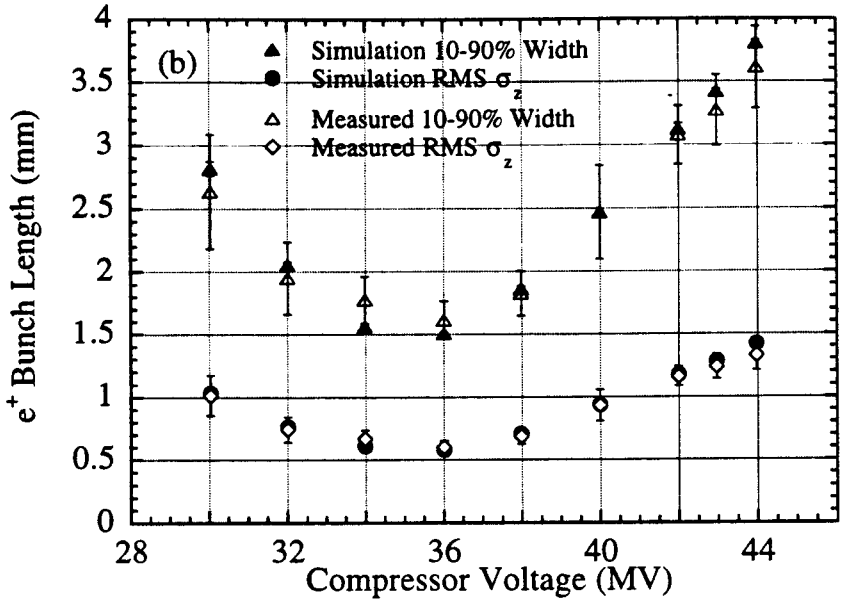

Figure 4.3.7. A comparison of the measured and simulated RMS and bunch widths as a function of compressor voltage for the (a) electron and (b) positron bunches.

A histogram of the simulated bunch distributions are displayed in figures 4.3.8 and 4.3.9 and they can be compared with the measured distributions in figures 4.2.4 and 4.2.5. There are several similarities between the measured and simulated distributions and they are: 1) The under compressed (30 MV) distributions have prominent tails. 2) The over compressed distributions are asymmetric in that they have a fast rise time and a more gradual fall time. 3) The fully compressed distributions are symmetric.

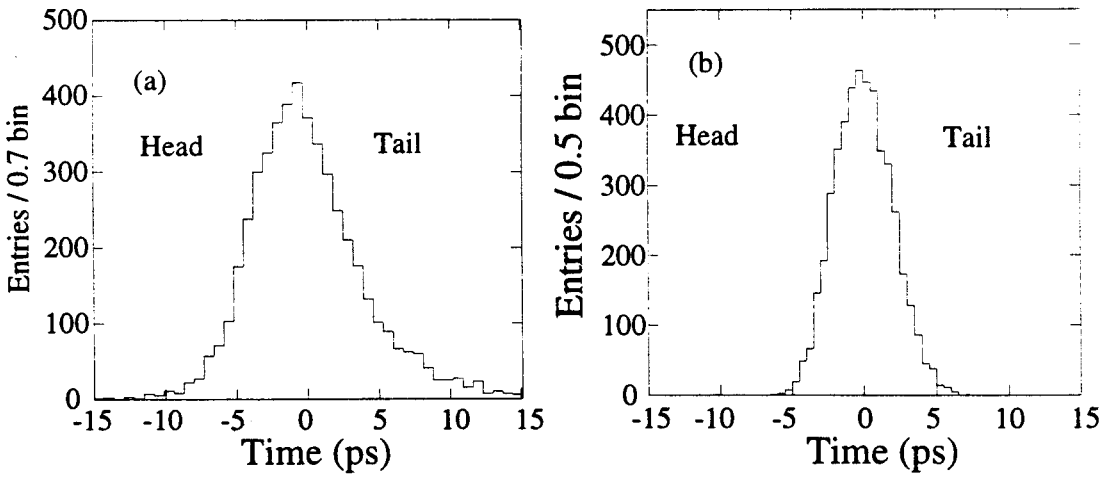

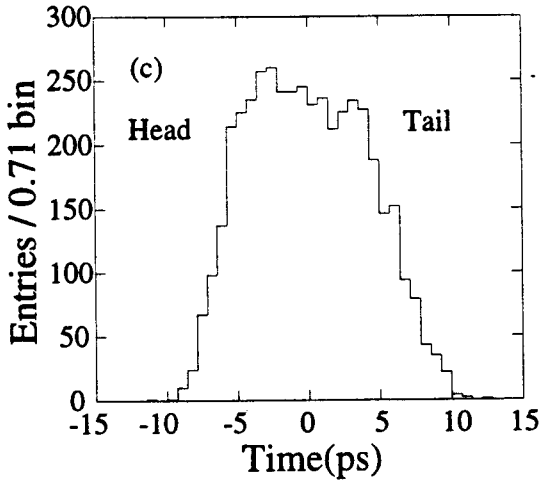

Figure 4.3.8. The simulated electron distributions for the compressor settings of (a) 30 MV, (b) 36 MV, and (c) 42.5MV.

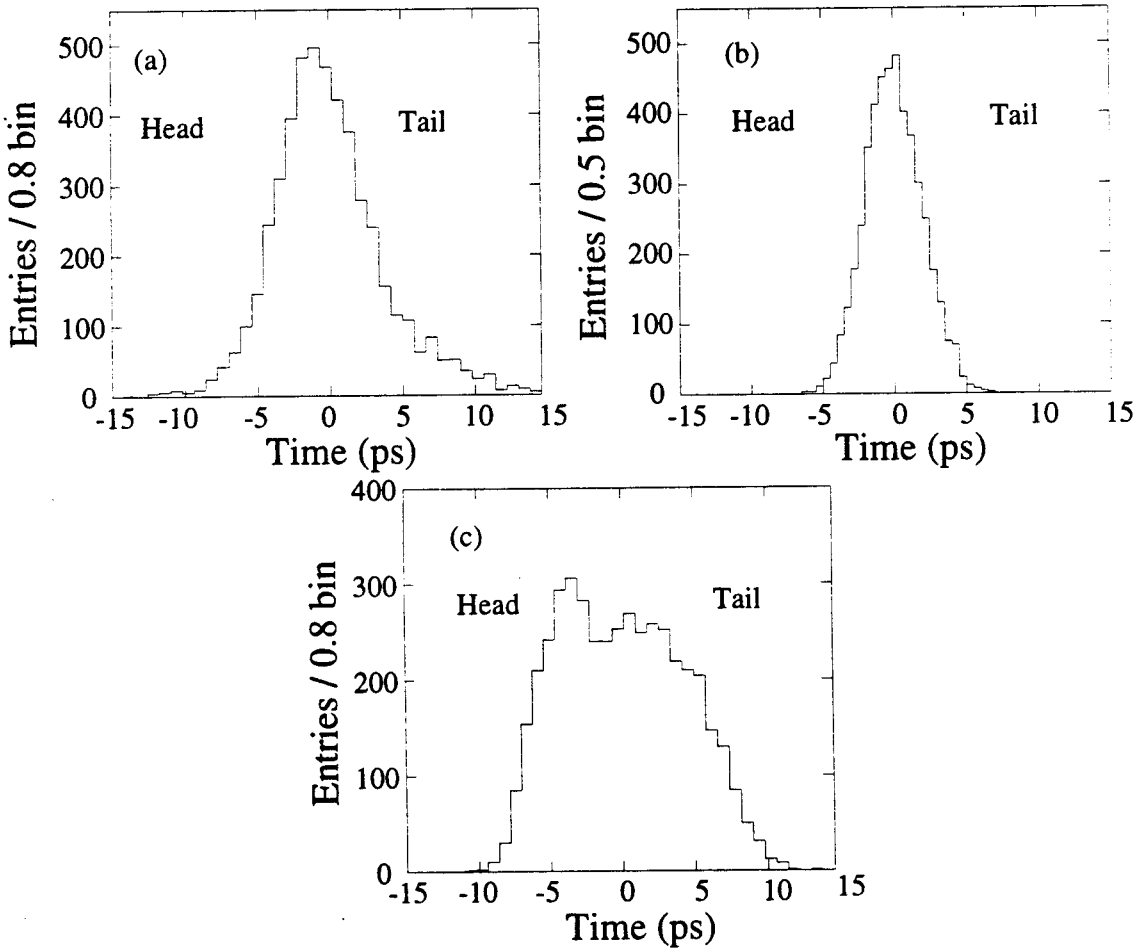

Figure 4.3.9. The simulated positron distributions for the compressor settings of (a) 30 MV, (b) 36 MV, and (c) 43MV.

Energy Spread at the End of the Linac

As described previously, the energy spread at the end of the linac is a result of the initial energy spread, the location of the bunch on the RF waveform, and the longitudinal wakefield energy losses in the accelerating structure cells. As described in section 4.2, the measured energy spread was minimized by adjusting the overall linac phase until the synchrotron light strip was minimized on the CCD camera. The energy spread was measured and then the overall linac phase was adjusted ±2 degrees and the measurement was repeated to verify that the minimum energy spread was indeed achieved. In several cases, most notably when the bunch was fully compressed, the minimum transverse size of the beam was not easily recognizable due to the large width on the synchrotron light strip. In most cases the minimum energy spread was measured and when the phase was adjusted, the width of the synchrotron light strip increased or the background in the arc and final focus was too large and a measurement could not be made.

For the simulation, the energy spread is minimized at each compressor setting, and a histogram of the resulting energy distribution is plotted and compared to the measured values. As an example, in figures 4.3.10-12 a, the results of the simulated energy distributions can be compared to the measured values in figure 4.2.7. The similarities worth noting are 1) When the bunch is under compressed there are a large number of high energy particles present in the tail. 2) The fully compressed distribution is quite wide, and this leads to a large energy spread. 3) The over compressed distribution is narrow, and it has a $\sigma_E = 23.4$ MeV when fit to a Gaussian distribution.

The longitudinal wakefield energy loss per accelerating structure cell is plotted for the three different compressor values in figure 4.3.10-12 b. It should be noted that by adjusting the bunch distribution the wakefield energy loss through the bunch can be altered, and this makes it possible for the wakefield energy loss to cancel out with the curvature of the RF waveform. This gives a substantial reduction in the energy spread of the bunch at the end of the linac (figure 4.3.10-4.3.12 c).

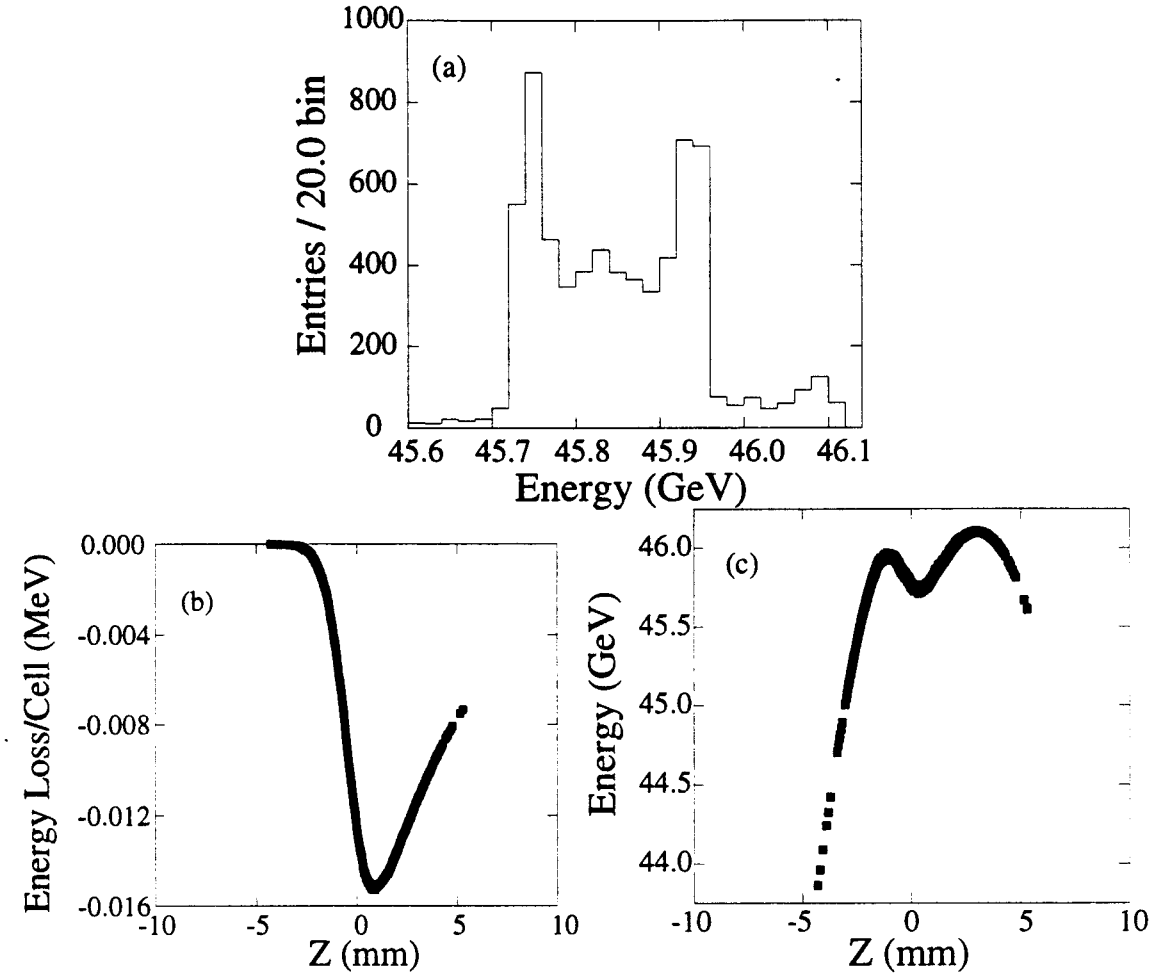

Figure 4.3.10. A (a) histogram of the energy distribution, (b) the longitudinal wakefield energy loss per cavity, and (c) the longitudinal phase space at the end of the linac for the electron bunch when the compressor voltage is 30 MV.

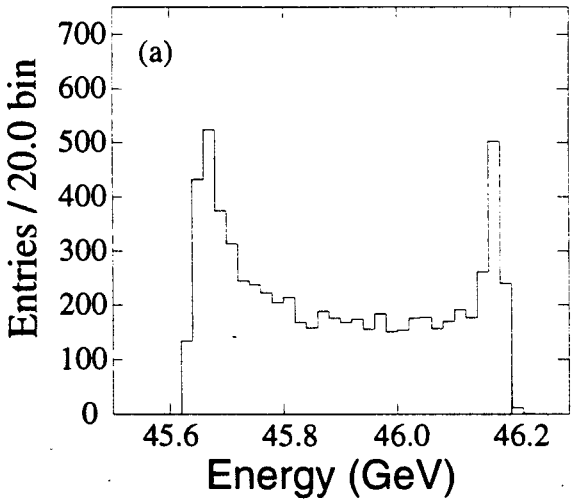

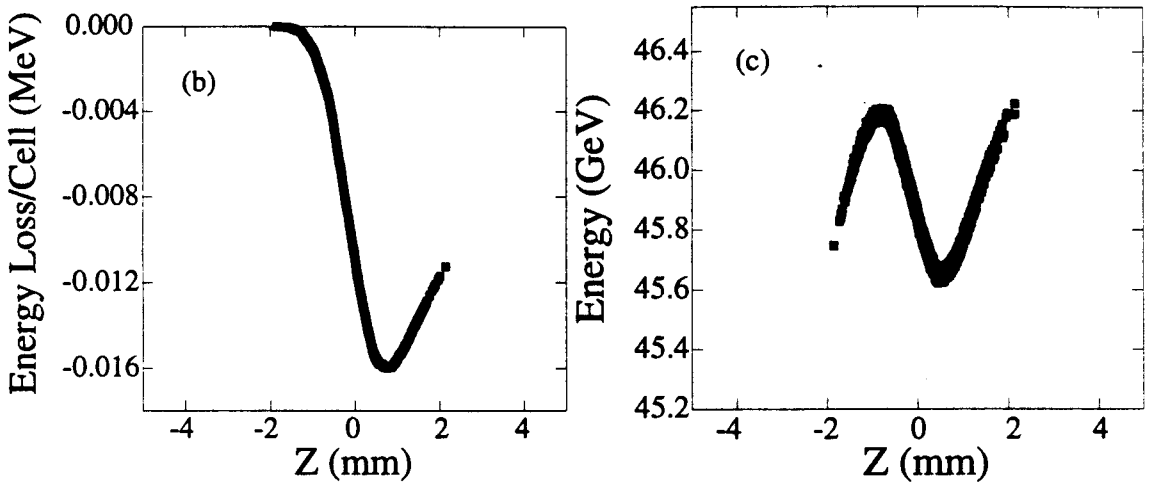

Figure 4.3.11. A (a) histogram of the energy distribution, (b) the longitudinal wakefield energy loss per cavity, and (c) the longitudinal phase space at the end of the linac for the electron bunch when the compressor voltage is 36 MV.

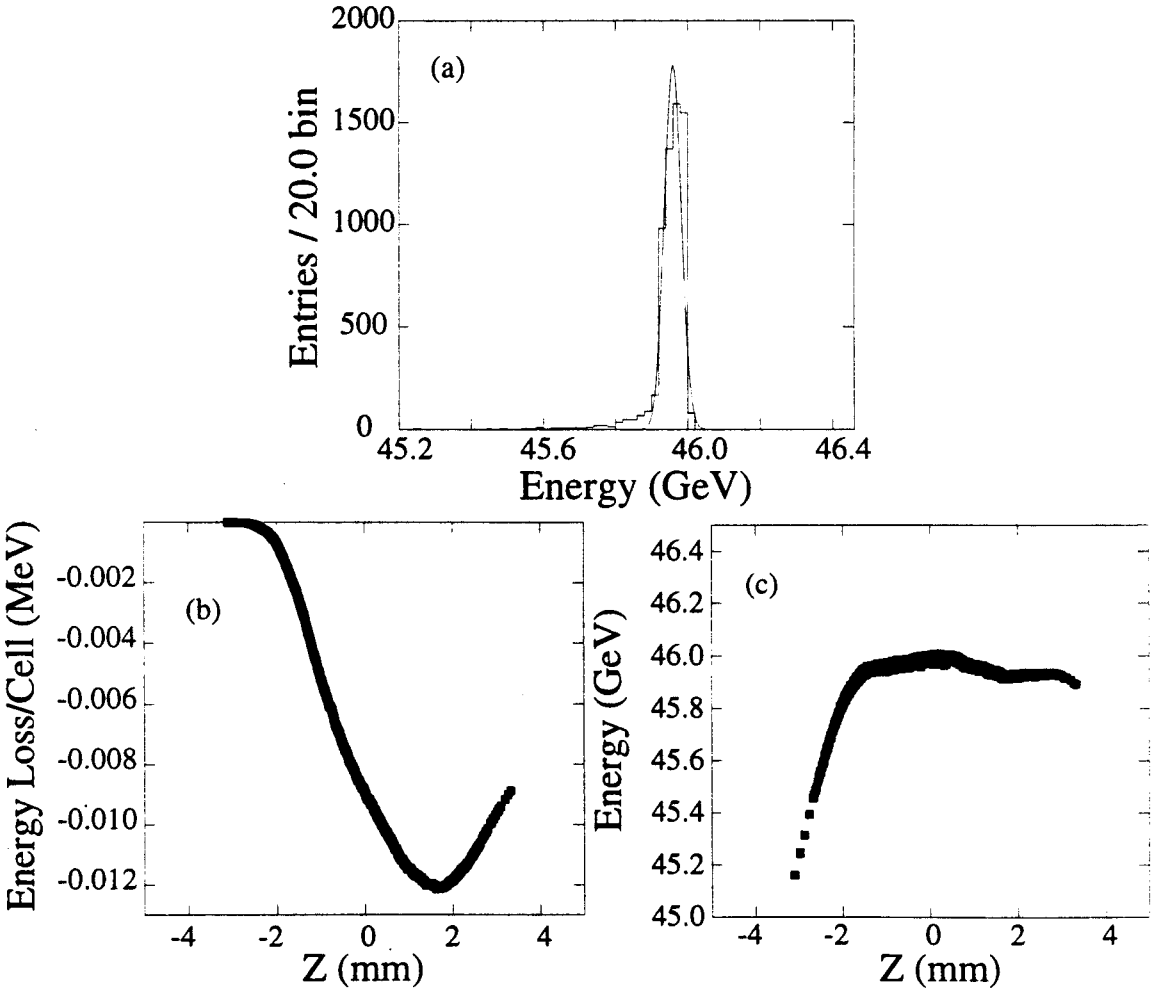

Figure 4.3.12. A (a) histogram of the energy distribution, (b) the longitudinal wakefield energy loss per cavity, and (c) the longitudinal phase space at the end of the linac for the electron bunch when the compressor voltage is 42 MV.

Comparisons between the measured and simulated energy widths at the end of the linac are displayed in figures 4.3.13 a and b.

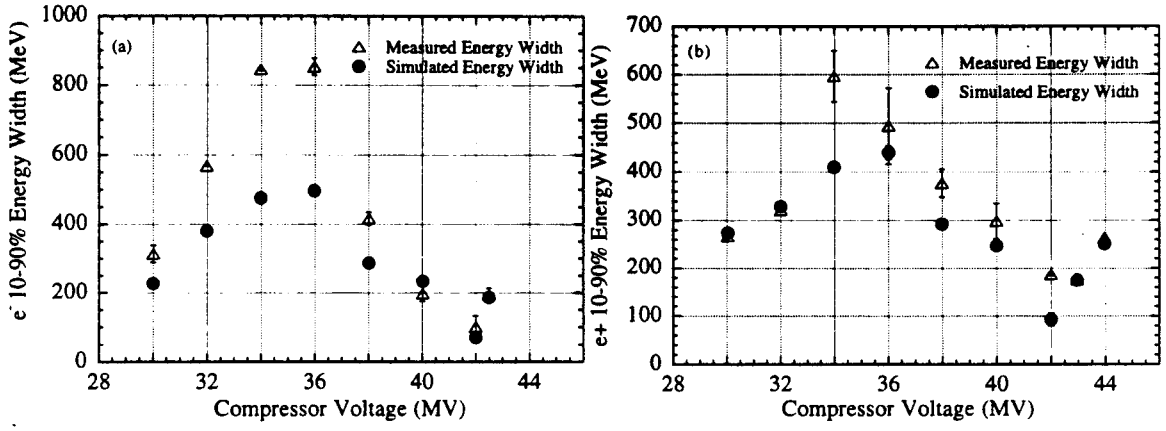

Figure 4.3.13. The simulated and measured energy width at the end of the linac for the (a) electron and (b) positron beams.

The measured and simulated results have the same general shape. As the bunch is fully compressed the energy width increases, however in the case of the electron measurements, the numbers disagree. The disagreement between the measured and simulated energy widths for the electron bunch results from the energy width not being properly minimized at the end of the linac. This conclusion can be reached in the following manner. For the compressor setting of 36 MV, the current for the electrons and positrons were nearly identical. Therefore one would expect that if the energy spread is minimized and all the other conditions are nearly identical the energy widths at the end of the linac should be identical, but they are not. The measured energy width for the electrons was 850 MeV and for positrons it was 500 MeV which is a 42% difference. By comparing the energy width for the case when the width was minimized and when the linac phase was adjusted by ±2 degrees it is evident that the energy width was not minimized (figures 4.3.14 a-b). The energy width when the phase increased by +2 degrees the energy width was 752 MeV which is 100 MeV lower than the alleged minimum energy width and when the energy width was decreased by -2 degrees the energy width was 1049 MeV. It is therefore evident that the minimum energy width was not measured for the electron bunch at the compressor voltage of 36 MV. If the wire scans are compared, figures 4.2.7 b and

4.3.14 b, it is hard to determine which scan is minimized thus it is hard to minimize the energy width for a near to fully compressed distribution.

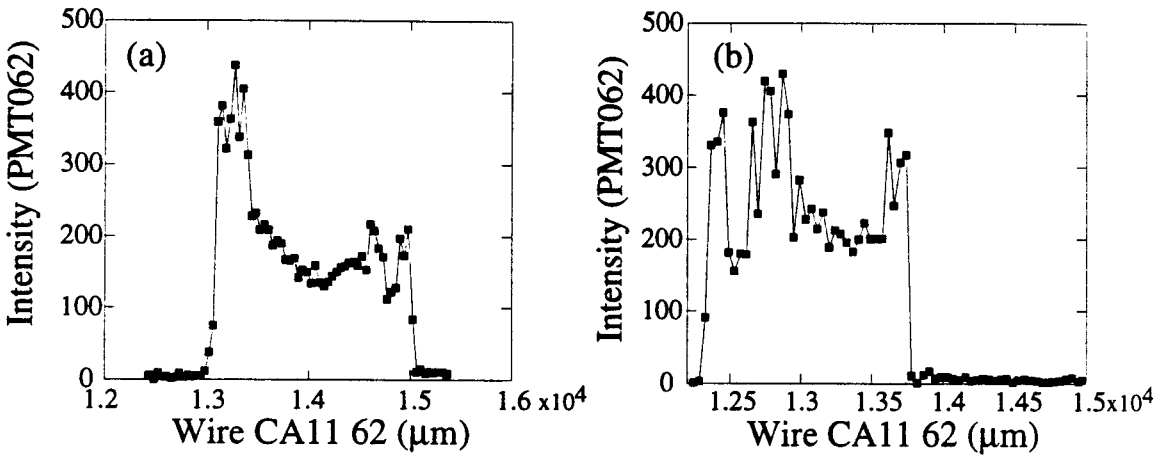

Figure 4.3.14. The measured energy distribution at the end of the linac when the compressor voltage is 36 MV and the phase of the linac is adjusted (a) -2 degrees, and (b) +2 degrees from the alleged minimized energy width.

Even though the simulation and measured energy widths differ in some cases it should not detract from the obvious benefits of an over compressed bunch distribution. By over compressing the bunch the energy width is reduced by a factor of 2, reducing the background in the detector region due to off energy particles and lowers the tolerance on chromatic tolerances in the final focus region.

Summary

The simulation of bunch compression and current losses in the electron and positron bunch compressors are in good agreement with the measured values validating our understanding of the bunch compressor. It also points out the systematic errors involved with the streak camera measurements. The energy spread measurement at the end of the linac agrees with the simulation in general but the systematic errors involved with the measurement are large. Measuring the transverse size of the beam at a smaller linac phase step is a possible method that can employed in the future to map out the energy spread phase space and reduce the systematic error of the location of the minimized energy spread.

Overall, the simulation of the longitudinal dynamics of the SLC provide a basis for our understanding of the machine and the method of bunch shaping to reduce the energy spread at the end of the linac is beneficial.

Chapter 5 Conclusions

Damping Rings

The measurements in the damping ring provided information about single particle as well as high current behavior of the bunch in the damping ring. The general conclusion from the measurements is that no difference between the positron and electron damping rings in terms of longitudinal dynamics. The new damping ring vacuum chamber installed prior to the 1994-1995 physics run of the SLC was a much needed improvement over the old chamber. It has allowed an increase in current from 3.0×10^{10} to 4.5×10^{10} particles per bunch without the pulse to pulse jitter that was characteristic of the old inductive impedance dominated vacuum chamber.

The injection and single particle measurements of the damping ring verify our understanding about the first 3 msec of the damping ring store. The bunch injected into the damping ring has a large energy spread and small bunch length. The bunch oscillates in size at the synchrotron frequency while it filaments and damps. Once the bunch has fully damped in longitudinal phase space it remains at its equilibrium bunch length until it is extracted from the ring.

As the current was increased in the damping ring several observations were made: 1) The bunch length increased due to the potential well distortion. With the old vacuum chamber the bunch distribution was parabolic in shape signifying that the dominate impedance is inductive. With the new vacuum chamber the distribution is asymmetric in shape signifying that the dominant impedance is resistive. 2) The energy spread increased as the current increased signifies a turbulent instability. 3) After the bunch length is fully damped, it is stable over the remaining store time of the ring.

These studies of the longitudinal dynamics in the damping ring serve as a basis for the design of the next generation damping rings. From these measurements several design aspects should be examined. For a linear collider to deliver high luminosity it needs to run at high current which creates problems for the damping ring in terms of longitudinal instabilities. The SLC damping rings vacuum chamber was rebuilt to eliminate this problem however an instability still exists. Another mode of operation which delivers high luminosity and eliminates the problems with running at high current is to increase the bunch repetition rate and lower the charge per bunch. In this dissertation it is shown that single particle (low current) behavior in the damping ring is understood, and it is not until the current is raised above 1.5×10^{10} particle per bunch that

an instability appears. This will reduce the chance of high current collective effects but at the same time wakefield effects between bunches should be studied.

Bunch Compressors and Linac

The effects of bunch shaping were measured in the compressor lines and in the linac. Even though they are separate transport lines and the bunches have slightly different initial conditions the bunch compressors for the electron and positron bunches give almost identical results. The expected minimum bunch length of 0.55 mm has been measured as well as the benefits of reducing the energy spread with an over compressed bunch distribution. The current losses in the compressor lines should be examined as to whether increasing the energy aperture will increase the luminosity without allowing unwanted low and high energy tails that are a nuisance in the final focus.

These studies of the bunch compressor and linac are also useful in terms of the design for the next generation linear collider. From these measurements it can be concluded that the following aspects should be examined. If the linac for the linear collider is x-band (11.424 GHz), the bunch length needs to be 5 times shorter than for an s-band collider. This creates several problems such as 1) How is a bunch that short created? Under normal compression techniques the initial energy spread must be small or two compressors are needed. 2) How is the bunch length that short measured? The best resolution streak camera right now is 180 fs and to reach that resolution will take a great effort. There are several other possible measurement techniques such as a wire scanner in a high dispersion region, but with an 0.2 mm bunch length a significantly high dispersion region is needed with a very small wire.

Overall

The longitudinal dynamics of the Stanford Linear Collider are understood. The measurements made on the damping ring, bunch compressor, and linac agree with theoretical predictions and simulation.

Although the longitudinal properties of the beam are not directly related to the luminosity of the collider, they do affect the luminosity in the following manner: 1) The spot size at the final focus is dependent on the energy spread. 2) the pinch effect is dependent on the bunch length. 3) BNS damping in the linac is dependent on the beam intensity and the bunch length. 4) The charge N, is dependent on the longitudinal

instabilities and energy spread. The largest gain in luminosity during the 1994-1995 run was done by increasing the charge per bunch.

The streak camera has been invaluable as a diagnostic device for the measurements of the longitudinal parameters of the SLC. There is no other tool at SLAC right now, other than the streak camera, which has the capability to measure sub millimeter bunch lengths in the linac. The systematic errors associated with the camera are now understood and the measured resolution matches its design specifications. The camera has now been upgraded with a GPIB interface and this will allow data acquisition without human feedback.

When calibrated, the bunch length cavities in the linac provide pulse to pulse measurements of the bunch length. The cavities are an ideal diagnostic tool that should be used to give up to date bunch length measurements for SLC operations.

The dominant impedance in the SLC damping rings is a resistive impedance, however there is still an instability in the rings. The instability does not place a limitation on running the SLC but its physics and effect on the impedance is unclear. A possible insight into this instability can be made by correlating the instability signal with streak camera bunch length measurements.

The pinch effects dependence on the bunch length has not been measured. By building a synchrotron light optics port for the streak camera at the final focus this dependence can be measured. Because the arcs are a bunch compressor, the bunch length at the final focus can be adjusted by varying the energy spread at the end of the linac with the linac phase. The quantification of the pinch effect with bunch length will help answer part of the luminosity questions for the next generation linear collider.

Appendix Feedback Circuit for the Pulsed Laser and Streak Camera

A Coherent Mira model 900-F titanium sapphire pulsed laser with a 200 femtosecond pulse length is used to measure the resolution of the streak camera. A feedback circuit was built to phase lock the laser with the SLC timing system. This makes it possible to trigger the streak camera off the SLC timing system while measuring the pulse width of the laser at the fastest streak speed. If the streak camera is triggered off of the laser the trigger jitter is ~ 200 ps and it is impossible to measure the pulse width on the two fastest streak speeds of the camera.

The laser frequency is 76.5 MHz, and the SLC timing system trigger used for the feedback circuit is 8.5 MHz. The two signals are input into the feedback circuit and are divided down to 4.25 MHz. The feedback circuit compares the phase between the two signals and drives the lasers piezo mirror which locks the frequency of the laser to the SLC timing system. The streak camera is then triggered at 60 Hz from the SLC timing system.

The laser signal is produced by a photodiode and is processed into a NIM signal as shown in figure AP1.1. The SLC timing signal is already a NIM signal so no processing is needed.

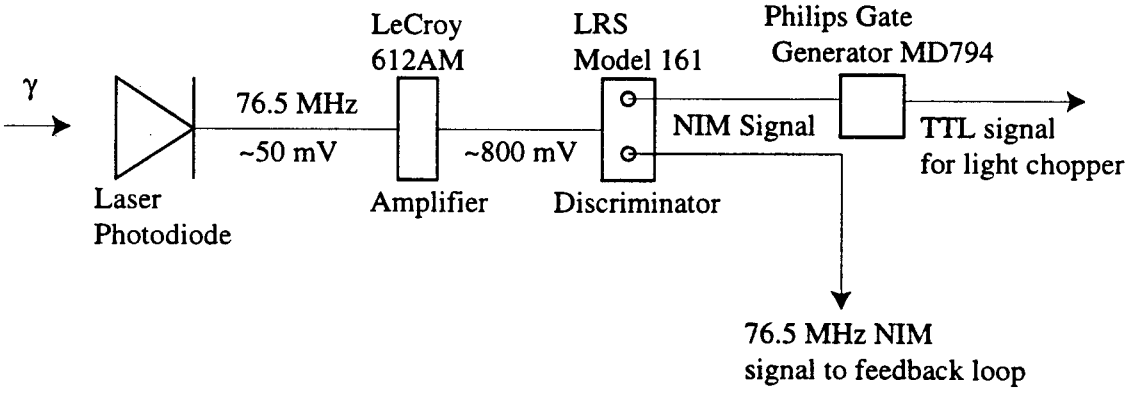

Figure AP1.1. A circuit diagram for the input signal from the laser photodiode signal. The light chopper is used in the set-up to reduce the overall laser intensity hitting the photocathaode of the streak camera.

The phase lock circuit is shown in figure AP.1.2. Because TTL logic is too slow at 76.5 MHz, MECL logic is used in the front end and then a switch is made to TTL. After the two signals have been divided down to 4.25 MHz, the phases of the two signals

are compared with a type D flip-flop. After the D flip-flop a low filter is used to remove noise while allowing one to track slow drifts in the laser frequency.

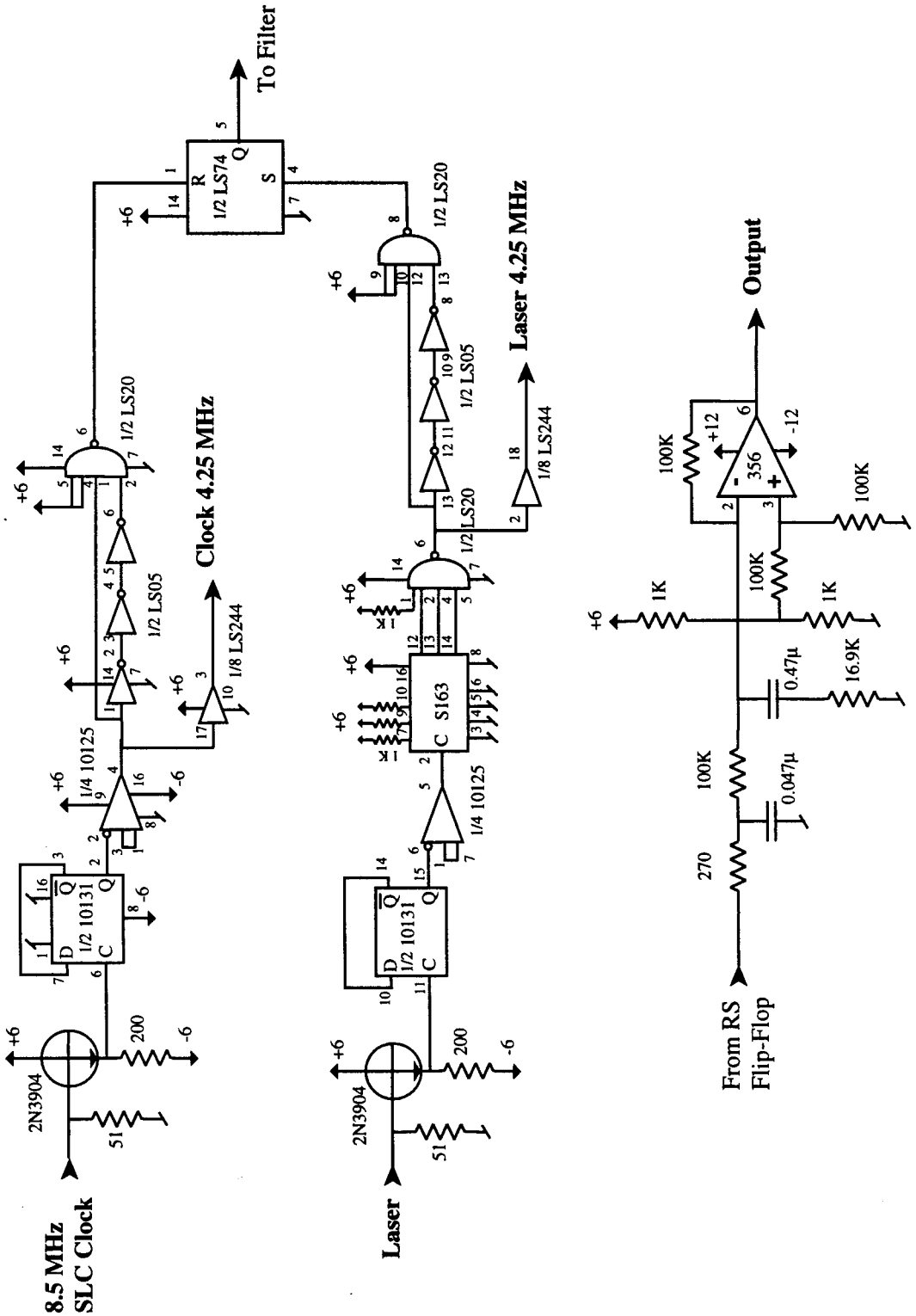

Figure AP1.2. A schematic of the feedback circuit.

The output voltage of the feedback loop is amplified with a Burleigh amplifier driver which drives the piezo mirror. The frequency change of the laser as a function of the driver voltage is plotted in figure AP1.3. The feedback circuit locks at a laser frequency of 76.500231 MHz, and the laser pulse is stable to ~20 ps on the fastest streak camera speed.

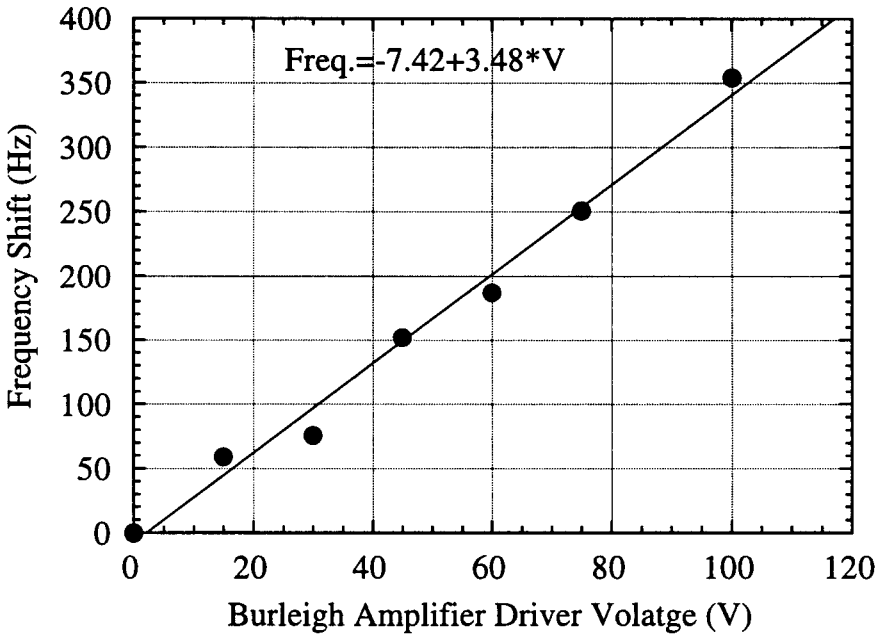

Figure AP1.3. A plot of the laser frequency as a function of the bias voltage of the Burleigh amplifier driver.

The feedback loop gain is given by

$$\text{Loop Gain} = K_p K_F K_{div} \frac{K_{VCO}}{jw}$$

where $K_{VCO} = 22$ rad / sec - V is the frequency change per volt due to the Burleigh amplifier, $K_p = 0.8$ V / rad is the voltage change per radian due to the phase detector, $K_{div} = 1/18$ is the laser frequency change in the feedback circuit, and , and $K_F = 1/RC$ is the desired frequency for the loop gain. For this circuit, it was chosen to run the circuit at 20 Hz so R=17 KΩ and C=0.47 μF.

Bibliography

Abe, F. et al, "Observation of Top Quark Production in Anti-P P Collisions"; FERMILAB-PUB-95-022-E, Mar 1995. 18pp. Published in Phys. Rev. Lett.74: 2626-2631,1995

Allen, M.A., J.M. Paterson, John R. Rees, P.B. Wilson, "Beam Energy Loss to Parasitic Modes in Spear II"; Presented at Part. Accel. Conf.., Washington, D.C., Mar 12-14, 1975. Published in Part. Accel. Conf. 1975: 1838.

Babenko, E., "Length Monitors for Single Bunches"; (Novosibirsk State U.). SLAC-CN-396; 18 pp, Mar 1993..

Balakin, V.E., A. Novokhatsky, V. Smirnov, "VLEPP: Transverse Beam Dynamics", Proc. 12th Int. Conf. High Energy Accel., Fermilab: 119; 1983.

Bane, K., P. Wilson, "Longitudinal and Transverse Wake Potential in SLAC," Geneva 1980, Proceedings, High Energy Accelerators, p592-596.

Bane, K. , et al, "High Intensity Single Bunch Instability Behavior in the New SLC Damping Ring Vacuum Chamber," SLAC-PUB-95-6895; May 1995. 3 pp. Presented at 16th IEEE Particle Accelerator Conference (PAC 95) and International Conference on High Energy Accelerators, Dallas, Texas, 1-5 May 1995.

Bane, K., " Bunch Lengthening in the SLC Damping Rings," SLAC-PUB-5177, Feb. 1990. 51 pp. Contributed to Impedance and Bunch Instability Workshop Adv. Photon Source, Argonne, IL, Oct 31 - Nov. 1, 1989.

Chao, A.W., "Physics of Collective Beam Instabilities in High-Energy Accelerators," New York, USA: Wiley (1993) 371 p. (Note: A good reference for Vlasov's equation.)

Decker, F.J., R. Holtzapple, T. Raubenheimer, " Over Compression, A Method to Shape the Longitudinal Bunch Distribution for a Reduced Energy Spread," SLAC-PUB-6604, Jul 1994, 3pp. Presented at 17th International Linear Accelerator Conference (LINAC 94), Tsukuba, Japan, 21-26 Aug 1994.

Early, R., et al, "Proposed Emittance Upgrade for the SLC Damping Rings," SLAC-PUB-6559, Jun 1994, 3pp. Presented at the 4th European Particle Accelerator Conference (EPAC 94), London, England, 27 Jun-1 Jul 1994.

Emma, Paul, " The Stanford Linear Collider," SLAC-PUB-95-6866, May 1995. 5pp. Talk given at the 15th IEEE Particle Accelerator Conference (PAC 95) and International Conference on High Energy Accelerators, Dallas, Texas, 1-5 May, 1995.

Farkas, Z.D., H.A. Hoag, G.A. Loew, P.B. Wilson. "SLED: A Method of Doubling SLAC's Energy," SLAC-PUB-1453, June, 1974. 7 pp. Presented at 9th Int. Conf. on High Energy Accelerators, SLAC, Stanford, Calif., May 2-7, 1974.

Haissinski, J., "Exact Longitudinal Equilibrium Distribution of Stored Electrons in the Presence of Self-Fields," Il Nuovo Cimento, Vol. 18B, N.1, 11 November 1973, p. 72.

Hollebeek, R., In Proceedings of the 1983 SLAC Summer Institute SLAC-Report-2167 (1984).

James, F., M. Roos, "'Minuit' A System for Function Minimization and Analysis of the Parameter Errors and Correlations," CERN-DD/75/20, Jul 1975. 38 pp. Computer Physic Commun. 10 (1975) 343-367.

Krejcik, P., (private communication) 1995.

Kulikov, A., et al, "The Monitor of Single Bunch Length," April 11, 1986, unpublished.

LEP Design Report: Vol. 2. "The LEP Main Ring", CERN-LEP/84-01, Jun 1984. 269pp.

Loew, G.A., J.W. Wang, "Minimizing the Energy Spread within a Single Bunch by Shaping its Charge Distribution," SLAC-PUB-3598, Mar. 1985. 3pp. Poster paper presented at Particle Accelerator Conf., Vancouver, Canada, May 13-16, 1985. Published in Particle Accel. Conf. IEEE 1985: 3228.

McCormick, D., "Fast Ion Chambers for SLAC," SLAC-PUB-6296, Jul 1993. 3pp. Presented at 1993 Particle Accelerator Conference (PAC 93), Washington, DC, 17-20 May 1993.

Minty, M., (private communication) 1996.

Montanet, L., et al, "Review of Particle Properties. Particle Data Group," Phys. Rev. D50: 1173-1823, 1994.

Munro, Ian H., Andrew P. Sabersky, " Synchrotron Radiation as Modulated Source for Fluorescence Lifetime Measurements and for Time-Resolved Spectroscopy," Synchrotron Radiation Research, Ed. by Herman Winick and S. Doniach, Plenum Press, New York and London, 1980, p. 323-350.

Myers, S., "LEP Status and Plans," CERN-SL-95-66-DI, Jun 1995. 6pp. Presented at the 16th Biennial Particle Accelerator Conference - PAC 95, Dallas, Texas 1-5 May 1995.

Panofsky, W.K.H., W. Wenzel, "Transverse Deflection of Charged Particles in Radiofrequency Fields," Rev. Sci. Instrum. 27: 967, 1956.

Richter, Burton, "Perspectives on Large Linear Colliders," SLAC-PUB-4482, Nov. 1987. 16 pp. Invited talk at Int. Conf. on Physics in Collision, Tsukuba, Japan, Aug 25-27, 1987. Published in Physics in Collision 1987: 423.

Robinson, K.W., "Radiation Effects in Circular Electron Accelerators," Physical Review, Volume 111, Number 2, July 15, 1958.

Ross, M.C., et al, "Wire Scanners for Beam Size and Emittance Measurements at the SLC," SLAC-PUB-5556, May 1991. 3pp. Presented at IEEE Particle Accelerator Conf., San Francisco, CA May 6-9, 1991. Published in Particle Accel. Conf: IEEE 1991: 1201-1203.

Ruggiero, A.G., "Theory of Longitudinal Instability for Bunched Electron and Proton Beams", IEEE Trans. Nucl. Sci. Ns-24 (1977) No.3, 1205, 1207.

Sacherer, F., "Methods for Computing Bunched-Beam Instabilities," CERN/SI-BR/72-5 September 1972.

Sands, M., "The Physics of Electron Storage Rings: An Introduction," SLAC-0121, Nov 1970. 172pp.

Seeman, J., "Observation of High Current Effects in High-Energy Linear Accelerators," SLAC-PUB-5707, Dec 1991. 39pp. Invited talk given at 1990 Join U.S.-CERN School on Particle Accelerators: Frontiers of Particle Beams, Intensity Limitations, Hilton Head Isl., S.C., Nov. 7-14, 1990. Published in CERN US PAS 1990: 255-292.

Siemann, R. H. , " Computer Models of Instabilities in Electron Storage Rings," CLNS 84/626, Oct 1984. 75pp. Presented at 3rd Summer School on High Energy Particle Accelerators, Upton, NY, Jul 6-16, 1983. Published in BNL Accel. School 1983: 368.

Siemann, R.H., "Bunched Beam Diagnostics," Batavia 1987/Ithaca 1988, Proceedings, Physics of Particle Accelerators, 430-471.

Simopoulos, C., R. L. Holtzapple, "Damping Rate Measurements in the SLC Damping Rings", SLAC-PUB-95-6813, Jun 1995. 3pp. Presented at 16th IEEE Particle Accelerator Conference (PAC 95) and International; Conference on High Energy Accelerators (IUPAP), Dallas, Texas, 1-5 May 1995.

SLAC Report No. 229, "SLAC Linear Collider Conceptual Design Report," June 1980. 188pp.

Tigner, M., Nuovo Cimento 37, 1228, 1965.

Weiland, T. , "On the Computation of Electromagnetic Fields Excited by Relativistic Bunches of Charged Particles in Accelerating Structures," CERN/ISR-TH/80-07, Jan 1980, 36pp.

Wiedemann, H., " Linear Collider: A Preview," SLAC-PUB-2849, Nov. 1982. 81 pp. Lecture given at 9th SLAC Summer School on Particle Physics, Stanford, Calif., Jul 27-Aug 7, 1981. Published in SLAC Summer Inst. 1981:313.

Wiedemann, H., "Bunch Length as a Function of the Compressor Voltage," SLAC-CN-117, Sept 1981. 2pp.

Wiedemann, H., Particle Accelerator Phyics: Basic Principles and Linear Beam Dynamics, 445pp, 1993.

Wiedemann, H., "Particle Accelerator Physics: 2: Nonlinear and Higher Order Beam Dynamics," Berlin, Germany: Springer, 1995, 464p.

Wilson, P. , "High-Energy Electron Linacs: Applications to Storage Ring RF Systems and Linear Colliders," SLAC-PUB-2884, Feb 1982. 200pp. Lecture given at 1981 Summer School on High Energy Particle Accelerators, Batavia, IL, Jul 13-24, 1981. Published in Fermilab Summer School, 1981 v.1:450.